Technische Universität München
TUM School of Natural Sciences

TUM

Ultrahigh Molecular Weight Polypropylene – Synthesis and Processing of a High-Performance Polymer

Lucas Stieglitz

Vollständiger Abdruck der von der TUM School of Natural Sciences der Technischen

Universität München zur Erlangung eines

Doktors der Naturwissenschaften (Dr. rer. nat.)

genehmigten Dissertation.

Vorsitz: Prof. Dr. Klaus Köhler

Prüfer*innen der Dissertation:

      1.   Prof. Dr. Dr. h.c. Bernhard Rieger
      2.   Prof. Dr. Tom Nilges

Die Dissertation wurde am 29.12.2022 bei der Technischen Universität München eingereicht

und durch die TUM School of Natural Sciences am 24.01.2023 angenommen.

"Success is not final; failure is not fatal:

it is the courage to continue that counts."

Winston Churchill

Acknowledgement

Zuletzt geht mein Dank an meine Studienkollegen und Freunde von *Lazio Chrom* für die tollen Abende und Ausflüge abseits der Chemie! Leider nahm die Häufigkeit der Events durch unsere Promotionen ab, doch umso mehr lernte ich diese zu schätzen.

Mein größter Dank geht an meine Familie: meiner Mutter, meinem Vater und meiner Schwester. Ohne euch wäre das Studium und die Promotion nicht möglich gewesen. Ihr habt mich immer sowohl moralisch als auch finanziell unterstützt, dafür bin ich euch unfassbar dankbar! Zuletzt geht mein allergrößter Dank an dich, liebe Tamara, dass du mich während des Studiums und der Promotion stets unterstützt, mir den Rücken gestärkt und mich die Arbeit vergessen lassen hast. Danke, dass du an meiner Seite bist!

Table of Contents

List of Publications

1. Stieglitz, L., Henschel, D., Pehl, T., and & Rieger, B., *In Situ* Activation: Chances and Limitations to Form Ultrahigh Molecular Weight Syndiotactic Polypropylene with Metallocene Dichlorides. *Organometallics*, **2021**, 40, 4055-4065.

2. Stieglitz, L.,[†] Lenz, T. M.,[†] Saurwein, A., and Rieger, B., Perfectly Isotactic Polypropylene upon *In Situ* Activation of Ultrarigid *meso* Hafnocenes. *Angew. Chem. Int. Ed.*, **2022**, *61*, e202210797. † These authors contributed equally.

3. Wu, R., Wu, W.K., Stieglitz, L., Gaan, S., Rieger, B., and Heuberger, M., Recent advances on α-diimine Ni and Pd complexes for catalyzed ethylene (Co)polymerization: A comprehensive review, *Coord. Chem. Rev.*, **2023**, 474, 214844.

4. Wu, R., Stieglitz, L., Lehner, S., Milijana, J., Rentsch, D., Neels, A., Rieger, B., Heuberger, M., Gaan, S., Fluorine and Hydroxyl Containing Unsymmetrical α-Diimine Ni (II) Dichlorides with Improved Catalytic Performance for Ethylene Polymerization, *Eur. Polym. J.*, **2023**, *186*, 111830.

5. Stieglitz, L., Geiger, C., Großmann, F. P., Kränzlein, M., Rodewald, K., Müller-Buschbaum, P., and Rieger, B., Fiber Spinning of Ultrahigh Molecular Weight Isotactic Polypropylene: Melt Spinning and Melt Drawing, *ChemPlusChem*, **2023**, *88*, e202300045.

6. Cholewa, S.,[†] Stieglitz, L.,[†] Jaksch, A., Rieger, B., and Drummer, D., Tailored Syndiotactic Polypropylene Feedstock Material for Laser-Based Powder Bed Fusion of Polymers: Material Development and Processability, *ACS Appl. Polym. Mater.*, **2023**, DOI: 10.1021/acsapm.2c02112.† These authors contributed equally.

Abstract

Since the discovery of commodity plastics in the 20th century, these polymers have been continuously improved in terms of macromolecular characteristics, thus opening up new applications and fields of use. Ultrahigh molecular weight polypropylene (UHMW-PP) is probably the most promising (commodity) polymer for future implementation as a high-performance material. Herein, the synthesis and subsequent processing of UHMW-PP is described. For many decades, the synthesis of UHMW-PP by metallocene catalysis revealed two main problems: the constrained productivity of the catalysts applied (1) and reduced molecular weight of the polymers produced (2). Both problems are avoided by replacing the commonly methylaluminoxane (MAO) activation of metallocene dichloride (pre-)catalysts by *in situ* activation using triisobutylaluminum (TIBA) and $[Ph_3C][B(C_6F_5)_4]$. This activation is already established for isotactic PP (iPP), but not yet for syndiotactic PP (sPP) – thus, the synthesis of UHMW-sPP in combination with a high catalyst's productivity was enclosed within this thesis. Simple polymer processing such as compression molding is feasible for all thermoplastics – however, advanced methods such as extrusion for fiber spinning are considered nearly impossible for UHMW polymers because the molecular weight tremendously increases the polymer's melt viscosity. Despite the poor omens, processing of UHMW-PP in terms of fiber spinning or additive manufacturing (AM) was investigated. Both techniques yielded final parts of great interest, both in the academic and industrial research. For the implementation of these polymers in various areas, the polymer production has to be highly economic. Unfortunately, catalysts for the synthesis of iPP accumulate wasteful C_S-symmetric *meso* metallocenes, which are known for producing atactic PP (aPP) and thus need to be separated. Therefore, the polymerization of propylene utilizing a C_S-symmetric *meso* hafnocene was investigated to expand the scope of synthesized catalysts, reveal unknown potential and thus improve the sustainability of the catalyst synthesis. Using the *in situ* activation, an isomerization was induced by aluminum-alkyls, leading to perfectly isotactic PP applying both, *meso* hafnocene and an isomeric *rac*/*meso* mixture.

Zusammenfassung

Seit der Entdeckung der Standardkunststoffe im 20. Jahrhundert wurden diese Polymere hinsichtlich ihrer makromolekularen Eigenschaften stetig verbessert und somit neue Anwendungen und Anwendungsgebiete erschlossen. Ultrahochmolekulares Polypropylen (UHMW-PP) ist das wohl vielversprechendste (Standard-)Polymer für den zukünftigen Einsatz als Hochleistungspolymer. In dieser Arbeit wird die Synthese und Verarbeitung von UHMW-PP beschrieben. Die Synthese von UHMW-PP durch Metallocenkatalyse offenbarte jahrzehntelang zwei Hauptprobleme: die verminderte Produktivität der verwendeten Katalysatoren (1) und das geringe Molekulargewicht der erzeugten Polymere (2). Beide Probleme werden vermieden, indem die übliche Methylaluminoxan (MAO) Aktivierung der verwendeten Metallocendichlorid (Vor-)Katalysatoren durch die *in situ* Aktivierung mit Triisobutylaluminium (TIBA) und $[Ph_3C][B(C_6F_5)_4]$ ersetzt wird. Diese Aktivierung ist für isotaktisches PP (iPP) bereits etabliert, jedoch noch nicht für syndiotaktisches PP (sPP) – daher war die Synthese von UHMW-sPP in Kombination mit einer hohen Produktivität des Katalysators ein zentrales Thema dieser Arbeit. Eine einfache Polymerverarbeitung, wie das Formpressen, ist für alle Thermoplaste möglich – fortgeschrittene Methoden, wie etwa die Extrusion für Faserspinnen, werden jedoch für UHMW-Polymere als nahezu unmöglich betrachtet, da das Molekulargewicht die Schmelzviskosität des Polymers enorm erhöht. Trotz der schlechten Vorzeichen wurde die Verarbeitung von UHMW-PP in Form von Faserspinnen oder Additive Fertigung (AM) untersucht. Beide Techniken führten zu Produkten, die sowohl in der akademischen als auch in der industriellen Forschung von großem Interesse sind. Für den Einsatz dieser Polymere in verschiedenen Bereichen muss die Polymerproduktion jedoch sehr wirtschaftlich sein. Leider fallen bei Katalysatoren, die für die Synthese von iPP geeignet sind, unwirtschaftliche C_s-symmetrische *meso* Metallocene an, die für die Herstellung von ataktischem PP (aPP) bekannt sind und daher abgetrennt werden müssen. Daher wurde die Polymerisation von Propylen unter Verwendung eines C_s-symmetrischen *meso* Metallocens untersucht, um das Anwendungsgebiet der synthetisierten Katalysatoren zu erweitern, unbekanntes Potenzial aufzudecken und somit die Nachhaltigkeit der Katalysatorsynthese zu verbessern. Mit der *in situ*-Aktivierung wurde eine Isomerisierung durch Aluminiumalkylen induziert, was zu perfekt isotaktischem PP führte, wenn sowohl *meso*-Hafnocen als auch eine isomere *rac*/*meso*-Mischung verwendet wurde.

List of Abbreviations

AM   additive manufacturing

aPP   atactic polypropylene

CAD   computer-aided design

Cp   cyclopentadienyl

DFT   density functional theory

EBFI ethylene bridged fluorenyl-indenyl

Flu   fluorenyl

HD-PE high density polyethylene

HT   high temperature

iPP   isotactic polypropylene

IR   infrared

LD-PE low density polyethylene

MAO   methylaluminoxane

PBF-LB/P laser-based powder bed fusion of polymers

PE   Polyethylene

PEEKs poly(ether ether ketone)s

PET   polyethylene terephthalate

PIs   polyimides

PP   polypropylene

PS   polystyrene

PSUs polysulfones

rac *racemic*

rds rate determining step

sPP syndiotactic polypropylene

TIBA triisobutylaluminum

TMA trimethylaluminum

TrBCF $[CPh_3][B(C_6F_4)_4]$

UHMW-aPP ultrahigh molecular weight atactic polypropylene

UHMW-iPP ultrahigh molecular weight isotactic polypropylene

UHMW-PE ultrahigh molecular weight polyethylene

UHMW-PP ultrahigh molecular weight polypropylene

UHMW-sPP ultrahigh molecular weight syndiotactic polypropylene

**UV** ultraviolet

XRD X-ray diffraction

1 Introduction

The term polymer was decisively coined by Hermann Staudinger in his work *Über Polymeri-sation* in 1920, when he claimed that polymers consist of many covalently bonded monomeric units.[1] However, the industrial large scale production of commodity polymers only became viable with the establishment of the coordinative polymerization of olefins by *Ziegler* and *Natta* in the 1950s.[2,3] 70 years after the industrialization of commodity plastics, the daily life of mankind has tremendously changed since that. Nowadays, polymers can be found in every sector of our life, e.g. as packaging materials, in the construction sector, in medical applications, in automobiles or in consumer products, such as a cutting board in our kitchen.

100 years after the initial manifesto of *Staudinger*, the polymer industry has been deeply researched and has come so far that for every specific application or problem a suitable polymer can be tailored. However, regarding the next century of polymer chemistry, three main aspects need to be covered according to the advisory board of *Macromolecular Chemistry and Physics*: new properties and applications (1), new synthesis methods (2), and sustainability (3). The majority of the advisory board clarified that "the development and discovery of polymers with new properties and applications will be one of the most important topics of the future".[4]

Nowadays, polyolefins are still the majority of mass-customized and used polymers globally (Figure 1). Within the last 70 years, their industrial production was improved to increase the productivity and thus profitability. Besides this, the final plastic has been consistently developed further, enabling to expand their application. Considering the three main aspects to be tackled in the next century of polymer research, the main goal for commodity plastics, particularly polyolefins, seems to be obvious: improve the properties and application of the well-known and deeply investigated polymers, even perhaps to be used as high performance polymers with surprisingly effective and outstanding properties.

Polyethylene (PE), number one world's produced polymer,[5,6] has already undergone this evolution: high density polyethylene (HD-PE) and low density polyethylene (LD-PE) with a low to medium high molecular weight is applied e.g. as packaging materials, films, toys or pipes, whereas ultrahigh molecular weight polyethylene (UHMW-PE) exhibits due to its ultrahigh molecular weight ($M_w > 1000$ kg/mol) enhanced mechanical properties compared to

HD-PE, enabling application as joint replacements or strong fibers in bulletproof fabrics.[7–9] Contrary to PE, polypropylene (PP) has not undergone this renaissance so far. However, due to its methyl moiety in the polymeric chain, the (degree of) tacticity and thus the macromolecular characteristics can be varied. In recent years of academic research, catalysts were consistently improved for gaining ultimate molecular weight, degree of tacticity and melting transition. However, the produced polymers are due to their molecular architecture by far more difficult to process than their 'industrial' analogues. Therefore, various synthesis and processing methods enclosed within this thesis aim to receive initial insights into improving PP as a feedstock material for new and unanticipated applications.
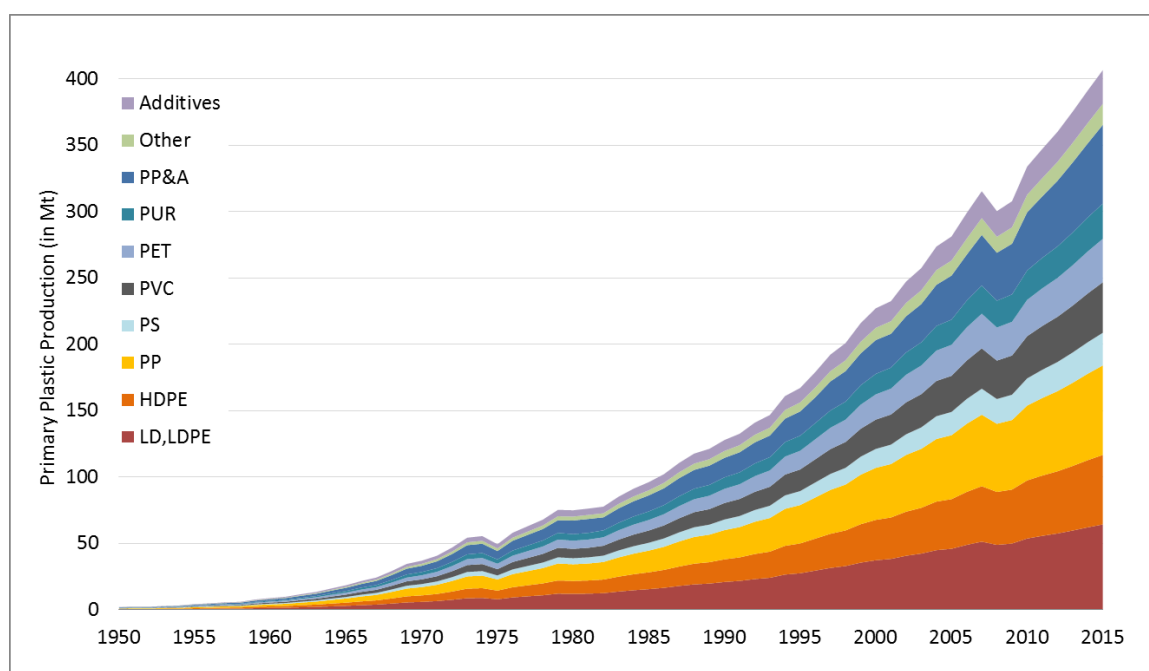

Figure 1: Global plastics production (in million metric tons) according to polymer type from 1950 to 2015. From R. Geyer, J. R. Jambeck, K. L. Law, *Sci. Adv.* **2017**, *3*, e1700782. Reprinted from Ref[5]. Copyright © the authors, some rights reserved; exclusive licensee AAAS. Distributed under a CC BY-NC 4.0 License.

2 Polypropylene – Theoretical Background

2.1 History of Polypropylene Production

The pioneering milestone in the history of coordinative polymerization of olefins was achieved by *Karl Ziegler* in 1953 – when he discovered that aluminum-compounds combined with transition-metal halides, such as $TiCl_4$, can polymerize ethylene to polyethylene and worked even at an ambient pressure.[2,10] One year later, *Giulio Natta* used this technique to polymerize propylene to polypropylene using a catalyst-mixture of $TiCl_4/AlR_3$ (R = alkyl, Cl).[3,11] This resulted in a sticky polymeric substance, that could be separated by a fractionated solvent-extraction, yielding four different polymers. One of them, insoluble in acetone, ether and boiling heptane, exhibited a melting transition higher than 160 °C. By using infrared (IR) and X-ray analysis, isotactic polypropylene (iPP) bearing a 3/1 helix was revealed to be this crystalline polymer.[12] Up to the present day, the heterogeneous Ti based multi-site catalysis remains state of the art polymerization technique of propylene in terms of an industrial large-scale production yielding iPP.[13]
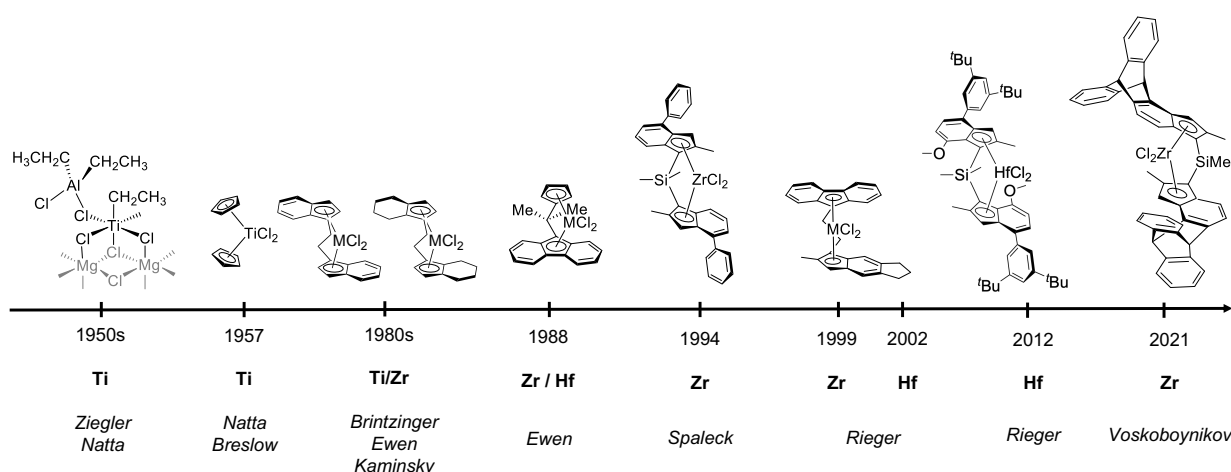
Figure 2: Timeline of selected substantial catalysts in the history of coordinative polymerization of propylene.

Fundamental research led to the first discovery of a homogeneous single-site metallocene catalyst by *Natta* and *Breslow* in 1957.[14,15] However, the polymerization of ethylene with the metallocene Cp_2TiCl_2 combined with the co-catalyst AlR_3 (R = alkyl, Cl) resulted in a small

yield of the obtained polymer, whereas other olefines showed no polymerization at all. As the catalytic activity of this species was by far reduced compared to the heterogeneous *Ziegler-Natta* based catalysts, the metallocene catalysis of olefins did not receive much attention in the following two decades. The big breakthrough in the homogeneous polymerization was achieved by *Sinn* and *Kaminsky* in 1980, when they used methylaluminoxane (MAO) as the activating agent.[16] MAO, obtained by a controlled partial hydrolysis of trimethylaluminum (TMA) and consisting of $[Al(Me)–O]_n$ oligomers (n = 5 – 25)[17], drastically increased the catalytic activity of the metallocene catalysts.

Unfortunately, so far these homogeneous catalysts were able to produce atactic polypropylene (aPP) lacking the stereoregularity polypropylene produced by heterogeneous *Ziegler-Natta* catalysts exhibited. In the 1980s, a plethora of *ansa*-metallocenes was isolated in order to tailor the properties of the resulting polypropylene. The first stereoregular PP was obtained by *Brintzinger* in 1982 by applying a *racemic* (rac) ethylene bridged tetrahydroindenyl titanocene yielding iPP.[18] Changing the central metal atom of the indenyl and tetrahydroindenyl ligand system towards Zr increased the catalystic activity even further.[19,20]. However, when the corresponding *meso* instead of the *rac* analogue was applied in the polymerization of propylene, aPP was obtained. In 1984, *Ewen* disclosed the fundamental relationship between the symmetry of the applied *ansa*-metallocene and the received polypropylene and established the model of a stereochemical enantiomorphic-site control.[21]

In the following years, structural motifs in the ligand design, such as the bridging unit or introduced substituents, were varied in order to tailor the polypropylene's macromolecular properties. *Spaleck* introduced a dimethylsilyl ($–SiMe_2–$) bridge connecting both indeyl moieties for the isospecific polymerization of propylene – resulting in an increased catalytic activity, molecular weight and degree of isotacticity.[22,23] Furthermore, he proved various substituents, especially in 2' and 4' indene position, to boost the catalytic activity and the polymer's molecular weight.[23] *Spaleck's* work was representative and pioneering for the isoselective polymerization of propylene and therefore, related 2' 4' substituted pre-catalysts were later often termed *Spaleck-type catalysts*.[24–26]

Besides iPP, syndiotactic polypropylene (sPP) became accessible through the synthesis of fluorenyl cyclopentadienyl C_s-symmetric *ansa*-metallocenes by *Ewen* in 1988.[27] Zr as the central metal atom showed a higher catalytic activity and degree of syndiotacticity of the ob-

tained polymer, whereas Hf yielded polymers with an increased molecular weight, however, a reduced activity and syndiotacticity.[27] This behavior is known as the *hafnium effect* and will be covered in more detail in 2.5. Regarding the fluorenyl cyclopentadienyl moiety, various structural motifs, such as the bridging motif[28–35] or the bulkiness of the fluorene moiety[36–38] were varied to enhance the catalytic activity, degree of syndiotacticity and polymer's molecular weight.

The combination of atactic and isotactic PP in a hemi-isotactic block structure yields an elastomeric thermoplastic polypropylene. This was achieved by *Coates* utilizing oscillating non-bridged 2'Ph-indene metallocenes[39,40] and by *Rieger* with the aid of *dual-side* ethylene bridged fluorenyl-indenyl (EBFI) *ansa*-metallocenes (M = Zr, Hf).[41,42]
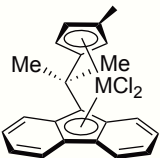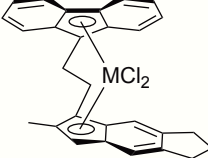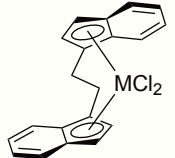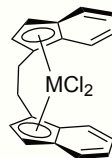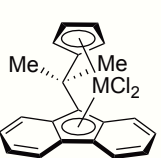
In the last two decades, the main goal of research was to further optimize the macromolecular characteristics of polypropylene. In 2011, *Kol et al.* isolated salalen titanium complexes, capable of producing iPP with an isotacticity of 99.6% and a melting transition of 169.9 °C.[43]. One year later, *Rieger et al.* reported a highly substituted ultrarigid bis-indenyl metallocene, enabling the synthesis of perfectly isotactic polypropylene, with a molecular weight of up to 5800 kg/mol and a melting transition of up to 171 °C.[44] Up to the present day, this catalyst remains a benchmark system yielding iPP with unsurpassed macromolecular characteristics. Unfortunately, this zirconocene and especially the corresponding hafnocene showed poor performance at elevated temperatures in terms of macromolecular characteristics – replacing the *tert*-butyl group by a hydrogen or methyl group even diminished this performance.[44,45] *Voskoboynikov et al.* investigated even more constrained zirconocenes achieving superior high-temperature performance.[24–26,46–49] Indeed, a triptycyl-based ligand with ‚absolute rigidity‘ yielded highly isotactic PP with almost no detectable stereoerrors, even if the polymerization was run at industrially relevant high temperatures (up to 150 °C).[26]

Considering the last seven decades of elaborative work to consistently improve the polymers of our academic and daily life, one major aspect seems to be untouched: contrary to the effortless and established processing of (industrial) medium high molecular weight polypropylene – is a conventional processing of ultrahigh molecular weight polypropylene (UHMW-PP) *via* e.g. melt-extrusion feasible and is it even possible to disclose parallels to UHMW-PE? In theory, UHMW-iPP should exhibit improved mechanical properties compared to UHMW-PE. This thesis aims to gain initial insights regarding this issue.

2.2 Structure – Performance Relation of *ansa*-metallocenes

In general, group-IV metallocene pre-catalysts consist of two cyclopentadienyl (Cp) moieties (η^5-coordinated) and two halogen substituents (σ-coordinated) attached to a group-IV (M^{4+} = Ti, Zr, Hf) central metal atom in a pseudo-tetrahedral coordination. However, metallocenes are not limited to two specific Cp ligands, rather substituted Cp moieties, an indene or a fluorene derived structure are feasible.[50] During the polymerization process, both Cp-ligands remain attached to the central metal atom center, whereas the halogen substituents need to be replaced by one alkyl moiety and a free coordination site to initiate the coordinative polymerization of olefins (see chapter 2.3). In order to introduce a stereogenic information towards the metallocene, both Cp ligands are connected by a bridge, such as $-SiMe_2-$, $-CH_2-CH_2-$ or $C(CH_3)_2$.[34] The bridging motif plays a crucial role in the performance of an *ansa*-metallocene in the coordinative polymerization, as it determines the Cp–M–Cp angle and thereby the coordination of an olefin.[34]

C_1	C_1	C_2 (rac)	C_s (meso) $\quad$ C_{2v}	C_s
hemiisotactic	blockisotactic	isotactic	atactic	syndiotactic

Figure 3: Selected examples for the correlation of metallocene symmetry and the obtained tacticity in the polypropylene microstructure.

As already described by *Ewen*'s symmetry rules, the implementation of a stereogenic information in the metallocene pre-catalyst enables the adjustment of the polymer's microstructure. Herein, C_1, C_2, C_{2v}- and C_s-symmetric metallocenes are distinguishable and these correlations are an auxiliary tool to estimate the correlation between complex symmetry and microstructure (Figure 3).[21] For C_2- and C_s-symmetric metallocenes, both coordination sites are isotropic and such are therefore termed single-site catalysts. Contrary to this, the C_1-symmetric EBFI metallocenes facilitate two different anisotropic coordination sites and are thus considered multi-site catalysts.[50]

The desired group-IV *ansa*-metallocenes are usually obtained by a reaction of the dilithiated ligand moiety with MCl_4 (M = Ti, Zr, Hf). Contrary to C_1- and C_s-symmetric species, the synthesis of C_2-symmetric metallocenes for the isospecific polymerization of propylene requires one additional step: the separation of the desired *rac* from the undesired *meso* analogue.[21] This synthetic step is mainly accomplished *via* a recrystallization and therefore drastically decreases the total amount of pure pre-catalyst. However, these *bis*-halogenated pre-catalysts are unable to polymerize olefins, as they lack a free coordination site. Therefore, they need to be transferred into the catalytically active, cationic species with the aid of a co-catalyst.
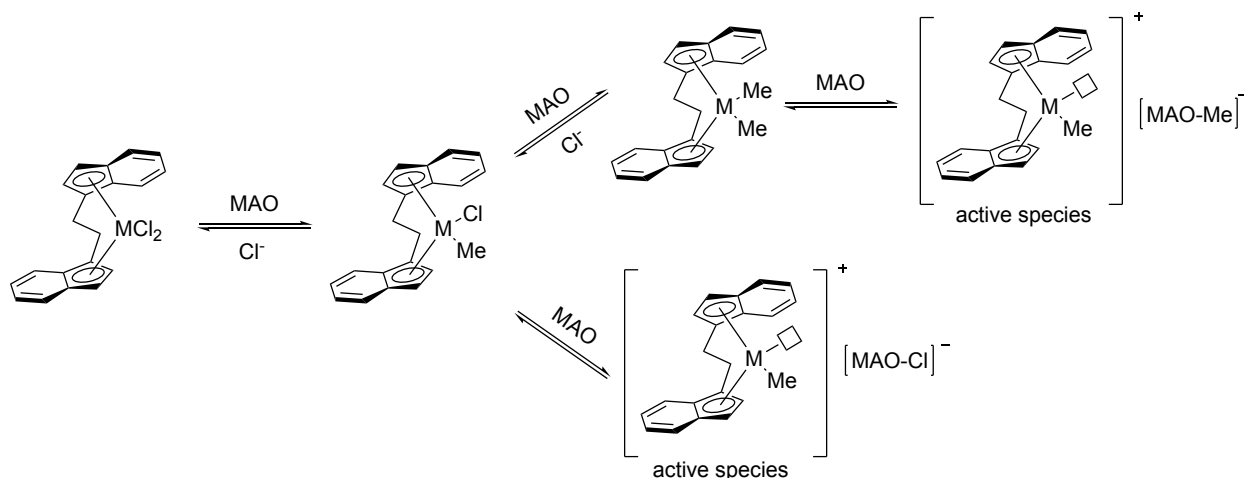
2.3 Metallocene Activation

Ever since the discovery of metallocene dichlorides for the polymerization of propylene, two main strategies have been established to transform the pre-catalyst into the catalytic active, cationic species with the aid of a co-cocatalyst – the activation using MAO and the borane/borate activation.

2.3.1 MAO Activation

MAO with the general formula $[Al(Me)-O]_n$ (n = 5 – 25) is prepared through partial hydrolysis of TMA and is up to the present day the most common activation reagent – used preferentially in the academic and industrial environment.[17] Despite extensive research, the exact structure of MAO is still unknown – MAO probably consists of linear, branched and cage-like oligomeric structures.[51–55] In course of the activation mechanism, MAO acts both as the alkylating and initiating reagent (Scheme 1).[17] However, the activation mechanism of MAO is simplified and includes a mono- or dialkylation of the metallocene dichloride – subsequently followed by the initiation due to its Lewis acidity forming the cationic species. The catalytic activity is significantly influenced by the generated counter-anion – a stronger coordination of the anion impedes the catalyst's activity. Since the form of MAO is highly variable and the activation mechanism is always different, the variety of catalysts using MAO as an activating reagent must be considered separately. In addition, a plethora of commercial substances for a better solubility is available, e.g. an *n*-octyl modification – therefore, an accurate determination of the MAO counter anions and their role in the polymerization process is almost
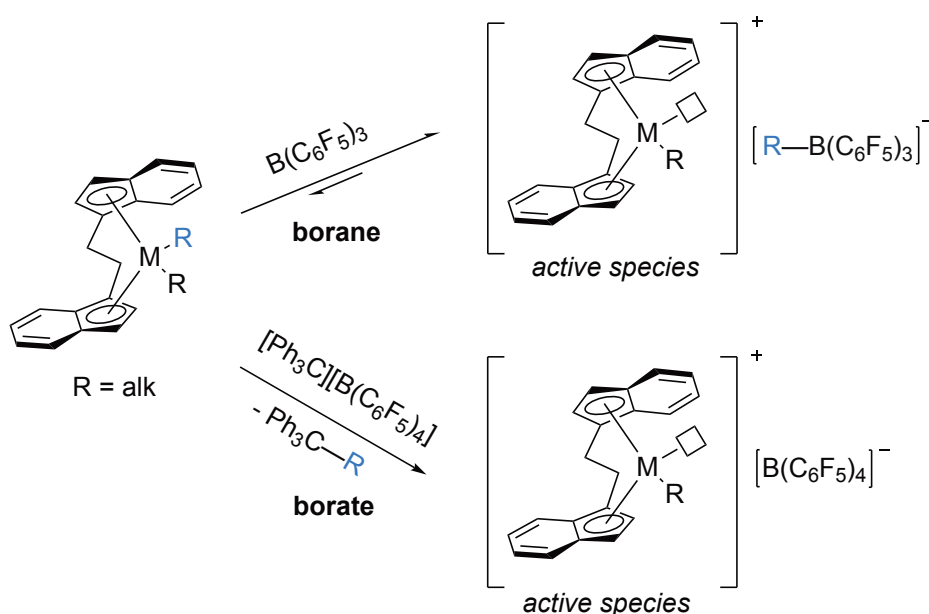
impossible.[17,52,56–58]

Scheme 1: Initiation mechanism of a C_2-symmetric *ansa*-metallocene (M = Ti, Zr, Hf) using MAO, generating the catalytically active, cationic species.[17,52]

However, as the activation method remains an equilibrium state, excess of MAO has to be applied for an increased amount of the catalytic active species (Al/M $\approx$ 1000 – 10000). Hereby, MAO acts not only as the alkylating and initiating agent, forming the cationic species – but additionally also protects the cationic species from degradation by moisture and air as a scavenger agent.[17,50] Due to the manufacturing process, especially commercial MAO contains a non-negligible content of remaining TMA. The activation of zirconocenes with remaining TMA in the MAO solution is not affected and generally provides a high catalytic activity – unfortunately, for Hf as the central metal atom, this activation is problematic and the activity is tremendously diminished.[17,27,36,57,58] This will be covered in more detail in 2.5.

2.3.2 Borane and Borate Activation

Contrary to the MAO activation – where both functional motifs of an alkylation and initiation reagent are combined in one co-catalyst – the borane and borate activation usually are a two-step mechanisms. In the first step, the metallocene dichloridie has to be converted into the corresponding dialkyl species *via* a transmetalation using *Grignard* or organolithium reagents. Usually, the dimethyl metallocene is prepared by reacting L_2MCl_2 with MeMgBr or MeLi in no to small excess (2.0 – 5.0 eq.). The catalytic active cationic species is then formed in the second step, applying the borane $B(C_6F_5)_3$ or the borate $[CPh_3][B(C_6F_4)_4]$ (TrBCF). However,

the borane activation with [alk–B(C$_6$F$_5$)$_3$]$^-$ as a moderately coordinating counter anion reduces the catalytic activity. Contrary to this, TrBCF yields a non-coordinating counter anion – [B(C$_6$F$_5$)$_4$]$^-$. Therefore, the cationic species is in a rather 'naked' conformation and the catalytic activity is enhanced. Moreover, stable PhC–R is formed and contrary to borane initiation, which remains in an equilibrium state, borate activation mechanism is considered quantitatively (Scheme 2). Usually, 1.0 – 5.0 eq. of borane or borate are applied for this activation method. [17,52,56,58–62]

Scheme 2: Borane (B(C$_6$F$_5$)$_3$) and borate ([CPh$_3$][B(C$_6$F$_5$)$_4$]) initiation mechanism of a C$_2$-symmetric *ansa*-metallocene (M = Ti, Zr, Hf), generating the catalytically active, cationic species. [17,52,56,58–60]

Due to the high sensitivity of the generated species to moisture and air, the application of scavengers like aluminum alkyls is mandatory. Worth mentioning in this context is the possible interaction between the used co-catalyst and the scavenger reagent, potentially forming multi-nuclear intermediate states. [58] *Rieger et al.* developed an elegant method, to directly convert the metallocene dichloride into the dialkyl species by using 200 eq. of triisobutylaluminum (TIBA) with no elaborative isolation of L$_2$MR$_2$ (R = alk, M = Ti, Zr, Hf). [63] This *in situ* activation is not yet fully elucidated, but a mechanism with the formation of a M–H intermediate is assumed. [58] The cationic species is thus formed by the addition of TrBCF, and TIBA acts as the scavenger reagent to protect the alkylated and cationic species from degradation. TIBA with its high steric demand does not form any dinuclear L$_2$M–alk$_2$–AlR$_2$ intermediate states [58] (see

chapter 2.5) which is particularly advantageous for hafnium as the central metal atom. The *in situ* activation is nowadays widely applied by academic researchers for the activation of metallocene dichlorides,[44,45,64–66] whereas TrBCF can be substituted by *N,N*-dimethylanilinium tetrakis(pentafluorophenyl)borate ($[HNMe_2Ph][B(C_6F_5)_4]$).[26,67,68]

2.4 Polymerization Mechanism

2.4.1 Chain Propagation

As early as the 1960s, scientists investigated the chain propagation mechanism of the coordinative polymerization of olefins. In 1960, *Cossee* proposed the first mechanism for heterogeneous *Ziegler-Natta* catalysts[69,70] and extended his postulation in 1964 together with *Arlman*.[71] They assumed, that three crucial steps are necessary for the polymer's chain growth: First, the monomer/olefin has to coordinate to the free coordination site of the cationic central metal. Subsequently, this π-intermediate is converted to a four-membered transition state in the π intermediate. Finally, the monomer unit is incorporated into the polymer chain *via* migratory insertion, and a free coordination site at the metal atom is generated yet again.
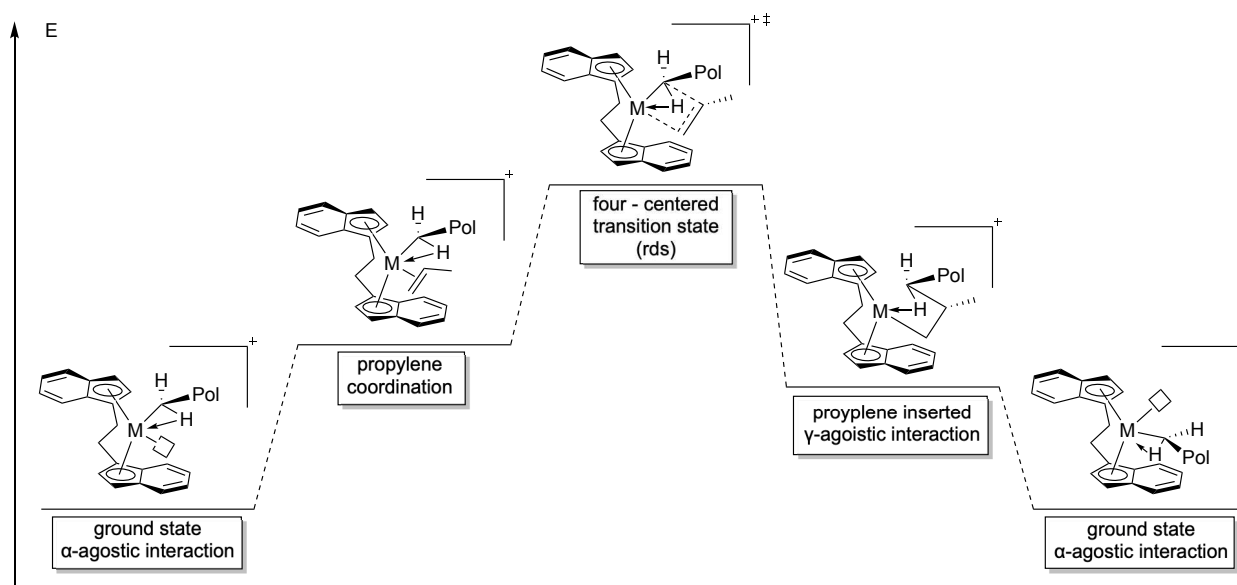

Scheme 3: Energetic consideration of the chain propagation described by the modified *Green-Rooney* mechanism considering agostic interactions with an exemplary *ansa*-bis(indenyl) metallocene catalyst. (M = Ti, Zr, Hf; Pol: polymer chain; counter-anion is omitted for clarity).[50,72–76]

However, the chain propagation mechanism of *Cossee* and *Arlman* lacked the consideration

10

of stabilizing agostic interactions. Nowadays, the modified *Green-Rooney* mechanism (see Scheme 3) is the most widely accepted one, as it implements such α- and γ-agostic interactions. As already assumed by *Cossee* and *Arlman*, DFT calculations revealed the four-membered cyclic transition state to be the rate determining step (rds) and additionally confirmed α- and γ-stabilizing agostic interactions, whereas the evidence of β-agostic interactions is still uncertain.[50,72–79]
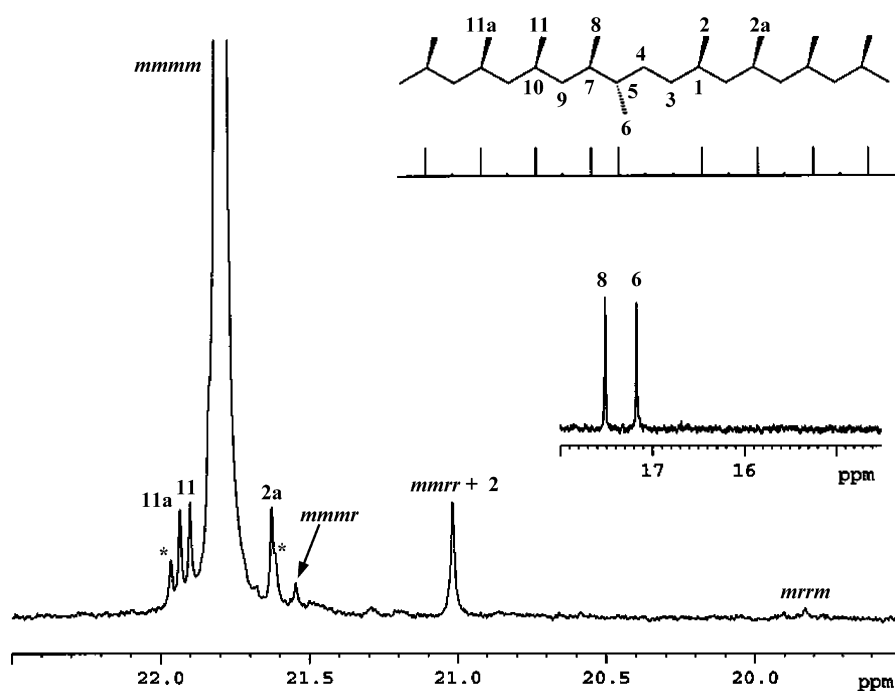
2.4.2 Regioregularity in the Migratory Insertion
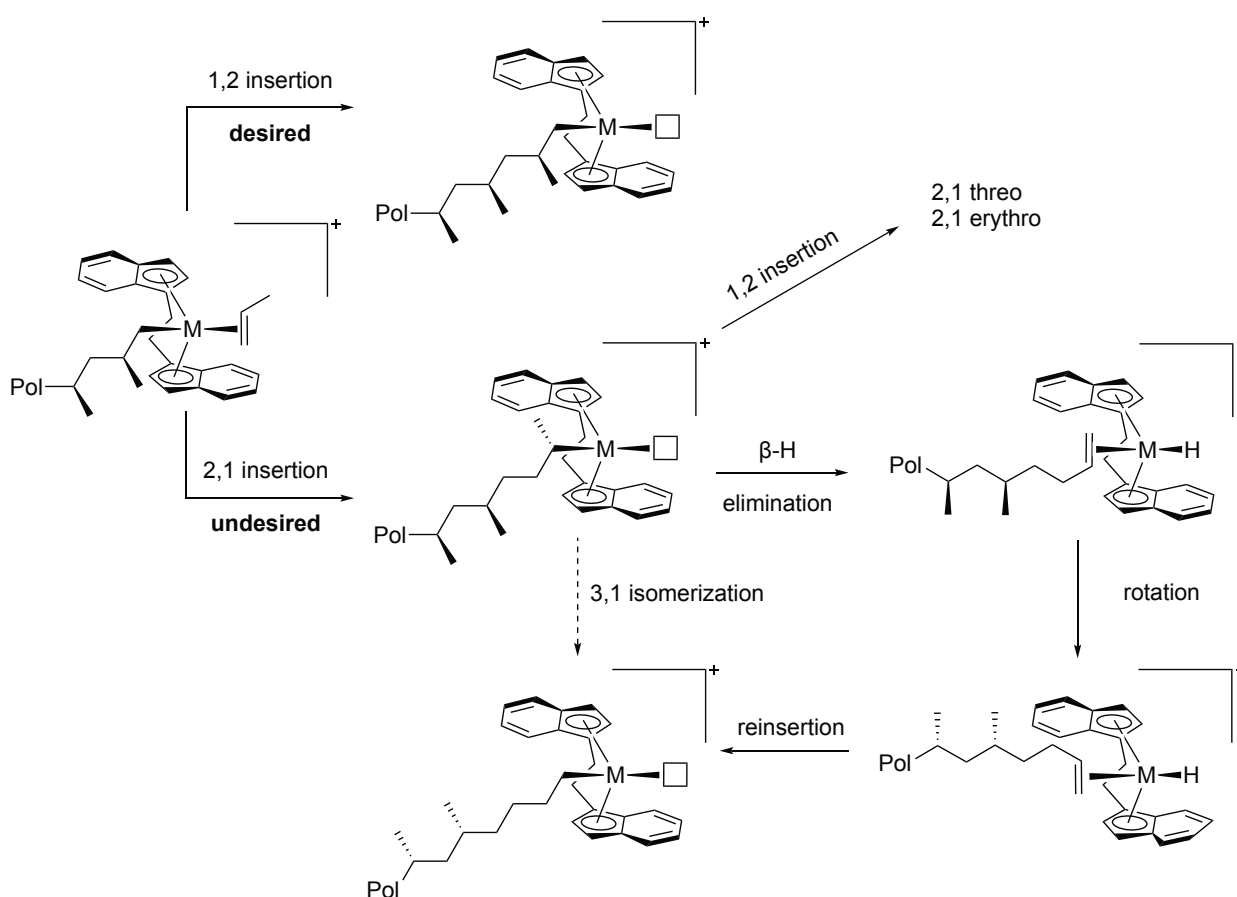
Scheme 4: Regioselective insertion mechanism and the resulting products with an exemplary *ansa*-bis(indenyl) metallocene catalyst. (M = Ti, Zr, Hf; Pol: polymer chain; counter-anion is omitted for clarity).[50,80–83]

As propylene is a prochiral olefin, the regioselectivity of the migratory insertion pathway plays a predominant role for the final polymer's microstructure and thus its thermal and mechanical properties.[84] The primary 1,2 insertion mechanism is highly desired, whereas the secondary

2,1 insertion rather undesired. A 2,1 misinsertion usually leads to an opposite enantiofacial selectivity compared to the regular primary 1,2 inserion (Scheme 4).[50,80,83] A 2,1 regioerror not only yields – depending on the primary insertion of a new propylene unit – either a 2,1 threo or 2,1 erythro regiodefect, it additionally also lowers the rate constant tremendously. Consequently, the probability of a chain release is increased – leading to an epimerization mechanism first through rotation and subsequent reinsertion of the coordinated polymer chain. This epimerization process is particularly dependent on the polymerization conditions, such as temperature and pressure, as well as the electronic and steric nature of the calayst's ligand moiety.[50,80–82] However, as misinsertions cause defects in the polymer's microstructure and therefore constrain the mechanical and thermal behavior,[85] the catalyst design as well as suitable polymerization conditions are important tools to tailor the properties of the obtained polypropylene. These misinsertions can be detected by using high-resolution ^{13}C NMR spectroscopy (Figure 4).[84]

Figure 4: Excerpt of the methyl region of a ^{13}C $\{^1H\}$ NMR spectrum of iPP, showing 2,1 erythro defects and pentad signals. Reprinted with permission from Ref.[84]. Copyright © 2005 by the American Chemical Society.

2.4.3 Stereoregularity in the Migratory Insertion

Besides regiodefects (see chapter 2.4.2), stereoregularity and stereoerrors are a key factor for the thermal and mechanical properties of polypropylene. Propylene as a prochiral monomer generates a new stereogenic center inside the polymer chain with every migratory insertion. These newly formed stereogenic centers are a key factor for the polymer's properties. The tacticity of polypropylene is usually described by the the relative stereoregular configuration of two alternated neighboring methyl groups inside the polymer chain. In this context, two neighbored methyl groups with the same stereoinformation (R/R, S/S) are called a *meso* (m) dyad, whereas two different stereoinformations (R/S, S/R) are termed *rac* (r) dyad.[86] If this concept is extended for several considered methyl groups, triads, pentades, heptades and even nonades are distinguishable.[86–89] If each dyad of the polymer chain has a *meso* configuration, the polymer is called isotactic – contrary to this, consistent racemic dyads lead to syndiotactic polymers.
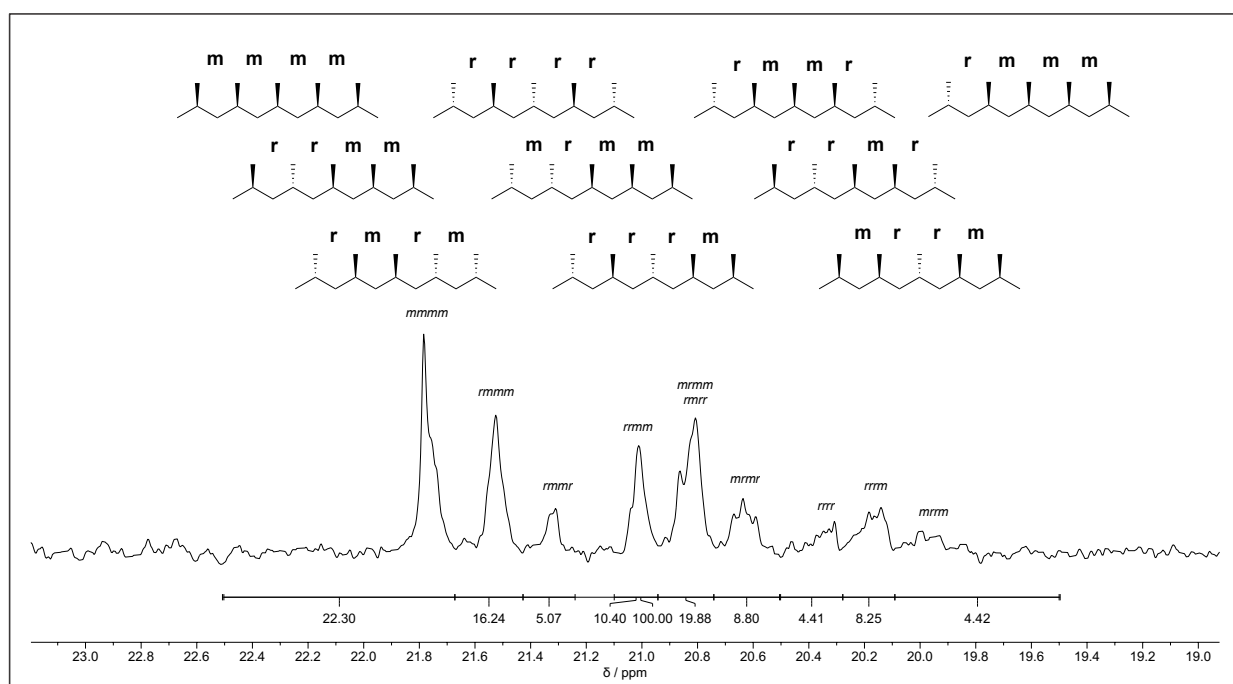
Figure 5: Pentad distribution and assignment of polypropylene, exemplary with a ^{13}C{^{1}H} NMR (300 MHz, 140 °C, C_6D_5Br) spectrum of iPP-enriched aPP (22% [mmmm]). Pentads were referenced to the [mmmm] pentad (21.85 ppm).[86]

Atactic polymers exhibit a random distribution of the dyads. The neighboring stereogenic cen-

ters of the methyl groups significantly change the chemical environment affecting a shift of the signals in the ^{13}C $\{^1H\}$ NMR spectrum. Usually, pentads are well resolved in the high temperature (HT) NMR spectrum and with an increased resolution of the used NMR spectrometer even nonades can be assigned. The degree of tacticity and the total count of stereoerrors is thus calculated by the molar amount of the [mmmm] (for isotactic PP) or [rrrr] (for syndiotactic PP) pentad divided by the sum of all pentads (Figure 5).[44,45] However, due to the low solubility, the NMR is usually measured in bromobenzene or tetrachloroethylene at elevated temperatures (120 – 140 °C).[50,82,87–91]

As already enclosed in 2.2, catalyst design plays a crucial role in the synthesis of stereoregular polypropylene. Due to the prochirality of propylene, two possible coordination modes are feasible according to the *Cahn-Ingold-Prelog* nomenclature: si-face or re-face.[50,88] After the activation of metallocenes (2.3), two coordination sites for olefins are accessible. C$_s$-symmetric bridged bis-indenyl *meso* catalysts have two diastereotopic coordination sites – neither site leads to a preferential orientation of the polymer chain and thus, si and re face of the monomeric propylene is equally likely. Contrary to this, C$_2$-symmetric bridged bis-indenyl *rac* catalysts with two homotropic (equivalent) coordination sites exhibit a directed orientation of the polymer chain away from the aryl moiety of the indene ligand system, causing a preferred si or re face insertion (depending on R/R or S/S indenyl enantiomer).[91]

For the stereoregularity of the PP chain, two main mechanism are responsible: the chain-end control and the enantiomorphic site control. The chain-end control claims that the last inserted monomer unit affects an coordination of the subsequent propylene molecule in an *anti* fashion to the growing polymer chain.[92,93] As the energy difference between the insertion of si and re face is small (about 2 kcal/mol), the chain-end control leads to a low enantioselectivity at temperatures higher than 0 °C.[50,92,94]

The enantiomorphic site model still considers an *anti* coordination of the monomer to the growing polymer chain in a same fashion as the chain-end-control, whereas the final conformation is independent on the lastly inserted monomer, but rather depends on the chiral environment of the catalyst's ligand system. The first propylene insertion mechanism into several cationic M–alkyl species proved the mandatory interaction between the polymer chain and the catalyst's chiral environment for an *anti*-selective insertion.[91,95–99] The most energetically favorable transition state occurs when the polymer chain is directed into the outer

sector of the ligand framework of the catalyst. The monomer thus coordinates *anti* to minimize the steric repulsion with the β-C–atom bearing the methyl group and the growing polymer chain.[91] Therefore, for enantiomorphic site controlled catalysts, two main mechanism for a stereoerror formation are feasible: first, if the propylene monomer is coordinated *anti*, while the growing polymer chain is in a unfavorable orientation.[50,75,83,99] Additionally, stereoerrors are formed for a *syn* coordination of the monomer to the polymer chain in a favored orientation (Figure 6).[50,75,96,98]
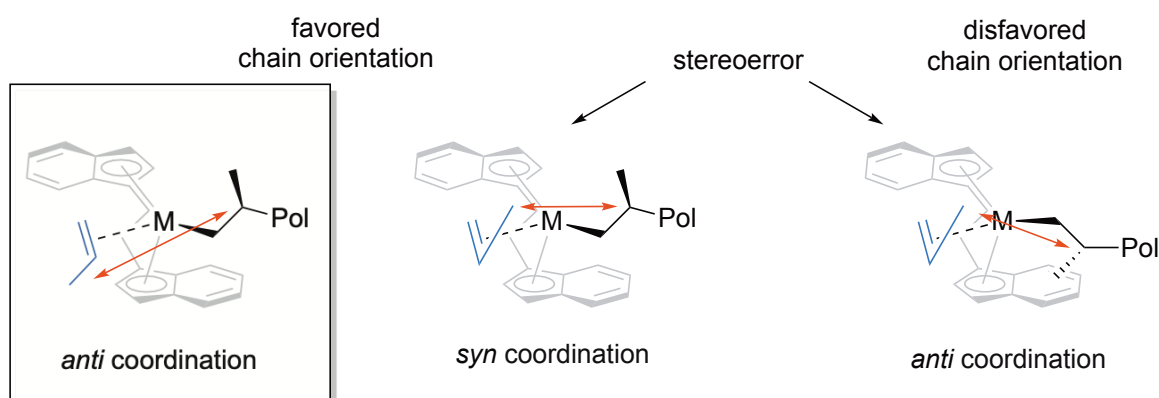
Figure 6: *Syn* and *anti* coordination of propylene to an exemplary *ansa*-bis(indenyl) metallocene catalyst, clarifying the enantiomorphic model site control.[50,91] (M = Ti, Zr, Hf; Pol: polymer chain; counter-anion is omitted for clarity)

However, by reference to the stereoerrors, the underlying mechanism for the stereoregularity can be identified. For chain-end controlled catalysts, an *error propagation* is observed, whereas enantiomorphic site controlled catalysts enable an *error correction*, leading to a 1:1 ratio of the [mmrr] and [mrrm] pentade.[91]

2.4.4 Chain Release

Metallocenes feature the benefit to be able to produce more than just one polymer chain by one active catalyst species. This is due to the fact that chain release reactions yield catalytically active cationic species with different alkly chains, both for 1,2- and 2,1-insertions (2.4.2). Herein, chain release reactions for the primary 1,2 insertion are considered.[50]

β-**H Elimination**   The most common chain release reactions terminating the chain propagation in the coordinative polymerization is the β-H elimination, either to the metal (Scheme 5,

A) or the monomer (Scheme 5, **B**). Both chain release reactions form a vinylidene end-group of the polymer chain.[45,50] The transfer to the metal occurs *via* the α-agostic transition state, forming a π-bond polymer chain with a vinylidene end-group. The polymer chain is thus released either by an associative or a dissociative mechanism, whereas the dissociative mechanism is less pronounced and occurs mainly at elevated temperatures.[100,101]
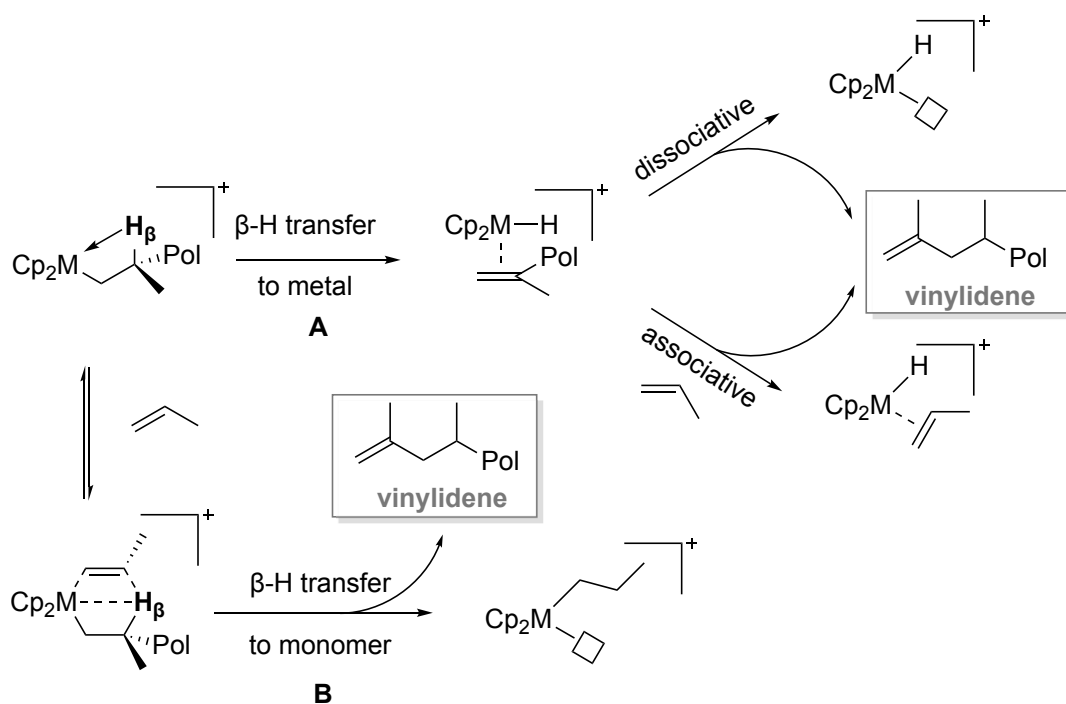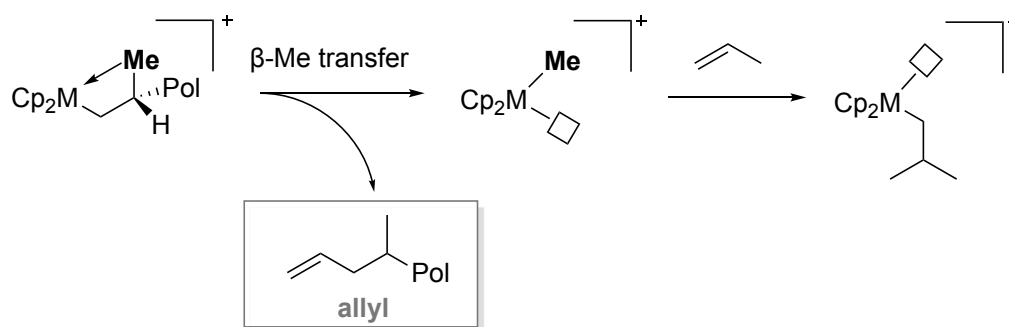

Scheme 5: Pathway of β-H elimination to metal (**A**) or monomer (**B**) after 1,2-regioinsertion in the polymerization of propylene (M = Ti, Zr, Hf; Pol: polymer chain; anion is omitted for clarity).

Likewise, a rotation and subsequent reinsertion of the polymer chain is feasible, leading to a chain-end epimerization.[102–104] However, using density functional theory (DFT) analysis the bimolecular pathway **B** was calculated to have a lower activation energy barrier compared to **A**.[100] So far, the intermediate state with or without involved agostic interactions is still uncertain.[101,105] Besides the vinylidene end-group produced by the chain release after a 1,2 insertion, 3-butenyl, *cis*- or *trans*-2-butenyl chain end-groups can be obtained for a 2,1 insertion.[45]

β**-Me Elimination** The β-Me elimination requires a primary 1,2 insertion prior to the chain release and forms an isobutyl cationic substituted complex and allyl polymer end-groups (Scheme 6). Theoretically, a transfer to metal as well as a transfer to monomer is feasible.

However, DFT measurements and experimental data revealed the unimolecular pathway similar to Scheme 5 to selectively emerge.[50,106–109] Mainly, β-Me elimination reactions are less provoked compared to β-H eliminations due to an increased activation energy barrier of a C–C compared to a C–H bond.[110] For Hf as the central metal atom or steric demanding ligand moieties, the probability of β-Me eliminations is enhanced (see chapter 2.5).[77,111]

Scheme 6: Pathway of β-Me elimination and allyl terminated polymer chain after 1,2-regioinsertion in the polymerization of propylene (M = Ti, Zr, Hf; Pol: polymer chain; anion is omitted for clarity).[50]

Chain Transfer Reactions   Additionally, a transmetalation with aluminum compounds is an important chain release pathway. Contrary to latter, the transmetalation forms saturated polymer end-groups. The chain transfer to aluminum is mainly considered for sterically less demanding aluminum compounds. Especially for a large proportion of unmodified MAO with residual TMA, this transmetalation is a big issue that consequently diminishes the polymer's molecular weight. This will be covered in more detail in 2.5. However, for sterically demanding aluminum compounds, such as TIBA, the probability of a transfer to aluminum is reduced.[50,56,58,112–114]

Besides aluminum, molecular hydrogen is a feasible chain transfer reagent that is widely applied in the industry for a precise control over the polymer's molecular weight. Moreover, it increases the productivity of the used catalyst, as chain transfers of stable resting states lowering the propagation rate of the catalyst are enhanced.[50,115,116]

Most recently, the concept of chain shuttling was investigated. Herein, the growing polymer chain is transferred onto another catalytic center, such as Mg or Zn. This enables the synthesis of copolymeric structures. With this chain transfer reactions and the combination of syndio- and isospecific catalysts, a sPP – iPP block-copolymeric structure is be feasible.[117]

2.5 Hafnium vs. Zirconium – Differences in Polymerization Performance

As indicated in 2.3 and 2.4, the group-IV central metal atom is one key factor determining the performance of metallocenes in the coordinative polymerization of olefins. Besides the productivity, the stereoregularity and regioregularity are significantly influenced by the applied metal atom. Back in the 1950s, when *Ziegler* and *Natta* utilized the heterogeneous polymerization of olefins, they incorporated Ti as the catalytically active metal center.[2,3] While the first metallocene catalyst contained a Ti moiety,[14,15] research of homogeneous catalysts was directed towards Zr (and Hf) as the central metal atom in the 1980s.[18,19,27]

Titanium is the tenth most common element in the world – even more abundant than nitrogen, carbon, chlorine or phosphorus. Zirconium is by far less common and hafnium only accessible as a by-product (1 – 5%) in the refinement of zirconium.[118,119] However, due to the lanthanoid-contraction, the heavier homolog Hf enables a smaller ionic radius compared to Zr under isoelectronic conditions $\left(\text{Ti}^{+4}\text{: } 0.42\,\text{Å, Zr}^{+4}\text{: } 0.59\,\text{Å, Hf}^{+4}\text{: } 0.58\,\text{Å}\right).$[120,121] As Ti as the central metal atom shows a decreased performance compared to Zr and Hf for the metallocene based polymerization[64] and is thus nowadays mainly applied in the heterogeneous polymerization, the performance of titanocenes is not considered herein.

Comparing hafnium and zirconium, hafnocenes were regarded less active for a long period of time.[27,36] In the early 1980s, MAO was the activation agent of choice. However, hafnocenes showed a by far diminished activity compared to its isostructural zirconocene analogue using MAO $\left(0.2\text{ kg}_{poly}/\text{g}_{Hf}\text{ and } 120\text{ kg}_{poly}/\text{g}_{Zr}\text{ for MCl}_2[\text{Me}_2\text{C}(\eta^5\text{–Flu})(\eta^5\text{–Cp})]\right).$[27,35] Initially, this was attributed mainly to the stronger σ-Hf–C bond in comparison to the σ-Zr–C bond, leading to a higher energy barrier decelerating the chain propagation. Indeed, *via* titration calorimetry, the σ-Hf–C bond was determined to be about 22 kJ/mol stronger for an isostructural Cp$^*_2$MMe$_2$ complex system (Hf–C, 306 ± 7 kJ/mol; Zr–C, 284 ± 2 kJ/mol).[122,123] However, the low activity of hafnocenes is not an intrinsic issue of these catalysts, it rather is affected by the employed activation method. Due to their manufacturing process, commercial MAO solutions always contains residual TMA. In several studies, TMA was attributed to play a crucial role in the depression of the activity of hafnocenes, as it forms a dinuclear cationic methyl-bridged complex [L$_2$M(μ–Me)$_2$AlMe$_2$]$^+$ with both metal centers.[56–58] For hafnium as the central metal atom, DFT calculations revealed a higher stability of this bridged hetero-bimetallic aluminum complex by 3.0 kcal/mol in comparison to the corresponding zirconium
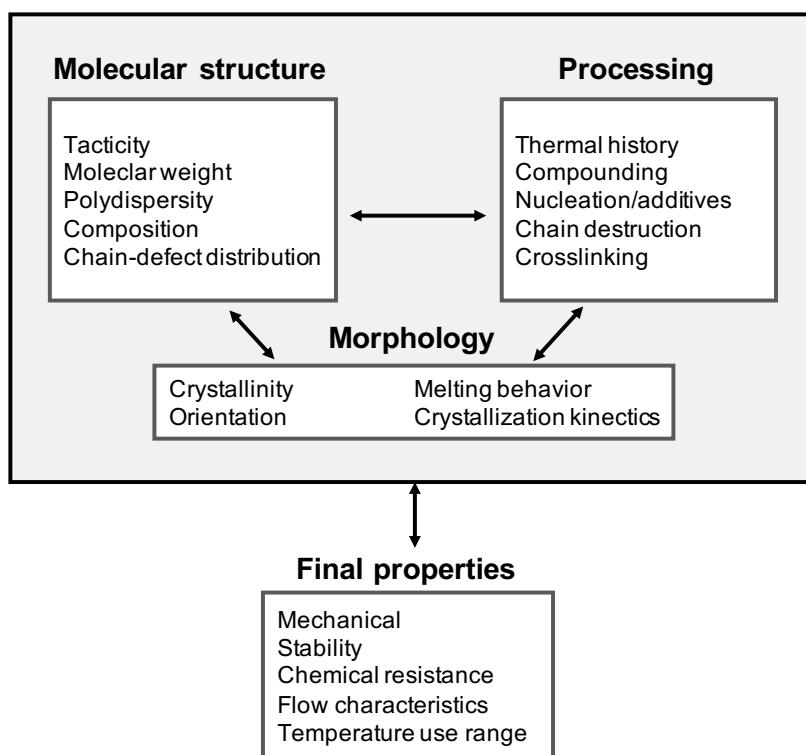
complex.[57] Therefore, the dinuclear complex $[L_2Hf(\mu-Me)_2AlMe_2]^+$ resembles a stable resting state in the polymerization of propylene diminishing the catalyst's activity, whereas the activity of zirconocenes is not as affected by TMA.[56–58] However, free TMA can be scavenged by using sterically demanding phenolic moieties increasing the activity of the corresponding catalyst.[57] With this disadvantage in mind, several two-step activations (2.3.2) were established. Specific hafnocenes even enabled a higher or at least comparable activities as their corresponding zirconocene analogues using the *in situ* activation with TIBA/TrBCF. Therefore, the reduced activity of hafnocenes is not an intrinsic property of the catalysts themselves, moreover it is implied by the slow and thus ineffective activation method.[42,44,63,111,124]

Besides the activity, the central metal atom is decisive for the polymer's molecular weight, as hafnocenes produce polymers with a significantly higher molecular weight. This was already observed by *Ewen* for C_s-symmetric metallocenes[27] and confirmed for further catalyst symmetries.[30,42,44] This *hafnium-effect* is assumed to be caused by the increased stability of the σ-Hf–C bond compared to the σ-Zr–C bond.[42] In addition to chain propagation, the chain release is determining the polymer's molecular weight. As various chain release reactions are feasible (see chapter 2.4.4), the major mechanism for each central metal atom has to be considered. Indeed, for hafnocenes an increased amount of β-Me eliminations, visible *via* end-group analysis, was observed compared to isostructural zirconocenes.[77,111,125] For polymerizations at industrially relevant elevated temperatures, hafnocenes showed a deteriorated performance.[44,45] Most recently, *Voskoboynikov et al.* investigated the root of the *hafnium-effect* and the inhibited performance at higher temperatures. They concluded, that the electrophilicity of the catalyst being a function of the surrounding ligand moiety and the central metal atom is responsible for the catalyst's performance. A higher electrophilicity thus leads to more stable olefin complexes, a lower energy barrier for β-H eliminations and β-Me eliminations and a higher energy barrier for a release of allyl- or vinyl-terminated polymer chains. Hafnocenes showed an increased probability of β-H elimination than zirconoces, but the chain release from the Hf–H (vinylidene-polymer) was less pronounced.[126]

Regarding stereoselectivity and regioselectivity, results in the literature are ambiguous and less studied so far due to the lack of precise analytics in previous publications and additionally, no comprehensive study of isostructural hafnocenes and zirconocenes was conducted so far. A computational study comparing Cp_2MCl_2 suggested a higher regioselectivity for Hf.[77]

However, for C_s-symmetric metallocenes, an increased syndiotacticity was obtained for Zr as the central metal atom compared to Hf.[27,36] Contrary to this, *Rieger* and co-workers observed a higher regio- and stereoregularity using ultrarigid C_2-symmetric metallocenes leading to elevated melting transitions of the received iPPs for Hf as the central metal atom.[44,85,124] Besides the catalyst, the regioregularity and stereoregularity is tremendously affected by the co-catalyst, as the counter-anion can either disturb or assist the coordination of a newly incoming monomeric unit.[127]

2.6 Polypropylene Morphology

Molecular structure

Tacticity
Moleclar weight
Polydispersity
Composition
Chain-defect distribution

Processing

Thermal history
Compounding
Nucleation/additives
Chain destruction
Crosslinking

Morphology

Crystallinity
Orientation

Melting behavior
Crystallization kinectics

Final properties

Mechanical
Stability
Chemical resistance
Flow characteristics
Temperature use range

Figure 7: Relationship between polymer's molecular structure, processing and morphology for the final end-use properties.[128]

As enclosed in 2.4.3, stereoregular polypropylene exhibits the presence of a certain tacticity. For highly orientated structures of consecutive methyl groups, a semi-crystalline polymer is obtained and the degree of tacticity is responsible for the crystallinity.[128] For metallocene catalysis, different tacticities (isotactic, syndiotactic, hemiisotactic, atactic) are feasible and the degree of tacticity can either be adjusted by changing the ligand moiety or the polymerization

parameters, such as temperature or pressure.[27,44,65] However, the polymer's morphology is a crucial bridge between the polymer structure, processing and end-use properties. Besides the tacticity, key molecular factors influencing the morphology and processability are the molecular weight, polydispersity, chain defect architecture and composition, such as blends or co-polymers.[128] In order to highlight the impact of a polymer's morphology especially onto the mechanical and thermal behavior, isotactic and syndiotactic polypropylene's polymorphism is briefly summarized in the following section. As atactic polypropylene has a maximum crystallinity of 15–20%[129] and is thus of less interest, it is hereby not considered.

2.6.1 Isotactic Polypropylene

For isotactic polypropylene with all methyl groups aligned in the same direction, a 3/1 helical arrangement is the energetically favored conformation with the lowest intramolecular interaction. The helical structure in the crystalline state can either be rotated left- or right-handed about the central axis (Figure 8). Four crystalline constitutions are reported for iPP: the α, β,
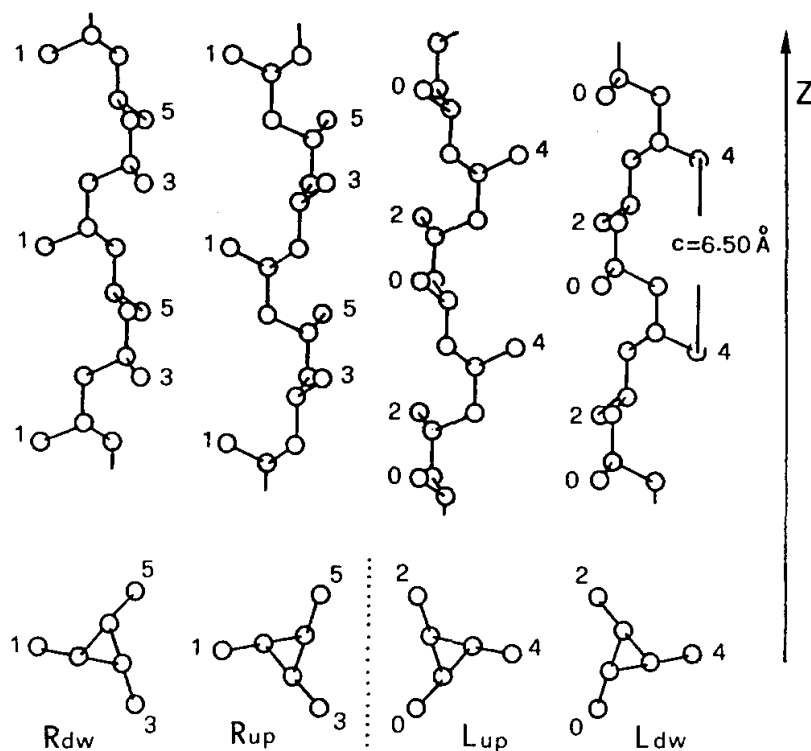
Figure 8: Chains of iPP in 3/1 helical conformation, left- (L) and right-handed (R) up and down. Reprinted with permission from Ref.[130] Copyright © 1991 by Elsevier.

γ and the mesomorphic (smectic) phase.[131–133] The α-phase which was already analyzed by *Natta* and *Corradini* in 1960 has an overall monoclinic cell with the parameters a = 6.65 Å, b = 20.96 Å, c = 6.50 Å and β = 99.8 °.[131,134,135] Furthermore, the α-phase is the most stable and dominant form of iPP and obtained *via* melt-crystallization and in drawn fibers. However, the α-crystalline modification is usually disordered in orientated fibers.[130,136,137] Particularly unique in polymer crystallography is the observation of lamellae branching in the monoclinic α-phase of iPP for a broad range of crystallization temperatures (90 °C > T > 160 °C).[131,138,139]

The β-phase of iPP has been known for many years, whereas the crystallographic details of this modification are still uncertain. It is accepted that the β-phase enables a lower degree of order in the crystalline state compared to the α-phase.[137] However, a hexagonal or trigonal structure is assumed – due to the transformation of the mechanically unstable β-phase into the α-phase by stretching, no orientated fibers can be obtained in order to clarify the exact structure.[130,131,133,139–141] By crystallization of a strained or sheared melt or with a temperature gradient, this modification can be obtained in a mixture with the α-modification. Furthermore, nucleating reagents, such as γ-quinacridone or di-sodium orthophthalate, assist the formation of the β-modification.[137] Compared to the α-phase, the β-phase has a lower melting transition ($T_{m,\alpha} \approx 165 - 170$ °C; $T_{m,\beta} \approx 155$ °C) and converts into the α-phase at elevated temperatures.[133] However, the β-phase reveals a higher toughness and ductility in comparison to the α-phase.[142,143]

The γ-modification of iPP is more frequently observed for metallocene catalyzed iPP. It has an orthorhombic unit cell with the parameters a = 8.54 Å, b = 9.93 Å and c = 42.41 Å and a non-parallelism of the chain axes.[131,137] *Ziegler-Natta* produced iPP is only converted from the melt into the γ-form for high molecular weights under high pressure (about 500 MPa) or for low molecular weights at atmospheric pressure.[131,133,137,144–146] In contrast to this, for metallocene-based iPP, the γ-form crystallizes from the melt at atmospheric pressure for high molecular weight. However, a mixture of the α-form and γ-form is obtained, but the amount of the γ-form increases with stereo- and regiodefects (see chapter 2.4) inside the polymer chain.[133,137,147–151] The γ-form exhibits a lower melting transition and is additionally also transformed into the α-form upon heating or annealing process.[133]

The mesomorphic (smectic) phase of iPP is formed from the melt at ambient temperatures and

usually obtained by a rapid cooling of the molten state, e.g. in water.[133,137] This metastable modification with a melting transition between $65 - 120\,^{\circ}C$ is converted into the α-form by an annealing process at elevated temperatures, which is completed at temperatures between 140 $- 150\,^{\circ}C$.[133,137,152–155] The different phases of iPP can be differentiated by X-ray diffraction (XRD) due to their specific reflexes (Figure 9).[137]
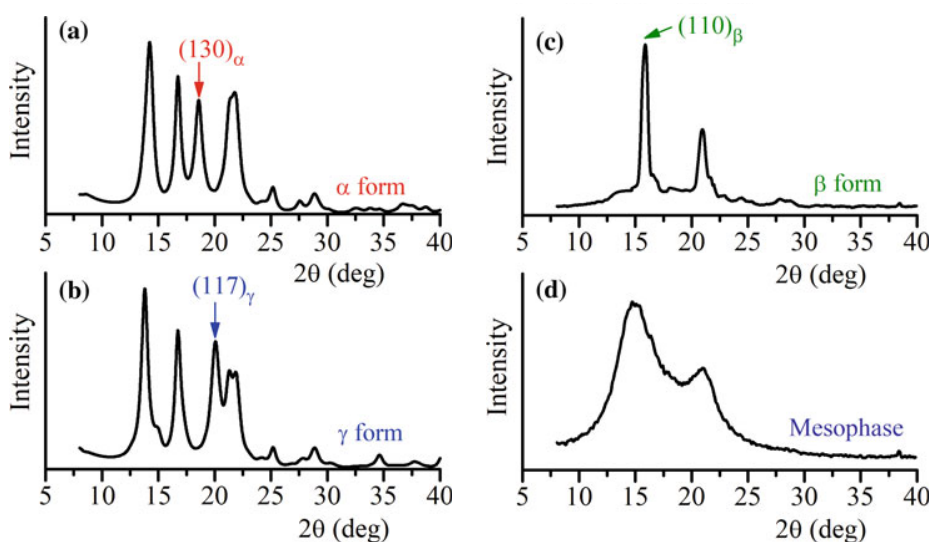
Figure 9: X-ray powder diffraction profiles (Ni filtered CuKα radiation) of the α, β, γ and mesomorphic (smectic) modification of iPP. Reprinted with permission from Ref.[137]. Copyright © 2019 by Springer.

2.6.2 Syndiotactic Polypropylene

Early work regarding the crystal structure of sPP was accomplished based on a heterogeneously prepared, regioirregular (2,1 insertion) polypropylene with a low syndioregularity and molecular weight. Two crystalline modifications, a s(2/1)2 helix and *trans*-planar zig-zag modification, were claimed.[133,137,156–159] The helical form, as it was observed by *Natta* and *Corradini* in 1960, is nowadays referred as the Form II. However, increased stereo- and regularity accessible through metallocene catalysis revealed an even more complex polymorphism of sPP than assumed. So far, four different polymorphic crystalline and two disordered mesomorphic modifications of sPP have been found.[137] Herein, only the four polymorphic crystalline modifications, Form I – IV (Figure 10) are discussed.

23
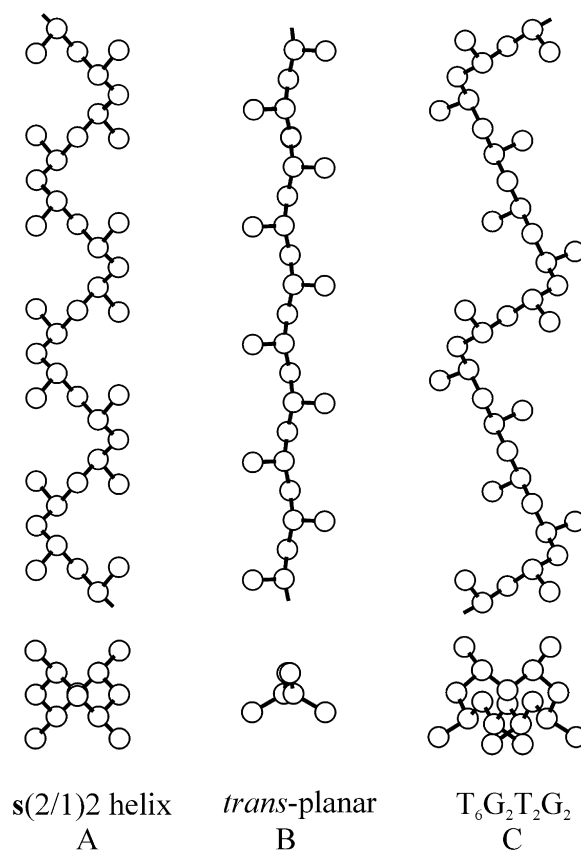
Figure 10: Polymer chains of sPP in helical s(2/1)2 (Form I and II, **A**), trans-planar (Form III, **B**) and $T_6G_2T_2G_2$ helical (Form IV, **C**) conformation. Reprinted with permission from Ref.[160]. Copyright © 2014 by Wiley.

The most stable modification of sPP is Form I, as identified by *Lotz* and *Lovinger*, and is obtained employing most crystallization conditions, including melt and solution crystallization.[137,161,162]. This antichiral packaged s(2/1)2 helical conformation (Figure 10,**A**) with the sequence $(TTGG)_n$ is described by an orthorhombic unit cell with the parameters a = 14.5 Å, b = 11.2 Å and c = 7.4 Å.[137,163] Refinements of Form I, though, suggest a monoclinic unit cell with a = 14.3 Å, b = 11.2 Å, c = 7.5 Å and γ = 90.3 °.[163,164] Form I is not only present for single crystals in ultrathin films, but also for thick films, materials directly from synthesis and for orientated thin films.[137] Isochiral helical Form II, which was considered the most stable crystal structure for more than three decades, is rather a metastable modification, also with a s(2/1)2 helical conformation and an orthorhombic unit cell with the parameters a = 14.5 Å, b = 5.6 Å and c = 7.4 Å.[137] This modification is present in orientated fibers and obtained by removing the tension of stretched stereoregular sPP fibers in the trans-planar Form III modifi-

cation or stretching low regio- and stereoregular *Ziegler-Natta* based sPP. Besides this, Form II mixed with Form I can be obtained by an annealing process of orientated stretched Form III fibers at temperatures between 90 and 120 °C, depending on the degree of syndiotacticity and melting transition.[137,165] Despite their similar diffraction profile, both crystal structures, Form I and Form II, can be differentiated *via* XRD by their characteristic 020 (Form I, 2θ = 15.9 °) and 110 (Form II, 2θ = 16.9 °) reflections.[137]
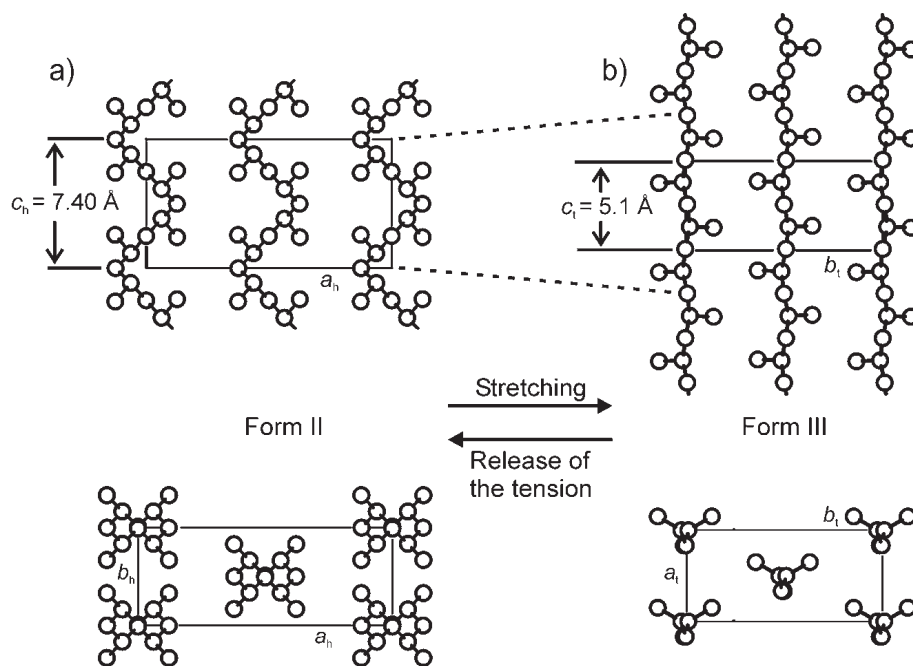
Figure 11: Packing models of helical s(2/1)2 form II (a) and trans-planar zig-zag formIII (b) of sPP in projections parallel (top) and perpendicular to the chain axes (bottom).[166] Reprinted with permission from Ref.[166]. Copyright © 2007 by Wiley.

Contrary to the helical modifications of Form I and Form II, Form III is characterized by a trans-planar zig-zag configuration with a $(TTTT)_n$ sequence (Figure 10**B**) and an orthorhombic unit cell with the parameters a = 5.2 Å, b = 11.2 Å and c = 5.1 Å.[167] This configuration is present for highly stereoregular metallocene based sPP being stretched at room temperature and high deformations. Equally, Form III is obtained if a Form I sPP material is stretched. However, releasing the tension of Form III was proven to yield Form II – even if the polymer was in the Form I modification prior stretching (Figure 11).[137,163,165,167–170] *De Rosa* and coworkers proved, that this polymorphic crystal–crystal phase transition is responsible for the high elasticity of sPP.[166,169,170] Form IV with a $T_6G_2T_2G_2$ sequence (Figure 10**C**) was observed by

Chatani by the exposure of stretched trans-planar Form III sPP to organic solvents, such as benzene, at temperatures below 50 °C. The helical conformation of Form IV is packed in a triclinic unit cell with the parameters a = 5.7 Å, b = 7.6 Å, c = 11.6 Å, α = 73.1 ° β = 88.8 ° and γ = 112.0 °. Form IV is exclusively found in orientated fibers and transformed into the two-fold helical conformations at temperatures above 50 °C.[137,163,171]

2.7 Processing of Polymers

For commodity polymers, such as PE, PP, polystyrene (PS) or polyethylene terephthalate (PET), various processing methods have been established over the last 70 years of polymer industrialization. Packaging materials for consumer goods in our everyday live are mainly produced *via* injection molding, compression molding, blow molding, calendering, deep drawing or thermoforming.[172] However, high performance polymers with outstanding tailored properties for specific applications require special methods for unleashing the ultimate potential of these polymers.

Polymerfibers are widely applied e.g. reinforced in concrete structures to increase the tension stabilization and elasticity of the concrete[173–175] or as non-woven fabrics for medical masks[176,177]. These fibers are usually produced by melt or electrospinning, yielding a thin and defined fiber.[178–180] Contrary to commercially available commodity polymer fibers, UHMW-PE fibers are used as a high performance material. However, due to the polymer's high melt viscosity, melt spinning of UHMW-PE is hardly feasible – therefore, gel-spinning is applied in the industrial production of high-performance UHMW-PE fibers.[7–9,181–184] Nevertheless, this process requires large amounts of organic solvents to dilute the polymer – hampering the sustainability of this process. *Kakiage* and co-workers established a combination of melt spinning and melt drawing of UHMW-PE, circumventing this issue. Therefor, the polymer was first melt extruded and afterwards, the as-spun fibers were melt drawn at a certain temperature.[185,186]

In addition to the processing methods described so far, additive manufacturing (AM) is a comparably new field of research. AM describes a variety of technologies that all have the same advantage: they build layer by layer directly from 3D computer-aided design (CAD) models and therefore do not require any tools. This process can either be applied to metals[187–189]

or polymers, such as polyamide-12,[190] polysulfones (PSUs),[191,192] poly(ether ether ketone)s (PEEKs)[192–194] or polyimides (PIs)[192,195].

However, among the variety of AM processes, the laser-based powder bed fusion of polymers (PBF-LB/P) has the greatest potential. In the first step, the powder is distributed in the build chamber with a roller or blade – the chamber is preheated under inert gas to a temperature between crystallization and melting transition, thus the polymer coexists in the melted and powdery state.[196,197] The powder is then exposed to a laser according to the sliced 3D CAD model, drawing a specific pattern onto the surface and fusing the particles to form a homogeneous melt. After exposure, the powder bed is lowered and a new layer of polymer is distributed on top of the previous one.[198–200] The three steps powder coating (1), laser fusion (2) and platform lowering (3) are repeated until the final part is manufactured. However, these process steps require high demands on the material – not comparable with classical manufacturing processes, such as injection or compression molding. Two main relations are important for a polymer to be used in the PBF-LB/P: (1) the polymer/process interaction for a successful production (printability triad) and (2) the process/final part properties interaction (printed parts triad).[201] Notwithstanding, this manufacturing technique is a very special process, not supportable for a high throughput of produced parts – contrary to injection molding. However, considering special requirements such as a complex part of any device, this procedure offers great chances, as the 3D CAD model can easily be modified and optimized.

3 Aim of this Thesis

In the last 70 years of research on the coordinative polymerization of propylene, a plethora of catalysts was established and such have been improved consistently, either regarding their catalytic performance or synthesis route. Nowadays, nearly every parameter of polypropylene can be adjusted as desired by implementing central aspects of metallocene catalysis. Isotactic or syndiotactic PP can be obtained by applying C_s- or C_2-symmetric metallocenes, respectively, and the macromolecular characteristics of the polymers tailored with an appropriate catalyst combined with suitable polymerization conditions and used co-catalyst. However, considering the latest advances in the extensively investigated field of coordinative polymerization, three main aspects seem to be untouched and are thus addressed in this thesis (Figure 12):

1) Boosting the catalytic performance of C_s-symmetric hafnocenes

2) Processing of UHMW-iPP for prototype production

3) Improving the yield of C_2(*rac*)-symmetric hafnocenes
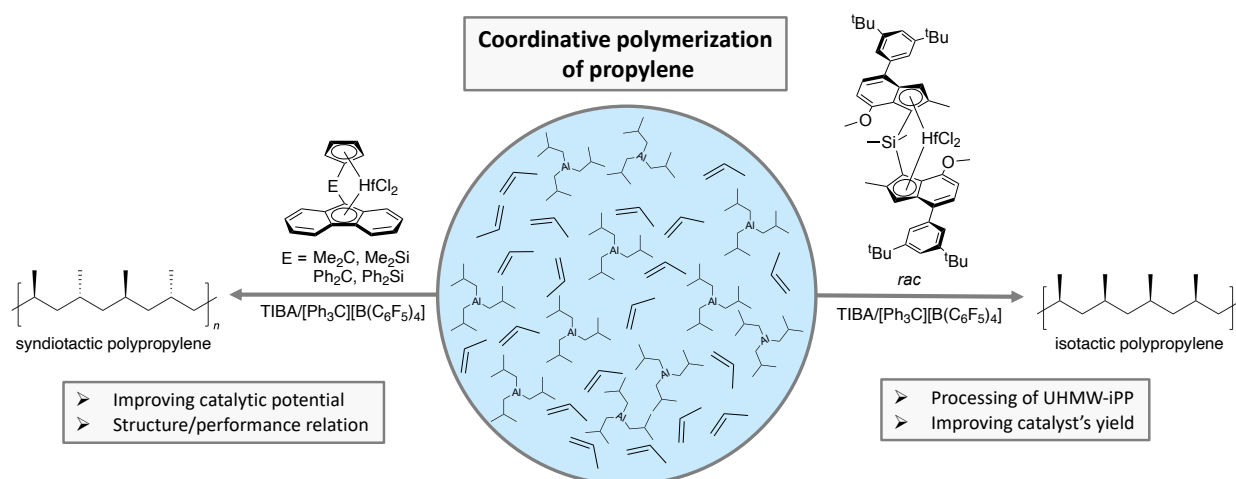
Figure 12: Aspects in the metallocene mediated coordinative polymerization of propylene to be covered in course of this thesis.

3.1 Boosting the Catalytic Performance of C_s-symmetric Hafnocenes

Since the first isolation of sPP by *Ewen* in 1988[27], a plethora of catalyst systems have been developed. Fundamental motifs in the catalyst design of group-IV metallocenes, such as the bridging motif or a modification of fluorene, were varied to tailor the properties of sPP.[28,31,35,36] However, so far mainly C_s-symmetric zirconocenes were investigated, as the corresponding hafnocenes showed a constrained catalytic activity with the co-catalyst MAO.[27,36–38] As already enclosed in 2.3 and 2.5, this is not caused by an intrinsic property of these hafnocenes themselves, it is rather induced by the MAO activation method forming the cationic resting state $[L_2Hf(\mu–Me)_2AlMe_2]^+$.[56–58] Therefore, an increase of the catalytic activity by changing the activation method is targeted: using the *in situ* activation using TrBCF and TIBA established by our group, overcoming the issues of the MAO activation. This variation should tremendously increase the catalytic activity and polymer's molecular weight due to the diminished chain transfer to Al (2.4.4).

The academic and industrial advantage of sPP compared to iPP comes into account considering the polymer's morphology: as enclosed in 2.6, besides a s(2/1)2 helix, sPP forms also a trans-planar zig-zag configuration.[131–133,137,156–159] Latter is comparable to the zig-zag chains of polyethylene[202] and thus, sPP is considered to exhibit a better processability for fiber spinning than iPP – especially for an ultrahigh molecular weight. Shifting a polymer's molecular weight to an ultrahigh regime is linked with an outstanding increase of the mechanical properties. For example, compared to high-density polyethylene, UHMW-PE has improved mechanical properties that even allow for its use as bulletproof vests or joint replacements.[7–9] This example highlights the great interest of UHMW polymers. However, the processing of UHMW polymers *via* the conventional melt extrusion becomes nearly impossible.[203,204] Despite that, UHMW-PE was proven to be processable, either *via* melt-extrusion or by gel-extrusion.[181,185,186,205–207] Considering the improved properties of PP compared to PE[208] in combination with an anticipated better processability of UHMW-sPP than UHMW-iPP, UHMW-sPP seems to be a very promising material for our daily life. Therefore, for a broad adaption of this polymer, a high catalytic activity of the used catalyst is mandatory and is therefore one central point to be covered in this thesis.

3.2 Processing of UHMW-iPP

In 2012, *Rieger et al.* established a catalyst system that remains a benchmark system in propylene polymerization up to the present day. Using this catalyst, iPP with unsurpassed macromolecular characteristics is obtained: perfectly isotactic PP with the so far highest molecular weight of up to 5800 kg/mol and a melting transition *ex reactor* up to 171 °C.[44,124,209]

As enclosed in 3.1, UHMW polymers exhibit greatly enhanced mechanical properties, leading to e.g. widely applied UHMW-PE fibers. UHMW polymers possess the ability of ultimate performance without the need of additional fillers – improving the recyclability with no interfering additives. For UHMW-PE, numerous studies proved the melt-processability, whereas other UHMW polymers received less attention due to the high melt viscosity and the thereby affected perspective of nearby impossible processability *via* common melt extrusion.[185,186,203,204] Notwithstanding, UHMW-iPP has serious advantages compared to UHMW-PE bearing a high potential for final part production: a nearly 25 °C higher melting temperature, a lower density, a higher impact resistance and tensile strength.[204] Theoretically, UHMW-iPP fibers could therefore outperform UHMW-PE *Dyneema* fibers, e.g. in terms of strength and weight of bulletproof vests.

Fiber spinning is generally accomplished by various kinds of extrusion processes. However, the major drawback in melt-extrusion of UHMW polymers is their high melt viscosity, which correlates with the polymer's molecular weight with $\eta_0 \propto M_w{}^{3.4}$.[210] This nonlinear behavior of the zero shear viscosity is caused by an increase of the entanglements per chain. Upon melting, these topological constraints, which are present in the amorphous phase of semi-crystalline polymers, distribute homogeneously.[204,211] Besides this, there is also the probability of further entanglement formation in the molten state.[212] This consequently enhances the melt-viscosity and thus hampers the processability of this polymer.

With such potential of UHMW-iPP, processing of this unique polymer is targeted. First, by classic melt-extrusion for fiber spinning to investigate the mechanical properties of UHMW-iPP fibers. In addition to that, an alternative method is strived for: selective laser sintering of polymers, diminishing the disadvantage of the molten state and the thereby negative aspects induced by the high melt-viscosity.

3.3 Improving the Yield of C$_2$(*rac*)-symmetric Hafnocenes

Catalysts for the isospecific polymerization of propylene reveal one major disadvantage, both industrial and academic researchers have to deal with: the tedious *rac*/*meso* separation of both isomers, as the *meso* isomer was proven to yield atactic PP rather than the desired isotactic analogue (2.4.3).[21]

In the last decades, several approaches were established for a synthesis of pure *rac* isomers. *Ivchenko* and co-workers applied a transmetalation of ethylene bridged (bis)-indenyl ligands yielding disilylated or distannylated ligands with 100% *anti* configuration after a convenient separation, which gave 98% *rac* zirconocene after reaction with ZrCl$_4$.[213] *Jordan* and co-workers investigated the application of Zr(NMe$_2$)$_4$[214] and chiral diamide[215] precursors for the diastereoselective synthesis of *rac*-isomers. Besides this, *meso*-to-*rac* isomerization protocols, e.g. using ultraviolet (UV)-light, were reported.[18,216] In 2007, *Jordan et al.* published the anion-promoted *meso*-to-*rac* isomerization, applying chloride salts in refluxing THF.[217] This isomerization is widely applied by *Voskoboynikov et. al* and was also proven to be transferable to *Rieger's* ultrarigid benchmark catalyst.[25,126] However, these protocols often lead to equilibria of *rac*/*meso* mixtures and are non-transferable to several catalyst systems.

With this tedious synthesis route and the so far wasteful *meso*-analogue in mind, the polymerization using pure *meso*-complexes and isomeric mixtures of *rac*- and *meso*-metallocenes is aimed for. This however should theoretically yield aPP or an aPP/iPP blend, respectively.

4 Boosting the Catalytic Performance of C$_s$-symmetric Hafnocenes

"*In Situ* Activation: Chances and Limitations to Form Ultrahigh Molecular Weight Syndiotactic Polypropylene with Metallocene Dichlorides"

4.1 Bibliographic Data

Title:	*In Situ* Activation: Chances and Limitations to Form Ultrahigh Molecular Weight Syndiotactic Polypropylene with Metallocene Dichlorides
Status:	Article, Publication Date: 13.09.2021
Journal:	Organometallics
Publisher:	American Chemical Society
DOI:	10.1021/acs.organomet.1c00397
Authors:	Lucas Stieglitz, Daniel Henschel, Thomas Pehl, and Bernhard Rieger[1]

4.2 Graphical Abstract (TOC)
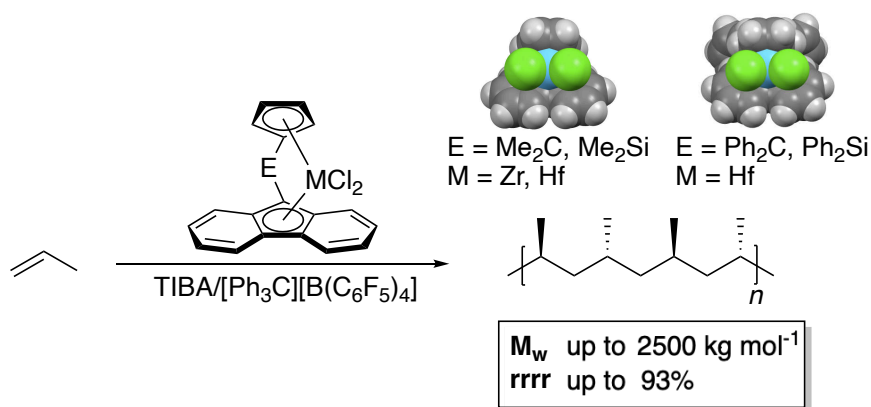
Figure 13: Graphical abstract (TOC) of the manuscript titled "*In Situ* Activation: Chances and Limitations to Form Ultrahigh Molecular Weight Syndiotactic Polypropylene with Metallocene Dichlorides".

---

[1]L. Stieglitz planned and performed all experiments and wrote the manuscript. D. Henschel conducted all SC XRD-measurements and processed the data. T. Pehl helped with data analysis and preparing the manuscript. All work was supervised by B. Rieger.

4.3 Content

Using the most common activating reagent, methylaluminoxane, hafnocene-dichlorides suffer from two major drawbacks in the synthesis of UHMW-PP: Inhibited catalytic activity and reduced molecular weight of the produced PP (see chapter 2.5). Therefore, our group established the *in situ* activation of C$_1$- and C$_2$-symmetric metallocene-dichlorides to overcome these drawbacks. Contrary to iPP, this convenient activation method has not yet been established for the synthesis of UHMW-sPP by C$_\text{S}$-symmetric metallocene-dichlorides.

In this manuscript, five C$_\text{S}$-symmetric *ansa*-metallocene dichlorides with different bridging motifs were synthesized to investigate structure-performance correlations in the coordinative polymerization of propylene after *in situ* activation with TIBA/TrBCF. Single crystals of complex **III** were isolated and with the aid of literature known data, the influence of various bridging motifs on structural parameters, such as bite- and dihedral angle or *D*-value, and the thereby affected performance in the polymerization of propylene after *in situ* activation was emphasized. The performance of the hafnocenes **Ib**, **II**, **III** and **IV** when *in situ* activated was compared with the classical MAO activation and benefits of the *in situ* activation in terms of productivity and molecular weights for hafnocene-dichlorides were highlighted. This study illustrates the impact of the bridging motif onto the geometry and structural parameters of the catalyst and the thereby associated polymerization performance.

All hafnocenes generated UHMW-sPP with a molecular weight up to 2500 kg/mol and a high syndiotacticity (up to 73%) using TIBA/TrBCF. Silicon-bridged hafnocenes showed a constrained stereoregularity and activity (4-fold to 20-fold, respectively), whereas the molecular weight was enhanced. In contrast to the *in situ* activation, MAO diminished the productivity and molecular weight (max. 530 kg/mol), whereas the degree of syndiotacticity was slightly enhanced (up to 80%). With this series of polymerizations, we proved the high potential of the *in situ* activation and the transferability of this activation method onto C$_\text{S}$-symmetric catalyst systems (M = Zr, Hf). However, one major disadvantage appeared in course of this activation: The obtained polymers after *in situ* activation did not exhibit melting transitions, which was feasible with MAO activation – probably due to the ultrahigh molecular weight and moderate degree of syndiotacticity combined with the innately low crystallization of sPP.

ORGANOMETALLICS

Article

In Situ Activation: Chances and Limitations to Form Ultrahigh Molecular Weight Syndiotactic Polypropylene with Metallocene Dichlorides

Lucas Stieglitz, Daniel Henschel, Thomas Pehl, and Bernhard Rieger*

Read Online

ACCESS | ⬛ Metrics & More | ▦ Article Recommendations | ⑤ Supporting Information

ABSTRACT: Fluorenyl cyclopentadienyl C_s-symmetric *ansa*-metallocene (M = Zr, Hf) complexes **I−IV** featuring different bridging motifs (C and Si) were synthesized and subsequently examined in the syndiospecific coordinative polymerization of propylene. All complexes were activated *in situ* with triisobutylaluminum (TIBA) and $[Ph_3C][B(C_6F_5)_4]$ (TrBCF) in order to highlight the benefits of this *in situ* activation, resulting in a significantly higher molecular weight and a significantly increased productivity in comparison to methylaluminoxane (MAO). The isopropylidene-bridged zirconocene **Ia** ($ZrCl_2[Me_2C(\eta^5\text{-Flu})(\eta^5\text{-Cp})]$) exhibited a high productivity (80000 kg_{PP} $(mol_{cat}\ h)^{-1}$) and stereoregularity ([rrrr] up to 93%) with a moderate molecular weight of polypropylene (PP), whereas the polymerization with the corresponding hafnocene **Ib** ($HfCl_2[Me_2C(\eta^5\text{-Flu})(\eta^5\text{-Cp})]$) resulted in a lower productivity and stereoregularity but yielded ultrahigh molecular weight polypropylene (M_w = 1100 kg mol^{-1}). The backbone in **II** ($HfCl_2[Ph_2C(\eta^5\text{-Flu})(\eta^5\text{-Cp})]$) was associated with a higher productivity and molecular weight, while the syndiotacticity was not affected. In contrast, SC-XRD revealed a reduced dihedral angle and D value for Si-bridged hafnocenes **III** ($HfCl_2[Me_2Si(\eta^5\text{-Flu})(\eta^5\text{-Cp})]$) and **IV** ($HfCl_2[Ph_2Si(\eta^5\text{-Flu})(\eta^5\text{-Cp})]$), resulting in a more constrained geometry of the catalyst. This led to an increased molecular weight, while the productivity as well as the syndiotacticity decreased due to these structural parameters. Activation of **Ib** and **II−IV** with *n*-octyl-modified methylaluminoxane (MMAO) resulted in a lower molecular weight of the polymer, because the transfer of the growing polymer chain onto the Al center was enhanced. Nevertheless, the stereoregularity of MMAO-activated catalysts was slightly increased, probably due to a coordination of the ill-defined MMAO anion during the polymerization. DSC analysis exposed for syndiotactic polypropylene (sPP) produced by the highly active zirconocene **Ia** a defined melting transition (T_m up to 145.2 °C), whereas TIBA/TrBCF-activated hafnocenes **Ib** and **II−IV** gave polymers with no observable T_m value.

E = Me₂C, Me₂Si
M = Zr, Hf

E = Ph₂C, Ph₂Si
M = Hf

TIBA/[Ph₃C][B(C₆F₅)₄]

M_w up to 2500 kg·mol^{-1}
rrrr up to 93%
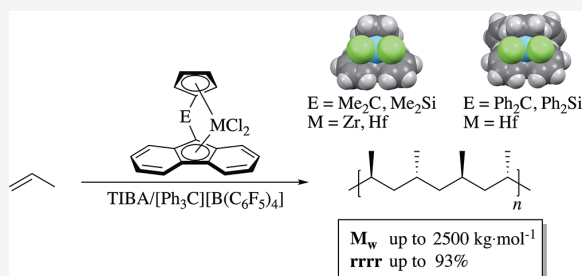
■ INTRODUCTION

The shift of the polymers' molecular weight to the ultrahigh regime is linked with enhanced properties, such as a further optimization of the polymer's mechanical behavior. For example, ultrahigh molecular weight polyethylene (UHMWPE) has greatly enhanced mechanical properties in comparison to high-density polyethylene, and the outstanding Young's modulus and tensile strength (>90 and >3 GPa, respectively) even enable its application in bulletproof fabrics.[1−4] In addition, polypropylene (PP) has further polymer advantages in comparison to PE: e.g., a higher service temperature. Furthermore, the availability of stereocenters allows the synthesis of stereocontrolled polymers, whereby highly isotactic polypropylene (iPP) builds a 3/1 helix by virtue of the repulsive interaction of the methyl groups,[5] whereas syndiotactic polypropylene (sPP) forms a trans-planar zigzag configuration in addition to a s(2/1)2 helix.[6,7] For the purpose of processing of UHMWPP in a fashion similar to that of UHMWPE, e.g., gel extrusion for fiber spinning, UHMW-

sPP is considered to be far better suited than the isotactic alternative, because the zigzag configuration is similar to the microstructure of the processable UHMWPE.[8] In general, the macromolecular characteristics of the resulting polypropylene, such as its molecular weight and melting transition, can be adjusted by a change in fundamental motifs in catalyst design: e.g., the ligand or the central group IV metal atom of *ansa*-metallocene dichlorides.[9−19] In the literature, for the synthesis of ultrahigh molecular weight polypropylene, hafnium is recommended instead of zirconium as the central metal atom, because the corresponding Hf homologues yielded up to a 10-fold higher molecular weight of polypropylene.[20,21]

4055

Scheme 1. Synthesis Route of Catalysts I and II

Ia: R = Me; M = Zr (40%)
Ib: R = Me; M = Hf (18%)
II: R = Ph; M = Hf (46%)
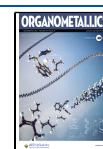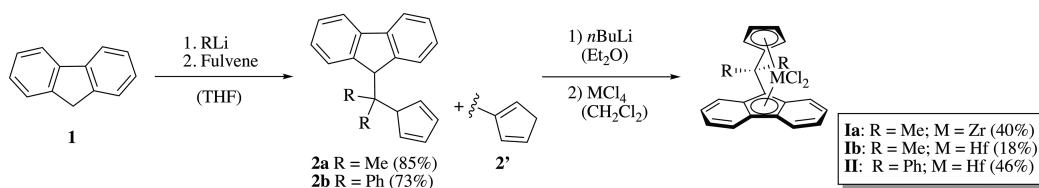
Scheme 2. Synthesis Route of Catalysts III and IV

III: R = Me (9%)
IV: R = Ph (27%)
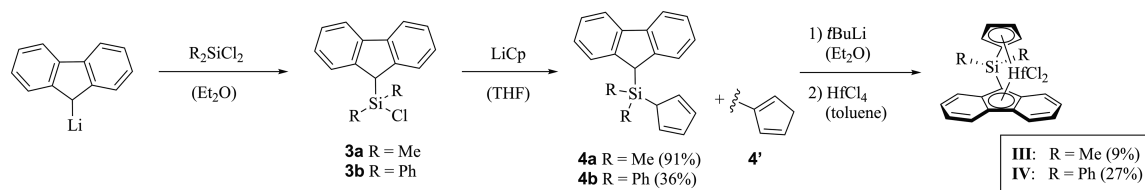
Table 1. Characteristic Angles and Distances of the Solid-State Structures I−IV[a]

catalyst	bite angle[a] γ (deg)	dihedral angle[a] β (deg)	Flu−M−Cp α (deg)	M−Cp$_{centroid}$ (Å)	M−Flu$_{centroid}$ (Å)	D^a (Å)
Ia	99.42	72.27	118.61	2.168	2.238	1.124
Ib	100.75	70.53	119.38	2.160	2.236	1.110
II	99.59	72.77	118.27	2.150	2.242	1.126
III	93.65	63.01	128.46	2.163	2.278	0.965
IV	96.28	62.03	129.81	2.163	2.302	0.946

[a]Determined from model systems known in the literature. See Figure S56.[30,31]

Nevertheless, prior to the polymerization of olefins, metallocene dichlorides require activation by an alkylating and initiating agent in order to form the catalytically active cationic species. The most common reagent for this, methylaluminoxane (MAO), has been deeply investigated for various *ansa*-metallocenes. However, whereas MAO-activated zirconocenes polymerized propylene with high activity, the corresponding hafnocenes showed comparatively low activities on activation with MAO.[12,14,15,21] This reduced activity is assumed to be induced by residual trimethylaluminum (TMA) in the MAO solution, because the dinuclear cationic methyl-bridged complex $[L_2M(\mu\text{-Me})_2AlMe_2]^+$ is formed.[20,22,23] For hafnium as the central metal atom, DFT calculations revealed a higher stability of this bridged heterobimetallic aluminum complex by 3.0 kcal mol^{-1} in comparison to the corresponding zirconium complex.[20] Therefore, $[L_2Hf(\mu\text{-Me})_2AlMe_2]^+$ resembles a stable resting state in the polymerization of propylene with hafnocenes, whereas the productivity of zirconocenes is not as affected by TMA. Since the low activity is not an intrinsic problem of the hafnocene itself and is more induced by the slow and thus inefficient activation method, our group established the *in situ* activation of metallocene dichlorides in 2003 by using triisobutylaluminum (TIBA) combined with the Lewis acid $[Ph_3C][B(C_6F_5)_4]$ (TrBCF).[24−26] The first step of this method includes preactivation through double alkylation of the metallocene dichloride with TIBA at 60 °C for 1 h, and the subsequent polymerization is initiated by the addition of the trityl salt to form the catalytically active cationic species. Additionally, TIBA not only acts as an alkylation reagent but also stabilizes the alkylated and cationic species as an oxygen or water scavenger.[25] Not forming the dinuclear stable resting state using TIBA, the *in situ* activation of hafnocenes resulted in productivities as high or even higher than those of the corresponding zirconocenes.[26]

The aim of this research was to enhance both the molecular weight of the received sPP and the productivity of several C_s-symmetric *ansa*-metallocene catalysts by using *in situ* activation, including TrBCF/TIBA instead of MMAO. The classic fluorenyl cyclopentadienyl system for sPP (**Ia,b** and **II**), as already described by Ewen and Razavi,[15,21] was additionally extended by isostructural Si-bridged catalysts (**III** and **IV**).

RESULTS AND DISCUSSION

Syntheses. A variety of fluorenyl cyclopentadienyl bridged group IV metallocenes **I−IV** with different Si and C bridging motifs were synthesized. Various synthesis strategies were applied, depending on the bridging atom. The ligand structure of the C-bridged catalysts **I** and **II** was isolated in a three-step synthesis (Scheme 1). In the first step, the corresponding fulvene was formed in a Knoevenagel-type reaction of the corresponding ketone.[27,28] Therefore, fluorene **1** was lithiated, the corresponding fulvene was added, and after aqueous workup **2** and its thermodynamically more stable configuration **2′** were formed. The *ansa*-metallocenes **I** and **II** were obtained after double deprotonation of **2** with *n*BuLi and the addition of MCl$_4$ (M = Zr, Hf).[12,15,21,29]

The silane-bridged catalysts **III** and **IV** were synthesized, with R$_2$SiCl$_2$ as the starting material (Scheme 2). A crucial step in this synthesis was the very slow addition of Flu-Li to a diethyl ether solution of the corresponding dichlorosilane with vigorous stirring and a high dilution in order to avoid a double substitution at the Si center. For the reaction with Me$_2$SiCl$_2$, Flu-Li was generated *in situ* by using excess MeLi and utilized without further purification, since possible side products in the reaction are volatile, as the precursor Me$_2$SiCl$_2$ itself. Ph$_2$SiCl$_2$

has a comparably high boiling point; therefore, an exact stoichiometric amount of Flu-Li was required. While the solvent THF led to a large proportion of the double-fluorene-substituted silane ligand, diethyl ether gave a perfect balance between reactivity and selectivity. After the solvent and all volatile compounds were removed, LiCp was added to the THF solution of **3**, and **4** was obtained after an aqueous workup. The corresponding ligand **4** was double-lithiated by *t*BuLi, and the *ansa*-hafnocenes **III** and **IV** were isolated after the addition of HfCl$_4$.

Single crystals for X-ray diffraction analysis were isolated for **III** by diffusing pentane into a saturated solution of the complex in toluene at 4 °C. The crystal structures of complex **Ia** (CCDC 1190113),[29] **Ib** (CCDC 1168308),[29] **II** (CCDC 1232978),[15] and **IV** (CCDC 152546)[18] have already been reported in the literature. The characteristic bond lengths and angles of all complexes were determined (see Figure S56) and are represented in Table 1. Changing the central metal atom of Zr in **Ia** to Hf in **Ib** resulted in a slightly increased bite angle and Flu$_{centroid}$−M−Cp$_{centroid}$ angle, whereas the dihedral angle and *D* value were diminished. By a comparison of the C- and Si-bridged hafnocenes **Ib** and **III**, a smaller dihedral angle, *D* value, and Flu$_{centroid}$−Cp$_{centroid}$ distance for a Si atom in the bridging motif was highlighted, whereas the Flu$_{centroid}$−Hf−Cp$_{centroid}$ angle was slightly enhanced. The same tendency was observed for **II** and **IV**. Therefore, C-bridged complexes presented a greater reaction surface of the metal center due to less obstruction by the ligand in comparison to Si-bridged complexes. A slightly higher M−Flu$_{centroid}$ bond length in comparison to the M−Cp$_{centroid}$ bond length was measured for all complexes; thus, the central metal atom was not precisely centered between the two η^5-bonded ligands.

Nevertheless, the SC-XRD space-filling representations of all complexes illustrated that changing the atom of the bridging motif had no great effect on the steric demand of the backbone toward the metal center (Figure 1), while it slightly changed
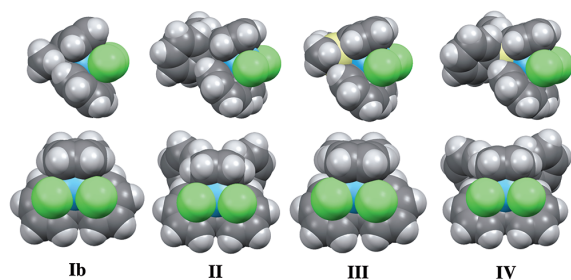
Figure 1. Space-filling representations of SC-XRD data of **Ib** and **II**−**IV** illustrating the change in the overall geometry of the catalyst by introducing various bridging motifs.

the overall geometry of the ligand (Figure 1 and Figure S56). Therefore, differences in catalytic activity and performance were mainly driven by the dihedral angle (the "openness" of the ligand system) and *D* value (the "exposedness" of the metal center) of the catalyst.

Productivity. All four catalysts **I**−**IV** were tested with respect to their catalytic performance in the polymerization of propylene (Table 2). The isopropylidene-bridged zirconocene **Ia** and hafnocene **Ib** were investigated in more detail with regard to the influence of the polymerization temperature T_p on the catalytic behavior in order to gain a deeper insight into

the capabilities of the *in situ* activation. Complexes **II**−**IV** were used for polymerization at 0 and 30 °C on activatation with TIBA/TrBCF so as to cover up the peak performance of these complexes, because a lower temperature leads to a higher molecular weight and stereoregularity of the resulting polymer.[25,32] Additionally, these complexes were activated with 2000 equiv of MMAO and polymerized with propylene at 30 °C in order to compare the *in situ* and the MMAO results. Below 30 °C, the activity of MMAO-activated hafnocenes is too low and was thus neglected.[12]

Table 2 clarifies the discrepancy resulting from different group IV metal centers, as **Ia** has a much higher productivity in comparison to the corresponding hafnocene **Ib**. For example, at lower temperatures in particular **Ia** shows a 32 times higher productivity for a polymerization temperature of 0 °C (entry 1, Table 2) in comparison to **Ib** (entry 6, Table 2). This discrepancy is assumed to be caused by the stronger σ-Hf−C bond in comparison to the σ-Zr−C bond in terms of energy barrier during the chain propagation that slows down bond formation processes in the polymerization. The σ-Hf−C bond was determined to be about 22 kJ mol^{-1} stronger in a model isostructural Cp*$_2$MMe$_2$ complex systems (Hf−C, 306 ± 7 kJ mol^{-1}; Zr−C, 284 ± 2 kJ mol^{-1}) via titration calorimetry.[33] Surprisingly and inexplicably, the high productivity of zirconocene **Ia** decreased at higher polymerization temperatures (entries 1−5, Table 2). As this behavior using **Ia** cannot be explained and was not observed with other activating agents,[12,15,21,29] the productivity of **Ia** was determined several times to authenticate these results. However, further investigations are required in order to better understand the effect of the alkylating reagent TIBA and the initiating compound TrBCF on the polymerization. In contrast to **Ia**, hafnocene **Ib** showed, as expected, an increased productivity at a higher polymerization temperature when activated *in situ* (Figure 2). The maximum productivity is probably between 40 and 60 °C, and the productivity decreases with a further increase in temperature, presumably due to the deactivation of the catalytically active species.

Complexes **II**−**IV** showed the same tendency as **Ib** by increasing their productivity in the polymerization of propylene at higher polymerization temperatures (Figure 3). Catalyst **II** had—especially at 0 °C (entry 13, Table 2)—enhanced productivity over **Ib**. In comparison to the study by Razavi et al. in 2009, the *in situ* activation, including the preactivation with TIBA at 60 °C for 1 h, resulted in a much higher productivity with catalyst **II**.[20] The activation of catalysts **Ib** and **II** with MMAO revealed the expected loss of activity due to residual TMA in the MMAO solution (entries 9, 15, 18, and 21 in Table 2). In contrast, the silane-bridged catalysts **III** and **IV** showed different results with TIBA/TrBCF. Whereas the C-bridged catalysts **Ib** and **II** were highly active on activation *in situ*, the Si-bridged hafnocenes **III** and **IV** were less active by far (4-fold and 20-fold loss of activity, respectively) at polymerization temperatures of 0 and 30 °C. The higher reaction space and exposedness for C-bridged hafnocenes, indicated by the higher bite angle and *D* value, probably leads to an easier activation and an enhanced coordination of propylene during the polymerization, so that the productivity of C-bridged hafnocenes **Ib** and **II** is boosted in comparison to **III** and **IV**. In addition, side reactions during the activation with TIBA/TrBCF of **III** and **IV** could occur. This hypothesis was corroborated, since the consistent bright yellow color got weaker over time immediately after TIBA

Table 2. Conditions and Results for the Polymerization of Propylene with Complexes I−IV[a]

entry	catalyst	n[b]	activation[c]	T_P[d]	t_P[e]	[rrrr][f]	M_w[g]	$Đ$[h]	P[i]
1	Ia	1.16	TIBA/TrBCF	0[j]	7.5	93	140	1.6	80000
2	Ia	1.16	TIBA/TrBCF	10[k]	10	88	130	1.6	45000
3	Ia	1.16	TIBA/TrBCF	20	20	86	93	1.5	23000
4	Ia	1.16	TIBA/TrBCF	40	20	75	57	1.4	3300
5	Ia	1.16	TIBA/TrBCF	60	20	56	36	3.1	2300
6	Ib	1.92	TIBA/TrBCF	0	30	73	1100	1.9	2500
7	Ib	1.15	TIBA/TrBCF	20	20	nd	920	2.1	6500
8	Ib	1.15	TIBA/TrBCF	30	10	67	740	1.6	11100
9	Ib	2.27	MMAO	30	30	80	360	1.4	230
10	Ib	1.44	TIBA/TrBCF	40	15	nd	450	2.0	14600
11	Ib	1.92	TIBA/TrBCF	60	10	nd	370	1.7	16400
12	Ib	1.92	TIBA/TrBCF	80	20	nd	140	2.4	3400
13	II	1.55	TIBA/TrBCF	0	15	72	2100	1.4	7400
14	II	1.55	TIBA/TrBCF	30	10	64	1400	1.3	13000
15	II	1.88	MMAO	30	30	79	530	1.3	460
16	III	1.87	TIBA/TrBCF	0	15	52	1900	1.8	530
17	III	1.87	TIBA/TrBCF	30	10	38	1800	1.5	3100
18	III	2.69	MMAO	30	30	43	430	1.2	600
19	IV	4.12	TIBA/TrBCF	0	45	35	2500	1.9	350
20	IV	4.18	TIBA/TrBCF	30	45	24	1500	1.6	650
21	IV	3.77	MMAO	30	30	38	530	1.2	1400

[a]Conditions: $V_{toluene}$ = 120 mL; $p = p_{Ar} + p_{propylene}$ = 6 bar; p_{Ar} = 1.3 bar. nd = not determined. [b]In mmol. [c]TIBA/TrBCF: initiator $[Ph_3C][B(C_6F_5)_4]$ 5.0 equiv, activator (TIBA) 200 equiv, scavenger (TIBA) 0.55 mmol; scavenger/activator MMAO 2000 equiv. [d]In °C ±2 °C. [e]Polymerization time in min. [f]In percent, determined via ^{13}C NMR spectroscopy assuming the enantiomorphic site model. [g]In kg mol^{-1}, determined absolutely via SEC-GPC in 1,2,4-trichlorobenzene at 160 °C with dn/dc = 0.097 mL g^{-1}. [h]$Đ = M_w/M_n$. [i]In kg$_{PP}$ (mol$_{cat}$ h)$^{-1}$. [j]±8 °C. [k]±5 °C.
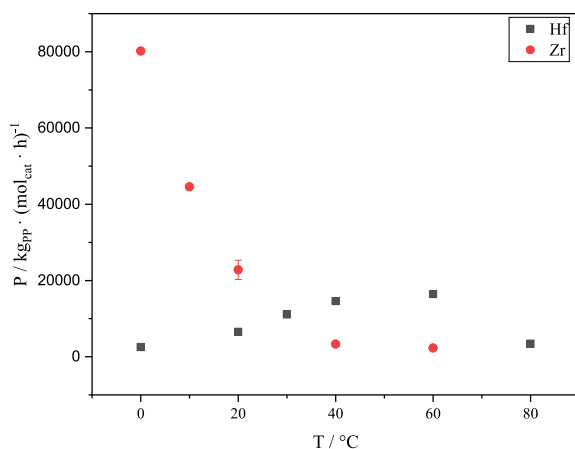
Figure 2. Productivity of *in situ* activated **Ia,b** in the polymerization of propylene at various temperatures. Error bars are depicted for possible deviations during the preparation process.

Figure 3. Productivity of different activated complexes **Ib** and **II−IV** in the polymerization of propylene at various polymerization temperatures.

addition to the catalyst solution. Furthermore, after the solution was heated to 60 °C, an entirely colorless solution was obtained after a few minutes instead of the pale yellow solution for TIBA-activated C-bridged hafnocenes. Both observations remain in crucial contrast to reported results for dimethylsilane-bridged SBI-type C_2-symmetric catalysts.[34,35] Nevertheless, catalyst **III** activated with MMAO also showed the expected deficit in productivity, whereas the productivity of **IV** slightly increased.

Molecular Weight. The zirconocene **Ia** produced PP with a molecular weight nearly 10 times lower than that for the corresponding hafnocene **Ib**. This was induced by a stronger σ-

Hf−C bond, as it slowed down bond-breaking processes during the polymerization, thus resulting in fewer termination reactions and, therefore, a higher molecular weight for the received polypropylene.[16,24] Increasing the polymerization temperature increased the probability of a bond-breaking mechanism, resulting in a reduced molecular weight of the obtained polymer. This behavior was clearly observed not only with **Ia,Ib** (Figure 4) but also with **II−IV** (Figure 5).

All four hafnocenes **Ib** and **II−IV** were able to produce UHMW-sPP up to 2500 kg mol^{-1} (entry 19, Table 2), especially on polymerization at lower temperatures (Figure 5). When the polymerization temperature was increased, a typical
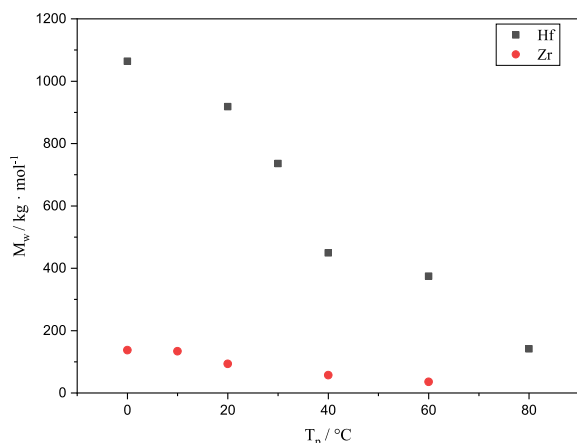
Figure 4. Molecular weight of PP after *in situ* activation of **Ia,b** in the polymerization of propylene at various temperatures.
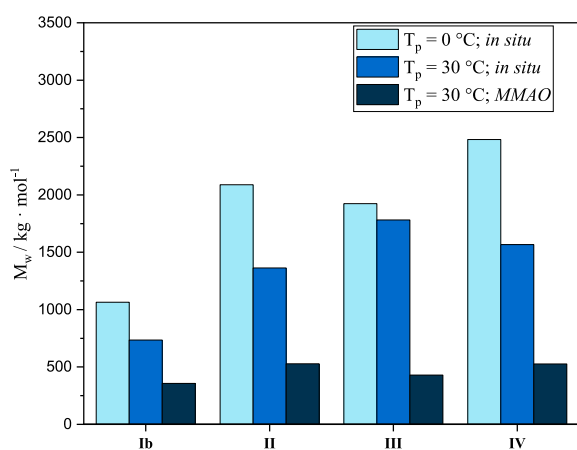
Figure 5. Molecular weight of PP after activation of hafnocenes **Ib** and **II−IV** at various polymerization temperatures.

decrease in the molecular weight through a higher probability of bond-breaking termination reactions was observed. As surprisingly highlighted by entries 16 and 17, **III** was not as strongly affected by the temperature in terms of molecular weight as were **Ib**, **II**, and **IV**. On comparison of the different bridged hafnocenes, an increased molecular weight of polypropylene was associated with a Si bridging moiety. The difference in their catalytic performance might be attributed to the higher constrained geometry of the Si-bridged hafnocenes by both the decreased bite and dihedral angles and the *D* value. The reduced reaction space could then lead to a decrease in *β*-H and *β*-Me elimination, as the polymer chain ends H and Me remain in a less favored configuration for any elimination. Electronic effects caused by the lower electronegativity of Si could have played a further role in the effect on the molecular weight of sPP due to pushing electron density into the ligand system and stabilizing the σ-Hf−C bond. This theory could be verified via a calorimetric titration of Si- and C-bridged isostructural L$_2$MMe$_2$ complexes for the determination of the corresponding σ-Hf−C bond energy, in a fashion similar to that for Cp*$_2$MMe$_2$.[20]

The discrepancy between the *in situ* activation and the MMAO activation was anticipated. All four complexes **Ib** and **II−IV** were profoundly influenced by MMAO, since the molecular weight decreased strongly when these complexes were activated with *MMAO* (entries 9, 15, 18, and 21, Table 2). Therefore, all of the complexes produced polypropylene with a molar mass of between 400 and 600 kg mol^{-1} instead of polymers featuring an ultrahigh molecular manner. The literature primarily attributes this phenomenon to an increased transfer of the growing polymer chain toward the Al center of MMAO and residual TMA.[25,32] When *MMAO* was replaced by a sterically more demanding alkylating agent such as TIBA, the rate of an Al transfer of the polymer chain was reduced to a minimum, thus resulting in a higher molecular weight.[22,36]

Stereoregularity. The zirconocene **Ia** produced highly syndiotactic PP. With regard to the polymerization at lower temperatures in particular, the overall performance of **Ia** in terms of syndioselectivity was outstanding ([rrrr] up to 93%, entry 1, Table 2). The nearly perfect stereoregularity control by the zirconocene **Ia** (NMR spectrum; cf. Figure S27) was highlighted by merely small quantities of misinsertions, such as back-skip processes ([rrrm], 20.2 ppm). The increase in temperature resulted in a greater degree of misinsertions; thus, the syndiotacticity decreased (Figures S28−S31). This behavior was consistent not only with an increased back-skip mechanism at an increasing temperature[37] but also through a general loss of stereocontrol. A difference in stereocontrol was observed when the central metal atom in **Ia** was changed to Hf. Even at lower temperatures, **Ib** was not capable of producing highly syndiotactic polypropylene ([rrrr] up to 73%, entry 6, Table 2). Both the degree of back-skip mechanism and the general misinsertions increased, thus leading to enhanced [rmmr]- and [mmrr]-pentades (Figure 6). This metal-linked discrepancy was previously observed by Ewen in 1988[21] and verified for other catalyst systems.[12,15,29]

Nevertheless, **Ib** exhibited the same temperature-induced decrease of stereoregularity as **Ia**. Like the isopropylidene-bridged catalysts **Ia,b**, the hafnocenes **II−IV** showed a similar tendency; both exhibited less stereoregularity at an increased temperature (Figure 7). Catalysts **Ib** and **II** verified that the steric demand of the bridging motif with a C atom had no greater effect on the stereoregularity in the polymerization of propylene. The change of the bridging atom from C toward Si fundamentally affected the syndiotacticity. While the silane-bridged **III** produced PP with a syndiotacticity 29% lower than that of the analogous C-bridged complex **Ib** (entry 17, Table 2), the diphenylsilane-bridged **IV** produced almost atactic polypropylene with [rrrr] = 24% (entry 20, Table 2). Nevertheless, given the smaller dihedral angle and *D* value of Si-bridged hafnocenes **III** and **IV**, accompanied by a more constrained geometry of the Si-bridged catalysts and the slower coordination of propylene to the complex, a rather controlled mechanism in terms of syndiotacticity was expected. Previous reports by Palackal and Chien observed a much lower stereoregularity for silicon-bridged zirconocenes ZrCl$_2$[R$_2$Si-(η^5-Flu)(η^5-Cp)] (R = Me, Ph) in comparison to the corresponding C-bridged catalysts.[17,19] To better understand this behavior, Chien et al. calculated the lack of stereoselectivity by means of molecular mechanics. The authors concluded that "The absence of syndioselectivity is attributable to the fact that its enantiofacial selection for the *re* olefin is always preferred over the *si* face."[17] The lack of reaction space for Si-bridged hafnocenes probably leads to a false
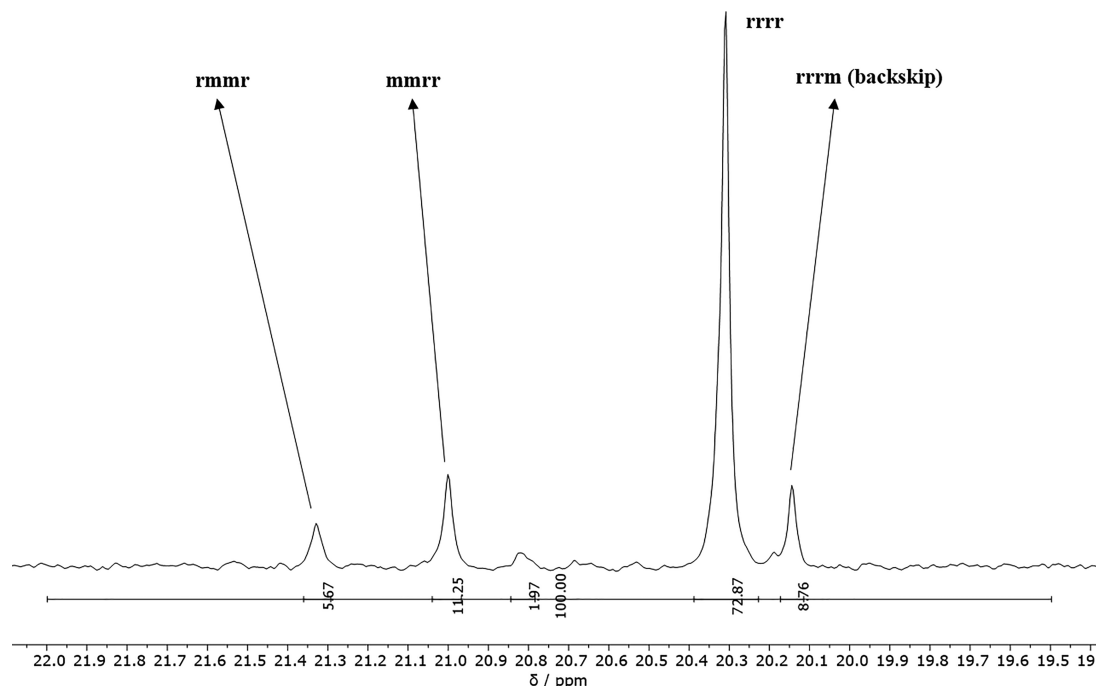
Figure 6. Pentades of **Ib**-produced sPP (entry 6, Table 2).
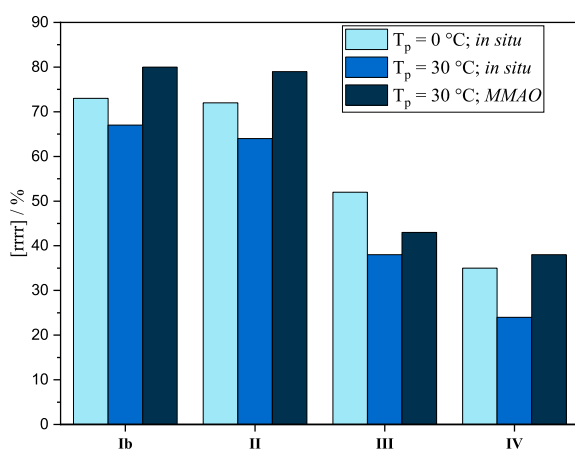
Figure 7. Degree of syndiotacticity of the PP produced by **Ib** and **II**−**IV** depending on the activation and polymerization temperature.

enantiofacial selection between the *re* and *si* faces of the olefin, as was assumed by Chien et al. Nevertheless, in the polymerization of propylene, both ZrCl$_2$[Me$_2$Si(η^5-Flu)(η^5-Cp)] and ZrCl$_2$[Ph$_2$Si(η^5-Flu)(η^5-Cp)] showed a similar stereoregularity,[19] which could not be confirmed for the corresponding hafnocenes **III** and **IV**.

Surprisingly, the MMAO activation formed a much higher syndiotacticity (80% vs 67% for **Ib**, respectively) with **Ib** and **II**−**IV** in comparison to the *in situ* activated hafnocenes (Figure 7). In particular, the degree of back-skip mechanism forming [rrrm] was reduced by up to 5% in addition to the [mmrr]-pentades (Figures S36 and S37). A previous study by Razavi et al. in 2009[20] also recognized a higher [rrrr] for MAO-activated metallocenes. Presumably, this could be attributed to a stronger coordination of the ill-defined MMAO anions toward the Hf catalyst during the polymerization.[20,36,38] In comparison to MMAO anions, [B(C$_6$F$_5$)$_4$]$^-$ is a noncoordinating counteranion; thus, the complex is in a rather exposed conformation.[22] Accordingly, the stereoselectivity in the polymerization with TIBA/TrBCF was driven more by the pure catalyst−polymer−monomer interaction and less by any coordination effects of the counteranion.

Melting Transitions. In general, the thermal melting behavior is mainly affected by the degree of tacticity. For polypropylene with short chain lengths, the average molecular weight of the polymer has more influence on the melting transition point of the polymer.[39] The corresponding melting transitions of zirconocene **Ia** produced sPP are shown (Figure 8). Melting transitions above 140 °C were observed for polymerization temperatures up to 20 °C and decreased with lower syndiotacticities (entries 1−5, Table 2) and molecular weights (Figure 4) caused by increased polymerization temperatures. For all **Ia** produced sPP two melting transitions were observed, probably due to two predominant crystallite structures (Figures S44−S48).

Hafnocenes **Ib** and **II**−**IV** produced elastic polypropylenes with no observable melting transitions on activation with TIBA/TrBCF. sPP forms—in comparison to iPP—more complex crystallites that reduce the rate of crystallization.[40] As a result, the ultrahigh molecular weight of sPP with a moderate degree of syndiotacticity combined with its innately low crystallization led to a noncrystalline elastic polymer that therefore had no melting transition. When the activation method was changed to MMAO, the polymer had a slightly increased syndiotacticiy and a lower molecular weight. For **Ib** (100.5 °C, entry 9, Table 2) and **II** (98.5 °C, entry 15, Table 2) this combination resulted in a crystalline polymer (Figures S50 and S51) with a defined melting transition. Nevertheless,
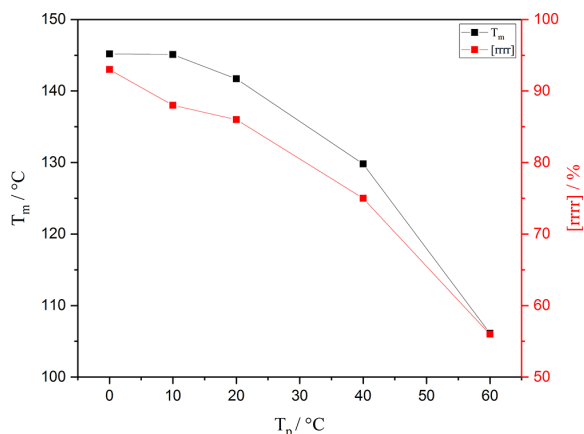
Figure 8. Melting transition and degree of syndiotacticity of polypropylene samples produced at various polymerization temperatures with **Ia** (see Table 2 for details).

Si-bridged hafnocenes **III** and **IV** were both too unselective in terms of stereoregularity; thus, a crystalline polymer was not isolated for either activation method.

■ CONCLUSION

In summary, we successfully transferred the *in situ* activation using TIBA/TrBCF to various C$_s$-symmetric *ansa*-metallocene dichlorides. We highlighted the benefits of the *in situ* activation via comparison with the commonly used MMAO, which resulted in both a higher molecular weight of the polymer and increased catalyst productivity on activation *in situ*. For this purpose, we isolated the various C$_s$-symmetric *ansa*-metallocene catalysts **I–IV**, which were capable of producing sPP with a 93% degree of syndiotacticity and a molecular weight of up to 2500 kg mol^{-1}. At 80000 kg$_{PP}$ (mol$_{cat}$ h)$^{-1}$, **Ia** exhibited extremely high productivity and produced a 93% syndiotactic PP with a melting transition of 145.2 °C. Using TIBA/TrBCF, the polymerization performance with hafnocene **Ib** yielded sPP with an ultrahigh molecular weight of 1100 kg mol^{-1} and a decent degree of syndiotactictiy of 73%. **II** provided enhanced productivity and, with 2100 kg mol^{-1}, nearly double the molecular weight, whereas the stereoregularity remained nearly constant. Furthermore, we are reporting the first coordinative polymerization of propylene by using the Si-bridged hafnocenes **III** and **IV**. The characteristic angles and distances of **III** in the solid state were compared by X-ray diffraction using the crystal structures of **Ia,b**, **II**, and **IV** known from the literature. The deviation in catalyst design illustrated the great effect of small changes: e.g., slightly enhanced or reduced dihedral and bite angles and distances inside the catalyst system. The more highly constrained Si-bridged hafnocenes **III** and **IV** were much less active than the corresponding C-bridged complex (4-fold and 20-fold, respectively) and exhibited weak syndioselectivity, especially on polymerization at elevated temperatures. Nevertheless, an SEC analysis of the resulting polymers showed ultrahigh molecular weights of up to 1900 and 2500 kg mol^{-1}. The MMAO activation of the hafnocene catalysts **I–IV** produced a maximum molecular weight of 530 kg mol^{-1} and diminished productivity by almost 50 times, thus highlighting the advantages of the *in situ* activation. Nevertheless, the MMAO activation showed a slightly enhanced stereoregularity, probably due to the

coordination of the ill-defined MMAO anion. However, C-bridged hafnocenes **Ib** and **II** produced PP with a defined melting transition on activation with MMAO. In contrast, **Ib**- and **II–IV**-mediated sPP had no defined melting transition on activation *in situ*.

Compendiously, the *in situ* activation offers a wide range of chances in the polymerization of C$_s$-symmetric catalysts, especially in combination with highly active C-bridged hafnocenes, in order to produce UHMW-sPP. In the future, it remains to be determined whether the lack of a melting transition can be avoided by enhancing the stereoregularity of the resulting polymer: for instance, by increasing the bulkiness of the fluorene moiety.

■ EXPERIMENTAL SECTION

General Considerations. All reactions with air- and moisture-sensitive substances were performed under an argon atmosphere using standard Schlenk techniques or in a glovebox. Prior to use, all glassware was heat-dried under vacuum. Unless stated otherwise, all chemicals were purchased from Sigma-Aldrich, ABCR, Acros, or VWR and used without further purification. Toluene, THF, pentane, dichloromethane, and diethyl ether were dried using a MBraun SPS-800 solvent purification system and stored over 4 Å molecular sieves. Acetone and methanol were refluxed over CaH$_2$ and distilled under reduced vacuum. Propylene (99.5% by Westfahlen AG) was purified by passage through two columns filled with BASF catalyst (R3-11) and 3–4 Å molecular sieves.

NMR spectra were recorded on Bruker AV-400HD and AVIII-500 Cryo spectrometers at 25 °C. ^{1}H and ^{13}C NMR spectroscopic chemical shifts δ are reported in ppm relative to tetramethylsilane and calibrated to the residual ^{1}H or ^{13}C signal of the solvent. Unless stated otherwise, the coupling constants J are average values and refer to couplings between two protons. The deuterated solvents (CDCl$_3$ and bromobenzene-d_S) were obtained from Sigma-Aldrich or Deutero. Polymer spectra were measured with an ARX-300 spectrometer at 140 °C in bromobenzene-d_S with 40–60 mg mL^{-1} and 1024 scans for zirconocene-produced PP and 10–20 mg mL^{-1} and at least 10k scans for hafnocene-produced PP. The degree of syndiotacticity was determined via the integration of the corresponding [rrrr]-pentade (20.3 ppm)[32] against the region of 19.5–22.0 ppm.

Gel permeation chromatography (GPC) was performed with a PL-GPC 220 instrument equipped with 2x Olexis 300 mm × 7.5 mm columns and triple detection via a differential refractive index detector, a PL-BV 400 HT viscometer, and light scattering (Precission Detectors Model 2040, 15 and 90°). Measurements were performed at 160 °C in HPLC-grade 1,2,4-trichlorobenzene (TCB; 100 mg L^{-1} BHT) from Sigma-Aldrich with a constant flow rate of 1 mL/min and a calibration set with narrow-MWD polyethylene (PE) and polystyrene (PS) standards. Samples were prepared by dissolving 0.5–0.7 mg of the polymer in 1.0 mL of stabilized TCB for 1 h at 140 °C immediately before each measurement. The molecular mass was determined absolutely against PS standards by using dn/dc = 0.097 mL g^{-1}.[41]

Differential scanning calorimetry (DSC) analysis was conducted on a DSC Q2000 instrument. The polymer (2–7 mg) was sealed into a DSC aluminum pan and heated from −50 to 200 °C at 10 °C/min. After the temperature was held for 2 min, the sample was cooled to −50 °C at 10 °C/min and heated again in the same manner. The reported values are those determined in the second heating cycle.

Spectra from a gas chromatograph coupled with a mass spectrometer (GC-MS) were measured on an Agilent GC 7890B instrument with an MS 5977A single-quadrupole mass detector and a 7693A automatic liquid sampler for 150 samples with a G4513A autoinjector. Column: HP-5MSUI, length 30 m, inside diameter 0.25 mm, film 0.25 μm. Samples were dissolved in chloroform (HPLC grade) at a maximum concentration of 1 mg mL^{-1}.

Liquid injection field desorption ionization mass spectrometry (LIFDI-MS) was carried out directly from an inert-atmosphere

glovebox with a Thermo Fisher Scientific Exactive Plus Orbitrap instrument equipped with an ion source from Linden CMS.[42]

Syntheses. *Flu-CMe$_2$-Cp (2a).* The synthesis of Flu-CMe$_2$-Cp took place by a modified literature procedure.[21] In a 250 mL Schlenk flask 3.00 g (17.9 mmol, 1.00 equiv) fluorene **1** was dissolved in 50 mL of dry THF. At 0 °C 11.2 mL (17.9 mmol, 1.00 equiv) of MeLi, 1.60 M in Et$_2$O, was added and the mixture stirred for an additional 3 h at room temperature. At −78 °C, 2.28 g (21.4 mmol, 1.20 equiv) of dimethylfulvene was added to the deep red solution and the mixture stirred overnight at room temperature. The reaction was quenched by the addition of 30 mL of water, and the mixture was extracted three times with Et$_2$O (30 mL). The combined organic phase was washed with brine (20 mL) and dried over MgSO$_4$, and the solvent was evaporated. The crude product was recrystallized in MeOH, leading to 6.91 g (85%) of yellowish needles (**2a**). ^{1}H NMR (400 MHz, CDCl$_3$, 298 K, ppm): δ 7.71 (d, [3]J = 7.5 Hz, 2H, H$_{aryl}$), 7.32 (tt, [3]J = 7.3, 1.8 Hz, 2H, H$_{aryl}$), 7.20−7.08 (m, 4H, H$_{aryl}$), 6.96−6.42 (m, 2H, H$_{cp}$), 6.15−5.89 (m, 1H, H$_{cp}$), 4.16−4.14 (s, 1H, Flu-H), 3.18−3.06 (m, 2H, H$_{cp}$), 1.08−1.06 (s, 6H, CH$_3$). Two stereoisomers (**2a** and **2a′**), 3:2 ratio, iPr bridge bonded to Cp vinyl carbon atoms. The NMR spectroscopic data match previously reported data.[21]

Flu-CPh$_2$-Cp (2b). The synthesis of Flu-CPh$_2$-Cp took place by a modified literature procedure.[15] In a 250 mL Schlenk flask 1.50 g (9.02 mmol, 1.00 equiv) of fluorene **1** was dissolved in 50 mL of dry THF. At 0 °C 3.97 mL (9.93 mmol, 1.10 equiv) of nBuLi, 2.50 M in hexanes, was added, and the solution was stirred for an additional 4 h at room temperature. At 0 °C, 2.08 g (9.02 mmol, 1.00 equiv) of diphenylfulvene was added to the deep green solution and the mixture stirred for 7 days at room temperature. The reaction was quenched by the addition of 30 mL of water, and the mixture was extracted three times with Et$_2$O (30 mL). The combined organic phase was washed with a saturated aqueous NH$_4$Cl solution (20 mL) and brine (20 mL) and dried over MgSO$_4$, and the solvent was evaporated. The crude product was recrystallized in Et$_2$O, giving 2.61 g (73%) of yellowish needles (**2b**). ^{1}H NMR (400 MHz, CDCl$_3$, 298 K, ppm): δ 7.54−6.61 (m, 18H, H$_{aryl}$), 6.58−6.10 (m, 3H, H$_{cp}$), 5.55−5.50 (s, 1H, Flu-H), 3.01−2.89 (s, 2H, H$_{cp}$). Two stereoisomers (**2b** and **2b′**), 3:1 ratio, CPh$_2$ bridge bonded to Cp vinyl carbon atoms. The NMR spectroscopic data match previously reported data.[15]

Flu-SiMe$_2$Cl (3a). The synthesis of FluSiMe$_2$Cl took place by a modified literature procedure.[17] In a 100 mL Schlenk flask 3.00 g (18.1 mmol, 1.00 equiv) fluorene **1** was diluted in 40 mL of dry Et$_2$O. At 0 °C 16.9 mL (27.1 mmol, 1.50 equiv) MeLi, 1.60 M in Et$_2$O, was added, and the solution was stirred for an additional 4 h at room temperature. At −78 °C, the red solution was transferred to a solution of 15.2 mL (126 mmol, 7.00 equiv) of dimethyldichlorosilane in 100 mL of dry Et$_2$O for 1.5 h. The solution was heated to room temperature and stirred overnight, and all the volatile reactants were removed *in vacuo*. The yellow crude product (**3a**) was not further purified, and NMR spectroscopy confirmed the formation and purity of the desired product. ^{1}H NMR (400 MHz, CDCl$_3$, 298 K, ppm): δ 7.87 (d, [3]J = 7.5 Hz, 2H, H$_{aryl}$), 7.67 (d, [3]J = 7.6 Hz, 2H, H$_{aryl}$), 7.40 (t, [3]J = 7.4 Hz, 2H, H$_{aryl}$), 7.34 (t, [3]J = 7.5 Hz, 2H, H$_{aryl}$), 4.10 (s, 1H, Flu-H), 0.17 (s, 6H, Si−CH$_3$). ^{13}C NMR (100 MHz, CDCl$_3$, 298 K, ppm): δ 143.02, 141.03, 126.61, 126.36, 124.90, 120.23, 43.65, −0.15. ^{29}Si NMR (80 MHz, CDCl$_3$, 298 K, ppm): δ 27.78. The NMR spectroscopic data match previously reported data.[17]

Flu-SiMe$_2$-Cp (4a). The synthesis of Flu-SiMe$_2$-Cp took place by a modified literature procedure.[17] In a 100 mL Schlenk flask, 4.67 g (18.1 mmol, 1.00 equiv) of FluSiMe$_2$Cl (**3a**) and 1.36 g (19.0 mmol, 1.05 equiv) of LiCp were dissolved in 60 mL of dry THF and the mixture was stirred overnight at room temperature. THF was removed under reduced pressure, and the resulting solid was quenched with water and extracted three times with dichloromethane (40 mL). The combined organic phase was washed with brine (20 mL) and dried over MgSO$_4$, and the solvent was evaporated *in vacuo*. A 4.71 (91%) amount of the product (**4a**) was obtained as an orange oil after silica filtration with cyclohexane. ^{1}H NMR (400 MHz, CDCl$_3$, 298 K, ppm): δ 7.90 (dt, [3]J = 7.7, 1.0 Hz, H$_{aryl}$), 7.84−7.78 (m, 1H, H$_{aryl}$), 7.58−7.55 (m, H$_{aryl}$), 7.42−7.28 (m, H$_{aryl}$), 7.27−7.21

(m, H$_{aryl}$), 6.70−6.48 (m, H$_{cp}$), 6.17 (br. s), 4.00−3.97 (s, Flu-H), 3.22 (br. s, H$_{cp}$), 3.05 (s, H$_{cp}$), 2.78−2.75 (m, H$_{cp}$), 0.10 (s, Si-CH$_3$), 0.02 (s, Si-CH$_3$), −0.20 (s, Si-CH$_3$). Mixture of several isomers. MS (GC-MS): m/z 288.1. The purity was determined to be ≥95% via GC-MS (see Figure S54). The NMR spectroscopic data match previously reported data.[17]

Flu-SiPh$_2$Cl (3b). The synthesis of Flu-SiPh$_2$Cl took place by a modified literature procedure.[18] In a 250 mL Schlenk flask, 1.83 mL (2.21 g, 8.71 mmol, 1.00 equiv) of diphenyldichlorosilane was diluted in 100 mL of dry Et$_2$O. Over 1.5 h, a solution of 1.50 g (8.71 mmol, 1.00 equiv) of Flu-Li in 30 mL of dry Et$_2$O was added and the mixture stirred overnight. The solvent and all volatile reactants were removed *in vacuo*. The yellow crude product (**3b**) was not further purified, and NMR spectroscopy confirmed the formation and purity of the desired product. ^{1}H NMR (400 MHz, CDCl$_3$, 298 K, ppm): δ 7.75 (d, [3]J = 7.6 Hz, 2H, H$_{aryl}$), 7.44−7.38 (m, 2H, H$_{aryl}$), 7.37−7.24 (m, 12H, H$_{aryl}$), 7.20−7.12 (m, 2H, H$_{aryl}$), 4.57 (s, 1H, Flu-H). ^{13}C NMR (100 MHz, CDCl$_3$, 298 K, ppm): δ 142.36, 141.43, 134.91, 131.34, 130.89, 128.03, 126.43, 126.42, 125.37, 120.05, 41.68. ^{29}Si NMR (80 MHz, CDCl$_3$, 298 K, ppm): δ 5.35. The NMR spectroscopic data match previously reported data.[18]

Flu-SiPh$_2$-Cp (4b). The synthesis of Flu-SiPh$_2$Cl took place by a modified literature procedure.[18] In a 250 mL Schlenk flask, 3.34 g (8.71 mmol, 1.00 equiv) of FluSiPh$_2$Cl (**3b**) and 660 mg (9.16 mmol, 1.05 equiv) of LiCp were dissolved in 80 mL of dry THF, and the mixture was stirred overnight at room temperature. THF was removed under reduced pressure and the resulting solid quenched with water and extracted three times with dichloromethane (50 mL). The combined organic phase was washed with brine (20 mL) and dried over MgSO$_4$, and the solvent was evaporated *in vacuo*. After recrystallization from Et$_2$O 1.29 g (36%) of the product (**4b**) was isolated as orange-yellow crystals. ^{1}H NMR (400 MHz, CDCl$_3$, 298 K, ppm): δ 7.65 (d, [3]J = 7.6 Hz, 2H, H$_{aryl}$), 7.37−7.10 (m, 18H, H$_{aryl}$), 6.56−6.38 (m, 4H, H$_{cp}$), 4.59 (s, 1H, Flu-H), 4.01 (s, 1H, Cp-H). MS (GC-MS): m/z = 412.2. The NMR spectroscopic data match previously reported data.[18]

ZrCl$_2$[Me$_2$C(η^5-Flu)(η^5-Cp)] (Ia). The synthesis took place by a modified literature procedure.[21] In a 250 mL Schlenk flask, 1.00 g (3.67 mmol, 1.00 equiv) of Flu-CMe$_2$-Cp (**2a**) was diluted in 25 mL of dry Et$_2$O. At 0 °C 3.52 mL (8.81 mmol, 2.40 equiv) of nBuLi, 2.50 M in hexanes, was added and the solution stirred for 4 h at room temperature. The solvent was removed *in vacuo*, and the dilithiated compound was washed twice with 10 mL of dry pentane. The solid was dissolved at −78 °C in 30 mL of dry CH$_2$Cl$_2$, and 855 mg (3.67 mmol, 1.00 equiv) of ZrCl$_4$ was added. After 1 h, the cooling bath was removed and the red slurry stirred overnight at room temperature. The mixture was filtered and the precipitate extracted with 30 mL of dry CH$_2$Cl$_2$. The combined organic phase was concentrated under reduced pressure. Crystallization at −32 °C gave 639 mg (40%) of the product (**Ia**) as a deep red crystalline solid. ^{1}H NMR (400 MHz, CDCl$_3$, 298 K, ppm): δ 8.14 (dt, [3]J = 8.4, 1.1 Hz, 2H, H$_{aryl}$), 7.85 (dt, [3]J = 8.8, 0.9 Hz, 2H, H$_{aryl}$), 7.59−7.52 (m, 2H, H$_{aryl}$), 7.30−7.23 (m, 2H, H$_{aryl}$), 6.33 (t, [3]J = 2.7 Hz, 2H, H$_{cp}$), 5.77 (t, [3]J = 2.7 Hz, 2H, H$_{cp}$), 2.40 (s, 6H, CH$_3$). ^{13}C NMR (100 MHz, CDCl$_3$, 298 K, ppm): δ 129.34, 125.29, 125.07, 123.56, 122.92, 119.45, 115.19, 102.39, 79.99, 40.85, 28.95. The NMR spectroscopic data match previously reported data.[14]

HfCl$_2$[Me$_2$C(η^5-Flu)(η^5-Cp)] (Ib). The synthesis took place by a modified literature procedure.[21] In a 250 mL Schlenk flask, 1.00 g (3.67 mmol, 1.00 equiv) of Flu-CMe$_2$-Cp (**2a**) was diluted in 25 mL of dry THF. At 0 °C 3.52 mL (8.81 mmol, 2.40 equiv) of nBuLi, 2.50 M in hexanes, was added and the solution stirred for 4 h at room temperature. The solvent was removed *in vacuo*, and the dilithiated compound washed twice with 10 mL of dry pentane. The solid was dissolved at −78 °C in 40 mL of dry CH$_2$Cl$_2$, and 1.18 g (3.67 mmol, 1.00 equiv) of HfCl$_4$ was added. After 1 h, the cooling bath was removed and the brown slurry stirred for 4 h at room temperature. The mixture was filtered and the precipitate extracted with 40 mL of dry CH$_2$Cl$_2$. The combined organic phases were concentrated under reduced pressure. Crystallization at −32 °C gave 364 mg (18%) of the

product (**Ib**) as a yellow crystalline solid. ^{1}H NMR (400 MHz, CDCl$_3$, 298 K, ppm): δ 8.10 (dt, ^3J = 8.5, 1.1 Hz, 2H, H$_{aryl}$), 7.88 (dt, ^3J = 8.9, 0.9 Hz, 2H, H$_{aryl}$), 7.56–7.50 (m, 2H, H$_{aryl}$), 7.29–7.20 (m, 2H, H$_{aryl}$), 6.27 (t, ^3J = 2.7 Hz, 2H, H$_{cp}$), 5.72 (t, ^3J = 2.7 Hz, 2H, H$_{cp}$), 2.39 (s, 6H, CH$_3$). ^{13}C NMR (100 MHz, CDCl$_3$, 298 K, ppm): δ 129.10, 124.97, 124.82, 123.28, 121.95, 121.79, 118.41, 117.73, 99.81, 80.06, 40.91, 29.17. The NMR spectroscopic data match previously reported data.[21]

HfCl$_2$[Ph$_2$C(η^5-Flu)(η^5-Cp)] (II). The synthesis took place by a modified literature procedure.[12] In a 250 mL Schlenk flask, 500 mg (1.26 mmol, 1.00 equiv) of Flu-CPh$_2$-Cp (**2b**) was diluted in 50 mL of dry Et$_2$O. At 0 °C, 1.16 mL (2.90 mmol, 2.30 equiv) of *n*BuLi, 2.50 M in hexanes, was added and the solution stirred for 6 h at room temperature. The solvent was removed *in vacuo* and the dilithiated compound washed with 10 mL of dry pentane. The solid was dissolved at −78 °C in 50 mL of dry CH$_2$Cl$_2$, and 404 mg (1.26 mmol, 1.00 equiv) of HfCl$_4$ was added. After 1 h, the cooling bath was removed and the brown slurry stirred overnight at room temperature. The mixture was filtered and the precipitate extracted with 30 mL of dry CH$_2$Cl$_2$. The combined organic phases were concentrated under reduced pressure. Crystallization at −32 °C gave orange crystals. The solid was suspended twice in 20 mL of dry pentane, and the solvent was immediately separated under high vacuum to remove complexed dichloromethane. A 376 mg (46%) amount of the product (**II**) was obtained as a yellow crystalline solid. ^{1}H NMR (400 MHz, CDCl$_3$, 298 K, ppm): δ 8.18 (dt, ^3J = 8.4, 1.1 Hz, 2H, H$_{aryl}$), 7.94 (dt, ^3J = 7.9, 1.6 Hz, 2H, H$_{aryl}$), 7.87 (dt, ^3J = 7.7, 1.8 Hz, 2H, H$_{aryl}$), 7.60–7.52 (m, 2H, H$_{aryl}$), 7.44 (td, ^3J = 7.5, 1.9 Hz, 2H, H$_{aryl}$), 7.34 (td, ^3J = 7.5, 1.7 Hz, 2H, H$_{aryl}$), 7.30 (tt, ^3J = 7.3, 1.3 Hz), 7.04–6.96 (m, 2H, H$_{aryl}$), 6.46 (dt, ^3J = 8.9, 1.0 Hz, 2H, H$_{cp}$), 6.33 (t, ^3J = 2.7 Hz, 2H, H$_{cp}$), 5.76 (t, ^3J = 2.7 Hz, 2H, H$_{cp}$). ^{13}C NMR (100 MHz, CDCl$_3$, 298 K, ppm): δ 145.06, 129.41, 129.29, 129.15, 128.29, 127.44, 126.76, 125.30, 124.83, 123.84, 123.78, 120.49, 117.80, 113.96, 101.55, 79.38, 58.47. The NMR spectroscopic data match previously reported data.[12]

HfCl$_2$[Me$_2$Si(η^5-Flu)(η^5-Cp)] (III). The synthesis took place by a modified literature procedure for the corresponding Zr complex.[17] In a 250 mL Schlenk flask, 500 mg (1.73 mmol, 1.00 equiv) of Flu-SiMe$_2$-Cp (**4a**) was diluted in 40 mL of dry Et$_2$O. At 0 °C, 2.38 mL (3.81 mmol, 2.20 equiv) of *t*BuLi, 1.60 M in pentane, was added and the solution stirred for 4 h at room temperature. The solvent was removed *in vacuo* and the dilithiated compound washed with 10 mL of dry pentane. The solid was dissolved in 50 mL of dry toluene, 555 mg (1.73 mmol, 1.00 equiv) of HfCl$_4$ added, and the orange-brown slurry stirred overnight at room temperature. The mixture was filtered and the precipitate extracted with 30 mL of dry toluene. The combined organic phase was concentrated under reduced pressure. Crystallization at −32 °C gave 80.5 mg (9%) of the product (**III**) as a yellow crystalline solid. ^{1}H NMR (400 MHz, CDCl$_3$, 298 K, ppm): δ 8.10 (dt, ^3J = 8.4, 1.1 Hz, 2H, H$_{aryl}$), 7.66–7.55 (m, 4H, H$_{aryl}$), 7.32–7.22 (m, 2H, H$_{aryl}$), 6.56 (t, ^3J = 2.4 Hz, 2H, H$_{cp}$), 5.74 (t, ^3J = 2.4 Hz, 2H, H$_{cp}$), 1.15 (s, 6H, Si-CH$_3$). ^{13}C NMR (125 MHz, CDCl$_3$, 298 K, ppm): δ 128.86, 128.26, 127.45, 126.47, 125.10, 124.04, 123.86, 108.68, 106.50, 66.02, −0.67. ^{29}Si NMR (100 MHz, CDCl$_3$, 298 K, ppm): δ −13.43. Anal. Calcd for C$_{20}$H$_{18}$Cl$_2$HfSi: C, 44.83; H, 3.39. Found: C, 46.22; H, 3.56. The larger deviation was caused by persistent toluene and pentane in the solid state. Freeze-drying resulted in a coordination of benzene to the complex in the solid state. LIFDI-MS: *m/z* calcd 535.9998, measd 535.9996 (see Figures S58 and S59).

HfCl$_2$[Ph$_2$Si(η^5-Flu)(η^5-Cp)] (IV). The synthesis took place by a modified literature procedure.[18] In a 250 mL Schlenk flask, 596 mg (1.44 mmol, 1.00 equiv) of Flu-SiPh$_2$-Cp (**4b**) was diluted in 50 mL of dry Et$_2$O. At 0 °C, 2.08 mL (3.32 mmol, 2.30 equiv) of *t*BuLi, 1.60 M in pentane, was added and the solution stirred for 4 h at room temperature. The solvent was removed *in vacuo* and the dilithiated compound washed with 10 mL of dry pentane. The solid was dissolved in 40 mL of dry toluene, 463 mg (1.44 mmol, 1.00 equiv) of HfCl$_4$ added, and the slurry stirred overnight at room temperature. The mixture was filtered and the precipitate extracted with 20 mL of

dry toluene. The combined organic phases were concentrated under reduced pressure. Crystallization at −32 °C gave 267 mg (27%) of the product (**IV**) as a yellow crystalline solid. ^{1}H NMR (400 MHz, CDCl$_3$, 298 K, ppm): δ 8.22–8.06 (m, 6H, H$_{aryl}$), 7.64–7.53 (m, 8H, H$_{aryl}$), 7.07–6.98 (m, 2H, H$_{aryl}$), 6.87 (dd, ^3J = 8.6, 1.2 Hz, 2H H$_{aryl}$), 6.67 (t, ^3J = 2.4 Hz, 2H, H$_{cp}$), 5.93 (t, ^3J = 2.4 Hz, 2H, H$_{cp}$). ^{13}C NMR (125 MHz, CDCl$_3$, 298 K, ppm): δ 134.66, 131.82, 131.22, 129.18, 128.78, 128.66, 127.20, 126.89, 124.92, 124.72, 124.37, 110.01, 102.56, 62.99. The NMR spectroscopic data match previously reported data.[18]

Polymerization. All polymerization reactions were performed in a 250 mL double-walled Büchi steel autoclave equipped with a KPG-stirrer (Heidolph, 1000 rpm), a temperature sensor, and a heating/cooling jacket attached to a cryo-/thermostat unit (Julabo F-25-ME). Ar pressure for all manipulations was set at 1.3 bar. Prior to polymerization, the autoclave was provided with 100 mL of dry toluene and 2.0 mL of 1.1 M TIBA in toluene and heated to 90 °C. After the temperature was maintained for 30 min, the scrubbing solution was released.

In Situ Activation. For the polymerization, the autoclave was charged with 100 mL of dry toluene and 0.5 mL of 1.1 M TIBA in toluene. The metallocene complex (1.0 equiv) was dissolved in 10 mL of dry toluene and preactivated with 200 equiv of TIBA at 60 °C for 1 h. After the desired temperature was adjusted, the metallocene solution was transferred into the autoclave and pressurized with propylene. When the system was equilibrated and stable in terms of temperature and pressure, the polymerization was initiated by placing 5.0 equiv of [Ph$_3$C][B(C$_6$F$_5$)$_4$] dissolved in 10 mL of dry toluene in the autoclave via a pressure buret (p_{poly} + 0.5 bar).

MAO Activation. For the polymerization, the autoclave was charged with 110 mL of dry toluene and 2000 equiv of a MMAO-12 solution in toluene (7 wt % Al in toluene, linear formula [(CH$_3$)$_{0.95}$(*n*-C$_8$H$_{17}$)$_{0.05}$AlO]$_n$) was added. After the desired temperature was adjusted, the autoclave was pressurized with propylene. When the system was equilibrated and stable in terms of temperature and pressure, the polymerization was initiated by adding the metallocene complex (1.0 equiv) dissolved in 10 mL of dry toluene. The polymerization was quenched with 2.0 mL of methanol, and the reaction mixture was poured into 600 mL of HCl-acidified methanol. The precipitated polymer was removed from the autoclave, and the combined polymer was washed thoroughly, first with methanol and then with acetone. The resulting polymer was suspended in acetone and treated with Irganox as a stabilizing agent in order to prevent rapid destruction of the polymer. After 20 min, the supernatant solution was decanted off and the resulting polymer was dried overnight at 70 °C.

■ ASSOCIATED CONTENT

⊙ Supporting Information

The Supporting Information is available free of charge at https://pubs.acs.org/doi/10.1021/acs.organomet.1c00397.

> Additional experimental procedures and analytical data for precursors, ^{1}H, ^{13}C, and ^{29}Si NMR spectra, GC-MS elugrams, DSC curves, polymer spectra, and LIFDI-MS and SC-XRD data of catalyst **III** (PDF)

Accession Codes

CCDC 2059775 contains the supplementary crystallographic data for this paper. These data can be obtained free of charge via www.ccdc.cam.ac.uk/data_request/cif, or by emailing data_request@ccdc.cam.ac.uk, or by contacting The Cambridge Crystallographic Data Centre, 12 Union Road, Cambridge CB2 1EZ, UK; fax: +44 1223 336033.

■ AUTHOR INFORMATION

Corresponding Author

   Bernhard Rieger − *Wacker-Lehrstuhl für Makromolekulare Chemie, Catalysis Research Center, Technische Universität München, 85748 Garching bei München, Germany;* ⊙ orcid.org/0000-0002-0023-884X; Phone: +49-89-289-13570; Email: rieger@tum.de; Fax: +49-89-289-13562

Authors

   Lucas Stieglitz − *Wacker-Lehrstuhl für Makromolekulare Chemie, Catalysis Research Center, Technische Universität München, 85748 Garching bei München, Germany*
   Daniel Henschel − *Wacker-Lehrstuhl für Makromolekulare Chemie, Catalysis Research Center, Technische Universität München, 85748 Garching bei München, Germany*
   Thomas Pehl − *Wacker-Lehrstuhl für Makromolekulare Chemie, Catalysis Research Center, Technische Universität München, 85748 Garching bei München, Germany*

Complete contact information is available at:
https://pubs.acs.org/10.1021/acs.organomet.1c00397

Author Contributions

The manuscript was written through the contributions of all the authors. All of the authors have given their approval to the final version of the manuscript.

Notes

The authors declare no competing financial interest.

■ REFERENCES

(1) van der Werff, H.; Heisserer, U., High-performance ballistic fibers: ultra-high molecular weight polyethylene (UHMWPE). In *Advanced fibrous composite materials for ballistic protection*; Elsevier: 2016; pp 71−107.

(2) Bracco, P.; Bellare, A.; Bistolfi, A.; Affatato, S. Ultra-high molecular weight polyethylene: influence of the chemical, physical and mechanical properties on the wear behavior. A review. *Materials* **2017**, *10*, 791.

(3) Kurtz, S. M. A Primer on UHMWPE. In *UHMWPE Biomaterials Handbook*, 3rd ed.; Kurtz, S. M., Ed.; William Andrew: 2016; Chapter 1, pp 1−6.

(4) Ruan, S.; Gao, P.; Yu, T. Ultra-strong gel-spun UHMWPE fibers reinforced using multiwalled carbon nanotubes. *Polymer* **2006**, *47*, 1604−1611.

(5) Konishi, T.; Nishida, K.; Kanaya, T.; Kaji, K. Effect of isotacticity on formation of mesomorphic phase of isotactic polypropylene. *Macromolecules* **2005**, *38*, 8749−8754.

(6) Chatani, Y.; Maruyama, H.; Noguchi, K.; Asanuma, T.; Shiomura, T. Crystal structure of the planar zigzag form of syndiotactic polypropylene. *J. Polym. Sci., Part C: Polym. Lett.* **1990**, *28*, 393−398.

(7) De Rosa, C.; Auriemma, F. Structure and physical properties of syndiotactic polypropylene: A highly crystalline thermoplastic elastomer. *Prog. Polym. Sci.* **2006**, *31*, 145−237.

(8) Odajima, A.; Maeda, T. Calculation of the elastic constants and the lattice energy of the polyethylene crystal. *J. Polym. Sci., Part C: Polym. Symp.* **1967**, *15*, 55−74.

(9) Spaleck, W.; Antberg, M.; Rohrmann, J.; Winter, A.; Bachmann, B.; Kiprof, P.; Behm, J.; Herrmann, W. A. High Molecular Weight Polypropylene through Specifically DesigneZirconocene Catalysts. *Angew. Chem., Int. Ed. Engl.* **1992**, *31*, 1347−1350.

(10) Spaleck, W.; Kueber, F.; Winter, A.; Rohrmann, J.; Bachmann, B.; Antberg, M.; Dolle, V.; Paulus, E. F. The Influence of Aromatic Substituents on the Polymerization Behavior of Bridged Zirconocene Catalysts. *Organometallics* **1994**, *13*, 954−963.

(11) Kaminsky, W.; Hopf, A.; Piel, C. Cs-symmetric hafnocene complexes for synthesis of syndiotactic polypropene. *J. Organomet. Chem.* **2003**, *684*, 200−205.

(12) Miller, S. A.; Bercaw, J. E. Highly stereoregular syndiotactic polypropylene formation with metallocene catalysts via influence of distal ligand substituents. *Organometallics* **2004**, *23*, 1777−1789.

(13) Hopf, A.; Kaminsky, W. Highly syndiotactic polypropene with Cs-symmetric metallocene/MAO catalysts. *Catal. Commun.* **2002**, *3*, 459−464.

(14) Razavi, A. Syndiotactic Polypropylene: Discovery, Development, and Industrialization via Bridged Metallocene Catalysts. *Adv. Polym. Sci.* **2013**, *258*, 43−116.

(15) Razavi, A.; Atwood, J. L. Preparation and crystal structures of the complexes (η5-C5H4CPh2-η5-C13H8) MCl2 (M= Zr, Hf) and the catalytic formation of high molecular weight high tacticity syndiotactic polypropylene. *J. Organomet. Chem.* **1993**, *459*, 117−123.

(16) Razavi, A.; Peters, L.; Nafpliotis, L. Geometric flexibility, ligand and transition metal electronic effects on stereoselective polymerization of propylene in homogeneous catalysis. *J. Mol. Catal. A: Chem.* **1997**, *115*, 129−154.

(17) Chen, Y.-X.; Rausch, M. D.; Chien, J. C. Silylene-bridged fluorenyl-containing ligands and zirconium complexes with C1 and Cs symmetry: general synthesis and olefin polymerization catalysis. *J. Organomet. Chem.* **1995**, *497*, 1−9.

(18) Izmer, V. V.; Agarkov, A. Y.; Nosova, V. M.; Kuz'mina, L. G.; Howard, J. A. K.; Beletskaya, I. P.; Voskoboynikov, A. Z. ansa-Metallocenes with a Ph2Si bridge: molecular structures of HfCl2-[Ph2Si(η5-C13H8)(η5-C5H4)] and HfCl2[Ph2Si(C13H9)(η5-C5H4)]2. *J. Chem. Soc., Dalton Trans.* **2001**, 1131−1136.

(19) Patsidis, K.; Alt, H. G.; Milius, W.; Palackal, S. J. The synthesis, characterization and polymerization behavior of ansa cyclopentadienyl fluorenyl complexes; the X-ray structures of the complexes [(C13H8)SiR2 (C5H4)] ZrCl2 (R = Me or Ph). *J. Organomet. Chem.* **1996**, *509*, 63−71.

(20) Busico, V.; Cipullo, R.; Pellecchia, R.; Talarico, G.; Razavi, A. Hafnocenes and MAO: Beware of Trimethylaluminum! *Macromolecules* **2009**, *42*, 1789−1791.

(21) Ewen, J. A.; Jones, R. L.; Razavi, A.; Ferrara, J. D. Syndiospecific propylene polymerizations with Group IVB metallocenes. *J. Am. Chem. Soc.* **1988**, *110*, 6255−6256.

(22) Bochmann, M. The Chemistry of Catalyst Activation: The Case of Group 4 Polymerization Catalysts. *Organometallics* **2010**, *29*, 4711−4740.

(23) Bryliakov, K. P.; Talsi, E. P.; Voskoboynikov, A. Z.; Lancaster, S. J.; Bochmann, M. Formation and Structures of Hafnocene Complexes in MAO- and AlBui3/CPh3[B(C6F5)4]-Activated Systems. *Organometallics* **2008**, *27*, 6333−6342.

(24) Rieger, B.; Troll, C.; Preuschen, J. Ultrahigh molecular weight polypropene elastomers by high activity "dual-side" hafnocene catalysts. *Macromolecules* **2002**, *35*, 5742−5743.

(25) Diesner, T.; Troll, C.; Rieger, B. Hafnocene-Based Olefin Polymerizations. *Top. Organomet. Chem.* **2009**, *26*, 47.

(26) Schloegl, M.; Troll, C.; Thewalt, U.; Rieger, B. Semi-hydrogenated, asymmetric metallocene catalysts for the propylene polymerization. *Z. Naturforsch., B: J. Chem. Sci.* **2003**, *58*, 533−538.

(27) Stone, K. J.; Little, R. D. An exceptionally simple and efficient method for the preparation of a wide variety of fulvenes. *J. Org. Chem.* **1984**, *49*, 1849−1853.

(28) Chajara, K.; Ottosson, H. An improved pathway to 6, 6-disubstituted fulvenes. *Tetrahedron Lett.* **2004**, *45*, 6741−6744.

(29) Razavi, A.; Ferrara, J. Preparation and crystal structures of the complexes (η5-C5H4CMe2η5-C13H8) MCl2 (M= Zr, Hf) and their role in the catalytic formation of syndiotactic polypropylene. *J. Organomet. Chem.* **1992**, *435*, 299−310.

(30) Shaltout, R. M.; Corey, J. Y.; Rath, N. P. The X-ray crystal structures of the ansa-metallocenes, Me2C (C5H4) 2MCl2 (M= Ti, Zr and Hf). *J. Organomet. Chem.* **1995**, *503*, 205−212.

(31) Wang, B. Ansa-metallocene polymerization catalysts: Effects of the bridges on the catalytic activities. *Coord. Chem. Rev.* **2006**, *250*, 242−258.

(32) Brintzinger, H. H.; Fischer, D.; Mülhaupt, R.; Rieger, B.; Waymouth, R. M. Stereospecific olefin polymerization with chiral metallocene catalysts. *Angew. Chem., Int. Ed. Engl.* **1995**, *34*, 1143−1170.

(33) Simoes, J. M.; Beauchamp, J. Transition metal-hydrogen and metal-carbon bond strengths: the keys to catalysis. *Chem. Rev.* **1990**, *90*, 629−688.

(34) Schöbel, A.; Herdtweck, E.; Parkinson, M.; Rieger, B. Ultra-rigid metallocenes for highly iso- and regiospecific polymerization of propene: the search for the perfect polypropylene helix. *Chem. - Eur. J.* **2012**, *18*, 4174−8.

(35) Machat, M. R.; Lanzinger, D.; Pöthig, A.; Rieger, B. Ultrarigid Indenyl-based Hafnocene Complexes for the Highly Isoselective Polymerization of Propene: Tunable Polymerization Performance Adopting Various Sterically Demanding 4-Aryl Substituents. *Organometallics* **2017**, *36*, 399−408.

(36) Resconi, L.; Cavallo, L.; Fait, A.; Piemontesi, F. Selectivity in Propene Polymerization with Metallocene Catalysts. *Chem. Rev.* **2000**, *100*, 1253−1346.

(37) Machat, M. R.; Lanzinger, D.; Drees, M.; Altmann, P. J.; Herdtweck, E.; Rieger, B. High-Melting, Elastic Polypropylene: A One-Pot, One-Catalyst Strategy toward Propylene-Based Thermoplastic Elastomers. *Macromolecules* **2018**, *51*, 914−929.

(38) Alt, H. G.; Köppl, A. Effect of the Nature of Metallocene Complexes of Group IV Metals on Their Performance in Catalytic Ethylene and Propylene Polymerization. *Chem. Rev.* **2000**, *100*, 1205−1222.

(39) Busico, V.; Cipullo, R. Microstructure of polypropylene. *Prog. Polym. Sci.* **2001**, *26*, 443−533.

(40) Calhoun, A. 3. Polypropylene. In *Multilayer Flexible Packaging*, 2nd ed.; Wagner, J. R., Ed.; William Andrew: 2016; pp 35−45.

(41) Coto, B.; Escola, J. M.; Suárez, I.; Caballero, M. J. Determination of dn/dc values for ethylene−propylene copolymers. *Polym. Test.* **2007**, *26*, 568−575.

(42) Muhr, M.; Heiß, P.; Schütz, M.; Bühler, R.; Gemel, C.; Linden, M. H.; Linden, H. B.; Fischer, R. A. Enabling LIFDI-MS measurements of highly air sensitive organometallic compounds: a combined MS/glovebox technique. *Dalton Trans.* **2021**, *50*, 9031−9036.

5   Improving the Yield of C$_2$(*rac*)-symmetric Hafnocenes

"Perfectly Isotactic Polypropylene upon *In Situ* Activation of Ultrarigid *meso* Hafnocenes"

5.1   Bibliographic Data

Title:	Perfectly Isotactic Polypropylene upon *In Situ* Activation of Ultrarigid *meso* Hafnocenes
Status:	Communication, Publication Date: 20.09.2022
Journal:	Angewandte Chemie International Edition
Publisher:	Wiley
DOI:	10.1002/anie.202210797
Authors:	Lucas Stieglitz,[†] Tim Maximilian Lenz,[†] Andreas Saurwein, and Bernhard Rieger[1]

5.2   Graphical Abstract (TOC)
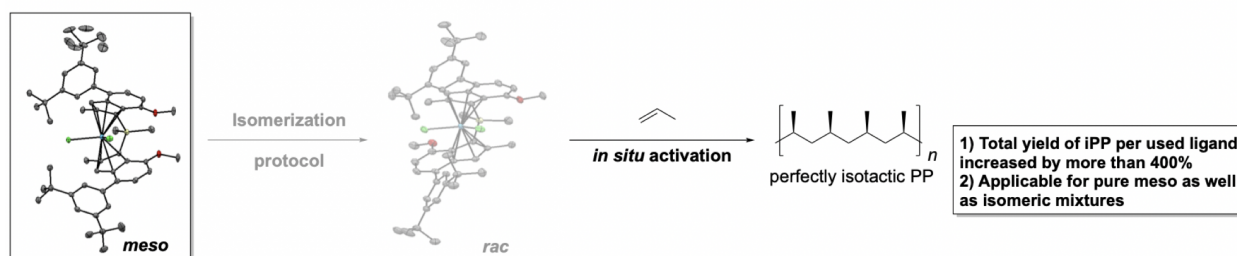
Figure 14: Graphical abstract (TOC) of the manuscript titled "Perfectly Isotactic Polypropylene upon *In Situ* Activation of Ultrarigid *meso* Hafnocenes".

---

[1] † Lucas Stieglitz and Tim Maximilian Lenz contributed equally. L. Stieglitz provided the original idea, planned experiments and wrote the manuscript. T. Lenz planned experiments, performed the syntheses and polymerizations, and revised the manuscript. A. Saurwein conducted all SC XRD-measurements and processed the data. All work was supervised by B. Rieger.

5.3 Content

In recent years, catalysts for the isoselective polymerization of propylene were modified and improved, leading to overall superior macromolecular characteristics[44] or an improved performance at elevated polymerization temperatures[26]. The synthesis of *racemic* indenyl-based metallocenes lacks two major disadvantages every research group in this field previously had to deal with: the tedious *rac/meso* separation and the associated low yield of pure *rac* metallocene as *meso* complexes are known to yield atactic polypropylene upon MAO activation[21]. Being curious about the performance of our previously reported benchmark catalyst's[44] *meso* analogue, we used catalyst *meso*-**I** in the polymerization of propylene combined with the *in situ* activation employing TIBA/TrBCF. Surprisingly, we obtained perfectly isotactic PP instead of atactic PP – both, with pure *meso*-**I**, as well as with *rac/meso* mixtures. Contrary to this, when activated with MAO, *meso*-**I** yielded a physically and chemically separable iPP/aPP blend. We investigated the cause of this phenomenon and proved via several NMR experiments that aluminum-alkyl compounds isomerize the *meso* compound to its *rac* analogue. We proved the steric bulk arising in course of the alkylation using TIBA to not trigger the isomerization, as we isolated *meso*-**I$_{Me}$** *via* an alkylation of *meso*-**I** using MeMgBr with no traces of the *racemic* isomer — both in solution and single crystals. Furthermore, we established an easy and convenient protocol to selectively isomerize the *meso* compound to its *rac* analogue *in situ*. This protocol was also applicable to *rac/meso* mixtures and other hafnocenes and if employed, the total yield of iPP per used ligand in the catalyst synthesis was increased by more than 400%; comparable macromolecular characteristics as for iPP produced by pure *rac* hafnocenes were obtained.

Polymerization

Perfectly Isotactic Polypropylene upon *In Situ* Activation of Ultrarigid *meso* Hafnocenes

Lucas Stieglitz⁺, Tim M. Lenz⁺, Andreas Saurwein, and Bernhard Rieger

Abstract: For more than 40 years, the synthesis of C_2-symmetric indenyl-based *racemic* metallocenes for the isoselective polymerization of propylene relied on a tedious separation of the produced *rac* and *meso* isomers. Status quo, latter are considered wasteful as they produce atactic polypropylene (aPP) rather than isotactic polypropylene (iPP) if activated with methylaluminoxane (MAO). Unexpectedly, the *in situ* activation of *meso* hafnocene **I** yielded perfectly isotactic polypropylene. We verified an isomerization of the *meso* compound to the corresponding *racemic* one upon triisobutylaluminum (TIBA) addition via nuclear magnetic resonance (NMR) spectroscopy and established an easy and convenient polymerization protocol, enabling productivities comparable to pure *rac*-**I** if applied to pure *meso*-**I** or a mixture of both isomers. With this established isomerization protocol, the potential yield of iPP was enhanced by more than 400 %. This protocol was also shown to be applicable to other *meso* hafnocenes and some initial mechanistic insights were received.

The discovery by Brintzinger and Kaminsky in 1985 producing narrow molecular weight distributed isotactic polypropylene (iPP) by employing *racemic ansa*-zirconocenes heralded a new chapter in the stereospecific polymerization of propylene besides its heterogeneous polymerization.[1] With the aid of Spaleck's pioneering preliminary work,[2] our group obtained the so far highest molecular weight and melting transition *ex reactor* of iPP by applying ultrarigid *ansa*-hafnocenes.[3] As these hafnocenes showed a poor performance at elevated temperatures, Voskoboynikov et al. investigated zirconocene-based cata-

lysts achieving superior high-temperature performance.[4] Nevertheless, all *ansa*-metallocenes lack the same issue: the crucial and tedious separation of *rac* and *meso* isomers. This generally requires several recrystallizations,[3b] whereas for some metallocene dichlorides no suitable separation conditions have been found yet.[5] Besides this tedious and elaborative separation, a lot of valueless *meso* catalyst accumulates as a side-product and remains unused in the polymerization procedures. In literature, various *meso*-to-*rac* isomerization protocols, e.g. by applying ultraviolet (UV) light,[6] were reported to circumvent this issue—nevertheless, these protocols often led to equilibrium states or are not suitable for some catalyst systems. In 2007, Jordan et al. reported the anion-promoted *meso*-to-*rac* isomerization by applying chloride salts, such as LiCl, in refluxing tetrahydrofuran (THF).[7] This procedure has widely been examined and enforced by Voskoboynikov and co-workers for several metallocenes.[5,8] Even though the anion-promoted *meso*-to-*rac* isomerization can improve the yield of *rac* catalysts, the additional synthetic step (e.g. refluxing and removal of LiCl) and the consumed time represent serious disadvantages.

For any reason, *meso* metallocenes have not received much attention and were rather considered undesired side-products than serious pre-catalysts in the polymerization of propylene. According to Ewen's symmetry rules, *meso* catalysts are presumed to yield atactic polypropylene (aPP), as the catalyst system has no preferred direction regarding the enantiomorphic-site-model.[9] In fact, Ewen obtained an iPP/aPP blend (2:1 ratio) when polymerizing *rac/meso* Et-(Ind)₂–TiCl₂ with methylaluminoxane (MAO).[9a]

Being curious about the performance of the *meso* isomer of our group's benchmark catalyst *rac*-**I**,[4] we isolated the hafnocene *meso*-**I** (Scheme 1) and investigated its polymerization of propylene upon *in situ* activation.[10]

Instead of aPP, the polymerization employing *meso*-**I** at 30 C yielded perfectly isotactic polypropylene if the *in situ* activation with triisobutylaluminum (TIBA) and subsequent initiation with [Ph₃C][B(C₆F₅)₄] (TrBCF) was employed. Nevertheless, the productivity and molecular weight decreased for pure *meso*-**I** compared to the polymerization using pure *rac*-**I**—the polymer revealed a slight degree of bimodality (see Table 1, entries 1–4). For the polymerization using a *rac/meso* mixture, literature values were achieved with no bimodality and no reduced molecular weight.

Voskoboynikov and co-workers applied the anion-promoted *meso*-to-*rac* isomerization to *meso*-**I** to obtain *rac*-**I** with a yield of 95 %.[8] Due to the observation that *meso*-**I** yielded perfectly isotactic polypropylene ([mmmm] > 99 %)

[*] L. Stieglitz,⁺ T. M. Lenz,⁺ A. Saurwein, Prof. Dr. B. Rieger
     Wacker-Lehrstuhl für Makromolekulare Chemie,
     Catalysis Research Center,
     Technische Universität München
     Lichtenbergstraße 4, 85748
     Garching bei München (Germany)
     E-mail: rieger@tum.de

[⁺] These authors contributed equally to this work.

GDCh

Communications

Angewandte
International Edition Chemie

Scheme 1. Synthesis of *rac*-**I** and *meso*-**I**.

Figure 1. Excerpts of the ¹H NMR spectra of the isomerization of *meso*-**I** to *rac*-**I** upon addition of 1.00 equiv triisobutylaluminum (TIBA) at 100 C.

under our polymerization conditions, we assumed that an aluminum-alkyl-induced isomerization of *meso*-**I** to *rac*-**I**—similar to the associative chloride-anion-induced one—occurs during the activation process. This was verified via nuclear magnetic resonance (NMR) analysis.

The ²⁹Si NMR of *meso*-**I** upon reaction with 20.0 equiv TIBA indicated an isomerization and subsequent alkylation of *meso*-**I** to *rac*-**I**$_{alk}$. Herein, between several non-identifiable species, the same signal as for the activation product of *rac*-**I** with 200 equiv TIBA was observed (Figure S4). However, 200 equiv TIBA led to decomposition of *meso*-**I** and no clean NMR analysis could be conducted (Figure S5). This degradation could even be observed visually (see Figure S2), was monitored via UV/Vis analysis (Figure S1) and is probably responsible for the slight bimodality of the polymers. To investigate the isomerization in more detail, we used ¹H NMR analysis, initially with only 1.00 equiv TIBA to avoid signal suppression. At 60 C, the reaction progress was rather slow, therefore, we increased the temperature to 100 C. The isomerization was monitored via the 5*H*-indene and 4-methoxy moiety for which an increase of the *rac*-signals and a decrease of the corresponding *meso* signals (Figure 1 and S6) was observed.

Additional signals besides *rac*-signals were formed after 15 h at 100 C, most of them can be assigned to non-identifiable degradation products. However, one signal ($\delta = -1.15$ ppm, ¹H NMR) can be assigned to the alkylated *rac*-**I**$_{alk}$ *Hf-iBu* species as it is also observable for the reaction of *rac*-**I** with 1.00 equiv TIBA under the same conditions

(Figure S7). In the absence of TIBA, the ¹H NMR spectrum of *meso*-**I** heated to 100 C for 15 h exhibited signals that may correspond to *rac*-**I**. However, the predominant species was still *meso*-**I**, accompanied by non-identifiable side-products, highlighting the importance of TIBA for an efficient isomerization. At 60 C using 10.0 equiv TIBA, an isomerization of *meso*-**I** was also observed (Figure S8). As expected, the intensity of the signals corresponding to alkylated *rac*-**I**$_{alk}$ ($\delta = -1.15$ ppm) was increased compared to the reaction with only 1.00 equiv TIBA. However, the signals corresponding to side-products were amplified, as well. We therefore concluded that the isomerization of *meso*-**I** would concur with its degradation and that higher TIBA concentrations would promote the degradation. Furthermore, the isomerization and subsequent activation using 200 equiv TIBA was monitored via ²⁹Si NMR (Figure S9). We observed that both, *meso*-**I** and *rac*-**I** yielded the same activation product if *meso*-**I** was isomerized (1.00 equiv TIBA, 100 C, 16 h) prior to its activation. With the isomerization using 1.00 equiv TIBA at 100 C being more effective, we established a simple protocol for polymerizations using *meso*-**I** to yield iPP with enhanced productivity. Initially, *meso*-**I** was isomerized at 100 C overnight—the isomerization was confirmed via NMR spectroscopy—and subsequently, the established *in situ* activation involving the pre-activation with 200 equiv TIBA was executed.[10b] This procedure yielded perfectly isotactic PP with molecular

Table 1: Conditions and results for the polymerization of propylene with hafnocene **I**.[a]

entry	catalyst	n[b]	activation[c]	[mmmm][d]	M_w[e]	T_m[f]	$Đ$[g]	P[h]
1	*meso*-**I**	1.65	TIBA/TrBCF	>99	900	165.9	2.5	500
2	*rac*-**I**	1.65	TIBA/TrBCF	>99	1600	165.1	1.6	6000
3	*rac*-**I**/*meso*-**I** (1/4)	3.30	TIBA/TrBCF	>99	1800	165.6	1.4	400
4[f]	*meso*-**I**[j]	1.65	TIBA/TrBCF	>99	700	165.0	2.4	7000
5	*rac*-**I**/*meso*-**I** (1/4) [j]	1.65	TIBA/TrBCF	>99	1300	165.0	1.6	5000
6	*meso*-**I**	3.30	MMAO	23[k]	500	163.4[k]	1.8	130

[a] $t_p = 30$ min; $T_p = 30$ C; $V_{toluene} = 120$ mL; $p = p_{Ar} + p_{propylene} = 4$ bar, $p_{Ar} = 1.5$ bar. [b] In µmol. [c] TIBA/TrBCF: initiator [Ph$_3$C][B(C$_6$F$_5$)$_4$] = 5.0 equiv, activator (TIBA) = 200 equiv, scavenger (TIBA) = 0.55 mmol; modified MAO (*MMAO*): scavenger = activator (*MMAO*) = 2000 equiv. [d] In %, determined via ¹³C NMR spectroscopy assuming the enantiomorphic site model. [e] In kg mol⁻¹, determined absolutely via SEC-GPC in 1,2,4-trichlorobenzene at 160 C with dn/dc = 0.097 mL g⁻¹. [f] In C. [g] $Đ = M_w/M_n$. [h] In kg$_{PP}$ [mol$_{cat}$ h]⁻¹. [i] $T_p \pm 15$ C. [j] Pre-isomerized with 1.00 equiv TIBA at 100 C for 15 h. [k] aPP/iPP blend.

Communications

Table 2: Selected bond lengths and characteristic angles in the solid-state according to Rath and Coville.[13]

	bite angle [deg]	dihedral angle [deg]	Hf-Cp$_{centroid}$ [Å]	*D* [Å]
rac-**I**	57.8	42.63	2.218	0.926
meso-**I**	57.1	31.6/44.0	42.230 ± 0.003	0.927 ± 0.009
meso-**I$_{Me}$**	56.6	32.3/44.4	2.239 ± 0.002	0.961 ± 0.004

weights, molecular weight distributions and productivities comparable to pure *rac*-**I** for a *meso/rac* mixture while the high activity and thus temperature increase for pure *meso*-**I** led to a broadened molecular weight distribution (see Table 1, entries 4 and 5).

Furthermore, we investigated the polymerization of propylene with *meso*-**I** employing MAO. The polymer obtained was a blend of iPP and aPP, chemically and physically separable (Figure S29). Unfortunately, no proper ^{1}H NMR study could be performed, as no defined catalyst species were distinguishable. We concluded that the short contact time of MAO and *meso*-**I** in the autoclave led to an incomplete isomerization of *meso*-**I** while a partial direct activation also occurred—the isomerized species yielded iPP and the directly activated one aPP. As commercial MAO always contains non-hydrolyzed trimethylaluminum (TMA),[11] the isomerization of *meso*-**I** with pure TMA at 100 C was investigated (Figure 2).

The ^{1}H NMR spectra confirm the isomerization of *meso*-**I** upon addition of TMA, occurring even faster than with TIBA—probably due to the lower steric hindrance of TMA. In addition to *rac*-**I**, several side-products were formed if the reaction was conducted in pure toluene. However, if THF was added to the reaction mixture, neither alkylation nor degradation products were observable—only *meso*-**I** or *rac*-**I** signals. We assume that THF attenuates the reactivity of TMA, probably due to its coordinating character (Figure S10).

Nevertheless, it was still uncertain whether the isomerization is initiated by the Lewis acidity (e.g. ability to coordinate to the hafnocene) of aluminum-alkyls or upon alkylation and thus the increase of steric hindrance of the newly formed diisobutyl-moiety. Therefore, we converted
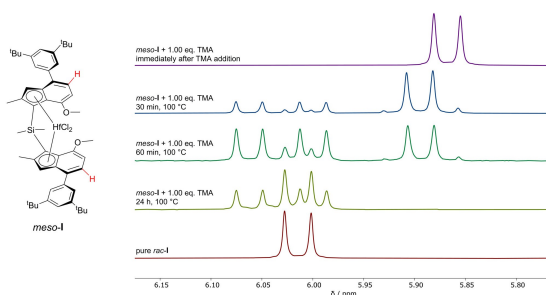
meso-**I** with Grignard reagents according to literature known procedures.[12] While the addition of MeMgBr to *meso*-**I** yielded pure *meso*-**I$_{Me}$**, the reaction of *meso*-**I** or *rac*-**I** with *i*BuMgBr did not yield the desired *meso*-**I$_{iBu}$** or *rac*-**I$_{iBu}$**, even if performed under various reaction conditions.

Compared to *meso*-**I**, single crystal X-ray diffraction (SC-XRD) revealed for *meso*-**I$_{Me}$** an increased C–Si–C angle, Hf–Cp$_{centroid}$ bond-length and *D*-value due to the enhanced bulkiness by the methyl groups, leading to a reduced bite angle (Table 2, Figure 3). Furthermore, *meso*-**I** and *meso*-**I$_{Me}$** feature two configurations of the 4(3,5tBu)-aryl substituents, probably due to the steric repulsion of the indenyl substituents. This explains the lack of a perfect symmetry of *meso* isomers, leading to a variation in Hf–Cp$_{centroid}$ and the dihedral angle, that was also observed for the respective *meso* zirconocene in a previous study.[3a] Nevertheless, the isolation of *meso*-**I$_{Me}$** illustrates that the steric repulsion arising from the activation is not responsible for the isomerization and that Grignard reagents lack the ability to isomerize *meso*-**I**.

The polymerization using *rac/meso* mixtures employing the *in situ* activation with TIBA/TrBCF enables a fast and convenient screening for the performance of ultrarigid hafnocenes, as no tedious separation is required and comparable molecular weights as for pure *rac* isomers are obtained. Furthermore, by using the established isomerization protocol, the potential yield of iPP per utilized ligand for the catalyst-synthesis is enhanced by a multiple (more than 400 % for **I**).

Up to now we cannot conclude whether the isomerization is caused by effects of the substituents inside the catalyst framework—especially the methoxy moiety—influencing the coordination of aluminum-alkyls. Nevertheless, the 4(3,5*R*)-aryl substituents were proven to not play a crucial role, as an isomeric *rac/meso* mixture (1/3) of a 4-Ph-indene hafnocene[3b] yielded perfectly isotactic PP as well. So far, we were not yet able to isolate the pure *meso* isomer but

Figure 2. Excerpts of the ^{1}H NMR spectra of the isomerization of *meso*-**I** to *rac*-**I** upon addition of 1.00 equiv trimethylaluminum (TMA) at 100 C.
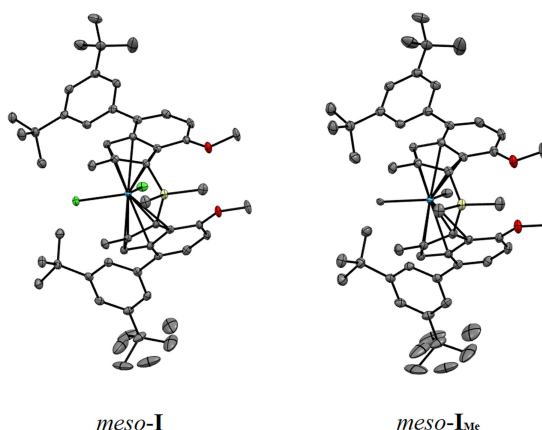
meso-**I**   *meso*-**I$_{Me}$**

Figure 3. ORTEP style representation of *meso*-**I** and *meso*-**I$_{Me}$** with ellipsoids drawn at 50 % probability level. Hydrogen atoms omitted for clarity.

no signals corresponding to the respective *meso* isomer were visible in the ^{1}H NMR spectrum after the mixture was isomerized according to our protocol. Additionally, the catalyst's productivity in propylene polymerization was enhanced for the isomerized mixture compared to the non-isomerized one.

In summary, we proved the isomerization of *meso*-**I** to *rac*-**I** with aluminum-alkyl species, yielding perfectly isotactic polypropylene with macromolecular characteristics equivalent to that of pure *rac*-**I** if activated *in situ.* Furthermore, the established isomerization protocol prior to *in situ* activation led to a productivity of pure *meso*-**I** comparable to pure *rac*-**I**, also adaptable for isomeric mixtures. Finally, via the synthesis of *meso*-**I$_{Me}$** we excluded the steric hindrance in the course of the activation to initiate the isomerization, as pure *meso*-**I$_{Me}$** was isolated without any trace of isomerization, both in solution and as single crystals. To further prove our hypothesized associative mechanism, additional catalyst systems with differing ligand frameworks and central metal atoms have to be examined and density functional theory (DFT) calculations have to be performed in the future.

Conflict of Interest

The authors declare no conflict of interest.

Data Availability Statement

SC-XRD data is available from https://www.ccdc.cam.ac.uk/products/csd with deposition numbers 2179591 (*meso*-**I**) and 2179592 (*meso*-**I$_{Me}$**).[13]

Keywords: Activation · Hafnocenes · Isomerization · Isotactic Polypropylene · Metallocenes

[1] W. Kaminsky, K. Külper, H. H. Brintzinger, F. R. W. P. Wild, *Angew. Chem. Int. Ed. Engl.* **1985**, *24*, 507–508; *Angew. Chem.* **1985**, *97*, 507–508.

[2] a) W. Spaleck, M. Antberg, J. Rohrmann, A. Winter, B. Bachmann, P. Kiprof, J. Behm, W. A. Herrmann, *Angew. Chem. Int. Ed. Engl.* **1992**, *31*, 1347–1350; *Angew. Chem.* **1992**, *104*, 1373–1376; b) W. Spaleck, F. Kueber, A. Winter, J. Rohrmann, B. Bachmann, M. Antberg, V. Dolle, E. F. Paulus, *Organometallics* **1994**, *13*, 954–963.

[3] a) A. Schöbel, E. Herdtweck, M. Parkinson, B. Rieger, *Chem. Eur. J.* **2012**, *18*, 4174–4178; b) M. R. Machat, D. Lanzinger, A. Pöthig, B. Rieger, *Organometallics* **2017**, *36*, 399–408.

[4] a) G. P. Goryunov, M. I. Sharikov, A. N. Iashin, J. A. M. Canich, S. J. Mattler, J. R. Hagadorn, D. V. Uborsky, A. Z. Voskoboynikov, *ACS Catal.* **2021**, *11*, 8079–8086; b) V. V. Izmer, A. Y. Lebedev, D. S. Kononovich, I. S. Borisov, P. S. Kulyabin, G. P. Goryunov, D. V. Uborsky, J. A. M. Canich, A. Z. Voskoboynikov, *Organometallics* **2019**, *38*, 4645–4657; c) P. S. Kulyabin, G. P. Goryunov, M. I. Sharikov, V. V. Izmer, A. Vittoria, P. H. M. Budzelaar, V. Busico, A. Z. Voskoboynikov, C. Ehm, R. Cipullo, D. V. Uborsky, *J. Am. Chem. Soc.* **2021**, *143*, 7641–7647.

[5] P. S. Kulyabin, V. V. Izmer, G. P. Goryunov, M. I. Sharikov, D. S. Kononovich, D. V. Uborsky, J. A. M. Canich, A. Z. Voskoboynikov, *Dalton Trans.* **2021**, *50*, 6170–6180.

[6] a) A. L. Rheingold, N. Robinson, J. Whelan, B. Bosnich, *Organometallics* **1992**, *11*, 1869–1876; b) W. Kaminsky, A.-M. Schauwienold, F. Freidanck, *J. Mol. Catal. A* **1996**, *112*, 37–42; c) F. R. Wild, L. Zsolnai, G. Huttner, H. H. Brintzinger, *J. Organomet. Chem.* **1982**, *232*, 233–247.

[7] R. M. Buck, N. Vinayavekhin, R. F. Jordan, *J. Am. Chem. Soc.* **2007**, *129*, 3468–3469.

[8] A. Vittoria, G. P. Goryunov, V. V. Izmer, D. S. Kononovich, O. V. Samsonov, F. Zaccaria, G. Urciuoli, P. H. Budzelaar, V. Busico, A. Z. Voskoboynikov, *Polymer* **2021**, *13*, 2621.

[9] a) J. A. Ewen, *J. Am. Chem. Soc.* **1984**, *106*, 6355–6364; b) H. H. Brintzinger, D. Fischer, R. Mülhaupt, B. Rieger, R. M. Waymouth, *Angew. Chem. Int. Ed. Engl.* **1995**, *34*, 1143–1170; *Angew. Chem.* **1995**, *107*, 1255–1283; c) L. Resconi, L. Cavallo, A. Fait, F. Piemontesi, *Chem. Rev.* **2000**, *100*, 1253–1346.

[10] a) M. Schloegl, C. Troll, U. Thewalt, B. Rieger, *Z. Naturforsch. B* **2003**, *58*, 533–538; b) L. Stieglitz, D. Henschel, T. Pehl, B. Rieger, *Organometallics* **2021**, *40*, 4055–4065.

[11] V. Busico, R. Cipullo, R. Pellecchia, G. Talarico, A. Razavi, *Macromolecules* **2009**, *42*, 1789–1791.

[12] M. R. Machat, A. Fischer, D. Schmitz, M. Vöst, M. Drees, C. Jandl, A. Pöthig, N. P. M. Casati, W. Scherer, B. Rieger, *Organometallics* **2018**, *37*, 2690–2705.

[13] a) P. C. Möhring, N. J. Coville, *Coord. Chem. Rev.* **2006**, *250*, 18–35; b) R. M. Shaltout, J. Y. Corey, N. P. Rath, *J. Organomet. Chem.* **1995**, *503*, 205–212, Deposition Numbers 2179591 (for *meso*-**I**) and 2179592 (for *meso*-**I$_{Me}$**) contain the supplementary crystallographic data for this paper. These data are provided free of charge by the joint Cambridge Crystallographic Data Centre and Fachinformationszentrum Karlsruhe Access Structures service.

6 Processing of UHMW-iPP for Prototype Production

"Fiber Spinning of Ultrahigh Molecular Weight Isotactic Polypropylene: Melt Spinning and Melt Drawing"

6.1 Bibliographic Data

Title:	Fiber Spinning of Ultrahigh Molecular Weight Isotactic Polypropylene: Melt Spinning and Melt Drawing
Status:	Article, Publication Date: 14.02.2023
Journal:	ChemPlusChem
Publisher:	Wiley
DOI:	10.1002/cplu.202300045
Authors:	Lucas Stieglitz, Christina Geiger, Paula F. Großmann, Moritz Kränzlein, Katia Rodewald, Peter Müller-Buschbaum and Bernhard Rieger[1]

6.2 Graphical Abstract (TOC)
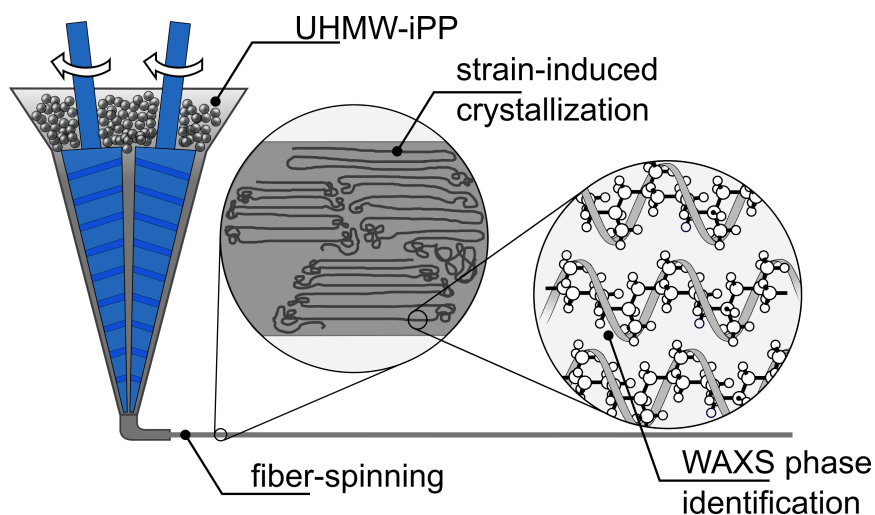
Figure 15: Graphical abstract (TOC) of the manuscript titled "Fiber Spinning of Ultrahigh Molecular Weight Isotactic Polypropylene: Melt Spinning and Melt Drawing".

---

[1]L. Stieglitz provided the original idea, planned all experiments and wrote the manuscript. C. Geiger planned and executed WAXS measurements and processed the data. P. F. Großmann and M. Kränzlein assisted polymer processing and helped with data analysis. K. Rodewald measured SEM images of the polymer fibers and processed the data. All work was supervised by P. Müller-Buschbaum and B. Rieger.

6.3 Content

The shift of the polymers' molecular weight to the ultrahigh regime is linked with enhanced properties, such as optimized mechanical behavior of the polymer. For example, UHMW-PE has greatly improved mechanical properties in comparison to HD-PE, and the Young's modulus and tensile strength ($>$90 and $>$3GPa, respectively) even enable its application in bullet-proof fabrics. Compared to PE, iPP has some major advantages: an almost 25 °C higher melting transition, a higher tensile strength and impact resistance as well as a lower mass density. However, due to the high melt viscosity, processing of UHMW polymers is very challenging and is regarded to be nearly impossible via the classical route (melt extrusion). Considering the advantages of iPP, UHMW-iPP is currently receiving more research focus. In a recent study[204] the viscosity of iPP/UHMW-iPP blends was reduced with the aid of oxalamide-based nucleating agents.

In 2012, *Rieger et al.* isolated perfectly isotactic PP with the so far highest molecular weight of up to 5800 kg/mol and melting transition *ex reactor* at 171 °C – this iPP remains until today as the benchmark iPP in terms of macromolecular characteristics.[44] With the advantages of iPP compared to PE in mind, we set ourselves the goal to process this UHMW polymer *via* common melt extrusion – despite the difficult circumstances. Therefore, we performed melt spinning of various iPP samples by using a modified extrusion set- up. We confirmed that no chain breakage occurs during the spinning process and investigated the crystallinity and phase crystallization *via* DSC and WAXS analysis. We proved that UHMW-iPP fibers enable a high tensile strength that was even increased after an annealing process (up to 400 MPa). However, UHMW-iPP exhibited a short melt spinning time window due to its increasing melt viscosity – after that, no more spinning was possible, only melt drawing. Unfortunately, after a specific time UHMW-iPP even led to agglutination of the compounder – hampering extrusion at all. Probably, the number of entanglements and consequently the polymer's melt viscosity were increased by the melting process, and thus the UHMW polymer was no longer extrudable. By mixing a lower molecular weight iPP fraction to the feedstock, extrusion rupture and agglutination of the compounder was avoided and a composite fiber with enhanced mechanical properties was obtained.

Check for updates

Chemistry
Europe
European Chemical
Societies Publishing

www.chempluschem.org

Fiber Spinning of Ultrahigh Molecular Weight Isotactic Polypropylene: Melt Spinning and Melt Drawing

Lucas Stieglitz,[a] Christina Geiger,[b] Paula F. Großmann,[a] Moritz Kränzlein,[a] Katia Rodewald,[a] Peter Müller-Buschbaum,[b, c] and Bernhard Rieger*[a]

Herein, this work reports fiber spinning of tailored isotactic polypropylene (iPP) by melt spinning and melt drawing, yielding an adjustable diameter of 40–400 μm. The crystallinity of all obtained fibers with a molecular weight between 330–1400 kg/mol is increased by thermal annealing and investigated *via* differential scanning calorimetry (DSC) as well as wide angle X-ray scattering (WAXS). The potential of ultrahigh molecular weight iPP (UHMW-iPP) fibers compared to fibers manufactured from industrially available iPP becomes evident when the mechanical performance is compared: fibers spun from UHMW-iPP (1400 kg/mol) enable a tensile strength of up to 400 MPa, whereas commercially available fibers (330 kg/mol) show a tensile strength of approximately 50 MPa. However, UHMW-iPP exhibits a short timeframe, in which extrusion is possible, thereafter extrusion rupture occurs, probably induced by an increased melt viscosity.

Introduction

Tailoring isotactic polypropylene (iPP) was first made possible by Brintzinger and Kaminsky with their discovery of the isospecific *ansa*-metallocene catalyzed polymerization of propylene in 1985.[1] In the following years, macromolecular characteristics, such as molecular weight, degree of isotacticity and melting transition were adjusted by a variation of the basic group (IV) metallocenes' scaffold.[2] By using the ultrarigid hafnocene dichloride **II** (Figure S45), Rieger *et al.* isolated in 2012 perfectly isotactic PP with the so far highest molecular weight of up to 5800 kg/mol and melting transition *ex reactor* at 171 C – this iPP remains until today as the benchmark iPP in terms of macromolecular characteristics.[2a] Recently, an improved polymerization procedure was established to tremendously increase this polymer's yield per utilized ligand system by avoiding the tedious *rac/meso* separation.[3]

[a] *L. Stieglitz, P. F. Großmann, M. Kränzlein, K. Rodewald, Prof. B. Rieger*
Wacker-Lehrstuhl für Makromolekulare Chemie
Catalysis Research Center
TUM School of Natural Sciences
Technische Universität München
Lichtenbergstraße 4, 85748 Garching bei München (Germany)
E-mail: rieger@tum.de
[b] *C. Geiger, Prof. P. Müller-Buschbaum*
TUM School of Natural Sciences
Department of Physics
Technische Universität München
James-Franck-Straße 1, 85748 Garching (Germany)
[c] *Prof. P. Müller-Buschbaum*
Heinz Maier-Leibnitz Zentrum (MLZ)
Technische Universität München
Lichtenbergstraße 1, 85748 Garching (Germany)

Supporting information for this article is available on the WWW under
https://doi.org/10.1002/cplu.202300045

Compared to polyethylene (PE), iPP has some serious advantages: an almost 25 C higher melting transition, a higher tensile strength and impact resistance as well as a lower mass density.[4] Therefore, ultrahigh molecular weight iPP (UHMW-iPP) fibers potentially could outperform UHMW-PE *Dyneema* fibers. However, the processing of UHMW polymer fibers *via* the classic melt extrusion route is considered very challenging and even a few claim it to be nearly impossible.[4] This is mainly attributed to the high melt viscosity, which correlates with the polymer's molecular weight with $\eta_0 \propto M_w^{3.4}$.[5] To circumvent this, a few attention was directed onto the gel-spinning process for UHMW-iPP fiber production.[6] However, extrusion for fiber spinning has not yet been reported for UHMW-iPP, probably caused by the inherent high melt viscosity impeding this process. Despite these difficult conditions, we isolated UHMW-iPP fibers of different molecular weights *via* melt extrusion and subsequently compared their mechanical properties to fibers of medium high molecular weight PP, both commercially available or received by homogeneous polymerization.

Results and Discussion

The list of iPP samples used for fiber spinning *via* melt extrusion in this study, ranging from medium high molecular weight to UHMW, is shown in Table 1. **iPP-1** was commercially available from *Ineos*, **iPP-2** to **iPP-5** were synthesized *via* single-site catalysis, using two literature known catalysts (Figure S45) –

Table 1. Tailored iPP for fiber spinning.				
	M_w [kg/mol]	*Đ* (−)	T_m [C]	[mmmm][%]
iPP-1	330	6.6	162.8	95
iPP-2	380	2.4	157.7	94
iPP-3	860	1.8	165.6	>99
iPP-4	1200	1.8	165.4	>99
iPP-5	1400	1.8	165.5	>99

iPP-2 was obtained by using **I**, and **II** was used for **iPP-3** to **iPP-5** combined with suitable polymerization conditions.[2c,7]

While **iPP-2** was received as a polymer powder, **iPP-3**–**iPP-5** were received as a fibrous material after synthesis. Therefore, these polymers were milled with an ultra-centrifugal mill to reduce the grain size. Chain destruction induced by oxidative stress during processing was avoided by applying an improved milling procedure (Figure S6–S10).

For subsequent fiber spinning, we combined a micro-compounder and a KPG-stirrer equipped with a manufactured spinning cone (Figure S24 and S25) – with this set-up (Figure 1, left), the spinning speed as well as the nozzle-cone distance could be adjusted to modify the fiber's diameter and ensure a solid phase. In preliminary experiments using a 0.50 mm spinning nozzle, it was shown that the commercial **iPP-1** has a good spinnability. The fiber's thickness could be adjusted arbitrarily up to 40 μm with no need for any stabilizing agent. In contrast to **iPP-1**, 1 wt% *Irganox* 1010 as stabilizing agent for UHMW-iPP could not prevent chain destruction and led to broadening of the polydispersity. Increasing the amount of *Irganox* to 3 wt% resulted in no spinnability and a checked-off extrudate. We therefore increased the nozzle's diameter to 2.00 mm – this resulted in a proper extrusion of the UHMW polymer. Screening for the appropriate amount of stabilizing agent revealed that the optimum amount is between 3 and 7 wt% (Figure S12). We decided to utilize the upper limit to avoid any chain destruction in the spinning or annealing process. To compare the mechanical properties of **iPP-1**–**iPP-5**, we used the same extrusion conditions and aimed for a fiber thickness of 200–400 μm, as, contrary to **iPP-1**, thin UHMW-iPP fibers were challenging to receive with our used set-up.

While spinning fine and thin fibers (40–120 μm) for **iPP-1** and **iPP-2** was comparably easy, an increase of the fiber's diameter turned out to be challenging when using the 0.50 mm fiber spinning nozzle. Therefore, we manufactured a 1.00 mm fiber spinning nozzle (Figure S23) combining the advantages of 0.50 mm fiber spinning and 2.00 mm extrusion nozzle: a smaller diameter as well as a longer nozzle distance for an improved

homogeneity of the polymer melt. Still, this manufactured 1.00 mm nozzle was not useful for **iPP-3**–**iPP-5**, as the high melt viscosity of the polymers caused inhomogeneities and partially extrusion rupture, leading to no proper fiber spinning (Figure S30 and S41). After changing to the 2.00 mm extrusion nozzle, the extrusion of **iPP-3**–**iPP-5** was smooth (Figure S31, S34 and S38), melt spinning with only a few inhomogeneities (Figure S35 and S37) was accessible and UHMW fibers with a diameter of about 300 μm were received.

After a few minutes in the compounder, the UHMW polymer's melt viscosity increased drastically, and extrusion ruptures occurred – yielding 2–4 cm long extrudates not suitable for melt spinning. However, with these molten extrudates, melt drawing instead of melt spinning was possible. This technique of post-extrusion drawing of as-spun fibers is applied e.g. by Kakiage et al. for fiber spinning of UHMW-PE fibers.[8] For this purpose, the molten extrudate with a diameter of 2.00 mm was stretched on both sides to a length of 20–30 cm with a stretching rate of 20 cm/sec. This consequently yielded a consistent fiber with a reduced diameter of 400 μm (Figure S33). After approximately ten minutes of the polymer inside the compounder, the UHMW polymer's melt agglutinated the compounder, and no extrusion was possible anymore (Figure 1, right). Adding new polymer or increasing the extrusion temperature up to 220 C did not sufficiently reduce the agglutination. The removed polymer revealed no variation in the molecular weight, and after milling, the polymer remained non extrudable. Probably, the number of entanglements and consequently the polymer's melt viscosity were increased by the melting process and the arising shear forces, and therefore, the UHMW polymer was no longer extrudable.

DSC measurements of e.g. **iPP-5** support this hypothesis, as it was observed that the first melting transition and crystallinity (167.4 C, 55.4% crystallinity) is increased compared to the second transition (165.5 C, 44.3% crystallinity) – nevertheless, further investigations comparing the nascent, melt-crystallized and agglutinated polymer need to be conducted.

A mixture of 70 wt% **iPP-4** and 30 wt% **iPP-1** gave a smooth extrusion using the manufactured 1.00 mm fiber spinning nozzle with no observation of an increased melt viscosity or extrusion rupture. This yielded a composite fiber with a diameter of about 200 μm. Probably, combining two iPPs – one with a high and one with a low melt viscosity – is a promising method to avoid agglutination of the compounder.

Figure 2 illustrates the optical differences between the UHMW **iPP-4** and medium high molecular weight **iPP-1** fiber. Commercial **iPP-1** bearing a reduced melt viscosity and crystallinity enabled a very smooth and even fiber surface, whereas our UHMW-iPP with its ultrahigh molecular weight and increased crystallinity led to a high surface roughness induced by fibrillation. This high surface roughness is well known for UHMW-PE fibers, especially for high draw ratios.[11] Surprisingly, annealing of the polymer fibers melted the fiber surface for all investigated fibers (Figure 2). Underneath that melted surface, the fibrillated structure was preserved for UHMW fibers (Figure 2, b).

Figure 1. Set-up for fiber spinning (left) and agglutinated compounder (right) after spinning of UHMW-iPP.
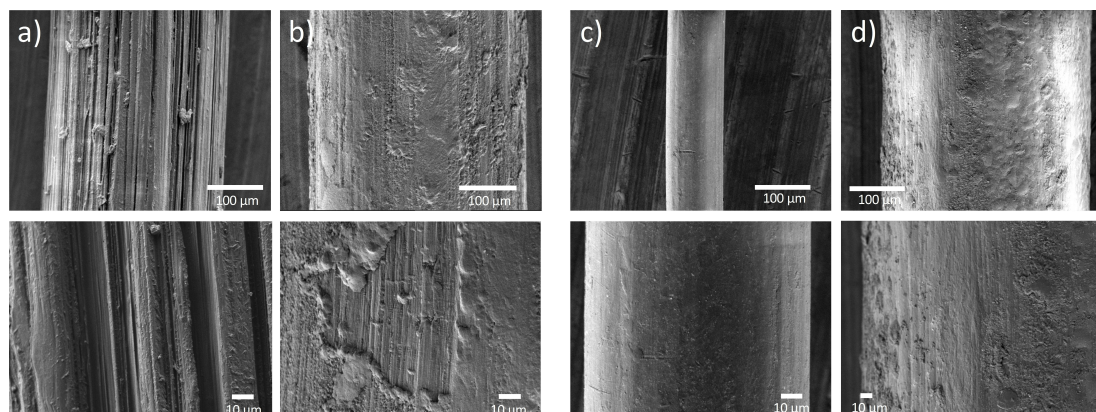
Figure 2. SEM images of a) melt drawn and b) annealed melt drawn **iPP-4** fiber compared to c) spun and d) annealed spun **iPP-1** fiber.

The mechanical properties of polymers, especially the tensile strength, highly depend on the crystallinity.[12] Besides increasing the isotacticity, annealing of the polymer is a commonly used technique to enhance the degree of crystallinity. In previous studies it was shown, that a higher annealing temperature leads to an increased crystallinity.[13] Furthermore, annealing prevents crazes and avoids coalescence, consequently improving the mechanical behavior.[13b] In preliminary experiments, an increased annealing temperature of 150 C for 67 h turned out to be suited better for UHMW-iPP fibers compared to a temperature of 140 C for 20 h (Figure S21 and S22). Actually, an even higher annealing temperature would be desirable, but due to an inaccurate temperature control this led to a partial melting of the polymer fibers. For **iPP-1** and **iPP-2** we reduced the annealing temperature to 143 C, as 150 C melted the polymer fibers.

The crystallization behavior of **iPP-5** during different stages of the fiber manufacturing process was analyzed by WAXS measurements (Figure 3). The crystalline fraction of the raw polymer sample consisted purely of the α-phase, which meets the expectation – it is reported that iPP from solution crystallization yields mostly the α-phase.[9] As expected for the raw polymer after precipitation synthesis without any further processing, there is no preferential orientation of the crystals, as seen from the uniform scattering intensity along the Debye-Scherrer rings. The extrudate still exhibited predominantly the α-phase for the crystalline fraction, but the formation of β-phase crystallites was detected as well. A weak preferential orientation of crystallites was observed. The sample exhibited a strong homoepitaxy[10] of the α-phase, identifiable by an intense (110)d reflex, originating from the daughter crystals, that were seen to orient roughly perpendicularly to the stretching direction, while the mother crystals orient roughly parallel to the stretching direction. In the spun fibers, the α-phase clearly predominated the crystalline fraction, but a small fraction of β-phase crystallites was still present (see Figure S44f). The crystallites in the spun fiber exhibited a strong preferential orientation. The sample, as already seen in the extrudate,
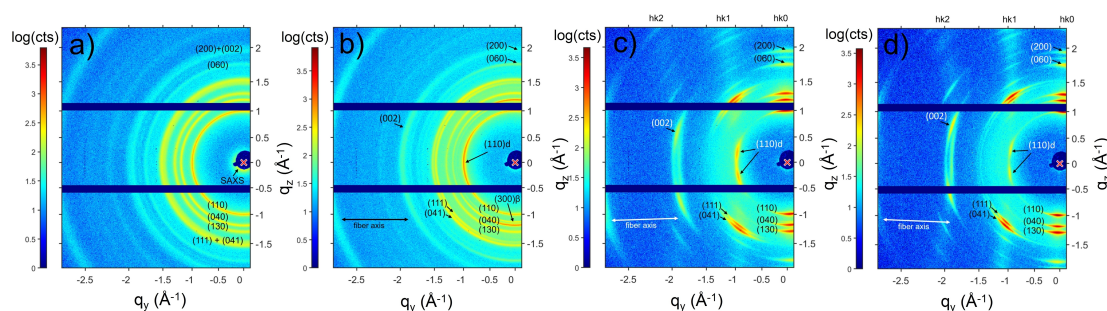
Figure 3. Transmission-mode WAXS data from UHMW **iPP-5** at different stages of the fiber fabrication process. a) raw polymer (obtained as fine mesh), b) extrudate, c) spun fiber, d) annealed fiber (fiber axis marked by arrow). Characteristic reflections belonging to the α-phase[9] of crystalline iPP predominantly found in all samples are marked with their corresponding *Miller* indices (exceptions are: (110)d marking the reflections of the daughter crystals resulting from iPP homoepitaxy[10] – all other indicated reflections belong to the mother crystals – and (300)β, marking the most intense reflection of the β-phase, seen most clearly in b) (extrudate)). A clear increase in preferential orientation of crystallites is seen from a) to d). Typical hk0 (equator) lines, hk1, and hk2 arcs, on which reflections sit, are marked for the spun and annealed fiber patterns in c) and d). Further information on WAXS measurements and data analysis is available in the Supporting Information.

showed a homoepitaxy of the α-phase, resulting in the (110)d daughter reflex appearing under the azimuthal angles 80 and 100 relative to the hk0 equator with the (110) mother reflex, as found in literature.[10] The separation of the daughter reflex is a result of the strong preferential orientation of all α-phase crystallites. A very similar scattering pattern was found in the annealed fiber as for the spun fiber. The main differences found were the depletion of the β-phase, which was no longer detectable, and the reduced intensity of the amorphous halo, as well as the increased sharpness (decreasing full width at half maximum (FWHM)) of the unique reflections of the α-phase.

We verified *via* GPC measurements (Figure 4, a), that neither the spinning process nor the annealing process led to bond breakage of the polymer fibers by an oxidative stress. Furthermore, we observed an increased melting transition temperature and crystallinity, especially after the annealing process, *via* DSC analysis (Figure 4, b), which is in agreement with the WAXS results. The degree of crystallinity was determined by using the melt enthalpy for polypropylene $\Delta H_{lit},$ 100 % = 207 J/g.[11] Table 2 illustrates the influence of the
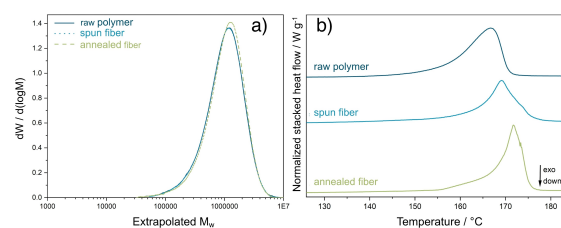
Figure 4. GPC (a) and DSC (b) analysis of **iPP-4**.

Table 2. Calculated Crystallinity *via* DSC analysis.

	iPP-1	iPP-2	iPP-3	iPP-4	iPP-5
raw	44.6 %	41.4 %	44.1 %	43.9 %	44.3 %
spun fiber	47.0 %	43.2 %	45.6 %	48.1 %	46.8 %
annealed fiber	50.1 %	46.0 %	53.0 %	52.2 %	53.5 %
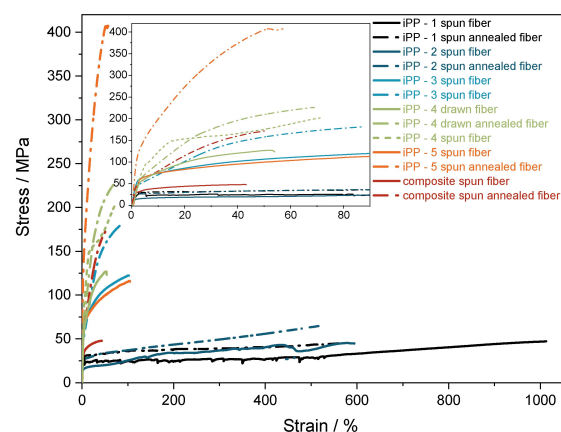
Figure 5. Stress strain mechanical behavior of spun and annealed fibers.

crystallite orientation induced by fiber spinning and increased lamellae thickness by the annealing process.

Examining their mechanical behavior *via* stress strain measurements, the extraordinary potential of UHMW-iPP fibers compared to fibers manufactured from industrially available iPP is highlighted (Figure 5). All UHMW-iPP fibers, due to their higher molecular weight and lower polydispersity, exhibited a higher tensile strength and a shortened elongation at break compared to the *Ziegler-Natta* based **iPP-1**.[14] The increase in crystallinity (Table 2) induced by the annealing process boosted the tensile strength of all polymer fibers **iPP-1**–**iPP-5** (e.g. **iPP-5** spun and annealed fiber, Figure 5) and a tensile strength of up to 400 MPa was received for UHMW-iPP fibers. The melt drawing process of **iPP-4** however yielded a decreased tensile strength compared to the melt spinning process – probably due to inhomogeneities in the molten extrudate. The composite fiber of 70 wt% **iPP-4** and 30 wt% **iPP-1** surprisingly showed a low tensile strength combined with a low elongation at break – despite the high amount of UHMW-iPP in the feedstock material. Presumably, the two different polymers were not evenly distributed in the composite polymer fiber, leading to defects and an overall deteriorated mechanical behavior. During the annealing process, defects in the composite structure are reduced and the crystalline fraction increased (see Figure S44), thus improving the stress strain behavior. Blending UHMW-iPP with an iPP bearing a lower melt viscosity not only avoids agglutination of the compounder, but also is a promising method to obtain strong iPP fibers. Clearly, this presented technique yields lower tensile strengths and an increased fiber's diameter compared to previous reported UHMW-iPP fibers accessed by gel-spinning[6a,c,d] – however, this study highlights, that extrusion of UHMW-iPP is feasible and thus may pave the way for an improved spinning technique of UHMW-iPP.

Conclusion

In summary, we performed melt spinning and melt drawing of various iPP samples, including the first reported extrusion processing of UHMW-iPP. We investigated the crystallinity and phase crystallization *via* DSC and WAXS analysis and confirmed no chain breakage occurring during the spinning process. We proved that UHMW-iPP fibers enable a high tensile strength that was even increased after an annealing process (up to 400 MPa). However, UHMW-iPP exhibited a short melt spinning time window due to its increasing melt viscosity – after that, no spinning was possible at all. Nevertheless, by mixing a lower molecular weight iPP fraction to the feedstock, extrusion rupture and agglutination of the compounder was avoided and a composite fiber with enhanced mechanical properties was obtained. As these findings are very promising, further studies need to be conducted to better understand the root cause of the agglutination and increased melt viscosity and also to improve the mechanical properties of the obtained fibers.

Experimental Section

Polymer ^{13}C NMR spectra were measured with an ARX-300 spectrometer at 140 C in bromobenzene-d^5 with 40–60 mg/mL and 14k scans with 5 mm OD tubes. Acquisition conditions were: 30 flip angle; 1.82 sec acquisition time, 2 sec relaxation delay. Broadband proton decoupling was achieved with a WALTZ16 sequence. The degree of isotacticity was determined via the integration of the corresponding [mmmm]-pentade (21.85 ppm)[15] against the region of 19.5–22.5 ppm.

Gel permeation chromatography (GPC) was performed with a PL-GPC 220 instrument equipped with 2x Olexis 300 mm ×7.5 mm columns and triple detection via a differential refractive index detector, a PL-BV 400 HT viscometer, and light scattering (Precision Detectors Model 2040, 15 and 90). Measurements were performed at 160 C using HPLC-grade 1,2,4-trichlorobenzene (TCB; 100 mg/L BHT) from Sigma-Aldrich with a constant flow rate of 1 mL/min and a calibration set with narrow-MWD polyethylene (PE) and polystyrene (PS) standards. Samples were prepared by dissolving 0.5–0.7 mg of the polymer in 1.0 mL of stabilized TCB for 1 h at 140 C immediately before each measurement. The molecular weight was determined absolutely against PS standards by using dn/dc= 0.097 mL/g.[16]

Differential scanning calorimetry (DSC) analysis was conducted on a DSC Q2000 instrument from TA Instruments. The polymer (4–5 mg) was sealed into a non-hermetic aluminum pan and heated from 50 to 200 C at 10 C/min. After the temperature was held for 2 min, the sample was cooled to 50 C at 10 C/min and heated again in the same manner. The reported values for raw polymers are those determined in the second heating cycle, for fibers those determined in the first heating cycle.

Optical light microscopy was carried out using a PantheraTEC-BD from Motic equipped with a MicroCam II camera from Bresser. The software MicroCamLabII was used for processing.

The surface of the fibers was determined by the images taken by JEOL JSM-7500F field-emission scanning electron microscope coupled with EDX INCA System (software) with 50 mm^2 X-MAX detector from Oxford Instruments.

As **iPP-3**–**iPP-5** were received as a fibrous material, these polymers had to be milled for an extrusion processing. The coarsely crushed polymer was frozen in liquid nitrogen and subsequently milled chunkwise by using a *Retsch ultra centrifugal mill ZM 200* (12-tooth rotor, sieve size 2.00 mm, trapezoid holes) at 1000 rpm.

Extrusion for fiber spinning was conducted using a Micro-Compounder from *DACA Instruments*. The temperature was set at 195 C and 7% wt. of the stabilizing agent *Irganox 1010* added to the polymer prior the extrusion. 2–2.5 g of the stabilized polymer were added to the compounder and after an appropriate mixing time (for iPP-1 and iPP-2 three minutes, for iPP-3–iPP-5 15 seconds) the extrusion was initiated. The molten extrudate was rolled onto the manufactured spinning cone's rod (Figure S24 and S25) – when the fiber's diameter was smooth, the spinning was conducted on the spinning cone. With the attached *Heidolph* KPG-stirrer, the distance between nozzle and cone and spinning speed was adjusted according to the desired fiber characteristics and polymer's melt viscosity. An increased KPG stirring speed gave a thinner polymer fiber, but the distance between nozzle and cone had to be increased to ensure an entire solidification of the fiber.

Data Availability Statement

The data that support the findings of this study are available from the corresponding author upon reasonable request.

[1] W. Kaminsky, K. Külper, H. H. Brintzinger, F. R. W. P. Wild, *Angew. Chem. Int. Ed. Engl.* **1985**, *24*, 507–508.

[2] a) A. Schöbel, E. Herdtweck, M. Parkinson, B. Rieger, *Chem. Eur. J.* **2012**, *18*, 4174–4178; b) M. R. Machat, C. Jandl, B. Rieger, *Organometallics* **2017**, *36*, 1408–1418; c) M. R. Machat, D. Lanzinger, A. Pöthig, B. Rieger, *Organometallics* **2016**, *36*, 399–408; d) M. R. Machat, A. Fischer, D. Schmitz, M. Vöst, M. Drees, C. Jandl, A. Pöthig, N. P. M. Casati, W. Scherer, B. Rieger, *Organometallics* **2018**, *37*, 2690–2705; e) P. S. Kulyabin, G. P. Goryunov, M. I. Sharikov, V. V. Izmer, A. Vittoria, P. H. Budzelaar, V. Busico, A. Z. Voskoboynikov, C. Ehm, R. Cipullo, *J. Am. Chem. Soc.* **2021**, *143*, 7641–7647; f) W. Spaleck, M. Antberg, J. Rohrmann, A. Winter, B. Bachmann, P. Kiprof, J. Behm, W. A. Herrmann, *Angew. Chem. Int. Ed. Engl.* **1992**, *31*, 1347–1350; g) W. Spaleck, F. Kueber, A. Winter, J. Rohrmann, B. Bachmann, M. Antberg, V. Dolle, E. F. Paulus, *Organometallics* **1994**, *13*, 954–963; h) G. P. Goryunov, M. I. Sharikov, A. N. Iashin, J. A. M. Canich, S. J. Mattler, J. R. Hagadorn, D. V. Uborsky, A. Z. Voskoboynikov, *ACS Catal.* **2021**, *11*, 8079–8086; i) V. V. Izmer, A. Y. Lebedev, D. S. Kononovich, I. S. Borisov, P. S. Kulyabin, G. P. Goryunov, D. V. Uborsky, J. A. M. Canich, A. Z. Voskoboynikov, *Organometallics* **2019**, *38*, 4645–4657; j) P. S. Kulyabin, V. V. Izmer, G. P. Goryunov, M. I. Sharikov, D. S. Kononovich, D. V. Uborsky, J. A. M. Canich, A. Z. Voskoboynikov, *Dalton Trans.* **2021**, *50*, 6170–6180; k) A. Vittoria, G. P. Goryunov, V. V. Izmer, D. S. Kononovich, O. V. Samsonov, F. Zaccaria, G. Urciuoli, P. H. Budzelaar, V. Busico, A. Z. Voskoboynikov, *Polymer* **2021**, *13*, 2621.

[3] L. Stieglitz, T. M. Lenz, A. Saurwein, B. Rieger, *Angew. Chem. Int. Ed.* **2022**, *61*, e202210797.

[4] R. Marroquin-Garcia, N. Leone, L. G. D. Hawke, D. Romano, C. H. R. M. Wilsens, S. Rastogi, *Macromolecules* **2022**, *55*, 2574–2587.

[5] R. H. Colby, L. J. Fetters, W. W. Graessley, *Macromolecules* **1987**, *20*, 2226–2237.

[6] a) C. Bastiaansen, P. Lemstra, in *Makromolekulare Chemie. Macromolecular Symposia, Vol. 28*, Wiley Online Library, **1989**, pp. 73–84; b) M. Matsuo, T. Hashida, K. Tashiro, Y. Agari, *Macromolecules* **2002**, *35*, 3030–3040; c) T. Ogita, Y. Kawahara, Y. Soga, M. Matsuo, *Colloid Polym. Sci.* **1992**, *270*, 833–839; d) Y. Ikeda, T. Ohta, *Sen'i Gakkaishi* **2002**, *58*, 444–450.

[7] L. Stieglitz, D. Henschel, T. Pehl, B. Rieger, *Organometallics* **2021**, *40*, 4055–4065.

[8] a) M. Kakiage, D. Fukagawa, *Mater. Today Commun.* **2020**, *23*, 100864; b) M. Kakiage, S. Takei, *Macromol. Mater. Eng.* **2020**, *305*, 2000252.

[9] A. T. Jones, J. M. Aizlewood, D. R. Beckett, *Makromol. Chem.* **1964**, *75*, 134–158.

[10] T. Raidt, R. Hoeher, F. Katzenberg, J. C. Tiller, *Macromol. Rapid Commun.* **2015**, *36*, 744–749.

[11] E. Wölfel, H. Brünig, I. Curosu, V. Mechtcherine, C. Scheffler, *Materials* **2021**, *14*, 722.

[12] A. Galeski, *Prog. Polym. Sci.* **2003**, *28*, 1643–1699.

[13] a) T. Parenteau, G. Ausias, Y. Grohens, P. Pilvin, *Polymer* **2012**, *53*, 5873–5884; b) P. Frontini, A. Fave, *J. Mater. Sci.* **1995**, *30*, 2446–2454.

[14] S. Misra, F.-M. Lu, J. E. Spruiell, G. C. Richeson, *J. Appl. Polym. Sci.* **1995**, *56*, 1761–1779.

[15] H. H. Brintzinger, D. Fischer, R. Mülhaupt, B. Rieger, R. M. Waymouth, *Angew. Chem. Int. Ed. Engl.* **1995**, *34*, 1143–1170.

[16] B. Coto, J. M. Escola, I. Suárez, M. J. Caballero, *Polym. Test.* **2007**, *26*, 568–575.

7 Processing of sPP for Prototype Production

"Tailored Syndiotactic Polypropylene Feedstock Material for Laser-Based Powder Bed Fusion of Polymers: Material Development and Processability"

7.1 Bibliographic Data

Title:	Tailored Syndiotactic Polypropylene Feedstock Material for Laser-Based Powder Bed Fusion of Polymers: Material Development and Processability
Status:	Article, Publication Date: 28.03.2023
Journal:	ACS Applied Polymer Materials
Publisher:	American Chemical Society
DOI:	10.1021/acsapm.2c02112
Authors:	Simon Cholewa,[†] Lucas Stieglitz,[†] Andreas Jaksch, Bernhard Rieger and Dietmar Drummer[1]

7.2 Graphical Abstract (TOC)
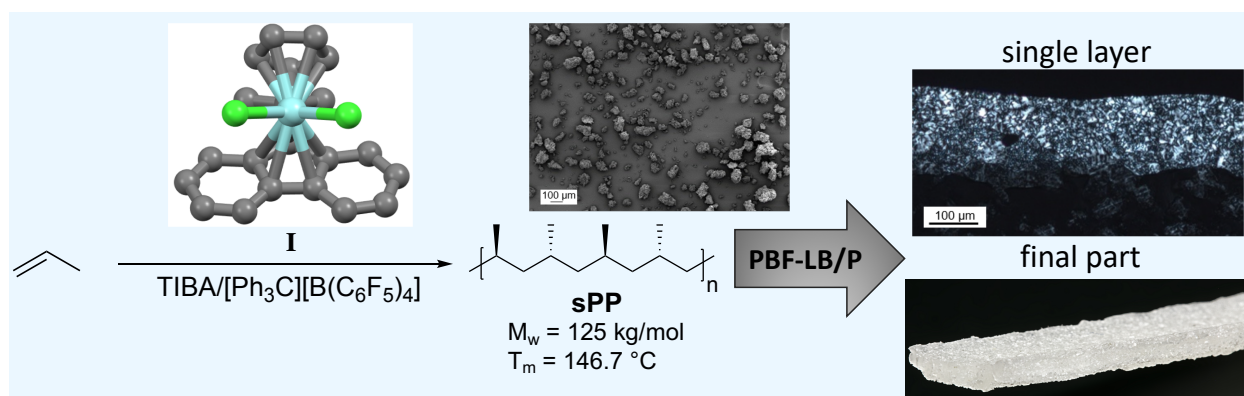
Figure 16: Graphical abstract (TOC) of the manuscript titled "Tailored Syndiotactic Polypropylene Feedstock Material for Laser-Based Powder Bed Fusion of Polymers: Material Development and Processability".

---

[1]† Simon Cholewa and Lucas Stieglitz contributed equally. S. Cholewa and L. Stieglitz provided the original idea, planned and performed all experiments and wrote the manuscript. A. Jaksch assisted polymer processing. All work was supervised by B. Rieger and D. Drummer.

7.3 Content

Additive manufacturing, especially PBF-LB/P, is gaining great interest in the field of polymer processing, as it enables a precise control over the final part and does not require any additional tools. Up to the present day, the benchmark, commercially available, polymer with a market share of roughly 90% is polyamide 12. Nevertheless, applications of commodity plastics, such as PP, are rarely to find in the literature. In this study we concentrated on sPP, since it has, compared to isotactic polypropylene, various advantages, such as a higher degree of entanglements and lower crystallite structures, causing a lower melting transition and a lower crystallization rate. With our deep knowledge in polyolefin chemistry, we are able to tune the macromolecular characteristics of the received polypropylene by a homogeneous polymerization of propylene with metallocene catalysts. In a previous study, we proved the potential of C_s-symmetric metallocenes to isolate designable sPP, yielding a molecular weight between $36 - 2500$ kg/mol and a syndiotacticity of up to 95%.[218] In this manuscript, we used a highly active literature known zirconocene dichloride catalyst $\left(ZrCl_2[Me_2C(\eta^5–Flu)(\eta^5–Cp)]\right)$ in conjunction with appropriate polymerization settings to yield highly syndiotactic polypropylene with a moderately high molecular weight. The polymer precipitated during the polymerization in a suitable particle size for the PBF and thus, the ability to obtain particles directly from synthesis without additional processing is one of the most promising features of this polymer.

Through multiple material process investigations, the key material properties for the process were determined, and the obtained material was analyzed in terms of melting and crystallization behavior. The findings showed that the thermal properties for the PBF process (e.g. process window) are better than existing systems. Furthermore, hot stage microscopy and viscosity studies demonstrated a sufficient coalescence under process conditions without any applied pressure. After processing experiments on an industrial machine, the production of multilayer components showed that the processability is given, and the assumption based on the material analyses was confirmed.

Tailored Syndiotactic Polypropylene Feedstock Material for Laser-Based Powder Bed Fusion of Polymers: Material Development and Processability

Simon Cholewa,[§] Lucas Stieglitz,[§] Andreas Jaksch, Bernhard Rieger,* and Dietmar Drummer*

Cite This: https://doi.org/10.1021/acsapm.2c02112

Read Online

| ACCESS | Metrics & More | Article Recommendations | Supporting Information |

ABSTRACT: Current research on laser-based powder bed fusion of polymers (PBF-LB/P) is heavily focused on the relationship between the process and component properties of existing commercially available powder materials, thus constraining the scope of application. An innovative approach is presented in this study, which first emphasizes the synthesis of a tailored polypropylene for PBF-LB/P, and subsequently the performance of the synthesized polymer in the process. Syndiotactic polypropylene (sPP) was chosen because of its advantageous properties, such as low crystallinity and crystallization kinetics compared to isotactic polypropylene. Therefore, a well-known, highly active zirconocene dichloride catalyst was used with appropriate polymerization settings to yield moderately high-molecular-weight sPP with high syndiotacticity. As the obtained product already precipitated directly from the synthesis in particle form, no further intermediate process step to the feedstock material for PBF-LB/P was required. The obtained polymer was analyzed in terms of molecular weight, polydispersity, and syndiotacticity. Furthermore, key properties of the PBF-LB/P process, such as thermal properties, melt viscosity, and powder flow behavior, were investigated. The initial PBF-LB/P processability was assessed by building single layers in a parameter study using an EOS P 396 machine. Based on these findings, a multilayer component was manufactured demonstrating the processability of the material system.

KEYWORDS: polypropylene, laser-based powder bed fusion of polymers, additive manufacturing, crystallization, melting transition
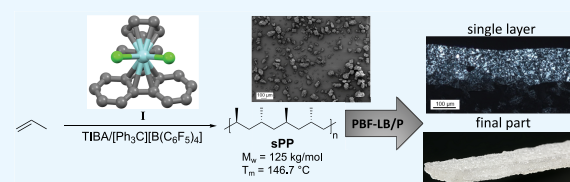
INTRODUCTION

Additive manufacturing (AM) is a collective term for a vast number of technologies that all share the same benefit: they build layer by layer directly from three-dimensional computer-aided design (3D CAD) models, and therefore do not require any shape-specific tools.[1] A fundamental difference between AM and conventional methods, such as injection molding or extrusion, is the independence of the number of units, and the degree of complexity with regard to cost-effectiveness.[2] Laser-based powder bed fusion of polymers (PBF-LB/P) is one of the most frequently used AM processes for the production of functional components thanks to its good mechanical properties.[1] In the first step of the process, the powder is spread with a roller or blade inside the building chamber. The chamber is preheated to a temperature close to the melting temperature of the semicrystalline polymer while being under an inert gas. The idealized theory of quasi-isothermal laser sintering signifies that the polymer melt and powder coexist during the building process.[3]

According to the Hoffmann–Lauritzen theory, the validity of the simplified quasi-isothermal model is limited to a specific time range.[4] This is because at temperatures below the equilibrium melting temperature (T_m^0), a transition from a liquid state to a solid state (crystallization) occurs.[5] Amado et al.'s[6] simulations of polyamide 12 (PA2200) explored the impact of temperature on material recoating. The results indicate that at a building temperature of 172 °C, a relative crystallization conversion of approximately 30% is achieved within 5 min during the building phase. Drummer et al.[7] confirmed the simulation results of Amado et al. experimentally using an in-house developed drop test for polyamide 12 (PA2200). The experiments showed that crystallization and thereby solidification of the material was already detected within the uppermost layers. Nevertheless, slow crystallization is beneficial for the process to take place.[8] Semicrystalline polymers allow these processes to take place for a certain timeframe and have a hysteresis between the melting and crystallization temperature. Once the powder reaches the building temperature, it is exposed by a focused laser via a galvanometer confocal scanning system. Due to the additional

A

Scheme 1. Synthesis Route of Catalyst I and sPP
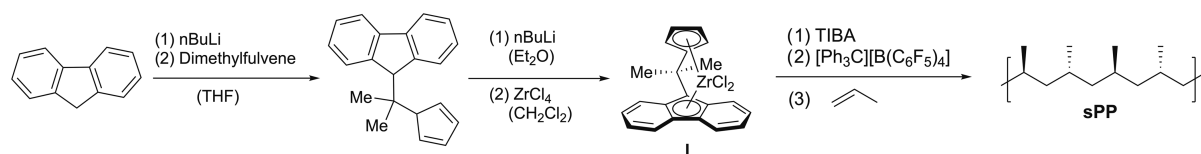
energy from the laser, the particles fuse together generating a homogeneous melt based on a sliced three-dimensional (3D) computer-aided design model. The coalescence is driven by surface tension and is counteracted by the viscosity of the melt.[9] The surrounding powder particles act as the supporting structure for the molten components in the building chamber. After exposure, the powder bed is lowered according to the adjusted layer thickness, typically set between 80 and 150 μm, and a new layer of powder is applied.[10] The steps of powder coating, energy input, and lowering the build platform are repeated until part completion. These process steps result in demanding requirements for the material that are not comparable to other manufacturing processes such as injection molding.[11] For the polymer in the PBF-LB/P process, two relationships are important: the interaction between the polymer and the process (process-suitable or not), and the interaction between the process and the final component properties.[11] The properties of the polymer are often classified into intrinsic and extrinsic powder properties.[11,12]

The intrinsic thermal and rheological properties among polymers significantly differ, whereas, e.g., the surface tension for unmodified polymers does not vary over magnitudes such as the zero-shear viscosity.[13] The thermal properties of the polymer are derived from the thermal process window—also known as the sintering window—which is typically characterized using dynamic differential scanning calorimetry (DSC) measurements and is defined as the temperature difference between the onset temperatures of melting and crystallization—and isothermal crystallization behavior. The thermal properties and the melt rheology of the polymer are what determine the melting and coalescence behavior of the molten polymer; this is important for producing dense parts with good inter and intralayer adhesion. Additional important thermal properties include, for example, thermal (linear expansion/contraction coefficient) and crystalline (phase transformation) shrinkage as well as heat capacity and thermal conduction.[14,15] Moreover, the intrinsic powder characteristics include their optical properties. The molecules are stimulated through CH_2 wagging for the CO_2 laser used.

Although intrinsic properties show a shift in optical properties at different degrees of crystallinity,[16] extrinsic properties such as shape, size, and thus the bulk density of the powder are accountable for the optical differences between polymers. Furthermore, powder properties are critical for creating a homogenous powder bed after powder application, which is essential for a homogeneous melt pool with low part porosity and subsequent acceptable mechanical qualities.[17]

The PBF-LB/P process in AM has benefits such as high modulus of elasticity and tensile strength, similar to injection molding.[18] However, its material options are limited to only a few polymers due to the conditions mentioned above.[12] Polyamides hold a dominant position in this regard; as a result, the fundamental hurdles for the PBF-LB/P process in terms of certifying new materials have remained relatively unchanged over the last two decades.[10,19,20] Nevertheless, further studies

have been published that have attempted to investigate new materials such as poly(butylene terephthalate) (PBT),[21] poly(phenylene sulfide) (PPS),[22] poly(ether ether ketone) (PEEK),[23] and others. However, this has made little difference to the dominant position of polyamides. Isotactic polypropylene (iPP), like polyethylene (PE), is a common commodity polymer because of its low cost, mechanical characteristics, and chemical resistance.[24] Because PP is often accessible as a homopolymer, several researchers have investigated homopolymers or composites of PP from injection molding for the use of PBF-LB/P, which is only processed to a limited extent with poor component quality.[25] This is explained as injection-molded polymers are not suitable for this unique PBF-LB/P method because they are not acclimated to the kinetics, low shear rates, and thermal treatment of this process. In addition, most PBF-LB/P research focuses on the impact that process factors have on the mechanical performance of commercially available PBF-LB/P polymers, particularly polyamides.[11]

This work takes an alternative approach to the problem, aiming to synthesize a material that has all of the necessary qualities for the process. Syndiotactic PP (sPP) is almost exclusively of scientific interest since the melting temperature and crystallinity caused by a lower crystal thickness are low in comparison with isotactic polypropylene for polymers with the same stereoregularity and molecular weight.[26,27] However, both properties are advantageous for the process, and additionally, the crystallization rate is lower.[28] Studies from the fused filament fabrication show that warpage can be reduced by lowering the degree of crystallization by blending amorphous PP.[29] A further anticipated advantage of sPP on mechanical properties results from the increased entanglements of the amorphous phases, whereby better toughness, ductility, and elasticity are expected.[30,31] The presence of complex polymorphism in sPP must be noted. Extensive studies have documented the presence of four distinct structures, which can arise due to a combination of temperature history and mechanical stress.[32] It has been demonstrated through research that crystallization perfection is the primary determinant at the relevant temperature ranges.[33] There are several PP systems on the market, but compared to PA12, they have the disadvantage that requires an additional processing step to transform them into a powder form that can be used as a starting material.

sPP is produced employing Cs-symmetric single-site metallocene dichlorides in both academic and industrial settings.[34] Since Ewen's first isolation of sPP in 1988 with fluorenyl-cyclopentadienyl bridged metallocene dichlorides, fundamental motifs of this catalyst system were modified in the last three decades with various structural parameters, such as the bridging motif,[35] the bridging atom,[36] or a modification of fluorene,[37] to tune the properties of the resulting sPP—leading to different molecular weights and melting temperatures of the polymer.[38]

In this study, the synthesis and the PBF/LB-P processability were investigated. The desired sPP was synthesized with the

aid of a literature-known isopropylidene-bridged zirconocene dichloride **I** ($ZrCl_2[Me_2C(\eta^5\text{-}Flu)(\eta^5\text{-}Cp)]$) at 0 °C, and a pressure of 6 bar of propylene, which exhibited a high productivity (up to 50,000 $kg_{PP}\cdot(mol_{cat}\cdot h)^{-1}$), a high stereo-regularity ([rrrr] of 95%), and a moderate molecular weight of the sPP. Furthermore, the resulting powder was analyzed by the powder size and flowability, thermal behavior and crystallization kinetics, and rheological melt behavior and coalescence. The suitable PBF/LB-P process parameters were determined through single-layer experiments and were used to manufacture a multilayer component.

■ RESULTS AND DISCUSSION

Polymer Synthesis and Characterization. Zirconocene **I** was previously proven to feature several advantages, if suitable polymerization conditions were applied: high productivity, a wide processing window with a peak melting temperature T_m of 145.2 °C, and a suitable particle size with no need for further processing.[39] However, these properties were only obtained for a medium-high molecular weight of 140 $kg\cdot mol^{-1}$—nevertheless, the molecular weight may be beneficial for the anticipated enhanced mechanical properties by entanglement formation.[39] Zirconocene **I** was isolated in a two-step synthesis starting with fluorene as the basic moiety of
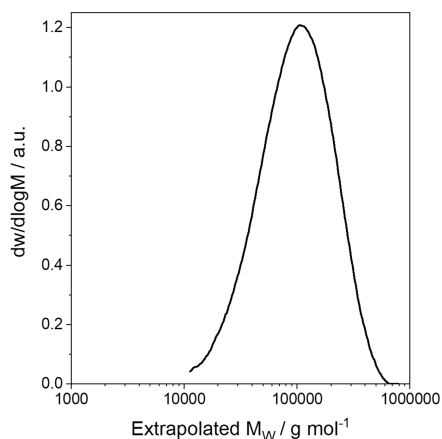
the catalyst system (see Scheme 1). However, prior to polymerization, zirconocene **I** required activation to form the catalytic active cationic species. As seen in the literature, methylaluminoxane (MAO) is the most commonly used activation agent.[40] Rieger's group established the *in situ* activation, which has for hafnocenes and also for zirconocenes, two major advantages compared to the classic MAO activation: a higher molecular weight of the received polymer and increased productivity of the catalysts. Consequently, better macromolecular characteristics and a higher yield of the polymer with the same amount of catalyst are accessible, being advantageous in any industrial process.[41] This activation first includes a preactivation using triisobutylaluminum (TIBA) as an alkylating reagent at 60 °C for one hour. TIBA not only acts as an alkylating agent but also additionally protects the highly sensitive cationic species as a scavenger from oxygen or water, as both destroy the catalyst irreparably. The catalytically active cationic species is formed by adding $[Ph_3C][B(C_6F_5)_4]$ (TrBCF) to the preactivated complex.

In a total of three polymerizations with identical polymerization conditions, almost 100 g of sPP was isolated and mixed together. HT-GPC measurements (160 °C, 1,2,4-trichlorobenzene as solvent) of the combined sPP revealed a molecular weight M_w of 125 $kg\cdot mol^{-1}$ and a narrow polydispersity ($Đ = 1.8$, see Figure 1). Nevertheless, the molecular weight differs slightly from literature-known data, possibly caused by a different polymerization setup and autoclave system.

As expected, zirconocene **I** with its C_s-symmetric scaffold yielded highly syndiotactic polypropylene. The produced sPP showed a small degree of misinsertions ([rrrr] = 95%, see Figure S2) mainly caused by back-skip processes ([rrrm], 20.2 ppm).

Powder Shape and Particle Size Distribution. A significant benefit of the produced sPP stems from the high activity of the catalyst, leading to a high yield per amount of the catalyst. On the other hand, the polymer is precipitated in a suitable particle size and conformation for the PBF/LB-P directly from the synthesis (Figures 2 and S1 and S2). Characteristic SEM images of the sPP particles from the synthesis without further processing like grinding are shown in Figure 2. The particles exhibit an elongated shape. An even higher magnification of 2000 revealed agglomerates of smaller particles. The particle size distributions of the manufactured sPP powders are depicted as the numeric weighted cumulative sum distribution $Q_0(x)$ and the numeric density distribution weighted numeric $q_0(x)$ in Figure 3. The particle size

Figure 1. Logarithmic molecular weight distribution obtained by HT-GPC. Extrapolated molecular weight after absolute determination of sPP (M_w = 125 $kg\cdot mol^{-1}$, $Đ$ = 1.8, see Table 1 for details) using dn/dc = 0.097 $mL\cdot g^{-1}$.
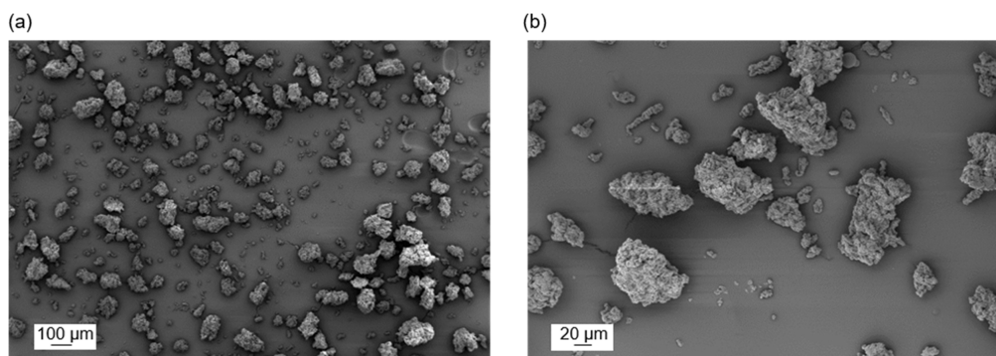
Figure 2. SEM images of homogeneously synthesized syndiotactic polypropylene with magnification (a) 500 and (b) 2000.

pubs.org/acsapm

Article
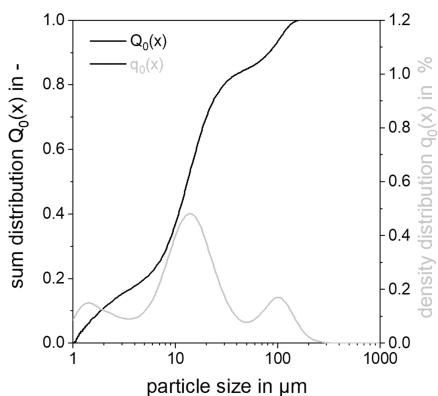
Figure 3. Numeric weighted sum distribution of the homogeneously synthesized powder (left) and numeric density distribution (right).

Figure 4. Rise of normal force during a constant compression rate of sPP and dry-coated sPP.

distributions illustrate that the samples exhibit broad distributions with a high numeric share with the finest particle being 10 μm or smaller. The D50 is 126 μm. According to existing research, the optimal range for D50 particle size is between 40 and 90 μm.[10] However, the processing of the layer thickness of up to 120 μm was observed to be feasible. Scanning electron microscopy (SEM) images of the powder exhibit the clustering of small particles. As a result, refinement of the synthesis procedure holds the potential for achieving smaller D50 values in the future. Improved polymerization conditions, such as variable agitator to avoid clustering effects or optimized stirring speed, may set the desired particle size.[21] In addition, further sieving of the particles could achieve the desired fraction.

Powder Characteristics. The compression depth described by Hesse et al.[42] is a well-repeatable characteristic value determining the static powder properties statically.

In a preliminary test, the powder flowability of the pure material without a flow aid was investigated. By adding 0.1 wt % to each of the pyrogenic alumina and silica by dry coating, the compression depth was significantly improved. The known additives in PBF/LB-P act as distance-increasing agents to lessen the adhesions between the particles. In addition, the pyrogenic alumina serves to prevent electromagnetic charge, which causes insufficient powder application.

In Figure 4, the normal force that builds up during uniaxial loading in the powder bed is shown for the pure sPP and the sPP with flow additives. The relative change in height is given by the depth of the indenter pushing at a constant compression rate of 1 μm·s^{-1} into a powder bed that has been loosely consolidated with a normal force of 0.2 N. The change in height for the unadded sPP yielded slightly increased normal forces, whereas higher forces are necessary for sPP with additives for the same height changes. This happens because the powder combined with flow additives has a larger powder bulk density than the pure powder; therefore, more normal force is necessary to reach the same change. The values reached here are comparable to the reused PA12 powder (to achieve a height change of 100 μm, a force of $\approx$1.5 N is required for the dry blended sPP, while the reused PA12 has $\approx$1.6 N after three cycles).[42] In addition, the optical properties also changed by the higher powder density and by the properties of the additives. Since the incorporation of additives influences the flow behavior of powders resulting in a higher
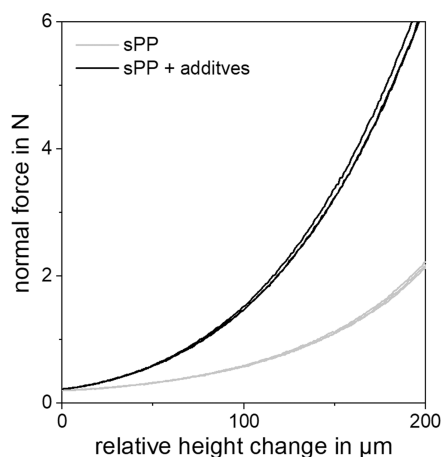
powder bed packing density, a decrease in optical penetration depth due to multiple reflections is possible.[43] At the same time, the presence of the additives acting as scattering centers also contributes to a reduction in the optical penetration depth.[44]

Thermal Analysis. The thermal behavior of a polymer is a key determinant for the process parameters and the process suitability overall. The dynamic thermogram (which describes the first heating and cooling cycle) and isothermal crystallization periods of the sPP powder are depicted in Figure 5. For a heating and cooling rate of 10 K·min^{-1}, respectively, the dynamic measurement revealed a melting peak at 146.7 °C, and a crystallization of roughly 100 °C. During the layered component generation, the quasi-isothermal process must be present between the melting and crystallization temperatures, and throughout this temperature range, the exposed melt and surrounding solid powder coexist. To enable a sufficient process window, the polymer's crystallization temperature must be significantly lower than its melting temperature, which is the specific difference between the onset temperatures of crystallization and melting. Polymers with a wide process window are preferred, as they are less susceptible to temperature variation in the process, and exhibit increased process robustness.[45] The thermal process windows, ΔT_s, were calculated by the difference of the melting and crystallization onset temperatures, $T_{m,on}$ and $T_{c,on}$, and were found to be 25 K for the powder. Thus, a hysteresis is achieved that is significantly greater than existing systems on the market (Figure 5 right). While commercially available PA12 exhibits a slightly larger window at 27.2 K, successful PBF/LB-P processing is reported with process windows as small as 2.2 K for random copolymers.[46] Additionally, the degree of crystallinity was calculated with a crystalline sPP phase of ΔH_f = 199.6 J·g^{-1}.[47] The degree of crystallinity is approximately 37% based on a total melting enthalpy of 73.4 J·g^{-1}. Crystallization half-times, $t_{1/2}$, of up to more than 40 min were seen in the isothermal measurements carried out at temperatures within the "process window" (Figure 5 a). The crystallization half-times for sPP show a significant enhancement, especially in direct comparison to PP1101. Here, observations for the same melt undercooling (in relation to T_m) indicate that PP1101 undergoes crystallization prior to
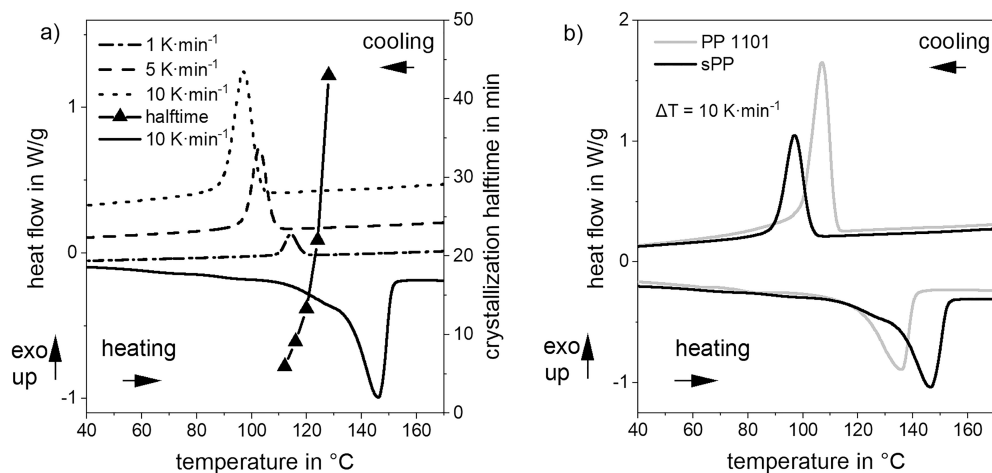
Figure 5. (a) Plot of dynamic DSC measurements and their corresponding melting and crystallization heat flow (left axis). Crystallization half-times for isothermal measurements (right axis). (b) Comparison of the process window between sPP and commercial powder PP1101 with a heating and cooling rate of 10 K·min^{-1}.
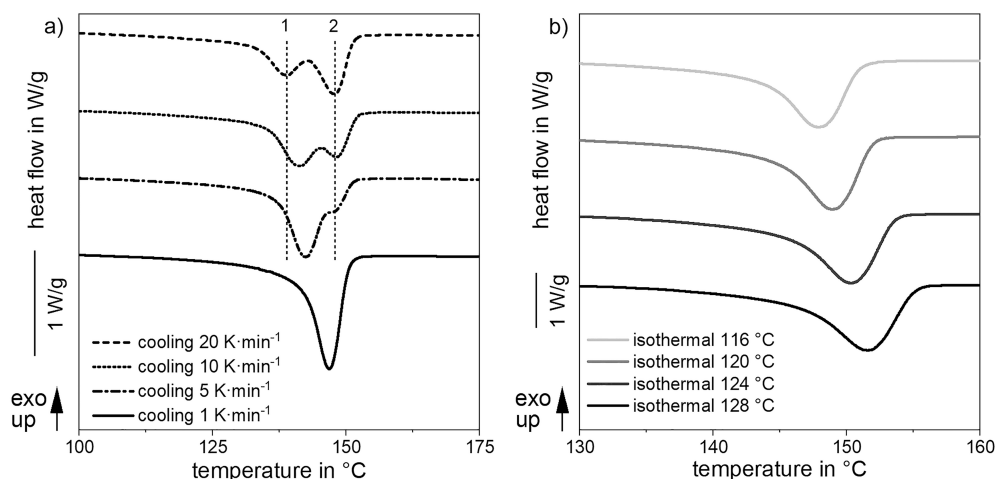
Figure 6. Melting endotherms of sPP recorded (a) at a heating rate of 10 K·min^{-1} after dynamic cooling at indicated rates of 1−20 K·min^{-1} and (b) after isothermal crystallization for shown temperatures.

achieving the designated holding temperature, whereas sPP displays a significantly slower crystallization progress for the same melt undercooling. The exhibiting crystallization progress (as measured by t peak) for sPP as 56.2 vs 3.1 min for PP101 is determined (Figure S4).

Figure 6 illustrates a series of second melt thermograms (10 K·min^{-1}) for the sPP samples after different dynamic cooling rates were performed, and their associated crystallization from the melt was determined. The characteristic double peak for the second heating (141.3 and 148.3 °C with a dynamic heating rate of 10 K·min^{-1}), which shifts depending on earlier cooling rates, is noteworthy when compared to the first heating (Figure 5). The first peak increases initially due to a reduction in the rate of cooling that occurs beforehand, while the second peak decreases and vanishes at a cooling rate of 1 K·min^{-1}, leaving only one peak at the temperature of 146.7 °C. This is traced back to the melting of the crystallized crystallites formed during the heating scan.[33] Since less stable primary crystals

form at higher cooling rates, the subsequent heating resulted in an increased formation of the second peak. Simultaneously, the melting temperature of the first peak shifts to higher temperatures.

Upon inspection, it was determined that there is just one melting peak following isothermal crystallization (Figure 6). The graphs also depict a perfect crystal process, where the melting peak shifts from 147.9 to 151.6 °C for isothermal temperatures of 116 and 128 °C, respectively.[48] Since the process has very weak cooling rates and is classified as quasi-isothermal, it is important to consider slow cooling rates and isothermal measurements.[49] Therefore, the component produced in the process exhibits crystallization at these temperatures. Concurrently, with increasing isothermal holding temperatures, the melting onset shifts to higher temperatures.

A direct transfer of the results of these measurements to an enlargement of the process window is not possible, as the measurements involve crystallization from the melt. To

E

simulate elevated temperature conditions or to investigate the potential for annealing the powder, measurements were conducted at a temperature of 128 °C for a duration of 2 h (see Figure S6). However, the results determined that the onset and T_m are almost identical. A significant difference is found in the width of the melting range, where a clearly sharp transition is seen for the annealed sPP compared to the first heating.

Melt Rheology. Alongside the thermal properties, the flow behavior of the melt is a vitally significant intrinsic property. The coalescence process and the development of a uniform melt pool of the powder particles after exposure is described by the Pokluda model, where the decisive factor for polymers is the viscosity η.[50] The rheological behavior of the powder for different temperatures is shown in Figure 7. The process-
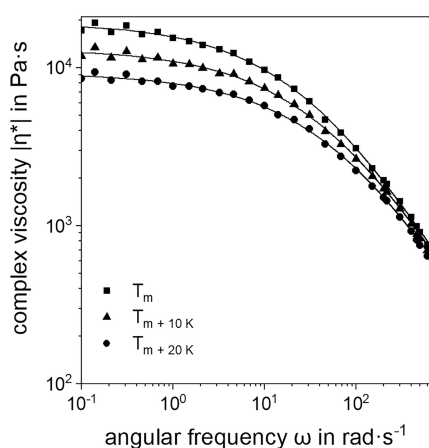
Figure 7. Viscosity as a function of angular velocity in oscillation, measured from low to high angular rates at different temperatures.

relevant area is the plateau for low angular frequencies, as the process takes place under atmospheric pressure. The complex viscosity η^* is used to characterize the flow behavior, as simple polymers are known to obey the Cox-Merz rule. The zero-shear viscosity according to the Carreau model for T_m, T_{m+10K}, and T_{m+20K} are 19,142, 13,099, and 9196 Pa·s, respectively. In direct comparison to the unrefreshed PA12 powders described in studies, the zero-shear viscosities appear high.[51] However, the Dadbakhsh et al.[52] study found that aged and mixed PA2200 powder (with an increased viscosity) result in lower mechanical values but still produced uniform layers with the adopted exposing strategy. Furthermore Verbelen et al.[13] showed that the commercial PA12 Orgasol (no postcondensating) at T_{m+20K} roughly has 8000 Pa·s. In general, components

with higher viscosities than virgin PA12 powder can be processed with PBF-LB/P.

The sPP viscosity values are between the commercial PP values for comparable process-relevant temperatures (zero-shear viscosity of 237 Pa·s for iPP and 14,813 Pa·s for coPP at T_{m+25K}).[22] Therefore, it is expected that the viscosity is a range where dense parts with low porosities are fabricated. For sPP, the seemingly high viscosity for such a molecular weight compared to iPP is characteristic of that molecular structure.[53]

Hot-Stage Microscopy. In Figure 8, the melting as well as the coalescence behavior of the particles is qualitatively shown using hot-stage measurements with a heating rate of 10 K·min⁻¹ up to 180 °C. During the heating process, the melting of the particles is detectable at a temperature of ~147 °C, in agreement with the thermal measurements. To alleviate the well-known thermal time lag in hot-stage microscopy, the same procedure is performed at a heating rate of 1 K·min⁻¹, and the results confirm the findings for the measurements conducted at 10 K·min⁻¹ (Figure S8).[54] After coalescence completion, a homogeneous melt pool was built at a temperature of 160 °C. Apart from the bright field, the investigation was carried out in polarized light where no birefringence indicative of a solid phase was detected in the melt (Figure S9).

PBF/LB-P Processing. The synthesized polypropylene was processed with an industrial EOS P396 machine system. To allow the processing of a small amount of powder, a modified building chamber with a size of 20 mm × 100 mm was used for processing a multilayer part of 180 mm × 10 mm × 1.5 mm. Before processing, single-layer experiments were conducted to determine the processing parameters.

Based on the DSC measurements and the evaluation of the powder bed after application, the building chamber temperature for the material was set to 128 °C due to the powder bed surface quality and caking. When considering a powder as the feedstock material, flowability at room temperature does not guarantee good spreadability as the temperature is evaluated. Nevertheless, these measurements are useful at room temperature since they are considered a criterion for exclusion at this point. The thickness was examined during single-layer processing to determine the influence of the various process parameters. At low energy densities, the energy was not sufficient to produce stable layers that remained unbroken during removal. As the laser power rose after passing the threshold of 0.01 J·mm⁻², the single-layer thickness also grew. As a result, the highest thickness was achieved with the highest energy density. The single-layer samples were characterized using optical microscopy to determine the component's qualities more precisely. The single layer printed with an energy density of 0.02 J·mm⁻² is depicted in Figure 9a. The increased single-layer thickness is well known and derives from a deeper heat penetration into the powder bed and melting of
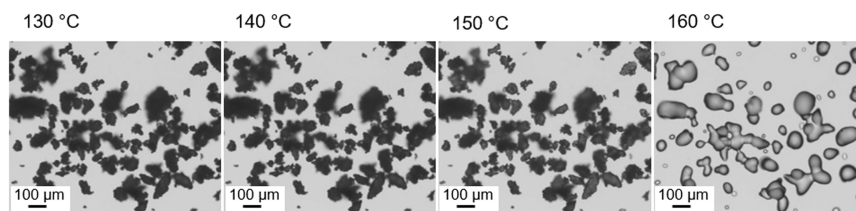
Figure 8. Powder particle coalescence detected by hot-stage microscopy with a constant heating rate of 10 K·min⁻¹.
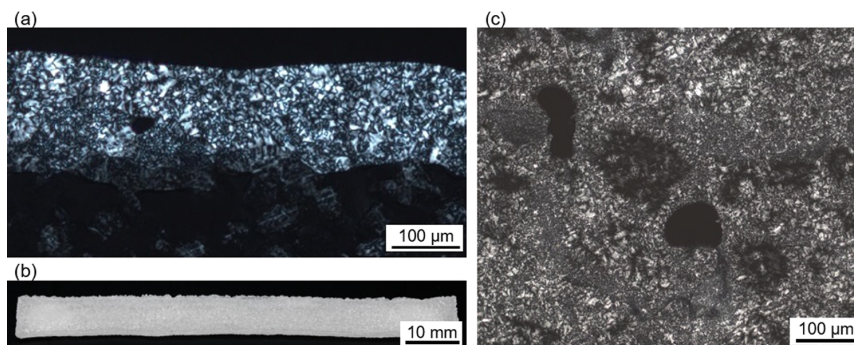
Figure 9. Processing results: (a) single layer for an energy density of 0.02 J·mm^{-2} visualized via transmitted polarized light microscopy (cut in z plane); (b) top view of the multilayer component; and (c) cross-section of the multilayer component cut in the z plane.

beneath particles. The component displays good densification and is free of unmelted particles within the layer.

Based on these findings, a multilayer component was manufactured, and a reliable statement on the processability of the material was understood. A rectangle sized 80 mm × 10 mm × 1.5 mm was fabricated for this purpose. During and after exposure, no curling on the sample was observed. Additionally, no burns or decompensation were visible on any produced part. This is shown in Figures 9b and S10. To exclude further faults that could arise through the process with repeated application and exposure, the component was again visually assessed. The component displayed good densification with typical porosity and was free of unmelted particles (Figure 9c). The presence of porosity is a common characteristic of the process. Even with the utilization of optimized material (PA12) and optimized process parameters, porosities of up to 5% are typically present.[55] Additionally, the largest pores can reach sizes of hundreds of microns.[56] The spherical shape of the pore can be interpreted as too high a thermal load.[57] Alternatively, the elongated pore shape may indicate incomplete coalescence or insufficient powder application. Despite these observations, the results from the cross-section analysis were considered promising as the process optimization was not fully implemented for this material, and the powder flowability and size did not match those of commercially available systems.

CONCLUSIONS

A process chain to produce micron-sized sPP polymer particles was successfully applied to produce an innovative feedstock material for PBF-LB/P. By vertically integrating the polymer chemistry and material characterization and processing, an sPP tailor made to the process requirements was created. The polymer was first synthesized using a highly active literature-known zirconocene catalyst **I** combined with suitable polymerization conditions, resulting in syndiotactic polypropylene with the desired macromolecular characteristics. The polymer was analyzed by GPC and NMR to reveal a molecular weight of 125 kg·mol^{-1}, a narrow polydispersity of Đ = 1.8, and a syndiotacticity of 95%, leading to a melting transition of 146.7 °C. The polymer precipitated directly from the synthesis in a suitable shape for the PBF-LB/P. The ability to obtain particles directly from synthesis without additional processing is one of the most promising features of this method. Dry-coating could increase the flowability of these particles, and in terms of the process window, crystallization enthalpy, and crystallization

kinetics, the material's thermal properties are better than existing commercial polypropylene systems on the market (Figures 6b and S4).[45] Investigations into viscosity and hot-stage microscopy demonstrated that particle coalescence is process-suitable. The initial process parameter studies on single layers, and particularly the multilayer part performance herein, showed highly promising results. The creation of smaller particles by improved polymerization conditions, specimens for mechanical testing, and a comprehensive processing investigation will all be addressed in the future. Thus, the range of materials is expanded for the process in the long term, and at the same time, a further production step, as is currently necessary for PP to achieve particle form, is saved.

■ EXPERIMENTAL SECTION

General. Catalyst **I** was isolated following a known literature procedure.[19] Toluene was dried using an *MBraun* SPS-800 solvent purification system and stored over 4 Å molecular sieves. Propylene (99.5% by Westfalen AG) was purified by passage through two columns filled with BASF catalyst (R3-11) and 3−4 Å molecular sieves.

Bromobenzene-d_5 was obtained from Sigma-Aldrich. Polymer spectra were measured with an ARX-300 spectrometer at 140 °C in bromobenzene-d_5 with 60 mg·mL^{-1} and 6k scans. The degree of tacticity was determined via the integration of the corresponding [rrrr]-pentade (20.3 ppm, for sPP)[31] against the region of 19.5−22.0 ppm.

Gel permeation chromatography (GPC) was performed with a PL-GPC 220 instrument equipped with 2x Olexis 300 mm × 7.5 mm columns and triple detection via a differential refractive index detector, PL-BV 400 HT viscometer, and light scattering (Precision Detector model 2040, 15 and 90°). Measurements were performed at 160 °C using HPLC-grade 1,2,4-trichlorobenzene (TCB; 100 mg·L^{-1} BHT) from Sigma-Aldrich with a constant flow rate of 1 mL·min^{-1} and a calibration set with narrow MWD polyethylene (PE) and polystyrene (PS) standards for detector calibration. Samples were prepared by dissolving 0.5−0.7 mg of polymer in 1.0 mL of stabilized TCB for 1 h at 140 °C immediately before each measurement. The molecular mass was determined absolutely by using dn/dc = 0.097 mL·g^{-1}.[32]

Polymerization. All polymerization reactions were performed in a 1.1 L double-wall Büchi steel autoclave equipped with a paddle agitator (800 rpm), an external temperature sensor, and a heating/cooling jacket attached to a cryo-/thermostat (Thermo Scientific HAAKE DynaMax). Ar (argon) pressure for all manipulations was set at 1.3 bar. Prior to polymerization, the autoclave was charged with 300 mL of dry toluene and 2.0 mL of 1.1 M TIBA in toluene and heated up to 90 °C. After maintaining the temperature for at least 30 min, the scrubbing solution was released. For the polymerization, the

G

autoclave was charged with 300 mL of dry toluene and 2 mL of 1.1 M TIBA in toluene. The metallocene complex (1.0 equiv) was dissolved in 10 mL of dry toluene and preactivated with 200 eq. of TIBA at 60 °C for 1 h. After the desired temperature was adjusted, the metallocene solution was transferred into the autoclave and pressurized with propylene. When the system was equilibrated and stable in terms of temperature and pressure, the polymerization was initiated by adding 5.0 equiv of $[Ph_3C][B(C_6F_5)_4]$ (TrBCF) dissolved in 10 mL of dry toluene to the autoclave via a pressure burette (p_{poly} + 0.5 bar). The polymerization was quenched with 2.0 mL of methanol, and the reaction mixture was poured into 600 mL of HCl (2 mL) acidified methanol. The precipitated polymer was removed from the autoclave, and all combined polymer was washed thoroughly, first with methanol and then with acetone. The resulting polymer was suspended in acetone and treated with *Irganox 1010* as a stabilizing agent to prevent rapid destruction of the polymer. After 20 min, the supernatant solution was decanted off, and the resulting polymer was dried overnight at 70 °C.

For the comparison of thermal properties, the commercially available polypropylene from EOS, PP1101 was used.

Material Investigations. The powders were observed by SEM to characterize the particle shape. The SEM images of the gold-sputtered powders were recorded using an Ultra Plus, Carl Zeiss, at a magnification of 500 and 2000 and an acceleration voltage of 5 kV.

Powder flowability investigations were performed on a Discovery HR-2 rheometer (TA Instruments). The setup consists of an upper 25 mm plate parallel to a container with an inner diameter of 27 mm. The powder was sieved loose and unpacked into the container. To establish a defined baseline, which results in better comparability, a normal force of 0.2 N was applied to the bulk powder. Afterward, the upper parallel plate was moved with a constant compression rate of 1 $\mu m \cdot s^{-1}$ into the powder bed, and the normal force was observed. The experiments were conducted at room temperature (22 °C).

The particle size distribution of the powder was measured using a Morphologi G3, Malvern. A quantity of 20,000 particles was used for the measurement. The particles are dispersed dry and measured optically.

Differential scanning calorimetry (DSC) analysis was conducted on a Discovery DSC 2500 (TA Instruments). The polymer (2−5 mg) was sealed into a DSC aluminum pan and heated from −20 to 180 °C at 10 $K \cdot min^{-1}$. After holding the temperature for 5 min, the sample was cooled down to 0 °C at 10, 5, and 1 $K \cdot min^{-1}$, and heated up again in the same manner. The reported values for the process window were determined in the first heating cycle, while the impact of different cooling rates was determined in the second heating cycle. The melting enthalpy was determined by integrating the endothermic peak at the initial heating rate of 10 $K \cdot min^{-1}$.

For the isothermal measurements, the same heating procedure was used, and afterward, the samples were cooled down with a cooling rate of 60 $K \cdot min^{-1}$ to the isothermal holding temperatures. The crystallization progress was analyzed via the crystallization half-time, which is the time after 50% of the crystallization was completed. To evaluate the crystal properties in dependence of the holding temperature, the samples were heated up with a heating rate of 10 $K \cdot min^{-1}$. Annealing experiments were evaluated with a heating rate of 10 $K \cdot min^{-1}$ after holding at a temperature of 128 °C for a duration of 2 h.

To understand the viscosity and the coalescence of the powders during the process, the zero-shear viscosity was determined by means of frequency sweeps in oscillation mode using the Carreau model at three different temperatures (T_m, T_{m+10K}, and T_{m+20K}). The measurements were carried out on a rational rheometer (HAAKE Mars 60) equipped with a 25 mm diameter and a deformation of 0.1%. For quick and good thermal settings, the rheometer is equipped with a heated upper plate. All measurements were conducted in the linear viscoelastic range determined by amplitude sweeps.

Hot microscopic observations for the sintering of polymer particles were performed using a Linkam FTIR600 heating and freezing microscope stages controlled with central processor Linksys 32 software. A glass plate was used as the substrate for the sintering

particles. The samples were heated with a constant heating rate of 10 and 1 $K \cdot min^{-1}$. For melting and coalescence investigations, the brightfield setting is used. Measurements for full melting of the particles were conducted with polarized light.

Parameter studies by means of single layers and the multilayer part were conducted on a P 396 (EOS) powder bed fusion machine. The system is equipped with a CO_2 laser (wavelength 10.6 μm) with a laser power of 70 Watts. The machine has a blade for powder application. For single-layer experiments, the powder was spread manually in crucibles and then exposed by 20 mm × 20 mm quarters with different process parameters. Manual spreading was conducted following the standard for "Standard Shear Test Method for Bulk Solids (ASTM D6773−02)." Additionally, the powder was sieved loose and unpacked into the container to ensure comparability. The laser power was changed, while the hatch distance, scan speed, and building temperature of 128 °C were kept constant. For all experiments, the hatch distance and scan speed were held constant at 0.2 mm and 2000 $mm \cdot s^{-1}$, while the laser power was changed (1, 2, 4, 8, 12, 16 W); therefore, an energy density range starting at 0.0025− 0.04 $J \cdot mm^{-2}$ was covered. The single-layer thickness was measured with a dial gauge dependent on the applied surface energy density. After defining the accurate process parameter, a self-constructed powder bed inlet with 100 mm × 20 mm was used to manufacture a rectangle with 80 mm × 10 mm × 1.5 mm due to the powder limitations. Here, the Meander hatching exposure strategy was used.

parameters	
laser power in W	1, 2, 4, 8, 12, 16
hatch distance in mm	0.2
scan speed in mm s^{-1}	2000
layer thickness in mm	0.12
building bed temperature in °C	128

Further microscopic investigations of the single layers, as well as the component, were conducted with thin cuts under polarized light using the Axiocam 305 (Zeiss). The specimen was embedded in cold-curing epoxy resin and then cut to 10 μm thickness with a Polycut E.

■ ASSOCIATED CONTENT

ⓢ Supporting Information

The Supporting Information is available free of charge at https://pubs.acs.org/doi/10.1021/acsapm.2c02112.

Additional polymerization information; ^{13}C NMR polymer spectrum; polymer directly after synthesis and before processing; additional thermal analysis; further microscopy investigations; and the lateral view of the final part (PDF)

■ AUTHOR INFORMATION

Corresponding Authors

Bernhard Rieger − *Wacker-Lehrstuhl für Makromolekulare Chemie, Catalysis Research Center, Technische Universität München, 85748 Garching bei München, Germany;* ⓘ orcid.org/0000-0002-0023-884X; Phone: +49-89-289-13570; Email: rieger@tum.de; Fax: +49-89-289-13562

Dietmar Drummer − *Institute of Polymer Technology, Friedrich-Alexander-Universität Erlangen-Nürnberg, 91058 Erlangen-Tennenlohe, Germany;* Phone: +49-9131-85-71001; Email: dietmar.drummer@fau.de; Fax: +49-9131-85-71007

Authors

Simon Cholewa − *Institute of Polymer Technology, Friedrich-Alexander-Universität Erlangen-Nürnberg, 91058 Erlangen-Tennenlohe, Germany*

Lucas Stieglitz − *Wacker-Lehrstuhl für Makromolekulare Chemie, Catalysis Research Center, Technische Universität München, 85748 Garching bei München, Germany*

Andreas Jaksch − *Institute of Polymer Technology, Friedrich-Alexander-Universität Erlangen-Nürnberg, 91058 Erlangen-Tennenlohe, Germany*

Complete contact information is available at:
https://pubs.acs.org/10.1021/acsapm.2c02112

Author Contributions

■ **REFERENCES**

(1) Schmid, M. *Laser Sintering with Plastics*; Carl Hanser Verlag: München, 2018; Vol. *1*, p 8.

(2) Ligon, S. C.; Liska, R.; Stampfl, J.; Gurr, M.; Mulhaupt, R. Polymers for 3D Printing and Customized Additive Manufacturing. *Chem. Rev.* **2017**, *117*, 10212−10290.

(3) Schmachtenberg, E.; Seul, T. In *Model of Isothermic Laser-Sintering*, Proceedings of the 60th Anual Technical Conference of the Society of Plastic Engineers (ANTEC): San Francisco, CA, USA, 2002; pp 5−9.

(4) Vyazovkin, S.; Sbirrazzuoli, N. Isoconversional Approach to Evaluating the Hoffman−Lauritzen Parameters(U* andKg) from the Overall Rates of Nonisothermal Crystallization. *Macromol. Rapid Commun.* **2004**, *25*, 733−738.

(5) Hoffman, J. D.; Weeks, J. J. Melting Process and the Equilibrium Melting Temperature of Polychlorotrifluoroethylene. *J. Res. Natl. Bur. Stand., Sect. A* **1962**, *66A*, 13−28.

(6) Amado, A.; Wegener, K. L. G.; Schmid, M. In *Characterization and modeling of non-isothermal crystallization of Polyamide 12 and co-Polypropylene during the SLS process*, 5th International Polymers & Moulds Innovations Conference (PMI), 2012; pp 207−216.

(7) Drummer, D.; Greiner, S.; Zhao, M.; Wudy, K. A novel approach for understanding laser sintering of polymers. *Addit. Manuf.* **2019**, *27*, 379−388.

(8) Benedetti, L.; Brulé, B.; Decraemer, N.; Evans, K. E.; Ghita, O. Evolution of PEKK crystallization measured in laser sintering. *Front. Manuf. Technol.* **2022**, *2*, No. 964450.

(9) Vasquez, M.; Hopkinsons, N.; Haworth, B. In *Laser Sintering Process: Practical Verification of Particle Coalescence for Polyamides and Thermoplastic Elastomers*, Annual Technical Conference - ANTEC, Conference Proceedings: Boston, 2011; pp pp 2458−2462.

(10) Goodridge, R. D.; Tuck, C. J.; Hague, R. J. M. Laser sintering of polyamides and other polymers. *Prog. Mater. Sci.* **2012**, *57*, 229−267.

(11) Chatham, C. A.; Long, T. E.; Williams, C. B. A review of the process physics and material screening methods for polymer powder bed fusion additive manufacturing. *Prog. Polym. Sci.* **2019**, *93*, 68−95.

(12) Schmid, M.; Amado, A.; Wegener, K. In *Polymer Powders for Selective Laser Sintering (SLS)*, AIP Conference Proceedings 1664; AIP Publishing LLC, 2015; p 160009.

(13) Verbelen, L.; Dadbakhsh, S.; Van den Eynde, M.; Kruth, J.-P.; Goderis, B.; Van Puyvelde, P. Characterization of polyamide powders for determination of laser sintering processability. *Eur. Polym. J.* **2016**, *75*, 163−174.

(14) Verbelen, L.; Van Humbeeck, J.; Van Puyvelde, P. Development of a method for pressure-free volumetric dilatometry of polymer melts and solids. *Polym Test* **2018**, *69*, 219−224.

(15) Benedetti, L.; Brulé, B.; Decreamer, N.; Evans, K. E.; Ghita, O. Shrinkage behaviour of semi-crystalline polymers in laser sintering: PEKK and PA12. *Mater. Des.* **2019**, *181*, No. 107906.

(16) Schuffenhauer, T.; Stichel, T.; Schmidt, M. Experimental determination of scattering processes in the interaction of laser radiation with polyamide 12 powder. *Procedia CIRP* **2020**, *94*, 85−88.

(17) Van den Eynde, M.; Verbelen, L.; Van Puyvelde, P. In *Influence of Temperature on the Flowability of Polymer Powders in Laser Sintering*, AIP Conf. Proc.; AIP Publishing LLC, 2017; Vol. *1914*, p 190007.

(18) Wörz, A.; Wudy, K.; Drummer, D.; Wegner, A.; Witt, G. Comparison of long-term properties of laser sintered and injection molded polyamide 12 parts. *J. Polym. Eng.* **2018**, *38*, 573−582.

(19) Associates, W.. Wohlers Report. 2009, p 250.

(20) Associates, W.. Wohlers Report. 2022, p 155.

(21) Dechet, M. A.; Bonilla, J. S. G.; Grunewald, M.; Popp, K.; Rudloff, J.; Lang, M.; Schmidt, J. A novel, precipitated polybutylene terephthalate feedstock material for powder bed fusion of polymers (PBF): Material development and initial PBF processability. *Mater. Des.* **2021**, *197*, No. 109265.

(22) Chatham, C. A.; Long, T. E.; Williams, C. B. Powder bed fusion of poly (phenylene sulfide) at bed temperatures significantly below melting. *Addit. Manuf.* **2019**, *28*, 506−516.

(23) Yi, N.; Davies, R.; Chaplin, A.; Ghita, O. Novel backbone modified polyetheretherketone (PEEK) grades for powder bed fusion with enhanced elongation at break. *Addit. Manuf.* **2022**, *55*, No. 102857.

(24) Moore, E. P.; Larson, G. A. *Introduction to PP in Business*; Carl Hanser Verlag: Munich, 1996; Vol. *1*, p 257.

(25) Lexow, M. M.; Drummer, D. New Materials for SLS: The Use of Antistatic and Flow Agents. *J. Powder Technol.* **2016**, *2016*, 1−9.

(26) Wang, Z.-G.; Phillips, R. A.; Hsiao, B. S. Morphology development during isothermal crystallization. II. Isotactic and syndiotactic polypropylene blends. *J. Polym. Sci., Part B: Polym. Phys.* **2001**, *39*, 1876−1888.

(27) Phillips, R. A.; Wolkowicz, M. D. *Polypropylene Morphology*; Carl Hanser Verlag: Munich, 2005; Vol. *2*, p 147.

(28) López-Moya, E.; van Grieken, R.; Carrero, A.; Paredes, B. Influence of stereospecificity and molecular weight on mechanical properties of iso-syndio-polypropylene obtained by combination of metallocene catalysts. *Eur. Polym. J.* **2017**, *90*, 183−194.

(29) Jin, M.; Neuber, C.; Schmidt, H.-W. Tailoring polypropylene for extrusion-based additive manufacturing. *Addit. Manuf.* **2020**, *33*, No. 101101.

(30) Auriemma, F.; De Rosa, C. New concepts in thermoplastic elastomers: the case of syndiotactic polypropylene, an unconventional elastomer with high crystallinity and large modulus. *J. Am. Chem. Soc.* **2003**, *125*, 13143−13147.

(31) Auriemma, F.; de Ballesteros, O. R.; Rosa, C. D. Origin of the Elastic Behavior of Syndiotactic Polypropylene. *Macromolecules* **2001**, *34*, 4485−4491.

(32) Auriemma, F.; De Rosa, C. Time-Resolved Study of the Martensitic Phase Transition in Syndiotactic Polypropylene. *Macromolecules* **2003**, *36*, 9396−9410.

(33) Supaphol, P. Crystallization and melting behavior in syndiotactic polypropylene: Origin of multiple melting phenomenon. *J. Appl. Polym. Sci.* **2001**, *82*, 1083−1097.

(34) Razavi, A.Syndiotactic polypropylene: Discovery, development, and industrialization via bridged metallocene catalysts. In *Polyolefins: 50 years after Ziegler and Natta II: Polyolefins by Metallocenes and Other Single-Site Catalysts*; Springer, 2013; pp 43−116.

(35) Razavi, A.; Peters, L.; Nafpliotis, L. Geometric flexibility, ligand and transition metal electronic effects on stereoselective polymer-

ization of propylene in homogeneous catalysis. *J. Mol. Catal. A: Chem.* **1997**, *115*, 129−154.

(36) Chen, Y.-X.; Rausch, M. D.; Chien, J. C. W. Silylene-bridged fluorenyl-containing ligands and zirconium complexes with C1 and Cs symmetry: general synthesis and olefin polymerization catalysis. *J. Organomet. Chem.* **1995**, *497*, 1−9.

(37) Kaminsky, W.; Hopf, A.; Piel, C. Cs-symmetric hafnocene complexes for synthesis of syndiotactic polypropene. *J. Organomet. Chem.* **2003**, *684*, 200−205.

(38) Ewen, J. A.; Jones, R. L.; Razavi, A.; Ferrara, J. D. Syndiospecific propylene polymerizations with Group IVB metallocenes. *J. Am. Chem. Soc.* **1988**, *110*, 6255−6256.

(39) Stieglitz, L.; Henschel, D.; Pehl, T.; Rieger, B. In Situ Activation: Chances and Limitations to Form Ultrahigh Molecular Weight Syndiotactic Polypropylene with Metallocene Dichlorides. *Organometallics* **2021**, *40*, 4055−4065.

(40) Busico, V.; Cipullo, R.; Pellecchia, R.; Talarico, G.; Razavi, A. Hafnocenes and MAO: beware of trimethylaluminum! *Macromolecules* **2009**, *42*, 1789−1791.

(41) Schloegla, M.; Trolla, C.; Thewaltb, U.; Riegera, B. Semi-hydrogenated, asymmetric metallocene catalysts for the propylene polymerization. *Z. Naturforsch. B* **2003**, *58*, 533−538.

(42) Hesse, N.; Winzer, B.; Peukert, W.; Schmidt, J. Towards a generally applicable methodology for the characterization of particle properties relevant to processing in powder bed fusion of polymers − From single particle to bulk solid behavior. *Addit. Manuf.* **2021**, *41*, No. 101957.

(43) Drummer, D.; Drexler, M.; Wudy, K. Density of Laser Molten Polymer Parts as Function of Powder Coating Process during Additive Manufacturing. *Procedia Eng.* **2015**, *102*, 1908−1917.

(44) Marschall, M.; Heintges, C.; Schmidt, M. Influence of flow aid additives on optical properties of polyamide for Laser-Based Powder Bed Fusion. *Procedia CIRP* **2022**, *111*, 51−54.

(45) Tan, L. J.; Zhu, W.; Sagar, K.; Zhou, K. Comparative study on the selective laser sintering of polypropylene homopolymer and copolymer: processability, crystallization kinetics, crystal phases and mechanical properties. *Addit. Manuf.* **2021**, *37*, No. 101610.

(46) Tan, L. J.; Zhu, W.; Zhou, K. Recent Progress on Polymer Materials for Additive Manufacturing. *Adv. Funct. Mater.* **2020**, *30*, No. 2003062.

(47) Haftka, S.; Könnecke, K. Physical properties of syndiotactic polypropylene. *J. Macromol. Sci., Part B* **1991**, *30*, 319−334.

(48) Schmidtke, J.; Strobl, G.; Thurn-Albrecht, T. A Four-State Scheme for Treating Polymer Crystallization and Melting Suggested by Calorimetric and Small Angle X-ray Scattering Experiments on Syndiotactic Polypropylene. *Macromolecules* **1997**, *30*, 5804−5821.

(49) Greiner, S.; Jaksch, A.; Cholewa, S.; Drummer, D. Development of material-adapted processing strategies for laser sintering of polyamide 12. *Adv. Ind. Eng. Polym. Res.* **2021**, *4*, 251−263.

(50) Pokluda, O.; Bellehumeur, C. T.; Machopoulos, J. Modification of Frenkel's Model for Sintering. *AIChE J.* **1997**, *43*, 3253−3256.

(51) Paolucci, F.; van Mook, M. J. H.; Govaert, L. E.; Peters, G. W. M. Influence of post-condensation on the crystallization kinetics of PA12: From virgin to reused powder. *Polymer* **2019**, *175*, 161−170.

(52) Dadbakhsh, S.; Verbelen, L.; Verkinderen, O.; Strobbe, D.; Van Puyvelde, P.; Kruth, J.-P. Effect of PA12 powder reuse on coalescence behaviour and microstructure of SLS parts. *Eur. Polym. J.* **2017**, *92*, 250−262.

(53) Eckstein, A.; Friedrich, C.; Lobbrecht, A.; Spitz, R.; Mülhaupt, R. Comparison of the viscoelastic properties of syndio- and isotactic polypropylenes. *Acta Polym.* **1997**, *48*, 41−46.

(54) Zhang, X.; Zuo, X.; Ortmann, P.; Mecking, S.; Alamo, R. G. Crystallization of long-spaced precision polyacetals I: melting and recrystallization of rapidly formed crystallites. *Macromolecules* **2019**, *52*, 4934−4948.

(55) Sindinger, S.-L.; Kralovec, C.; Tasch, D.; Schagerl, M. Thickness dependent anisotropy of mechanical properties and inhomogeneous porosity characteristics in laser-sintered polyamide 12 specimens. *Addit. Manuf.* **2020**, *33*, No. 101141.

(56) Flodberg, G.; Pettersson, H.; Yang, L. Pore analysis and mechanical performance of selective laser sintered objects. *Addit. Manuf.* **2018**, *24*, 307−315.

(57) Han, W.; Kong, L.; Xu, M. Advances in selective laser sintering of polymers. *Int. J. Extreme Manuf.* **2022**, *4*, No. 042002.

8 Summary and Outlook

In course of this thesis, metallocene catalysis was applied for the synthesis of designable PP and subsequently, the isolated polymers were characterized and processed for prototype production, including the first processing of UHMW-iPP *via* classical melt extrusion. Considering the variety of literature known catalyst moieties leading to different stereoregularities and thus featuring outstanding macromolecular properties, the synthesis of tailored (UHMW-)iPP and (UHMW-)sPP was strived for.

The research area of sPP was initialized by *Ewen* in 1988 by using a C_s-symmetric metallocene. In the following years, the polymer's macromolecular characterisitcs were varied by changing fundamental catalyst motifs. However, despite a few catalysts accomplishing the formation of UHMW-sPP, the productivity of the applied catalysts was inhibited by the activation method, leading to a non-profitable and non-sustainable polymerization. By replacing the MAO activation – which is particularly known for hafnocenes to constrain their activity – by the *in situ* activation using TIBA/TrBCF, the productivity as well as the polymer's molecular weight was tremendously increased. Furthermore, by a set of hafnocenes bearing a different bridging motif, structure-performance relations were manifested. Unfortunately, the obtained UHMW-sPP polymers lacked the nature of a melting transition – probably caused by the inherent slow nucleation of sPP combined with the ultrahigh molecular weight and the comparable low degree of syndiotacticity (max. [rrrr] of 73%).[218] Consequently, this UHMW-sPP polymer can not be processed by classical routes, such as melt spinning for fiber production. In order to circumvent this issue, an increased syndiotacticity has to be be aimed for in future studies. Modifications towards a substituted 2,7-tBu-fluorenyl or octamethyloctahydrodibenzofluorenyl hafnocene was shown to enhance the syndiotacticity and yielded sPP featuring an observable melting transition, but the productivity was constrained due to the chosen MAO activation.[36–38] Therefore, increasing the steric bulkiness of the used hafnocene in combination with *in situ* activation is the most promising approach for the isolation of UHMW-sPP *with* a melting transition and high productivity of the catalyst.

Besides C_s-symmetric hafnocenes, the most prominent isopropylidene-bridged zirconocene $\left(ZrCl_2[Me_2C(\eta^5-Flu)(\eta^5-Cp)]\right)$ was activated *in situ* as well. This resulted in a medium high molecular, highly syndiotactic PP featuring a very high productivity of the zirconocene (up to

12 g sPP by applying 1.2 µmol of the corresponding catalyst).[218] The polymer precipitated during the polymerization as agglomerations of small particles – perfectly suited for PBF-LB/P without requiring additional processing. Therefore, after upscaling of the polymerization process, 100 g of the desired sPP were isolated, characterized, and investigated in the PBF-LB/P. Prior processing, the key material properties for the process were determined, and the obtained material was analyzed in terms of melting and crystallization behavior. The findings highlighted that the thermal properties for the PBF process (e.g. process window) are better than existing PP systems. Furthermore, hot stage microscopy and viscosity studies demonstrated a sufficient coalescence under process conditions without any applied pressure. After processing experiments on an industrial machine, the production of multilayer components showed that the processability is given, and the assumption based on the material analyses was confirmed.[219] With the great chances of this material given, combined with the high productivity of the catalyst leading to a highly profitable polymer production, future research has to focus on the final part production and the optimization thereof.

In addition to sPP, the main focus in polymer synthesis and processing in this thesis has been on iPP – probably one of the best studied areas of propylene polymerization. Commodity iPP for packaging material is produced widely by heterogeneous *Ziegler-Natta* polymerization. However, in this thesis metallocene catalysis for tailoring properties was used. As already enclosed in 2.2, the biggest disadvantage of homogeneous propylene catalysis is the separation of the corresponding *rac* and *meso* C_2-symmetric analogue – tremendously hampering the profitability of the polymer production and thus increasing the average prize per kg of produced polymer. Therefore, the polymerization of *Rieger's* C_2-symmetric *rac* hafnocenes benchmark catalyst's[44] C_s-symmetric *meso* analogue accumulating as side product in the synthesis was investigated. Theoretically, according to *Ewen's* symmetry rules[21] this should have yielded UHMW-aPP. Instead of this, using the *in situ* activation protocol purely isotactic PP was obtained, both for the pure *meso* isomer as well as for *rac*/*meso* isomeric mixtures. After several NMR experiments, the root cause of this phenomenon was ascertained: an isomerization using aluminumalkyls (both for TMA and TIBA) that was not simply affected by the induced sterical bulkiness of the activated Hf_{alk}-species introduced by the activation. However, using the (classical) MAO activation, a chemically and physically separable aPP/iPP blend was

received – probably, due to a parallel activation (initiated by MAO) and isomerization (caused by residual TMA in the solution). Nevertheless, with the isomerization using aluminumalkyls at hand, a simple and convenient isomerization protocol to selectively isomerize the *meso* compound to its corresponding *rac* analogue *in situ* was established. If employed, the total yield of iPP is increased by far more than 400% per used ligand – being of great interest in terms of profitability and sustainability. This protocol was shown to be also applicable to *rac*/*meso* mixtures and other hafnocenes, yielding comparable macromolecular characteristics as for iPP produced by pure *rac* hafnocenes.[220] With this study, the isoselective metallocene-mediated polymerization of propylene may be revolutionized: if this isomerization is applicable to the C_2-symmetric catalysts used in the industry, the average prize per kg of iPP could be decreased by a multiple. Future research has to check the main cause of this phenomenon and which structural motifs inside the catalyst moiety are responsible for this: for example, a metallocene structure not bearing the methoxy group or lacking the 4' aryl modification has to be examined as well as zirconones, to check and better understand the isomerization process and maybe transfer it onto other metallocene catalyst generations (Figure 17).

Which motifs trigger the isomerization?
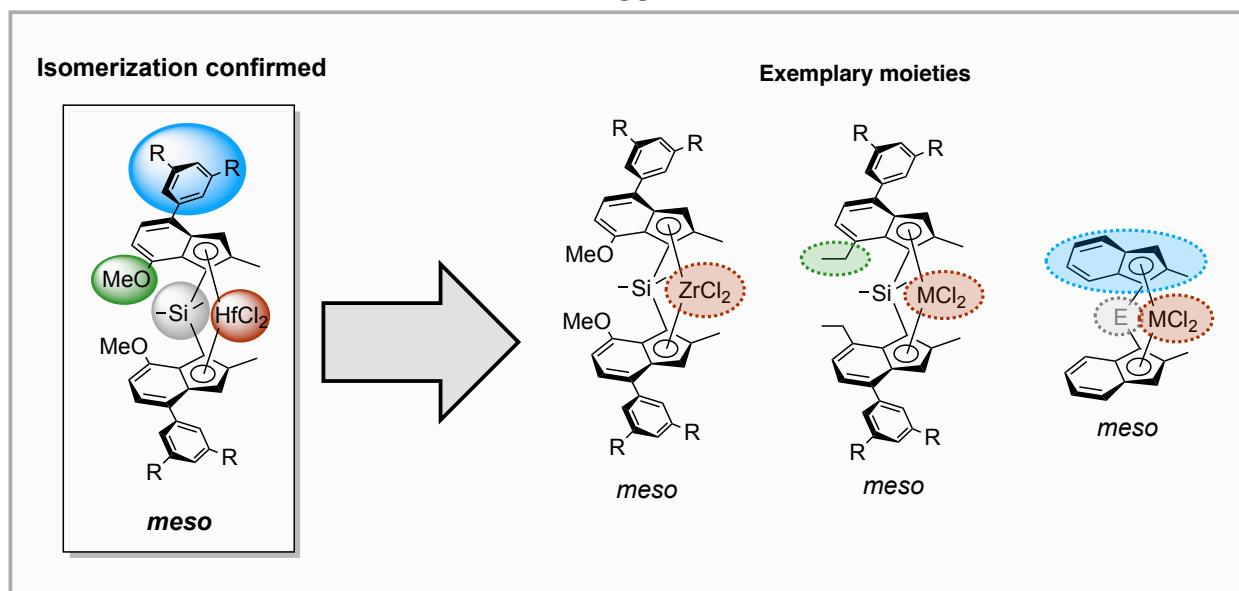
Figure 17: Selected examples for identifying the fundamental motif as the root cause of the *meso*-to-*rac* isomerization.

In addition to the synthesis of UHMW-iPP, the major goal of this thesis was processing for final part and prototype production. Obviously, a simple and convenient processing, such as

compression moulding, is feasible, as the demands of the process on the polymer used are comparatively low. Therefore, extrusion for fiber spinning was aimed for, as UHMW-iPP fibers should benefit two main advantages compared to UHMW-PE (*Dyneema*) fibers: a higher impact resistance and a lower density;[204] consequently resulting in lighter and stronger fibers than commercially available. However, processing of UHMW polymers *via* classical (melt) extrusion is hardly feasible due to their ultrahigh molecular weight resulting in a high melt viscosity. However, despite these bad omens, melt extrusion for fiber spinning of UHMW-iPP was achieved.[221] Unfortunately, the melt viscosity increased with an incremental time in the compounder, probably caused by the formation of new entanglements in the molten state. In addition to melt spinning, melt drawing was proven to be an effective and promising way for fiber production, extending the time window of feasible fiber production. Nevertheless, the compounder was agglutinated after a specific time and thus no extrusion possible at all. This highlights the complexity of UHMW polymers in an extrusion process and the imperative necessity of a deeper understanding of polymer processing in combination with polymer physics. Notwithstanding, the first isolation of UHMW-iPP fibers was achieved within this thesis.[221] The isolated fibers enabled – especially after an annealing process – very promising mechanical properties that surely can be improved by an advanced fiber spinning set-up. Future research has to cover two main issues to fulfill the industrialization and implementation of this unique polymer into mass fiber spinning: circumventing the agglutination of compounder (1) and establishing new processing methods comparable to UHMW-PE fibers (2), such as electrospinning or gel-extrusion. Probably, blending with flow aids is also a promising method; a composite fiber structure with medium high molecular weight iPP acting as a lubricant resulted neither in agglutination of the compounder nor extrusion ruptures. Besides fiber spinning, AM for final part production with complex structures is a very promising method for processing of this high-performance polymer. The general processability was proven in preliminary tests and must now be implemented into the final part prototype production.

This thesis has described the synthesis of tailored ultrahigh molecular weight polypropylene and subsequent processing of this high performance polymer. The initial hypothesis that classical melt processing for greatly mechanical properties is not feasible due to the high melt viscosity was disproved – heralding a new chapter in the polypropylene area.

9 References

[1] Staudinger, *Ber Dtsch Chem Ges* **1920**, *53*, 1073–1085.

[2] K. Ziegler, E. Holzkamp, H. Brei, H. Martin, *Angew. Chem.* **1955**, *67*, 541 – 547.

[3] G. Natta, *Angew. Chem.* **1956**, *68*, 393–403.

[4] A. S. Abd-El-Aziz, M. Antonietti, C. Barner-Kowollik, W. H. Binder, A. Böker, C. Boyer, M. R. Buchmeiser, S. Z. D. Cheng, F. D'Agosto, G. Floudas, et al., *Macromol. Chem. Phys.* **2020**, *221*, 2000216.

[5] R. Geyer, J. R. Jambeck, K. L. Law, *Sci. Adv.* **2017**, *3*, e1700782.

[6] G. W. Coates, Y. D. Getzler, *Nat. Rev. Mater.* **2020**, *5*, 501–516.

[7] S. Ruan, P. Gao, T. Yu, *Polymer* **2006**, *47*, 1604–1611.

[8] H. van der Werff, U. Heisserer, „High-performance ballistic fibers: Ultra-high molecular weight polyethylene (UHMWPE)" in *Advanced fibrous composite materials for ballistic protection*, Elsevier, **2016**, S. 71–107.

[9] P. Bracco, A. Bellare, A. Bistolfi, S. Affatato, *Materials* **2017**, *10*, 791.

[10] K. Ziegler, *Angew. Chem.* **1952**, *64*, 323 – 329.

[11] K. Soga, T. Shiono, *Prog. Polym. Sci.* **1997**, *22*, 1503–1546.

[12] V. Busico, *Giulio Natta and the Development of Stereoselective Propene Polymerization*, S. 37–57, Springer Berlin Heidelberg, Berlin, Heidelberg, **2013**.

[13] H.-G. Elias, *Makromoleküle, Band 3: Industrielle Polymere und Synthesen*, Bd. 3, John Wiley & Sons, **2009**.

[14] D. S. Breslow, N. R. Newburg, *J. Am. Chem. Soc.* **1957**, *79*, 5072–5073.

[15] G. Natta, P. Pino, G. Mazzanti, U. Giannini, *J. Am. Chem. Soc.* **1957**, *79*, 2975–2976.

[16] H. Sinn, W. Kaminsky, H.-J. Vollmer, R. Woldt, *Angew. Chem. Int. Ed.* **1980**, *19*, 390–392.

[17] E. Y.-X. Chen, T. J. Marks, *Chem. Rev.* **2000**, *100*, 1391–1434.

[18] F. R. W. P. Wild, L. Zsolnai, G. Huttner, H. H. Brintzinger, *J. Organomet. Chem.* **1982**, *232*, 233–247.

[19] F. R. W. P. Wild, M. Wasiucionek, G. Huttner, H. H. Brintzinger, *J. Organomet. Chem.* **1985**, *288*, 63–67.

[20] W. Kaminsky, K. Külper, H. H. Brintzinger, F. R. W. P. Wild, *Ang. Chem. Int. Ed.* **1985**, *24*, 507–508.

[21] J. A. Ewen, *J. Am. Chem. Soc.* **1984**, *106*, 6355–6364.

[22] W. Spaleck, M. Antberg, J. Rohrmann, A. Winter, B. Bachmann, P. Kiprof, J. Behm, W. A. Herrmann, *Angew. Chem. Int. Ed.* **1992**, *31*, 1347–1350.

[23] W. Spaleck, F. Kueber, A. Winter, J. Rohrmann, B. Bachmann, M. Antberg, V. Dolle, E. F. Paulus, *Organometallics* **1994**, *13*, 954–963.

[24] C. Ehm, A. Vittoria, G. P. Goryunov, V. V. Izmer, D. S. Kononovich, O. V. Samsonov, P. H. M. Budzelaar, A. Z. Voskoboynikov, V. Busico, D. V. Uborsky, R. Cipullo, *Dalton Trans.* **2020**, *49*, 10162–10172.

[25] P. S. Kulyabin, V. V. Izmer, G. P. Goryunov, M. I. Sharikov, D. S. Kononovich, D. V. Uborsky, J. A. M. Canich, A. Z. Voskoboynikov, *Dalton Trans.* **2021**, *50*, 6170–6180.

[26] P. S. Kulyabin, G. P. Goryunov, M. I. Sharikov, V. V. Izmer, A. Vittoria, P. H. M. Budzelaar, V. Busico, A. Z. Voskoboynikov, C. Ehm, R. Cipullo, D. V. Uborsky, *J. Am. Chem. Soc.* **2021**, *143*, 7641–7647.

[27] J. A. Ewen, R. L. Jones, A. Razavi, J. D. Ferrara, *J. Am. Chem. Soc.* **1988**, *110*, 6255–6256.

[28] A. Razavi, J. L. Atwood, *J. Organomet. Chem.* **1993**, *459*, 117–123.

[29] M. H. Lee, J.-W. Park, C. S. Hong, S. I. Woo, Y. Do, *J. Organomet. Chem.* **1998**, *561*, 37–47.

[30] A. Razavi, L. Peters, L. Nafpliotis, *J. Mol. Cat. A Chem.* **1997**, *115*, 129–154.

[31] Y.-X. Chen, M. D. Rausch, J. C. W. Chien, *J. Organomet. Chem.* **1995**, *497*, 1–9.

[32] K. Patsidis, H. G. Alt, W. Milius, S. J. Palackal, *J. Organomet. Chem.* **1996**, *509*, 63–71.

[33] V. V. Izmer, A. Y. Agarkov, V. M. Nosova, L. G. Kuz'mina, J. A. K. Howard, I. P. Beletskaya, A. Z. Voskoboynikov, *Dalton Trans.* **2001**, 1131–1136.

[34] B. Wang, *Coord. Chem. Rev.* **2006**, *250*, 242–258.

[35] A. Razavi, *Polyolefins: 50 years after Ziegler and Natta II* **2013**, 43–116.

[36] S. A. Miller, J. E. Bercaw, *Organometallics* **2004**, *23*, 1777–1789.

[37] A. Hopf, W. Kaminsky, *Catal. Commun.* **2002**, *3*, 459–464.

[38] W. Kaminsky, A. Hopf, C. Piel, *J. Organomet. Chem.* **2003**, *684*, 200–205.

[39] G. W. Coates, R. M. Waymouth, *Science* **1995**, *267*, 217–219.

[40] M. D. Bruce, G. W. Coates, E. Hauptman, R. M. Waymouth, J. W. Ziller, *J. Am. Chem. Soc.* **1997**, *119*, 11174–11182.

[41] U. Dietrich, M. Hackmann, B. Rieger, M. Klinga, M. Leskelä, *J. Am. Chem. Soc.* **1999**, *121*, 4348–4355.

[42] B. Rieger, C. Troll, J. Preuschen, *Macromolecules* **2002**, *35*, 5742–5743.

[43] K. Press, A. Cohen, I. Goldberg, V. Venditto, M. Mazzeo, M. Kol, *Angew. Chem.* **2011**, *123*, 3591–3594.

[44] A. Schöbel, E. Herdtweck, M. Parkinson, B. Rieger, *Chem. Eur. J.* **2012**, *18*, 4174–4178.

[45] M. R. Machat, D. Lanzinger, A. Pöthig, B. Rieger, *Organometallics* **2017**, *36*, 399–408.

[46] V. V. Izmer, A. Y. Lebedev, D. S. Kononovich, I. S. Borisov, P. S. Kulyabin, G. P. Goryunov, D. V. Uborsky, J. A. M. Canich, A. Z. Voskoboynikov, *Organometallics* **2019**, *38*, 4645–4657.

[47] C. Ehm, A. Vittoria, G. P. Goryunov, V. V. Izmer, D. S. Kononovich, O. V. Samsonov, R. Di Girolamo, P. H. M. Budzelaar, A. Z. Voskoboynikov, V. Busico, et al., *Polymers* **2020**, *12*, 1005.

[48] C. Ehm, A. Vittoria, G. P. Goryunov, V. V. Izmer, D. S. Kononovich, P. S. Kulyabin, R. Di Girolamo, P. H. M. Budzelaar, A. Z. Voskoboynikov, V. Busico, et al., *Macromolecules* **2020**, *53*, 9325–9336.

[49] G. P. Goryunov, M. I. Sharikov, A. N. Iashin, J. A. M. Canich, S. J. Mattler, J. R. Hagadorn, D. V. Uborsky, A. Z. Voskoboynikov, *ACS Catal.* **2021**, *11*, 8079–8086.

[50] L. Resconi, L. Cavallo, A. Fait, F. Piemontesi, *Chem. Rev.* **2000**, *100*, 1253–1346.

[51] P. L. Bryant, C. R. Harwell, A. A. Mrse, E. F. Emery, Z. Gan, T. Caldwell, A. P. Reyes, P. Kuhns, D. W. Hoyt, L. S. Simeral, et al., *J. Am. Chem. Soc.* **2001**, *123*, 12009–12017.

[52] J.-N. Pédeutour, K. Radhakrishnan, H. Cramail, A. Deffieux, *Macromol. Rapid Commun.* **2001**, *22*, 1095–1123.

[53] I. I. Zakharov, V. A. Zakharov, A. G. Potapov, G. M. Zhidomirov, *Macromol. Theory Simul.* **1999**, *8*, 272–278.

[54] M. Ystenes, J. L. Eilertsen, J. Liu, M. Ott, E. Rytter, J. A. Støvneng, *J. Polym. Sci., Part A: Polym. Chem.* **2000**, *38*, 3106–3127.

[55] J. Stellbrink, A. Niu, J. Allgaier, D. Richter, B. W. Koenig, R. Hartmann, G. W. Coates, L. J. Fetters, *Macromolecules* **2007**, *40*, 4972–4981.

[56] K. P. Bryliakov, E. P. Talsi, A. Z. Voskoboynikov, S. J. Lancaster, M. Bochmann, *Organometallics* **2008**, *27*, 6333–6342.

[57] V. Busico, R. Cipullo, R. Pellecchia, G. Talarico, A. Razavi, *Macromolecules* **2009**, *42*, 1789–1791.

[58] M. Bochmann, *Organometallics* **2010**, *29*, 4711–4740.

[59] X. Yang, C. L. Stern, T. J. Marks, *J. Am. Chem. Soc.* **1991**, *113*, 3623–3625.

[60] X. Yang, C. L. Stern, T. J. Marks, *J. Am. Chem. Soc.* **1994**, *116*, 10015–10031.

[61] J. C. W. Chien, W. M. Tsai, M. D. Rausch, *J. Am. Chem. Soc.* **1991**, *113*, 8570–8571.

[62] J. C. W. Chien, W. Song, M. D. Rausch, *Macromolecules* **1993**, *26*, 3239–3240.

[63] M. Schloegl, C. Troll, U. Thewalt, B. Rieger, *Z. Naturforsch. B* **2003**, *58*, 533–538.

[64] M. R. Machat, C. Jandl, B. Rieger, *Organometallics* **2017**, *36*, 1408–1418.

[65] M. R. Machat, D. Lanzinger, M. Drees, P. J. Altmann, E. Herdtweck, B. Rieger, *Macro-molecules* **2018**, *51*, 914–929.

[66] M. R. Machat, A. Fischer, D. Schmitz, M. Vöst, M. Drees, C. Jandl, A. Pöthig, N. P. M. Casati, W. Scherer, B. Rieger, *Organometallics* **2018**, *37*, 2690–2705.

[67] L. Resconi, I. Camurati, C. Grandini, M. Rinaldi, N. Mascellani, O. Traverso, *J. Organomet. Chem.* **2002**, *664*, 5–26.

[68] F. A. R. Kaul, G. T. Puchta, H. Schneider, M. Grosche, D. Mihalios, W. A. Herrmann, *J. Organomet. Chem.* **2001**, *621*, 177–183.

[69] P. Cossee, *Tetrahedron Lett.* **1960**, *1*, 12–16.

[70] P. Cossee, *Tetrahedron Lett.* **1960**, *1*, 17–21.

[71] E. Arlman, P. Cossee, *J. Catal.* **1964**, *3*, 99–104.

[72] Z. Dawoodi, M. L. Green, V. S. Mtetwa, K. Prout, *Chem. Commun.* **1982**, 1410–1411.

[73] M. Brookhart, M. L. Green, *J. Organomet. Chem.* **1983**, *250*, 395–408.

[74] G. F. Schmidt, M. Brookhart, *J. Am. Chem. Soc.* **1985**, *107*, 1443–1444.

[75] A. K. Rappé, W. Skiff, C. J. Casewit, *Chem. Rev.* **2000**, *100*, 1435–1456.

[76] R. Leino, S. Lin, „Isotactic Polypropylene from C2-and Pseudo-C2-Symmetric Cata-lysts" in *Stereoselective Polymerization with Single-Site Catalysts*, CRC Press, **2007**, S. 4 – 6.

[77] A. Laine, M. Linnolahti, T. A. Pakkanen, J. R. Severn, E. Kokko, A. Pakkanen, *Organometallics* **2010**, *29*, 1541–1550.

[78] A. Laine, M. Linnolahti, T. A. Pakkanen, J. R. Severn, E. Kokko, A. Pakkanen, *Organometallics* **2011**, *30*, 1350–1358.

[79] C. Ehm, P. H. M. Budzelaar, V. Busico, *J. Organomet. Chem.* **2015**, *775*, 39–49.

[80] R. Leino, S. Lin, „Isotactic Polypropylene from C2-and Pseudo-C2-Symmetric Catalysts" in *Stereoselective Polymerization with Single-Site Catalysts*, CRC Press, **2007**, S. 6 – 7.

[81] A. Grassi, A. Zambelli, L. Resconi, E. Albizzati, R. Mazzocchi, *Macromolecules* **1988**, *21*, 617–622.

[82] B. Rieger, X. Mu, D. T. Mallin, M. D. Rausch, J. C. W. Chien, *Macromolecules* **1990**, *23*, 3559–3568.

[83] G. Guerra, P. Longo, L. Cavallo, P. Corradini, L. Resconi, *J. Am. Chem. Soc.* **1997**, *119*, 4394–4403.

[84] C. De Rosa, F. Auriemma, M. Paolillo, L. Resconi, I. Camurati, *Macromolecules* **2005**, *38*, 9143–9154.

[85] D. Tranchida, D. Mileva, L. Resconi, B. Rieger, A. Schöbel, *Macromol. Chem. Phys.* **2015**, *216*, 2171–2178.

[86] H. H. Brintzinger, D. Fischer, R. Mülhaupt, B. Rieger, R. M. Waymouth, *Angew. Chem. Int. Ed.* **1995**, *34*, 1143–1170.

[87] A. Zambelli, P. Locatelli, G. Bajo, F. A. Bovey, *Macromolecules* **1975**, *8*, 687–689.

[88] G. W. Coates, *Chem. Rev.* **2000**, *100*, 1223–1252.

[89] T. Hayashi, Y. Inoue, R. Chujo, T. Asakura, *Polymer* **1988**, *29*, 138–143.

[90] H.-G. Elias, H. Dietschy, *Makromol. Chem.* **1967**, *105*, 102–121.

[91] R. Leino, S. Lin, „Isotactic Polypropylene from C2-and Pseudo-C2-Symmetric Catalysts" in *Stereoselective Polymerization with Single-Site Catalysts*, CRC Press, **2007**, S. 9 – 15.

[92] L. Resconi, L. Abis, G. Franciscono, *Macromolecules* **1992**, *25*, 6814–6817.

[93] V. Venditto, G. Guerra, P. Corradini, R. Fusco, *Polymer* **1990**, *31*, 530–537.

[94] G. Erker, C. Fritze, *Angew. Chem. Int. Ed.* **1992**, *31*, 199–202.

[95] Y. Van der Leek, K. Angermund, M. Reffke, R. Kleinschmidt, R. Goretzki, G. Fink, *Chem. Eur. J.* **1997**, *3*, 585–591.

[96] T. Yoshida, N. Koga, K. Morokuma, *Organometallics* **1996**, *15*, 766–777.

[97] H. Kawamura-Kuribayashi, N. Koga, K. Morokuma, *J. Am. Chem. Soc.* **1992**, *114*, 8687–8694.

[98] L. A. Castonguay, A. K. Rappé, *J. Am. Chem. Soc.* **1992**, *114*, 5832–5842.

[99] G. Guerra, L. Cavallo, G. Moscardi, M. Vacatello, P. Corradini, *J. Am. Chem. Soc.* **1994**, *116*, 2988–2995.

[100] L. Cavallo, G. Guerra, *Macromolecules* **1996**, *29*, 2729–2737.

[101] L. Caporaso, C. De Rosa, G. Talarico, *J. Polym. Sci., Part A: Polym. Chem.* **2010**, *48*, 699–708.

[102] V. Busico, R. Cipullo, *J. Am. Chem. Soc.* **1994**, *116*, 9329–9330.

[103] V. Busico, L. Caporaso, R. Cipullo, L. Landriani, G. Angelini, A. Margonelli, A. L. Segre, *J. Am. Chem. Soc.* **1996**, *118,* 2105–2106.

[104] V. Busico, D. Brita, L. Caporaso, R. Cipullo, M. Vacatello, *Macromolecules* **1997**, *30*, 3971–3977.

[105] G. Talarico, P. H. M. Budzelaar, *J. Am. Chem. Soc.* **2006**, *128*, 4524–4525.

[106] Z. Guo, D. C. Swenson, R. F. Jordan, *Organometallics* **1994**, *13*, 1424–1432.

[107] S. Hajela, J. E. Bercaw, *Organometallics* **1994**, *13*, 1147–1154.

[108] P. Yang, M. C. Baird, *Organometallics* **2005**, *24*, 6013–6018.

[109] Y. Suzuki, T. Yasumoto, K. Mashima, J. Okuda, *J. Am. Chem. Soc.* **2006**, *128*, 13017–13025.

[110] G. Sini, S. A. Macgregor, O. Eisenstein, J. H. Teuben, *Organometallics* **1994**, *13*, 1049–1051.

[111] A. Schöbel, D. Lanzinger, B. Rieger, *Organometallics* **2013**, *32*, 427–437.

[112] L. Resconi, S. Bossi, L. Abis, *Macromolecules* **1990**, *23*, 4489–4491.

[113] J. C. W. Chien, B.-P. Wang, *J. Polym. Sci., Part A: Polym. Chem.* **1988**, *26*, 3089–3102.

[114] F. Ghiotto, C. Pateraki, J. R. Severn, N. Friederichs, M. Bochmann, *Dalton Trans.* **2013**, *42*, 9040–9048.

[115] P. Pino, P. Cioni, M. Galimberti, J. Wei, N. Piccolrovazzi, „Asymmetric hydrooligomerization of propylene" in *Transition Metals and Organometallics as Catalysts for Olefin Polymerization*, Springer, **1988**, S. 269–279.

[116] V. Busico, R. Cipullo, J. C. Chadwick, J. F. Modder, O. Sudmeijer, *Macromolecules* **1994**, *27*, 7538–7543.

[117] M. Zintl, B. Rieger, *Angew. Chem. Int. Ed.* **2007**, *46*, 333–335.

[118] A. F. Holleman, *Lehrbuch der anorganischen Chemie*, Walter de Gruyter GmbH & Co KG, **2019**.

[119] H. H. Binder, *Lexikon der chemischen Elemente: das Periodensystem in Fakten, Zahlen und Daten; mit vielen tabellarischen Zusammenstellungen*, S. Hirzel Verlag, **1999**.

[120] R. D. Shannon, C. T. Prewitt, *Acta Crystallogr. B* **1969**, *25*, 925–946.

[121] R. D. Shannon, *Acta Crystallogr. A* **1976**, *32*, 751–767.

[122] J. A. M. Simoes, J. L. Beauchamp, *Chem. Rev.* **1990**, *90*, 629–688.

[123] L. E. Schock, T. J. Marks, *J. Am. Chem. Soc.* **1988**, *110*, 7701–7715.

[124] A. Schöbel, Dissertation, TU München, WACKER-Lehrstuhl für Maktromolekulare Chemie, **2012**.

[125] G. Talarico, P. H. Budzelaar, *Organometallics* **2008**, *27*, 4098–4107.

[126] A. Vittoria, G. P. Goryunov, V. V. Izmer, D. S. Kononovich, O. V. Samsonov, F. Zaccaria, G. Urciuoli, P. H. M. Budzelaar, V. Busico, A. Z. Voskoboynikov, et al., *Polymers* **2021**, *13*, 2621.

[127] A. K. Rappé, O. G. Polyakov, L. M. Bormann-Rochotte, „Catalyst structure and polymer tacticity: the theory behind site control in propylene polymerization" in *Stereoselective polymerization with single-site catalysts*, CRC Press, **2007**, S. 179–189.

[128] R. A. Phillips, M. D. Wolkowicz, „Polypropylene Morphology" in *Polypropylene Handbook*, Carl Hanser Verlag, Munich, **2005**, S. 147 – 152.

[129] G. Farrow, *Polymer* **1963**, *4*, 191–197.

[130] S. Brückner, S. V. Meille, V. Petraccone, B. Pirozzi, *Prog. Polym. Sci.* **1991**, *16*, 361–404.

[131] B. Lotz, J. C. Wittmann, A. Lovinger, *Polymer* **1996**, *37*, 4979–4992.

[132] A. T. Jones, J. M. Aizlewood, D. R. Beckett, *Macromol. Chem. Phys.* **1964**, *75*, 134–158.

[133] R. A. Phillips, M. D. Wolkowicz, „Polypropylene Morphology" in *Polypropylene Handbook*, Carl Hanser Verlag, Munich, **2005**, S. 153 – 210.

[134] G. Natta, P. Corradini, *Nuovo Cimento* **1960**, *15*, 40–51.

[135] G. Natta, P. Corradini, „Structure and properties of isotactic polypropylene" in *Stereoregular Polymers and Stereospecific Polymerizations*, Elsevier, **1967**, S. 743–746.

[136] Z. Mencik, *J. Macromol. Sci. Part B* **1972**, *6*, 101–115.

[137] F. Auriemma, C. D. Rosa, A. Malafronte, M. Scoti, R. D. Girolamo, „Solid state polymorphism of isotactic and syndiotactic polypropylene" in *Polypropylene Handbook*, Springer, **2019**, S. 37–120.

[138] B. Lotz, J. C. Wittmann, *J. Polym. Sci., Part B: Polym. Phys.* **1986**, *24*, 1541–1558.

[139] J. Varga, *J. Mater. Sci.* **1992**, *27*, 2557–2579.

[140] J. Varga, *J. Macromol. Sci. Part B* **2002**, *41*, 1121–1171.

[141] B. Lotz, *Polymer* **1998**, *39*, 4561–4567.

[142] H. Chen, J. Karger-Kocsis, J. Wu, J. Varga, *Polymer* **2002**, *43*, 6505–6514.

[143] C. Zhong, B. Mao, *J. Appl. Polym. Sci.* **2009**, *114*, 2474–2480.

[144] J. L. Kardos, A. W. Christiansen, E. Baer, *J. Pol. Sci., Part A-2: Polym. Phys.* **1966**, *4*, 777–788.

[145] A. Turner-Jones, *Polymer* **1971**, *12*, 487–508.

[146] K. D. Pae, D. R. Morrow, J. A. Sauer, *Nature* **1966**, *211*, 514–515.

[147] D. Fischer, R. Mülhaupt, *Macromol. Chem. Phys.* **1994**, *195*, 1433–1441.

[148] R. Thomann, C. Wang, J. Kressler, R. Mülhaupt, *Macromolecules* **1996**, *29*, 8425–8434.

[149] D. L. VanderHart, R. G. Alamo, M. R. Nyden, M.-H. Kim, L. Mandelkern, *Macromolecules* **2000**, *33*, 6078–6093.

[150] R. Thomann, H. Semke, R.-D. Maier, Y. Thomann, J. Scherble, R. Mülhaupt, J. Kressler, *Polymer* **2001**, *42*, 4597–4603.

[151] C. De Rosa, F. Auriemma, T. Circelli, R. M. Waymouth, *Macromolecules* **2002**, *35*, 3622–3629.

[152] V. Vittoria, *J. Macromol. Sci. Part B: Phys.* **1989**, *28*, 489–502.

[153] H. W. Wyckoff, *J. Polym. Sci.* **1962**, *62*, 83–114.

[154] T. Konishi, K. Nishida, T. Kanaya, K. Kaji, *Macromolecules* **2005**, *38*, 8749–8754.

[155] C. De Rosa, F. Auriemma, *Angew. Chem. Int. Ed.* **2012**, *51*, 1207–1211.

[156] P. Corradini, G. Natta, P. Ganis, P. A. Temussi, *J. Polym. Sci., Part C: Polym. Symp.* **1967**, *16*, 2477–2484.

[157] G. Natta, P. Corradini, P. Ganis, *Makromol. Chem.* **1960**, *39*, 238–242.

[158] B. Pirozzi, R. Napolitano, *Eur. Polym. J.* **1992**, *28*, 703–708.

[159] P. Corradini, R. Napolitano, V. Petraccone, B. Pirozzi, A. Tuzi, *Macromolecules* **1982**, *15*, 1207–1210.

[160] C. De Rosa, F. Auriemma, *Configuration and Conformation of Macromolecules in Polymer Crystals*, S. 1–87, John Wiley & Sons, Inc., Hoboken, New Jersey, **2013**.

[161] B. Lotz, A. J. Lovinger, R. E. Cais, *Macromolecules* **1988**, *21*, 2375–2382.

[162] A. J. Lovinger, B. Lotz, D. D. Davis, *Polymer* **1990**, *31*, 2253–2259.

[163] R. A. Phillips, M. D. Wolkowicz, „Polypropylene Morphology" in *Polypropylene Handbook*, Carl Hanser Verlag, Munich, **2005**, S. 210 – 223.

[164] C. De Rosa, F. Auriemma, P. Corradini, *Macromolecules* **1996**, *29*, 7452–7459.

[165] C. De Rosa, F. Auriemma, V. Vinti, *Macromolecules* **1998**, *31*, 7430–7435.

[166] F. Auriemma, C. De Rosa, S. Esposito, G. R. Mitchell, *Angew. Chem.* **2007**, *119*, 4403–4406.

[167] Y. Chatani, H. Maruyama, K. Noguchi, T. Asanuma, T. Shiomura, *J. Polym. Sci., Part C: Polym. Lett.* **1990**, *28*, 393–398.

[168] C. De Rosa, P. Corradini, *Macromolecules* **1993**, *26*, 5711–5718.

[169] F. Auriemma, O. Ruiz de Ballesteros, C. De Rosa, *Macromolecules* **2001**, *34*, 4485–4491.

[170] C. De Rosa, M. C. Gargiulo, F. Auriemma, O. R. de Ballesteros, A. Razavi, *Macromolecules* **2002**, *35*, 9083–9095.

[171] Y. Chatani, H. Maruyama, T. Asanuma, T. Shiomura, *J. Polym. Sci., Part B: Polym. Phys.* **1991**, *29*, 1649–1652.

[172] J. Vlachopoulos, D. Strutt, *Mater. Sci. Technol.* **2003**, *19*, 1161–1169.

[173] S. M. Abtahi, M. Sheikhzadeh, S. M. Hejazi, *Constr. Build. Mater.* **2010**, *24*, 871–877.

[174] S. Yin, R. Tuladhar, F. Shi, M. Combe, T. Collister, N. Sivakugan, *Constr. Build. Mater.* **2015**, *93*, 180–188.

[175] S. Kakooei, H. M. Akil, M. Jamshidi, J. Rouhi, *Constr. Build. Mater.* **2012**, *27*, 73–77.

[176] M. Liao, H. Liu, X. Wang, X. Hu, Y. Huang, X. Liu, K. Brenan, J. Mecha, M. Nirmalan, J. R. Lu, *Curr. Opin. Colloid Interface Sci.* **2021**, *52*, 101417.

[177] C. Tsutsumi-Arai, Y. Iwamiya, R. Hoshino, C. Terada-Ito, S. Sejima, K. Akutsu-Suyama, M. Shibayama, Z. Hiroi, R. Tokuyama-Toda, R. Iwamiya, et al., *Int. J. Environ. Res. Public Health* **2022**, *19*, 3639.

[178] C. Luo, S. D. Stoyanov, E. Stride, E. Pelan, M. Edirisinghe, *Chem. Soc. Rev.* **2012**, *41*, 4708–4735.

[179] E. Wölfel, H. Brünig, I. Curosu, V. Mechtcherine, C. Scheffler, *Materials* **2021**, *14*, 722.

[180] D. M. Rein, L. Shavit-Hadar, R. Khalfin, Y. Cohen, K. Shuster, E. Zussman, *J. Polym. Sci. B: Polym. Phys.* **2007**, *45*, 766–773.

[181] P. Smith, P. J. Lemstra, *Journal Mater. Sci.* **1980**, *15*, 505–514.

[182] P. Smith, P. J. Lemstra, *Polymer* **1980**, *21*, 1341–1343.

[183] I. P. Barham, A. Keller, *J. Mater. Sci.* **1985**, *20*, 2281–2302.

[184] Y. Fukushima, H. Murase, Y. Ohta, „Dyneema®: Super fiber produced by the gel spinning of a flexible polymer" in *High-Performance and Specialty Fibers*, Springer, **2016**, S. 109–132.

[185] M. Kakiage, D. Fukagawa, *Mater. Today Commun.* **2020**, *23*, 100864.

[186] M. Kakiage, S. Takei, *Macromol. Mater. Eng.* **2020**, *305*, 2000252.

[187] W. E. Frazier, *J. Mater. Eng. Perform.* **2014**, *23*, 1917–1928.

[188] T. DebRoy, H. Wei, J. Zuback, T. Mukherjee, J. Elmer, J. Milewski, A. M. Beese, A. d. Wilson-Heid, A. De, W. Zhang, *Prog. Mater. Sci.* **2018**, *92*, 112–224.

[189] A. Roschli, K. T. Gaul, A. M. Boulger, B. K. Post, P. C. Chesser, L. J. Love, F. Blue, M. Borish, *Addit. Manuf.* **2019**, *25*, 275–285.

[190] S. Schlicht, S. Greiner, D. Drummer, *Polymers* **2022**, *14*, 1428.

[191] Z. Miao, J. Seo, M. A. Hickner, *Polymer* **2018**, *152*, 18–24.

[192] C. W. Weyhrich, T. E. Long, *Polym. Int.* **2022**, *71*, 532–536.

[193] M. Vaezi, S. Yang, *Virtual Phys. Prototyp.* **2015**, *10*, 123–135.

[194] A. R. Zanjanijam, I. Major, J. G. Lyons, U. Lafont, D. M. Devine, *Polymers* **2020**, *12*, 1665.

[195] A. Abbott, T. Gibson, G. Tandon, L. Hu, R. Avakian, J. Baur, H. Koerner, *Addit. Manuf.* **2021**, *37*, 101636.

[196] D. Drummer, S. Greiner, M. Zhao, K. Wudy, *Addit. Manuf.* **2019**, *27*, 379–388.

[197] P. Chen, H. Cai, Z. Li, M. Li, H. Wu, J. Su, S. Wen, Y. Zhou, J. Liu, C. Wang, et al., *Addit. Manuf.* **2020**, *36*, 101615.

[198] J.-P. Kruth, X. Wang, T. Laoui, L. Froyen, *Assem. Autom.* **2003**, *23*, 357–371.

[199] R. Goodridge, C. Tuck, R. Hague, *Prog. Mater. Sci.* **2012**, *57*, 229–267.

[200] F. Fina, A. Goyanes, S. Gaisford, A. W. Basit, *Int. J. Pharm.* **2017**, *529*, 285–293.

[201] C. A. Chatham, T. E. Long, C. B. Williams, *Prog. Polym. Sci.* **2019**, *93*, 68–95.

[202] U. W. Gedde, A. Mattozzi, *Polyethylene Morphology*, S. 29–74, Springer Berlin Heidelberg, Berlin, Heidelberg, **2004**.

[203] S. Rastogi, D. R. Lippits, G. W. Peters, R. Graf, Y. Yao, H. W. Spiess, *Nat. Mater.* **2005**, *4*, 635–641.

[204] R. Marroquin-Garcia, N. Leone, L. G. Hawke, D. Romano, C. H. Wilsens, S. Rastogi, *Macromolecules* **2022**, *55*, 2574–2587.

[205] H. Uehara, M. Nakae, T. Kanamoto, A. E. Zachariades, R. S. Porter, *Macromolecules* **1999**, *32*, 2761–2769.

[206] M. Kakiage, T. Yamanobe, T. Komoto, S. Murakami, H. Uehara, *Polymer* **2006**, *47*, 8053–8060.

[207] H. Uehara, T. Tamura, M. Kakiage, T. Yamanobe, *Adv. Funct. Mater.* **2012**, *22*, 2048–2057.

[208] H. A. Maddah, *Am. J. Polym. Sci* **2016**, *6*, 1–11.

[209] M. R. Machat, Dissertation, TU München, WACKER-Lehrstuhl für Maktromolekulare Chemie, **2018**.

[210] R. H. Colby, L. J. Fetters, W. W. Graessley, *Macromolecules* **1987**, *20*, 2226–2237.

[211] A. Pawlak, *Macromol. Chem. Phys.* **2019**, *220*, 1900043.

[212] D. R. Lippits, S. Rastogi, S. Talebi, C. Baillv, *Macromolecules* **2006**, *39*, 8882–8885.

[213] I. E. Nifant'ev, P. V. Ivchenko, *Organometallics* **1997**, *16*, 713–715.

[214] G. M. Diamond, R. F. Jordan, J. L. Petersen, *J. Am. Chem. Soc.* **1996**, *118*, 8024–8033.

[215] X. Zhang, Q. Zhu, I. A. Guzei, R. F. Jordan, *J. Am. Chem. Soc.* **2000**, *122*, 8093–8094.

[216] W. Kaminsky, A.-M. Schauwienold, F. Freidanck, *J. Mol. Catal. A: Chem* **1996**, *112*, 37–42.

[217] R. M. Buck, N. Vinayavekhin, R. F. Jordan, *J. Am. Chem. Soc.* **2007**, *129*, 3468–3469.

[218] L. Stieglitz, D. Henschel, T. Pehl, B. Rieger, *Organometallics* **2021**, *40*, 4055–4065.

[219] S. Cholewa, L. Stieglitz, A. Jaksch, B. Rieger, D. Drummer, *ACS Appl. Polym. Mater.* **2023**, *Article ASAP*, DOI: 10.1021/acsapm.2c02112.

[220] L. Stieglitz, T. M. Lenz, A. Saurwein, B. Rieger, *Angew. Chem. Int. Ed.* **2022**, *61*, e202210797.

[221] L. Stieglitz, C. Geiger, P. F. Großmann, M. Kränzlein, K. Rodewald, P. Müller-Buschbaum, B. Rieger, *ChemPlusChem* **2023**, *88*, e202300045.

10 Appendix

10.1 Supporting Information

10.1.1 Supporting Information for Chapter 4

In situ Activation: Chances and Limitations to Form Ultrahigh Molecular Weight Syndiotactic Polypropylene with Metallocene-dichlorides

Lucas Stieglitz, [a] Daniel Henschel, [a] Thomas Pehl[a] and Bernhard Rieger[a]*

[a]Wacker-Lehrstuhl für Makromolekulare Chemie, Catalysis Research Center, Technische Universität München, Lichtenbergstrasse 4, 85748 Garching bei München, Germany.

Table of contents:

Syntheses

Cyclopentadienyllithium (LiCp). The synthesis of LiCp took place in a modified literature known procedure.[1] In a 500 mL 2-necked Schlenk flask 100 mL of dry pentane and 12.1 mL (9.50 g, 144 mmol, 1.00 eq.) of freshly cracked dicyclopentadiene was submitted. At -78 °C 69.0 mL (172 mmol, 1.20 eq.) of nBuLi, 2.50 M in hexanes, was added dropwise to the solution. The mixture was heated up to room temperature and stirred overnight. The resulting white solid was filtrated using a Schlenk-frit, washed twice with dry pentane (20 mL) and dried exhaustively under vacuum. The product was obtained as a white powder in a quantitative yield. ^{1}H-NMR (400 MHz, CDCl$_3$, 298 K, ppm): δ 5.70 (s, 1H). The NMR spectroscopic data match previous reported data.[2]

Fluorenyllithium (Flu-Li). The synthesis of Flu-Li took place in a modified literature known procedure.[3] In a 250 mL *Schlenk* flask 10.0 g (60.2 mmol, 1.00 eq.) fluorene **1** was dissolved in 100 mL of dry Et$_2$O. At 0 °C 31.2 mL (78.2 mmol, 1.30 eq.) of *n*BuLi, 2.50 M in hexanes, was added and stirred for additional 4h at room temperature. The remaining solution was removed *via* filtration, the bright yellow solid was washed twice with 10 mL of dry pentane and dried under vacuum. 9.84 g (95%) of Flu-Li was obtained as a yellow powder. The product forms an adduct with Et$_2$O (4 Flu-Li · 3 Et$_2$O). ^{1}H-NMR (400 MHz, CDCl$_3$, 298 K, ppm): δ 7.87 (d, J = 7.7 Hz, 2H), 7.26 (d, J = 8.1 Hz, 2H), 6.76 (ddd, J = 8.0, 6.5, 1.2 Hz, 2H), 6.38 (ddd, J = 7.1, 6.5, 1.2 Hz, 2H), 5.87 (s, 1H). The NMR spectroscopic data match previous reported data.[3]

Dimethylfulvene. The synthesis of *dimethylfulvene* took place in a modified literature known procedure.[4] In a 250 mL *Schlenk* flask 35.9 mL (415 mmol, 2.01 eq.) of freshly cracked cyclopentadiene and 15.3 mL (207 mmol, 1.00 eq.) of dry acetone were dissolved in 50 mL of dry methanol. At 0 °C 20.4 mL (248 mmol, 1.20 eq.) of pyrrolidine was added, the yellow solution stirred for 2h at room temperature and 14.2 mL (248 mmol, 1.20 eq.) of acetic acid was added and stirred for additional 2h. The solution was poured into 100 mL of water and extracted three times with Et$_2$O (50 mL). The combined organic phase was washed with an aqueous solution of 1 M NaOH (20 mL) and brine (20 mL), dried over MgSO$_4$ and the solvent evaporated *in vacuo*. Fractionated distillation of the crude product gave 16.1 g (84%) of the product as an orange-red oil. ^{1}H-NMR (400 MHz, CDCl$_3$, 298 K, ppm): δ 6.55 – 6.48 (m, 4H, H$_{Cp}$), 2.21 (s, 6H, CH$_3$). The NMR spectroscopic data match previous reported data.[4]

Diphenylfulvene. The synthesis of *diphenylfulvene* took place in a modified literature known procedure.[5] In a 250 mL *Schlenk* flask 1.53 g (21.8 mmol, 2.10 eq.) of LiCp was dissolved in 50 mL of dry THF, 1.82 g (10.0 mmol, 1.00 eq.) benzophenone added and refluxed for 2h. 1.24 mL (15.0 mmol, 1.50 eq.) pyrrolidine was added and refluxed for an additional hour. The reaction was quenched by the addition of 50 mL water and extracted three times with Et$_2$O (30 mL). The combined organic phase was subsequently washed with an aqueous solution of 1 M HCl (25 mL) and brine (25 mL), dried over MgSO$_4$ and the solvent evaporated *in vacuo*. Column chromatography (pentane, R$_f$ = 0.24, KMnO$_4$) gave 1.92 g (84%) of the product as dark-red crystals. ^{1}H-NMR (400 MHz, CDCl$_3$, 298 K, ppm): δ 7.43 – 7.30 (m, 10H, H$_{aryl}$), 6.63 – 6.57 (m, 2H, H$_{cp}$), 6.34 – 6.28 (m, 2H, H$_{cp}$). ^{13}C-NMR (100 MHz, CDCl$_3$, 298 K, ppm): δ 152.14, 143.99, 141.42, 132.44, 132.25, 128.84, 127.85, 124.51. The NMR spectroscopic data match previous reported data.[5]

^{1}H, ^{13}C and ^{29}Si spectra
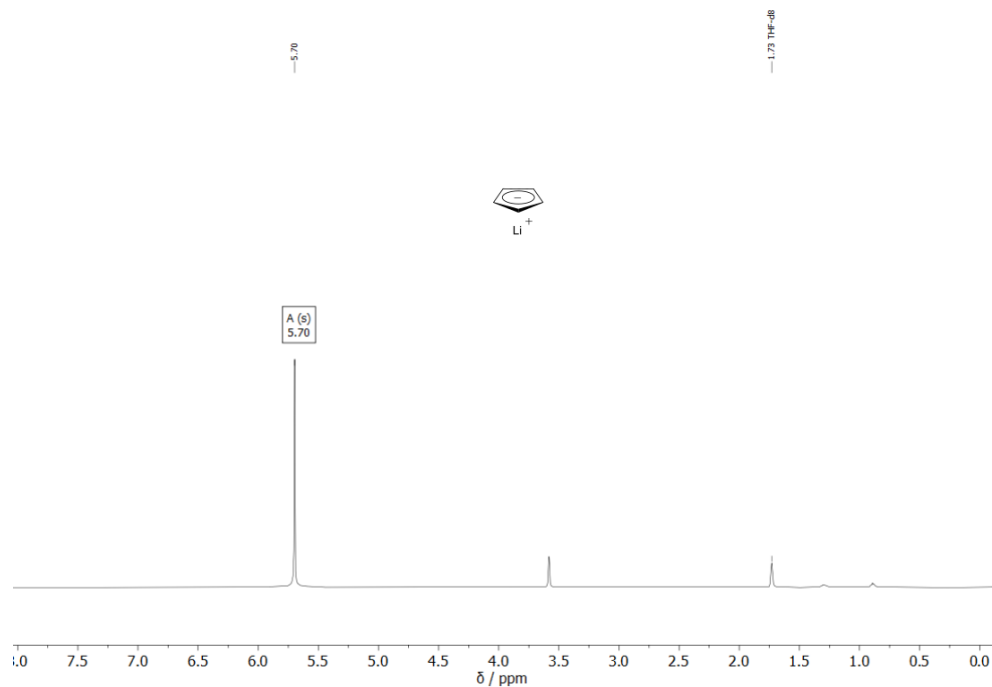
Figure S1: ^{1}H NMR (400 MHz) spectrum of LiCp in THF-d8.
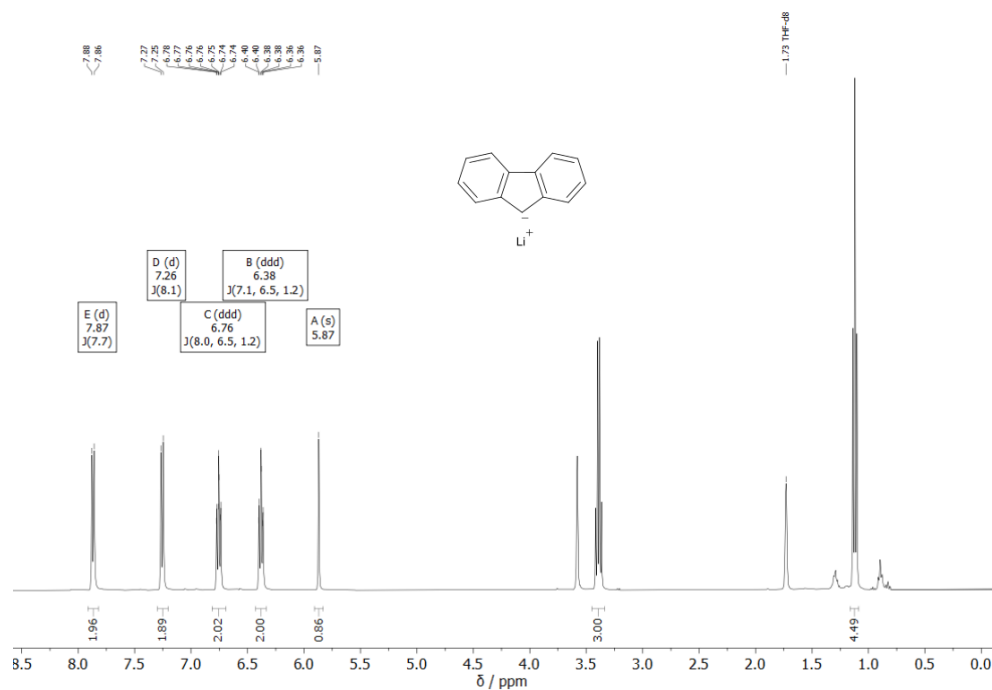
Figure S2: ^{1}H NMR (400 MHz) spectrum of Flu-Li in THF-d8.
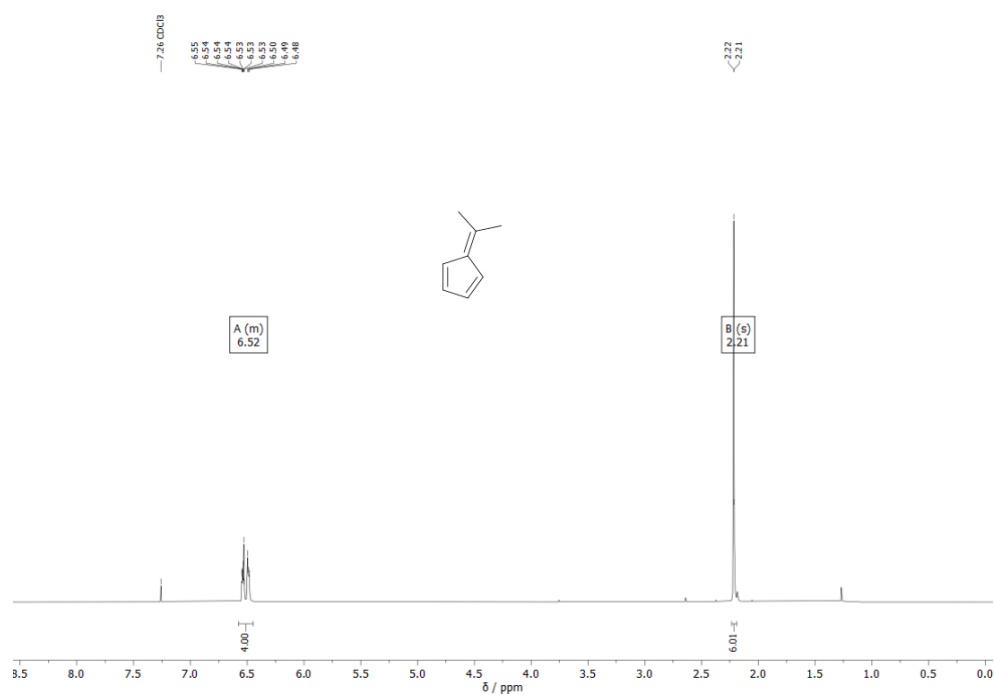
Figure S3: ^{1}H NMR (400 MHz) spectrum of dimethylfulvene in CDCl$_3$.
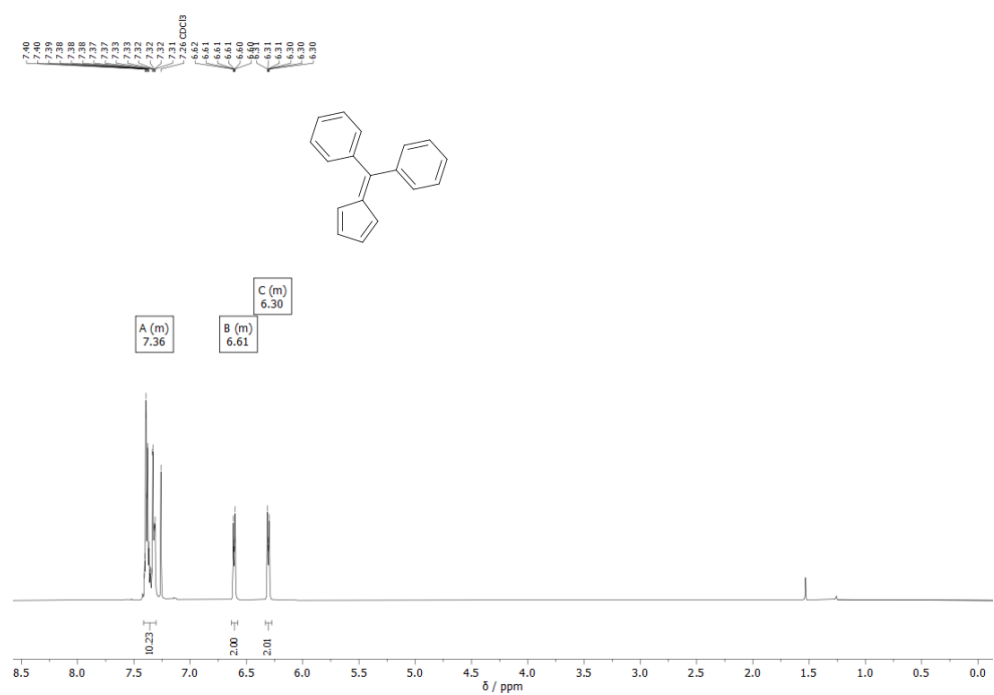
Figure S4: ^{1}H NMR (400 MHz) spectrum of diphenylfulvene in CDCl$_3$.
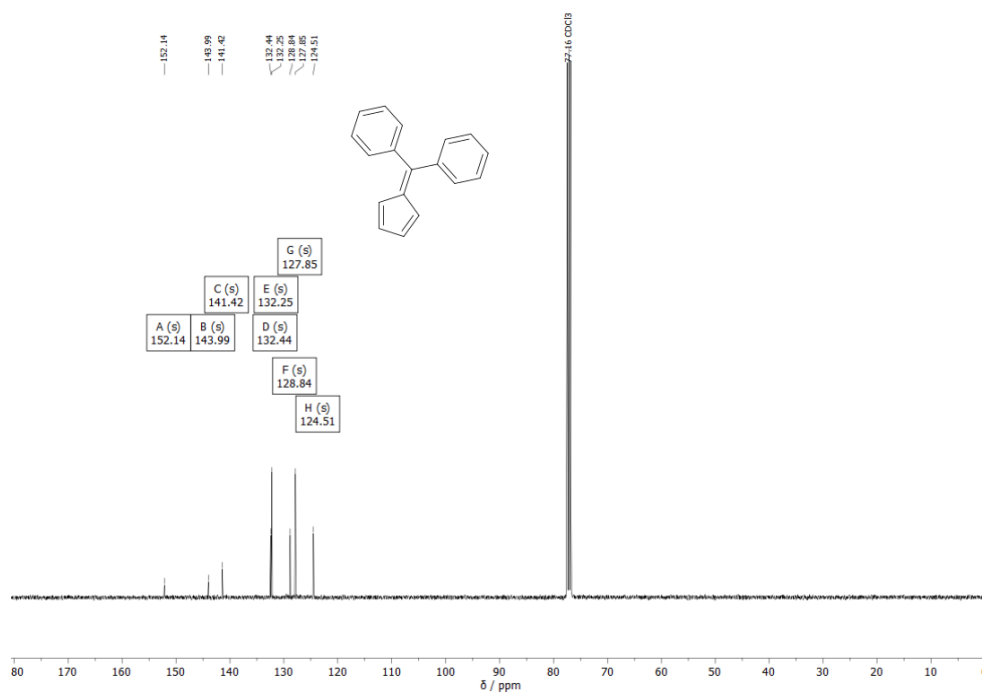
Figure S5: $^{13}C\{^1H\}$ NMR (100 MHz) spectrum of diphenylfulvene in CDCl$_3$.
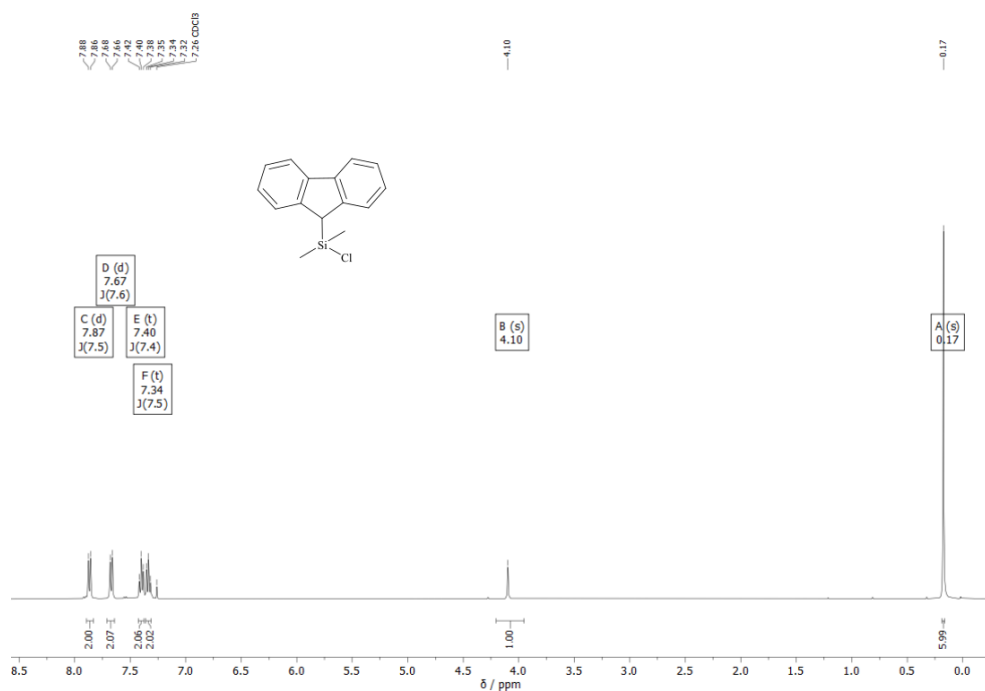
Figure S6: ^1H NMR (400 MHz) spectrum of *Flu-SiMe$_2$Cl **3a*** in CDCl$_3$.
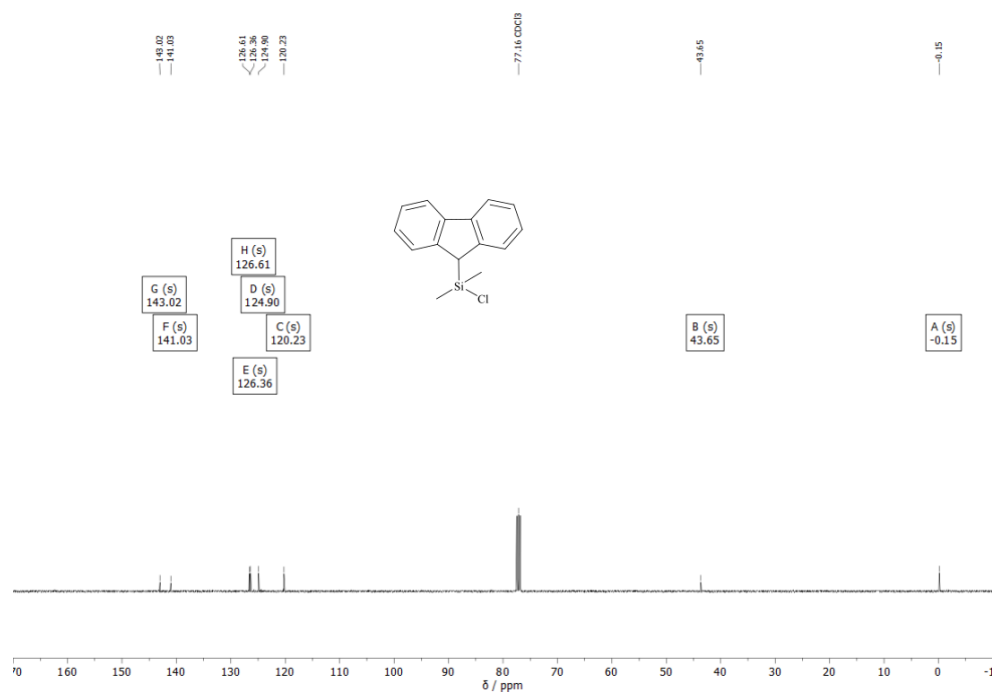
Figure S7: ^{13}C {^{1}H} NMR (100 MHz) spectrum of *Flu-SiMe$_2$Cl 3a* in CDCl$_3$.
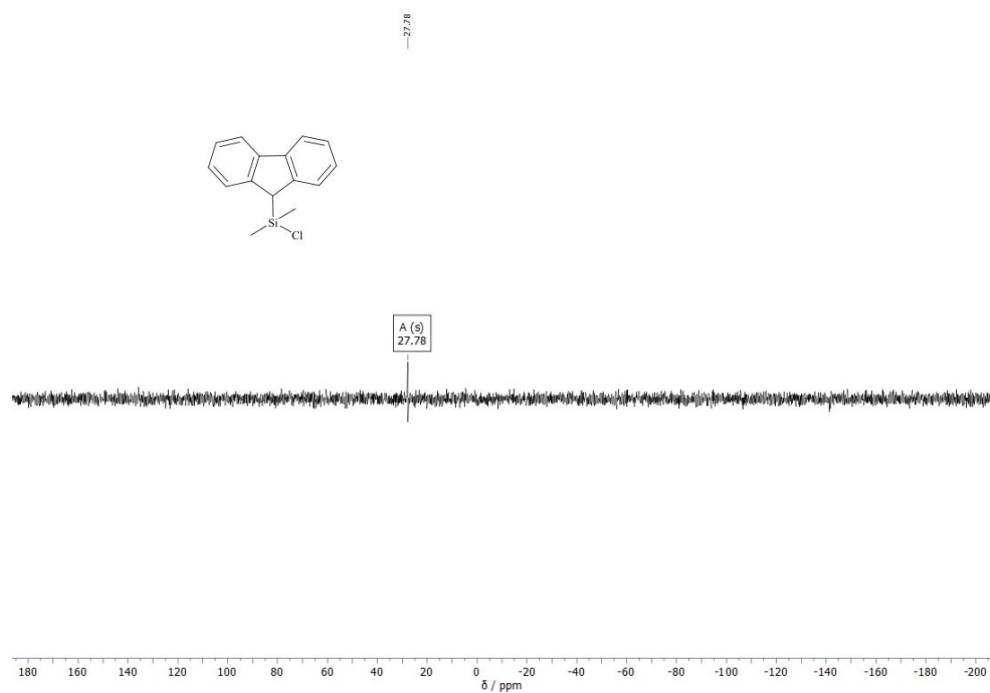
Figure S8: ^{29}Si NMR (80 MHz) spectrum of *Flu-SiMe$_2$Cl 3a* in CDCl$_3$.
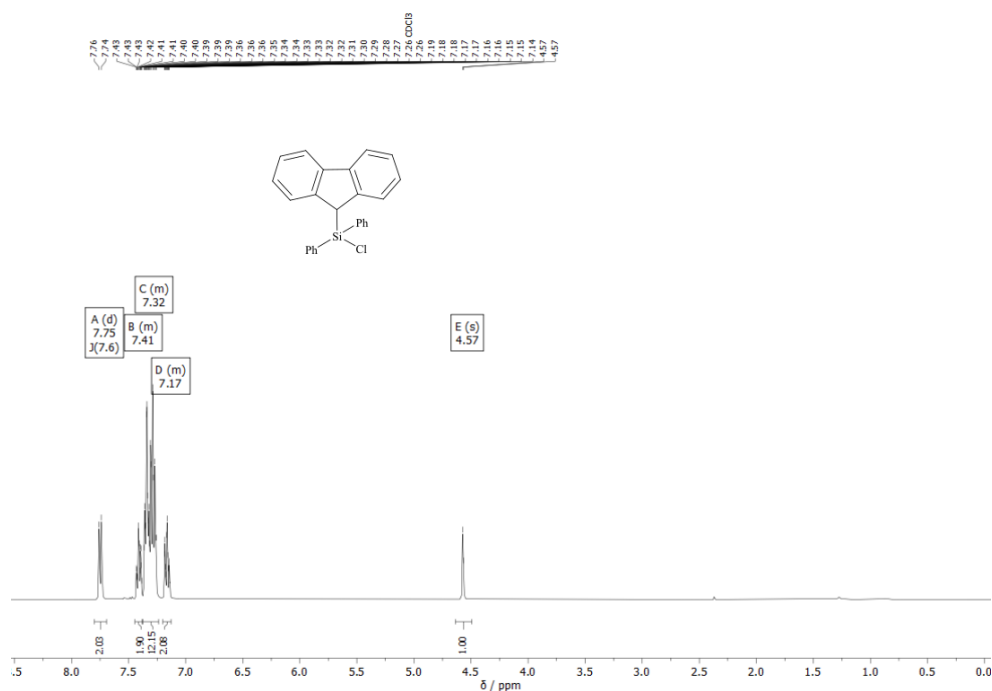
Figure S9: ^{1}H NMR (400 MHz) spectrum of *Flu-SiPh₂Cl* **3b** in CDCl₃.
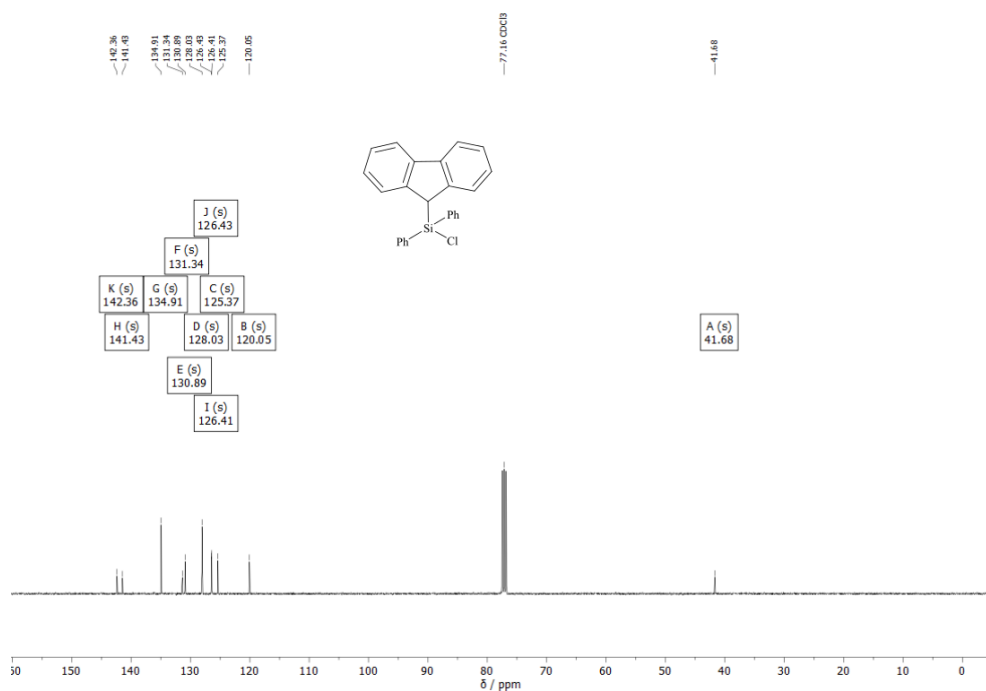
Figure S10: ^{13}C {^{1}H} NMR (100 MHz) spectrum of *Flu-SiPh₂Cl* **3b** in CDCl₃.

96
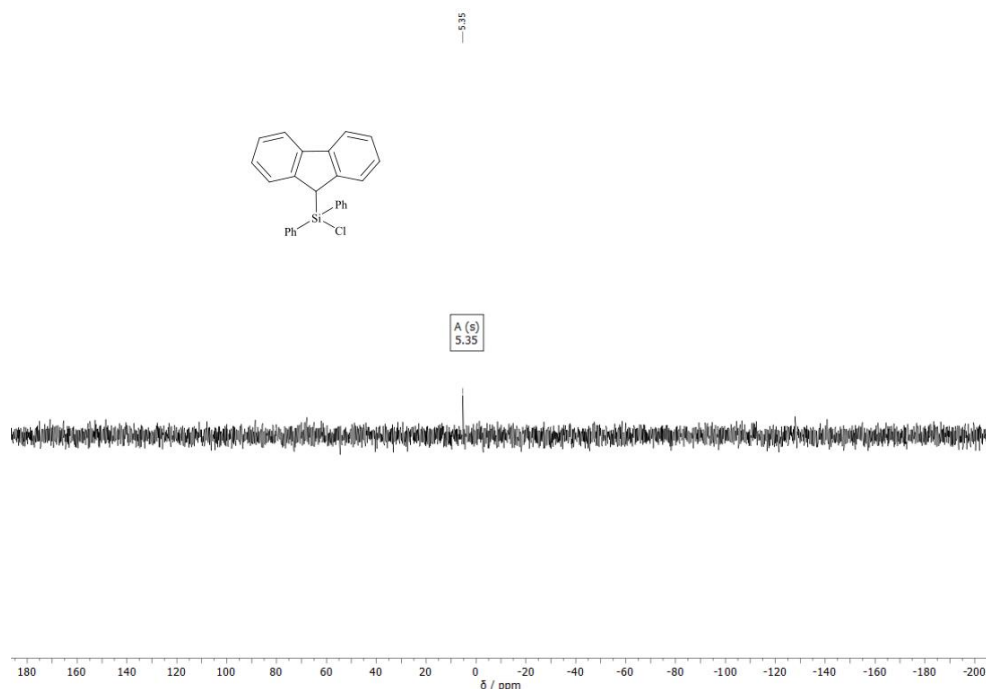
Figure S11: ^{29}Si NMR (80 MHz) spectrum of *Flu-SiPh₂Cl **3b*** in CDCl₃.
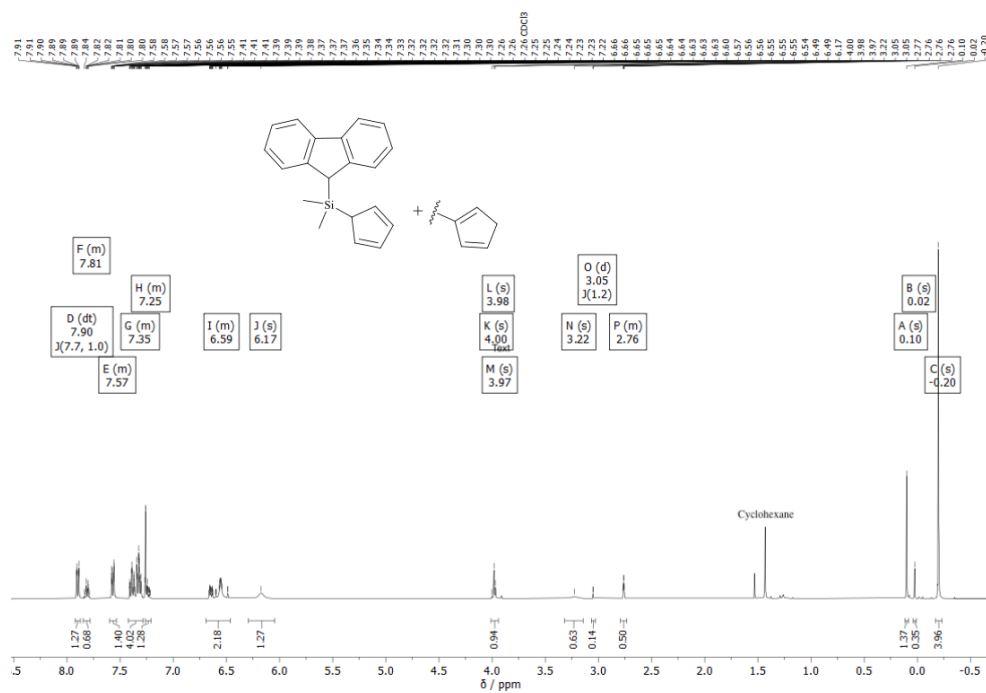
Figure S12: ^{1}H NMR (400 MHz) spectrum of *Flu-SiMe₂Cp **4a*** in CDCl₃. Normalized to 20 protons.
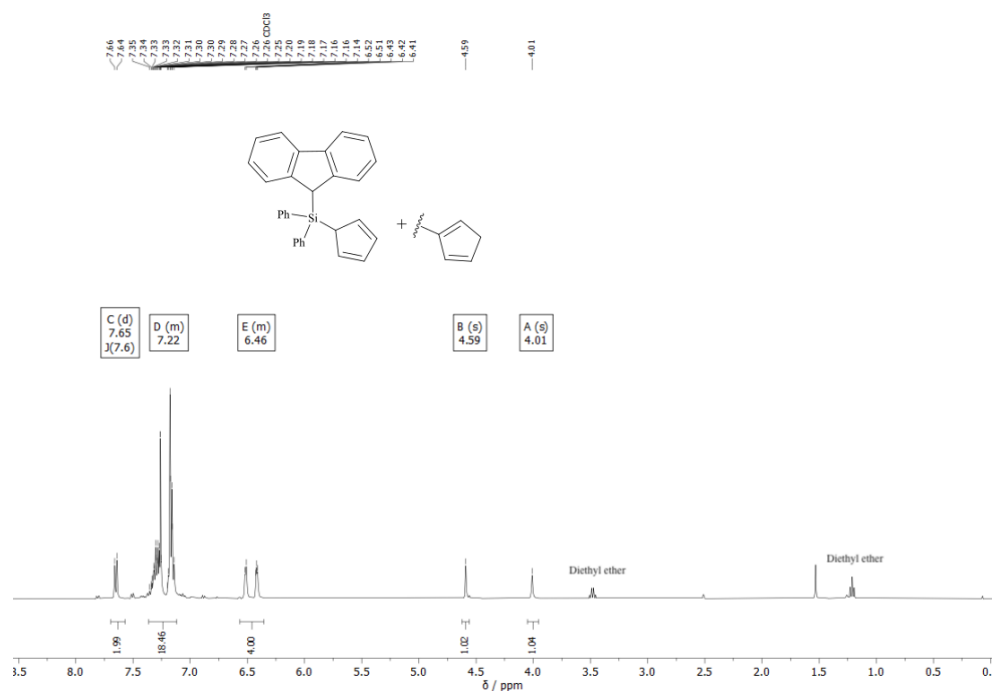
Figure S13: ^{1}H NMR (400 MHz) spectrum of *Flu-SiPh$_2$Cp* **4b** in CDCl$_3$.
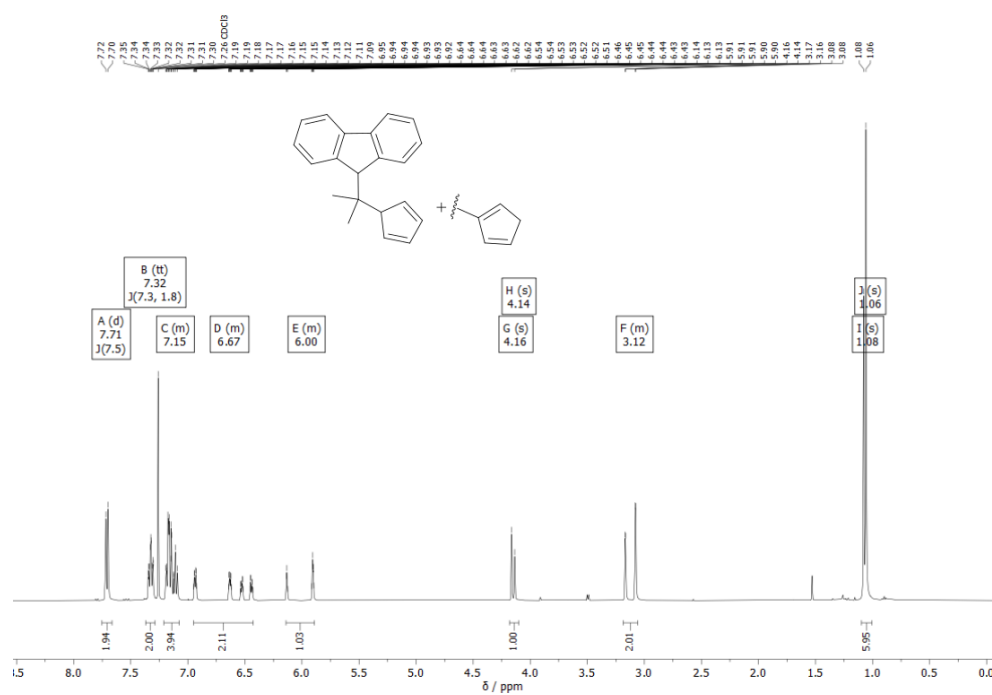
Figure S14: ^{1}H NMR (400 MHz) spectrum of *Flu-CMe$_2$Cp* **2a** in CDCl$_3$.
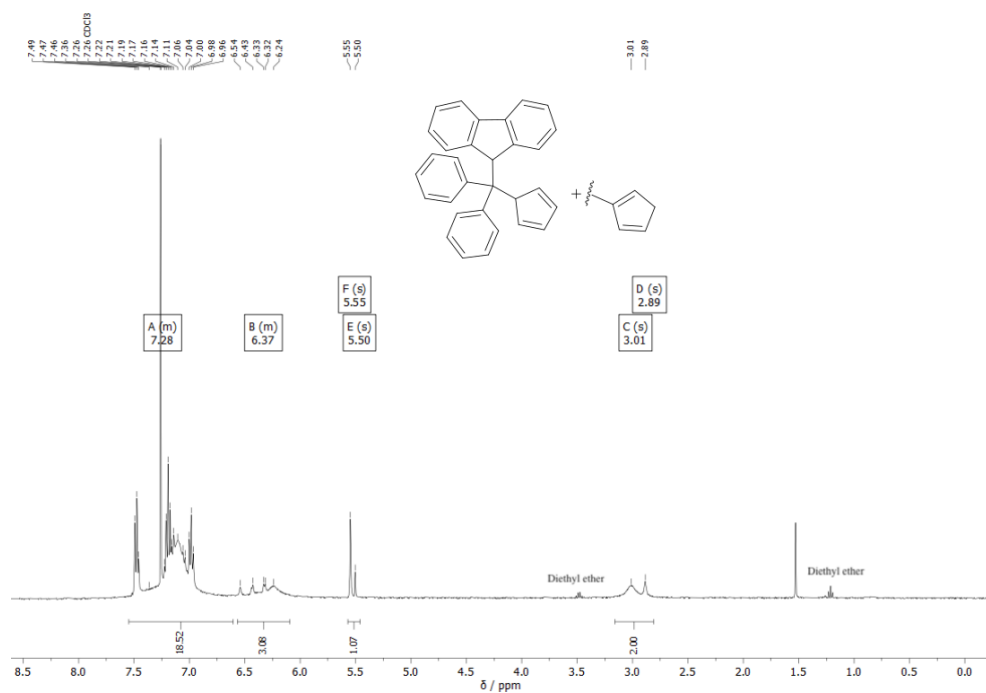
Figure S15: ^{1}H NMR (400 MHz) spectrum of *Flu-CPh$_2$Cp* **2b** in CDCl$_3$.
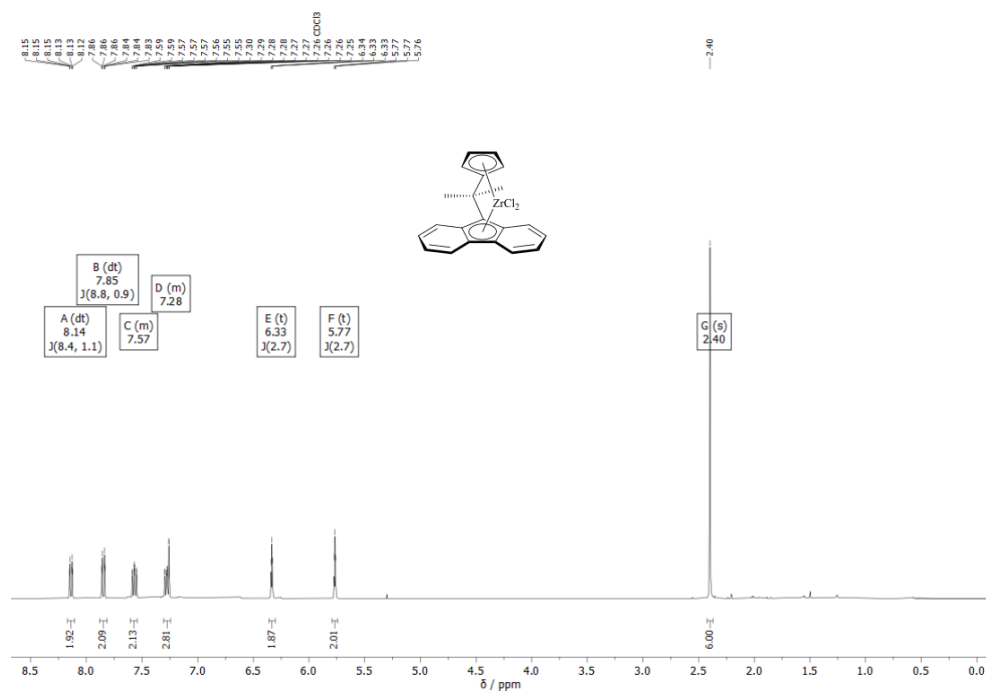
Figure S16: ^{1}H NMR (400 MHz) spectrum of **Ia** in CDCl$_3$.
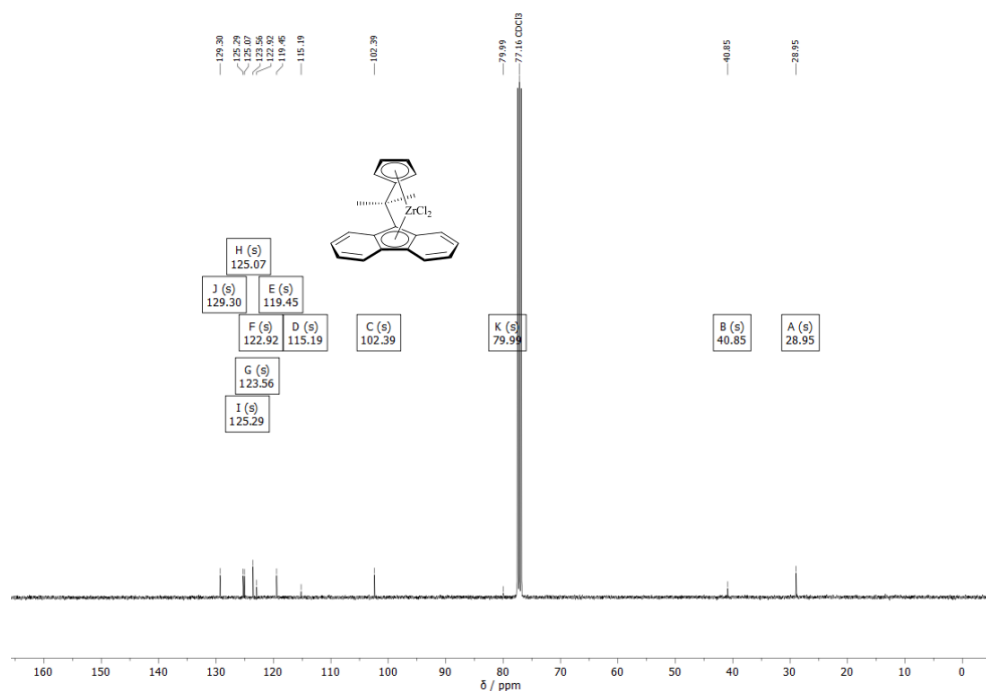
Figure S17: $^{13}C\{^1H\}$ NMR (100 MHz) spectrum of **Ia** in CDCl$_3$.
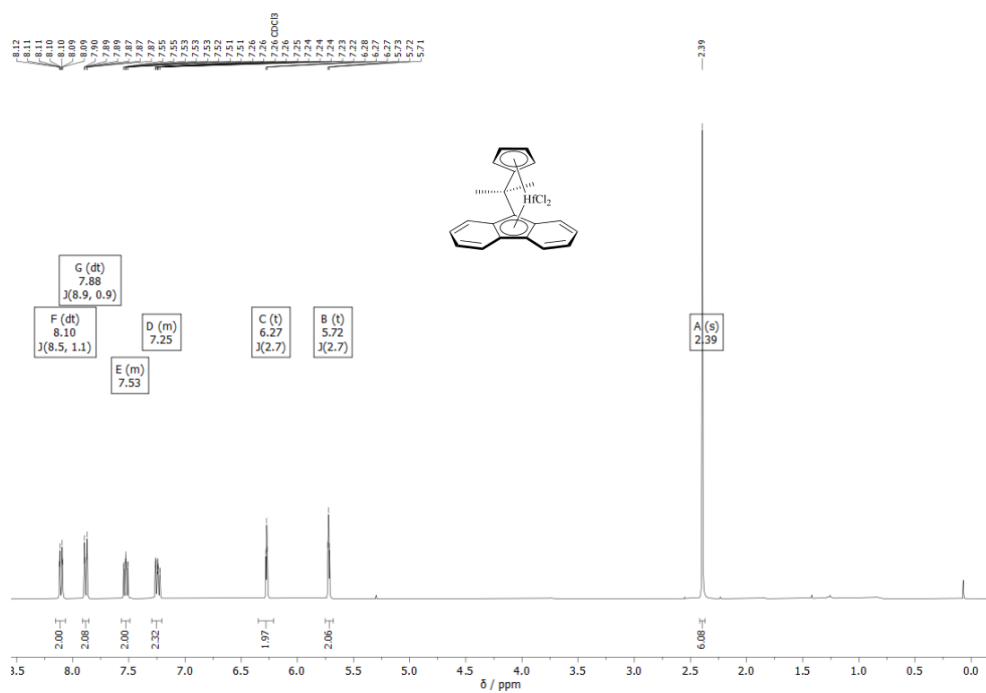
Figure S18: ^1H NMR (400 MHz) spectrum of **Ib** in CDCl$_3$.
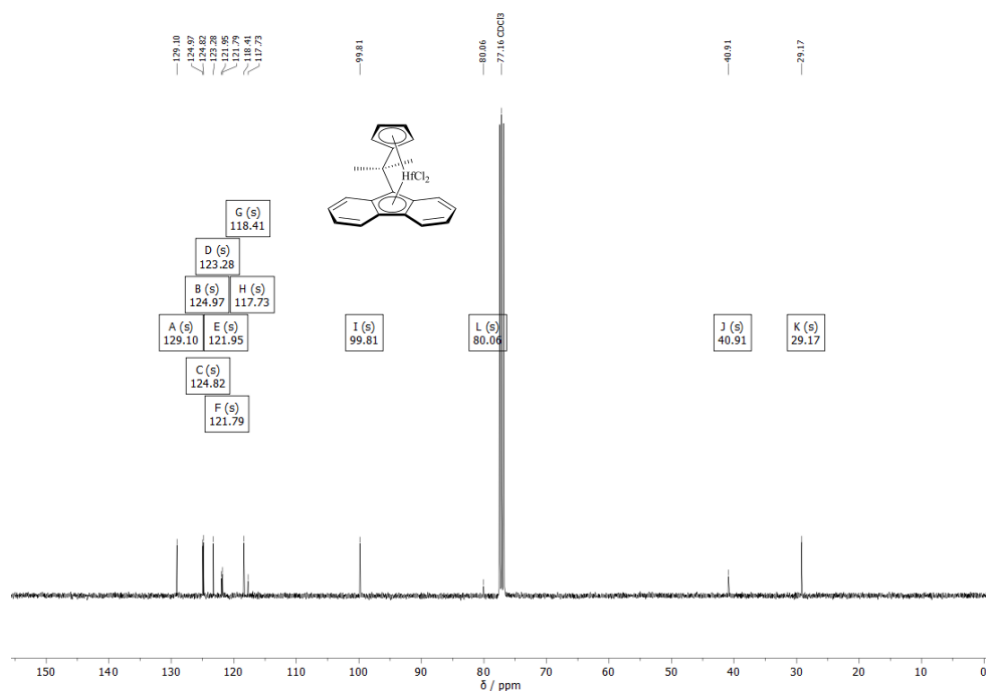
Figure S19: $^{13}C\{^1H\}$ NMR (100 MHz) spectrum of **Ib** in CDCl$_3$.
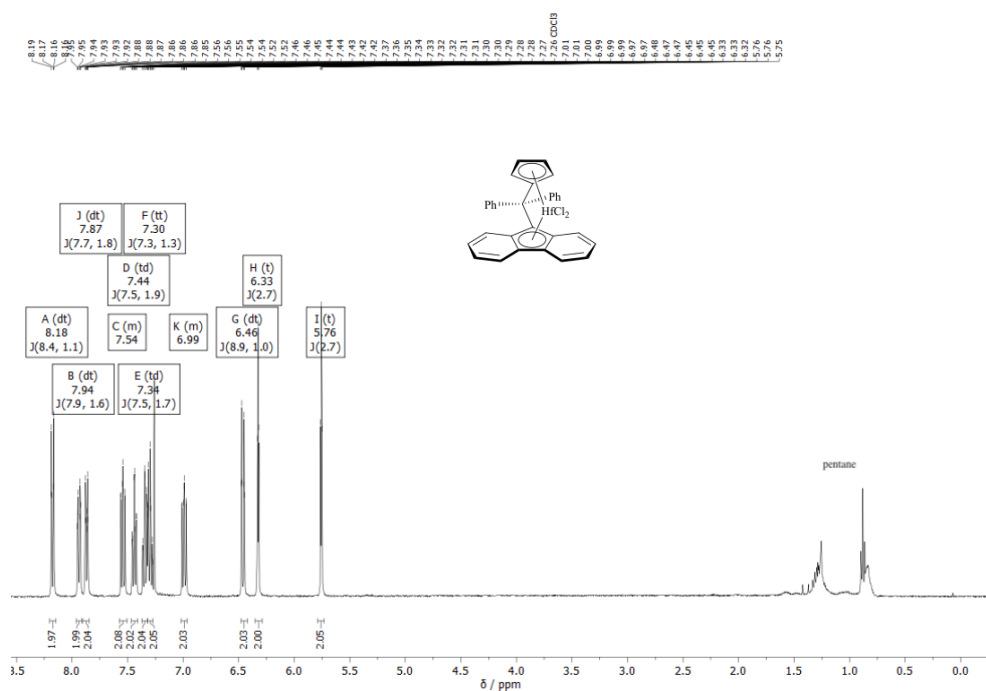
Figure S20: ^1H NMR (400 MHz) spectrum of **II** in CDCl$_3$.
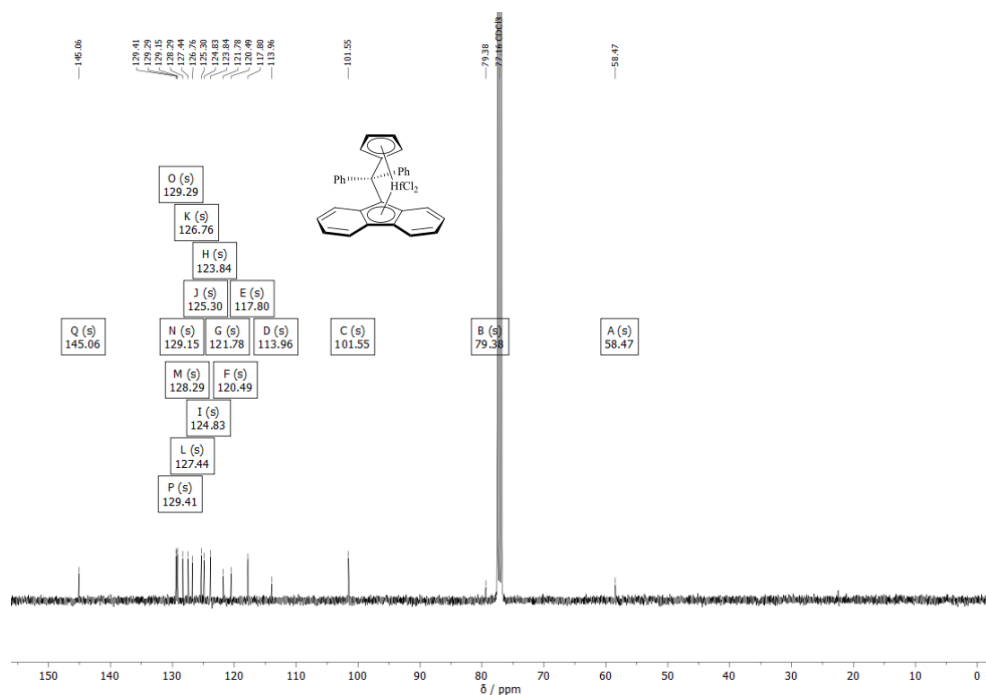
Figure S21: ^{13}C {^1H} NMR (100 MHz) spectrum of **II** in CDCl$_3$.
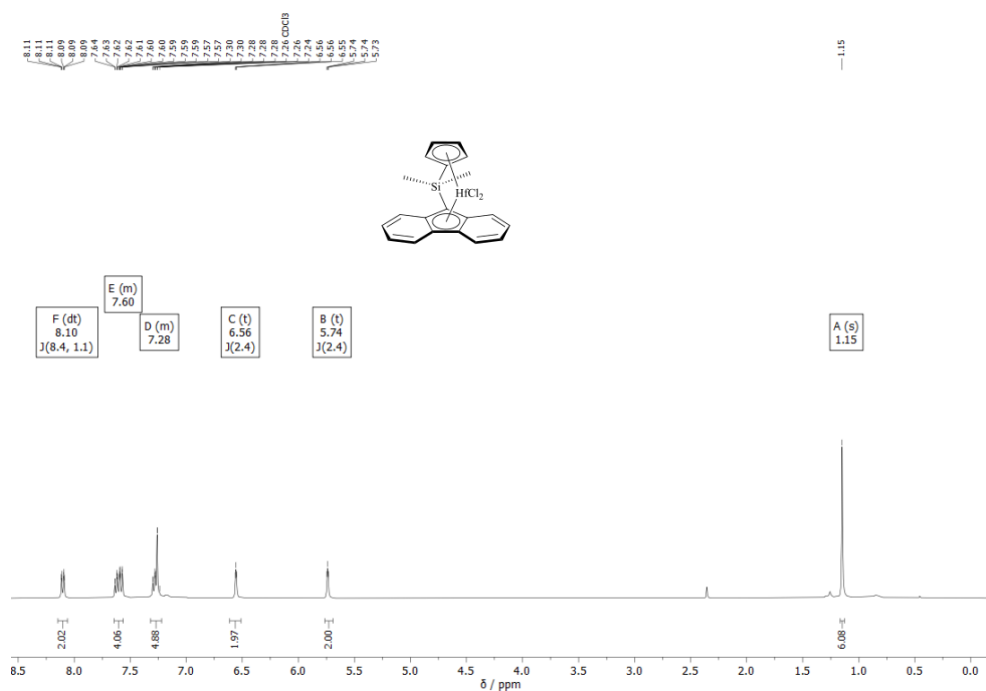
Figure S22: ^1H NMR (400 MHz) spectrum of **III** in CDCl$_3$.
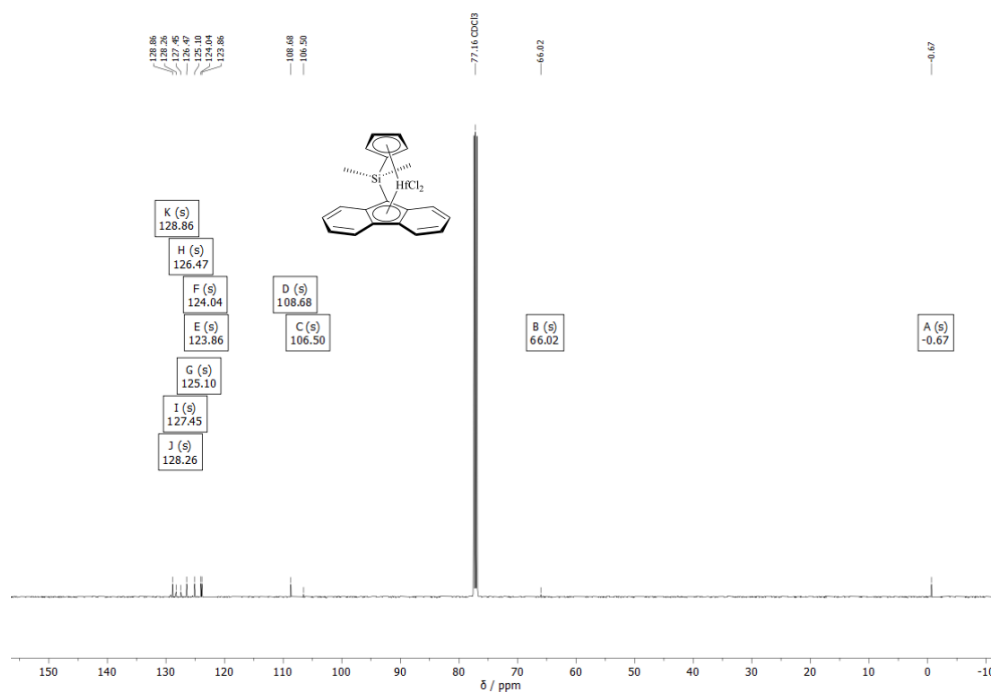
Figure S23: $^{13}C\{^{1}H\}$ NMR (125 MHz) spectrum of **III** in CDCl$_3$.
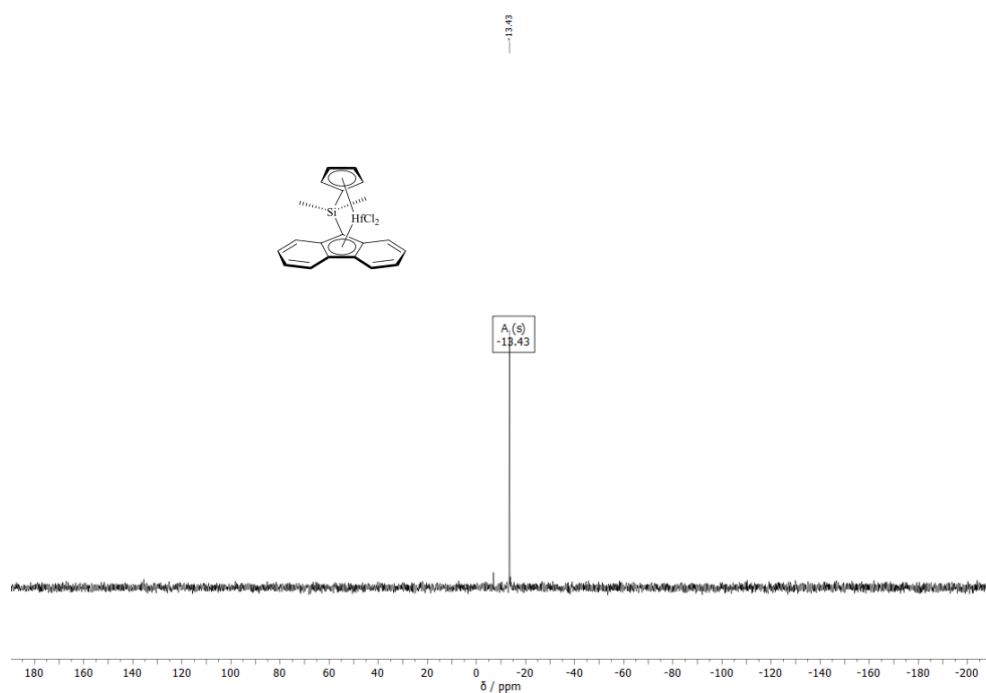
Figure S24: ^{29}Si NMR (100 MHz) spectrum of **III** in CDCl$_3$.
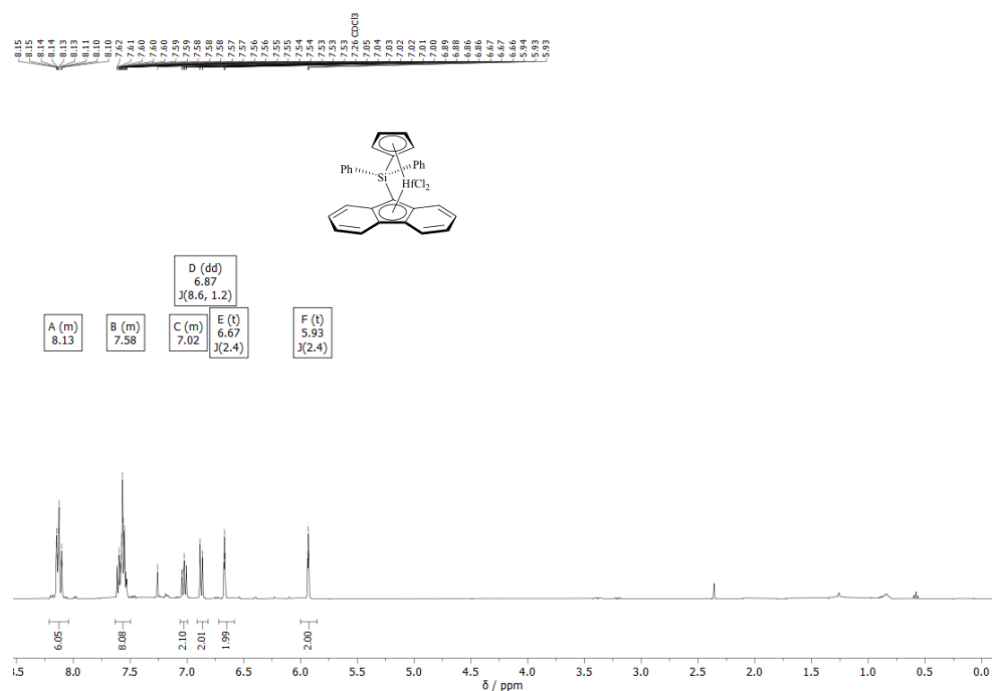
Figure S25: ^{1}H NMR (400 MHz) spectrum of **IV** in CDCl$_3$.
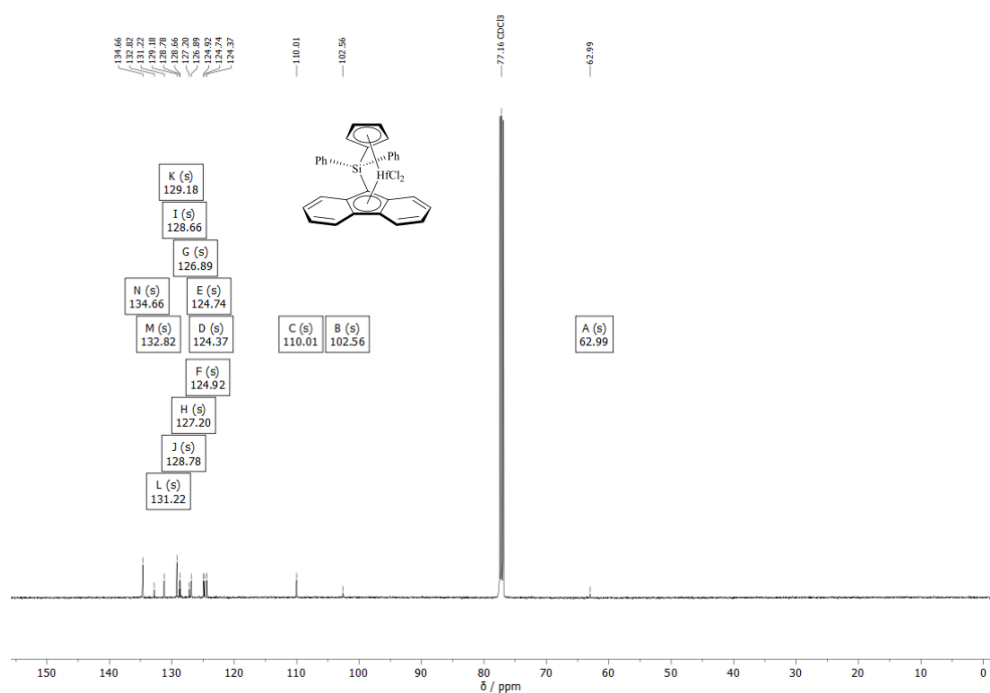
Figure S26: ^{13}C {^{1}H} NMR (125 MHz) spectrum of **IV** in CDCl$_3$.

Polymer spectra

All ^{13}C {^1H} NMR spectra were measured in C_6D_5Br at 140 °C. The tacticity distribution was quantified *via* integration of the methyl region between 22.0 – 19.5 ppm. The content of syndiotactic [rrrr] pentad is reported as a mole fraction (in percent) with respect to the sum of all pentads.
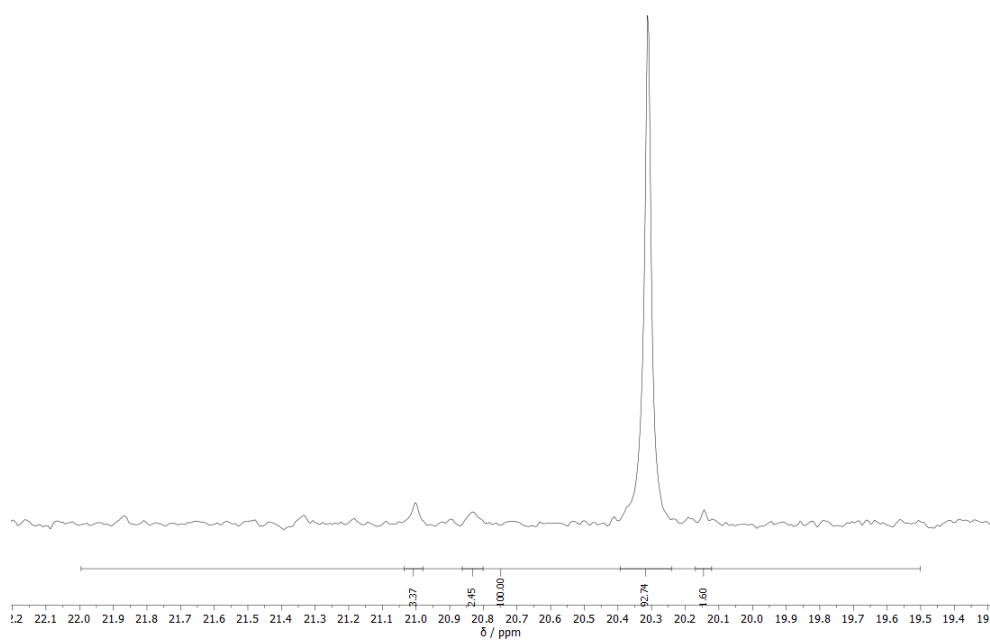
Figure S27: Pentad distribution of entry 1 in the ^{13}C {^1H} NMR spectrum.
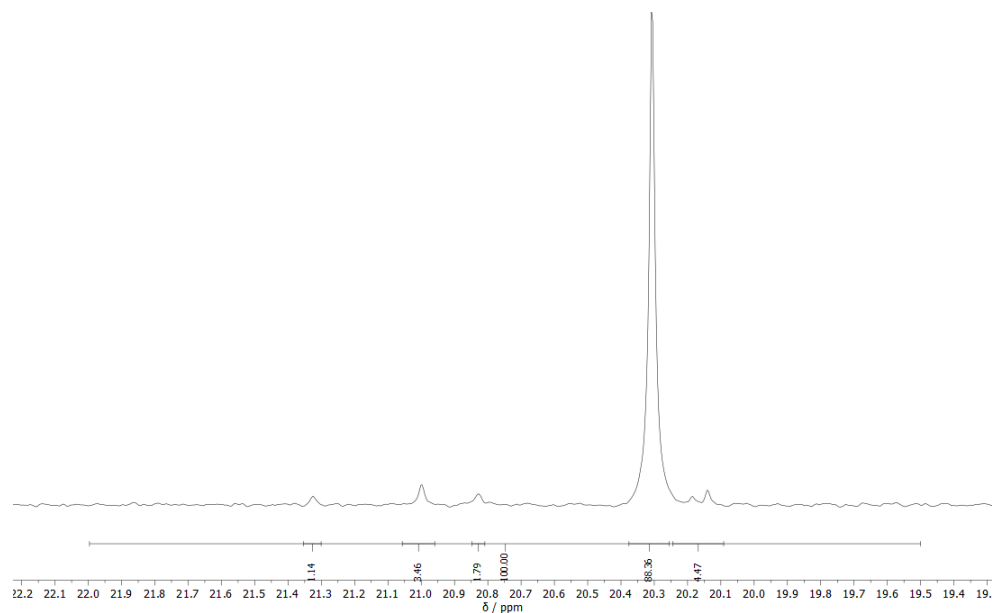
Figure S28: Pentad distribution of entry 2 in the ^{13}C {^{1}H} NMR spectrum.
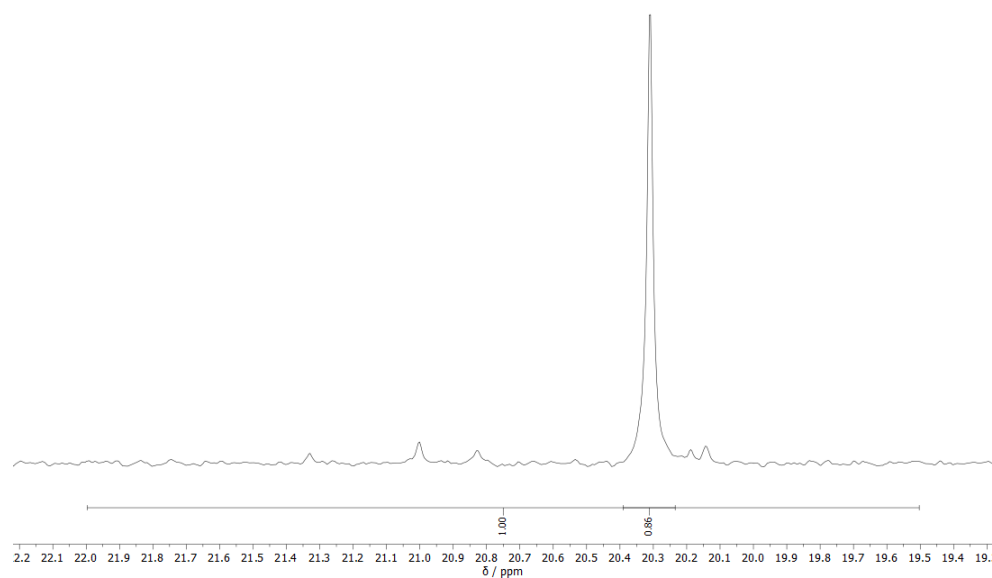
Figure S29: Pentad distribution of entry 3 in the ^{13}C {^{1}H} NMR spectrum.
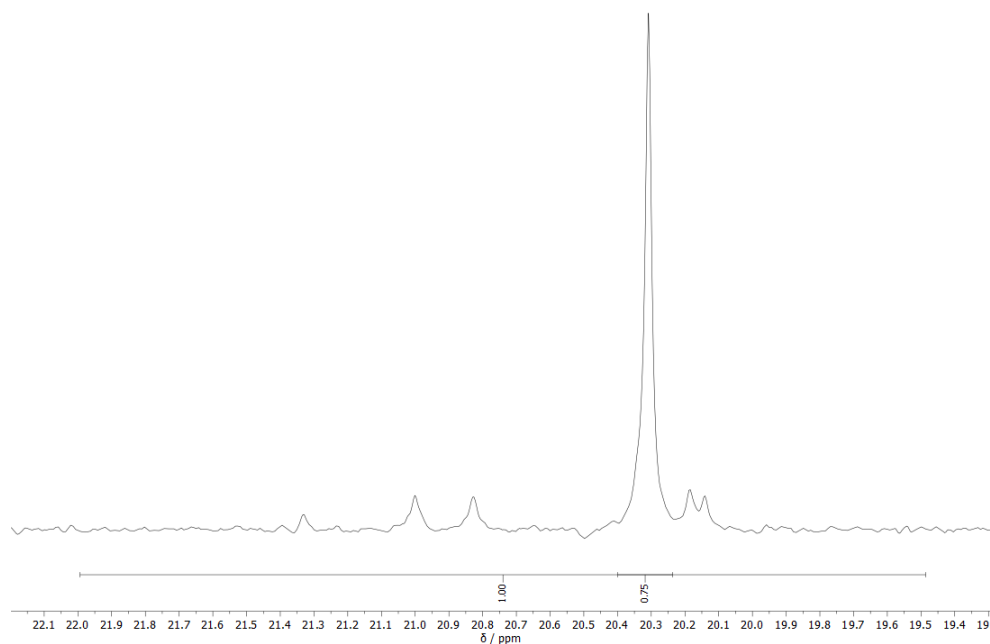
Figure S30: Pentad distribution of entry 4 in the ^{13}C {^{1}H} NMR spectrum.
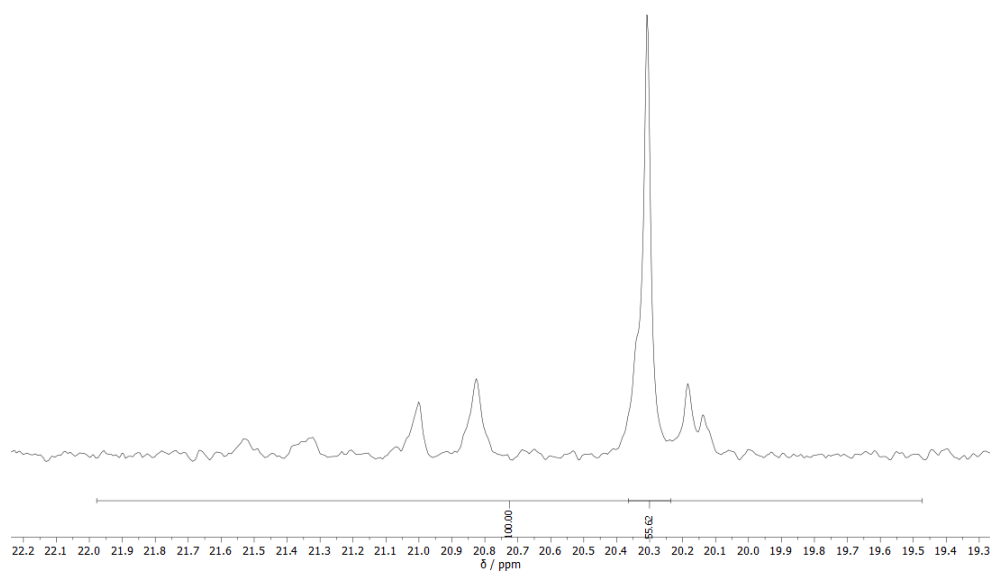
Figure S31: Pentad distribution of entry 5 in the ^{13}C {^{1}H} NMR spectrum.
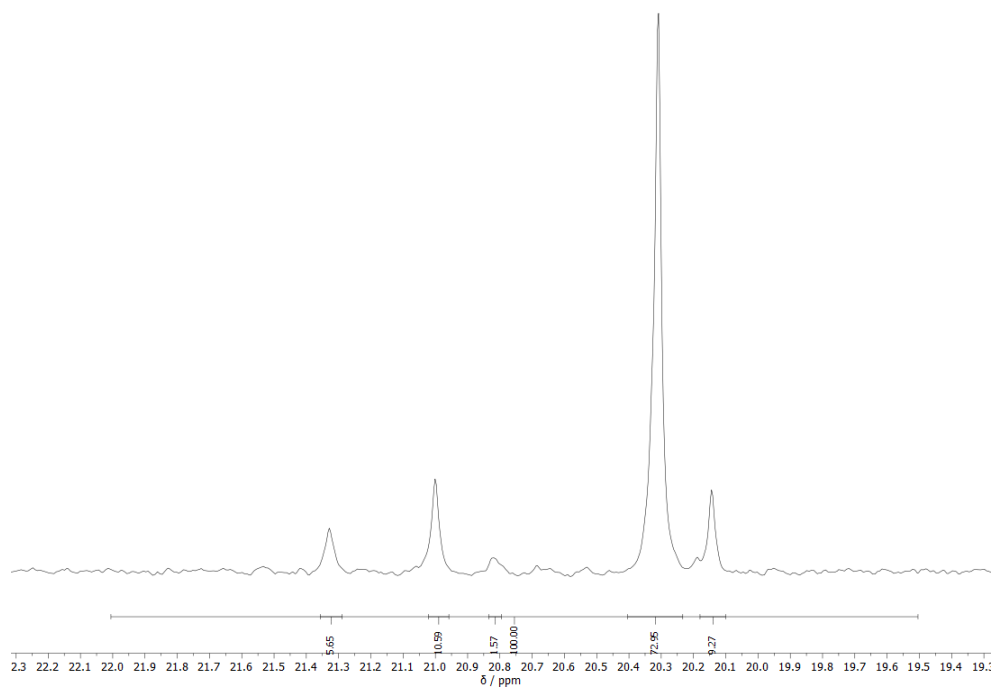
Figure S32: Pentad distribution of entry 6 in the ^{13}C {^1H} NMR spectrum.
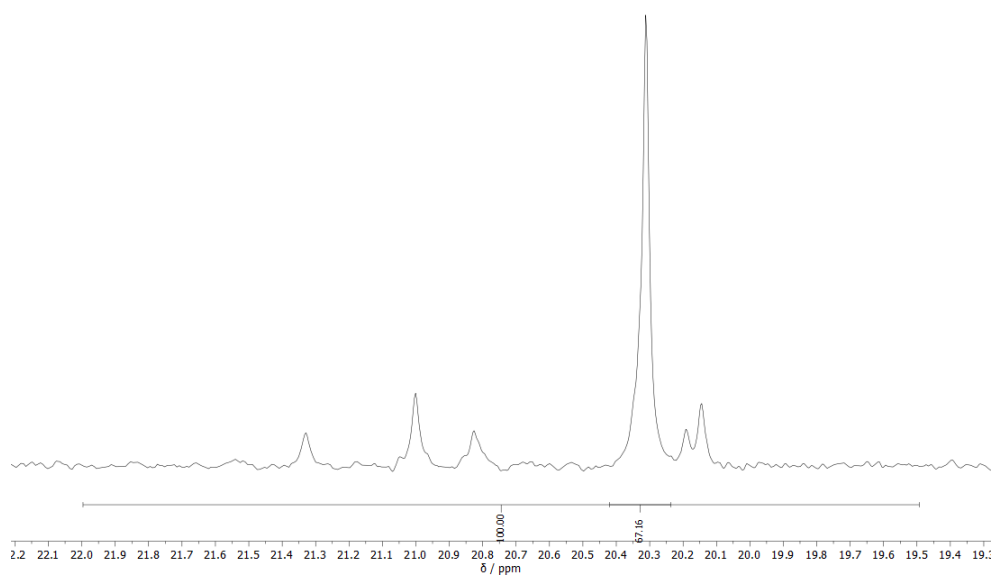
Figure S33: Pentad distribution of entry 8 in the ^{13}C {^1H} NMR spectrum.
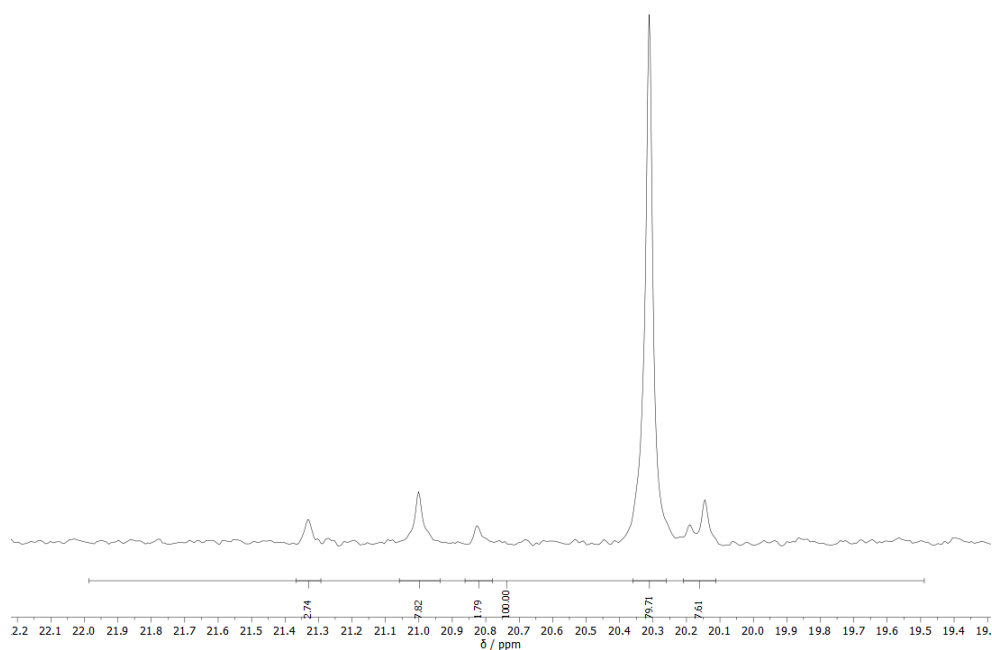
Figure S34: Pentad distribution of entry 9 in the ^{13}C {^{1}H} NMR spectrum.
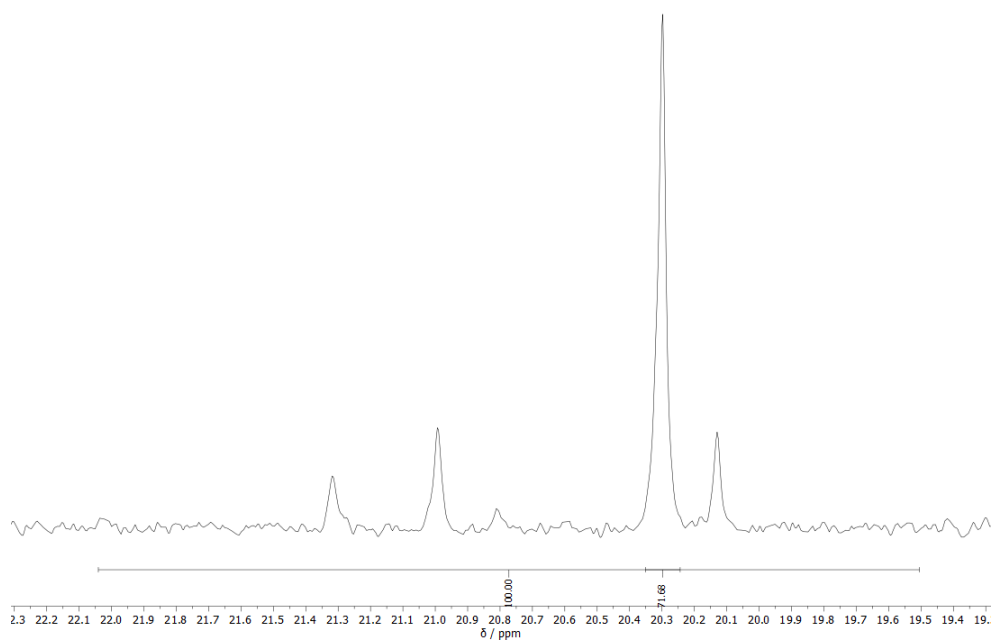
Figure S35: Pentad distribution of entry 13 in the ^{13}C {^{1}H} NMR spectrum.
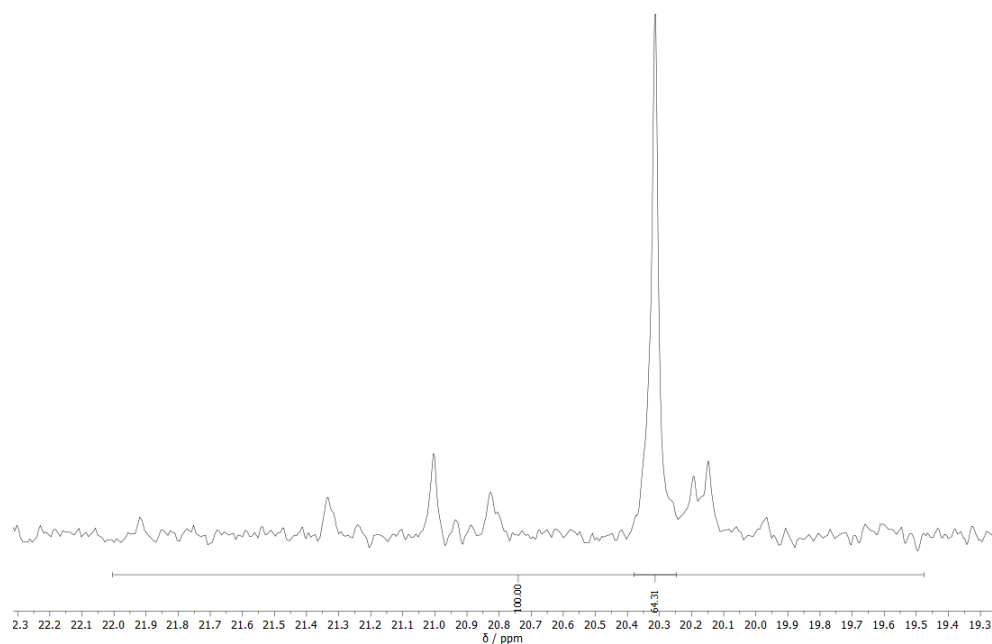
Figure S36: Pentad distribution of entry 14 in the ^{13}C {^{1}H} NMR spectrum.
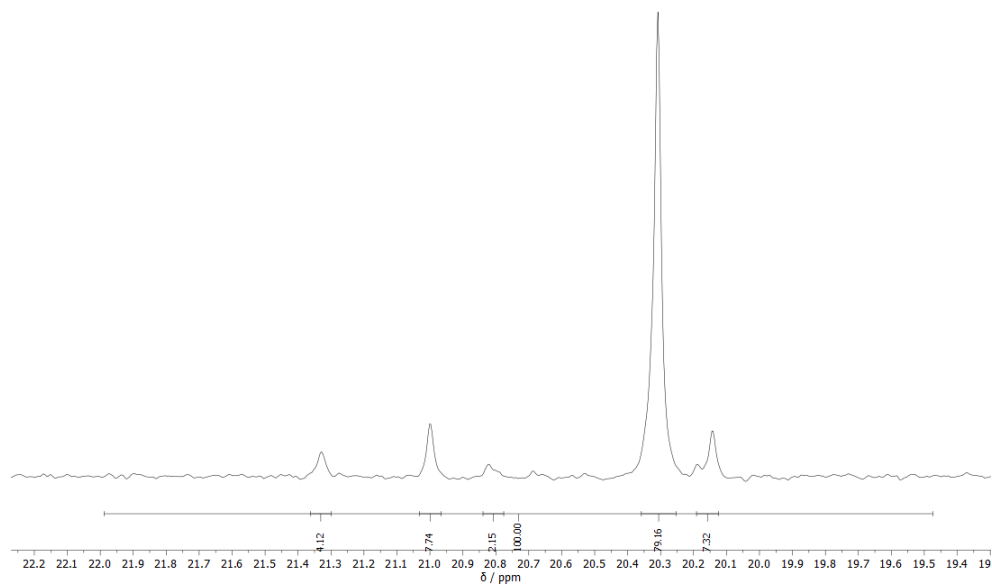
Figure S37: Pentad distribution of entry 15 in the ^{13}C {^{1}H} NMR spectrum.

110
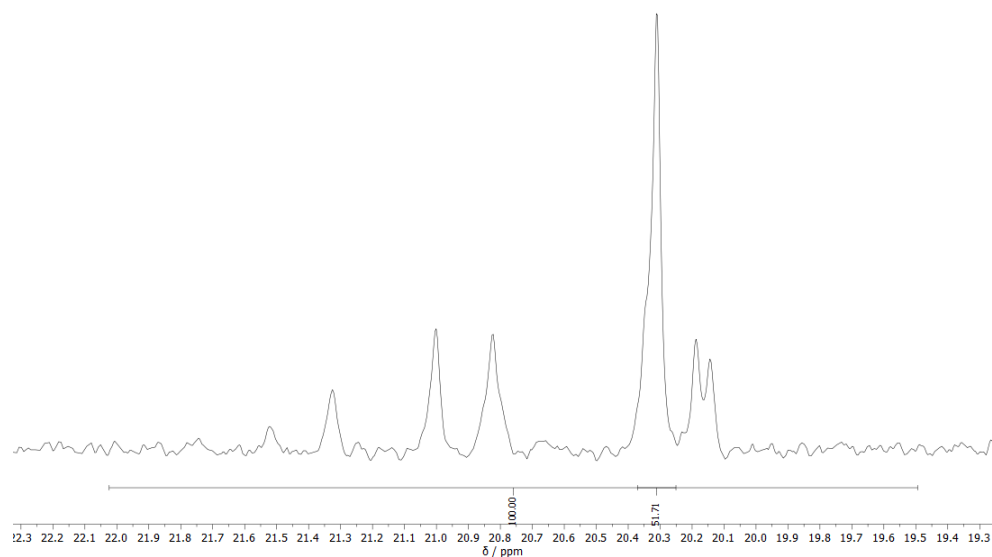
Figure S38: Pentad distribution of entry 16 in the ^{13}C {^{1}H} NMR spectrum.
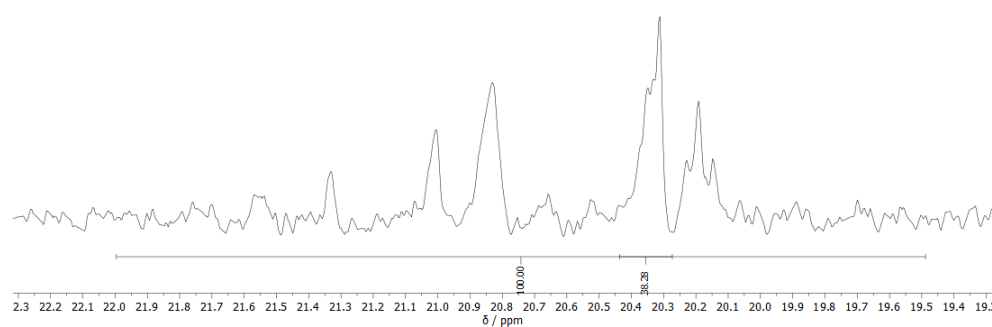
Figure S39: Pentad distribution of entry 17 in the ^{13}C {^{1}H} NMR spectrum.

111
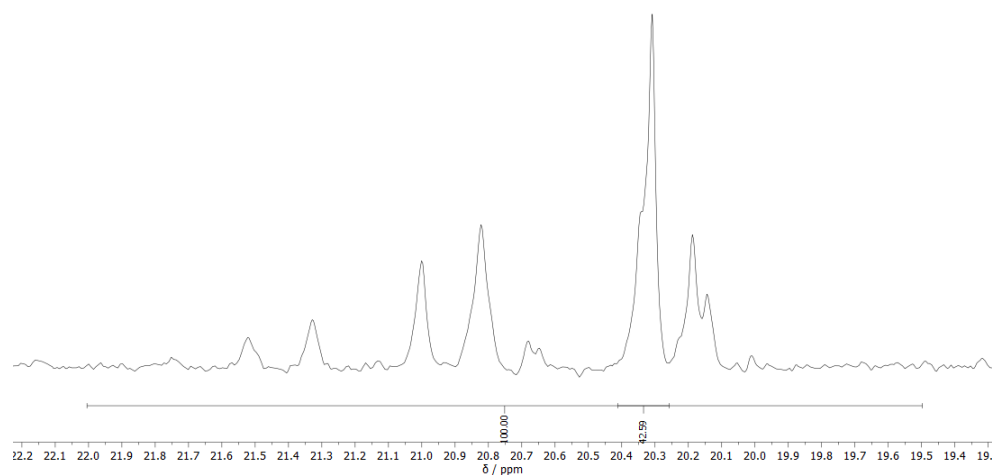
Figure S40: Pentad distribution of entry 18 in the ^{13}C {^{1}H} NMR spectrum.
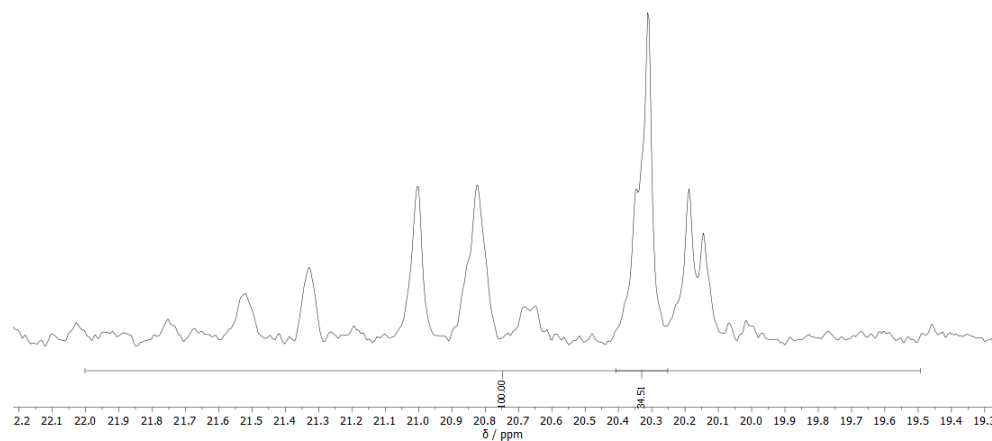
Figure S41: Pentad distribution of entry 19 in the ^{13}C {^{1}H} NMR spectrum.
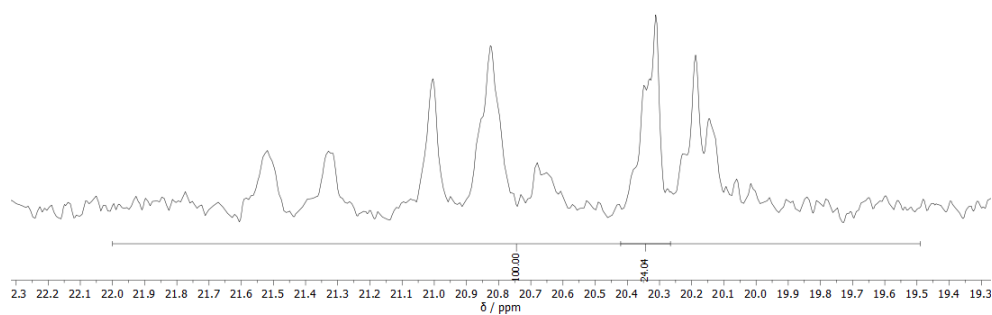
Figure S42: Pentad distribution of entry 20 in the ^{13}C {^{1}H} NMR spectrum.
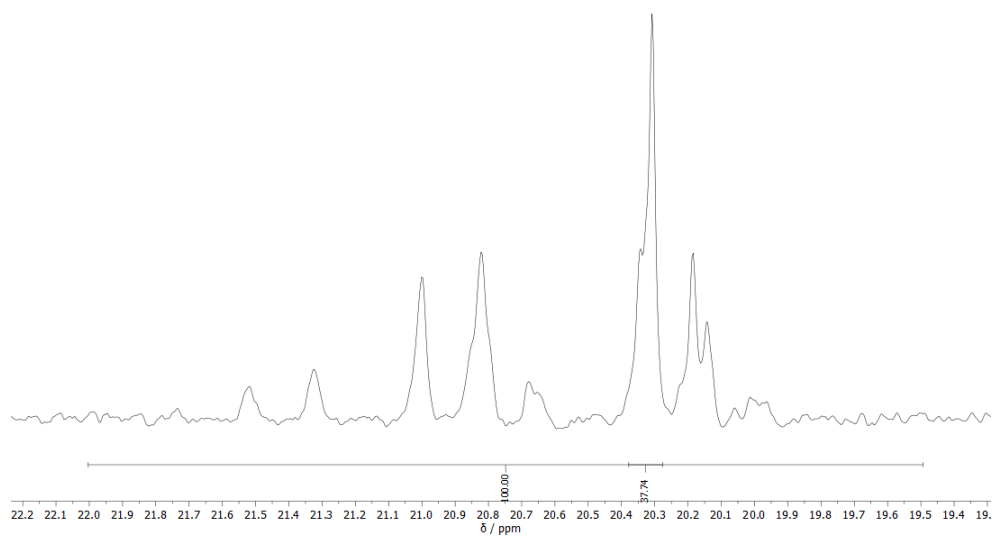
Figure S43: Pentad distribution of entry 21 in the ^{13}C {^{1}H} NMR spectrum.

113
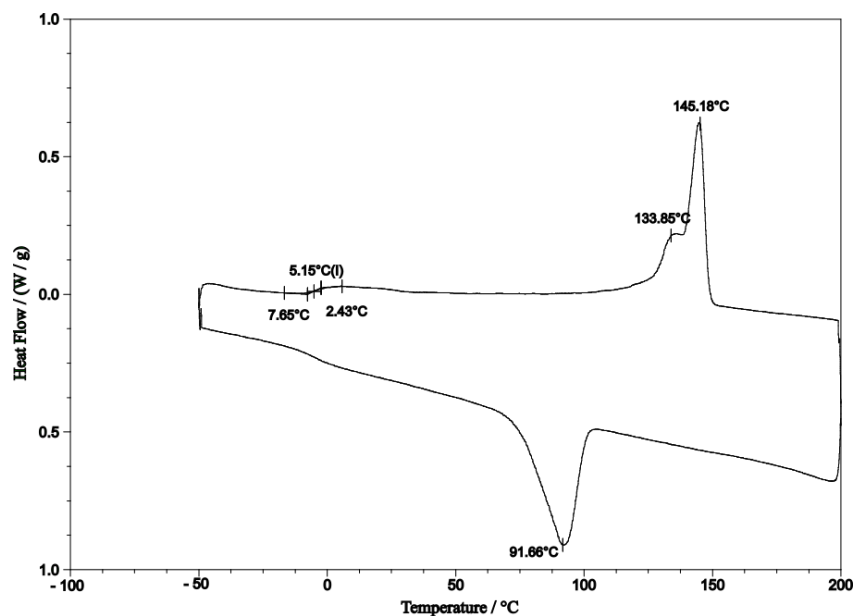
DSC analysis

Figure S44: DSC analysis of entry 1.
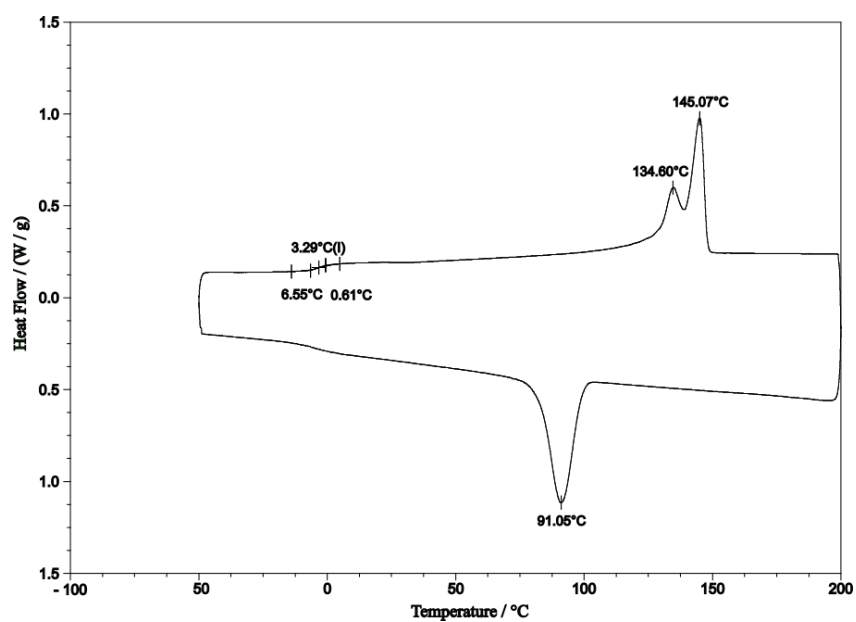
Figure S45: DSC analysis of entry 2.
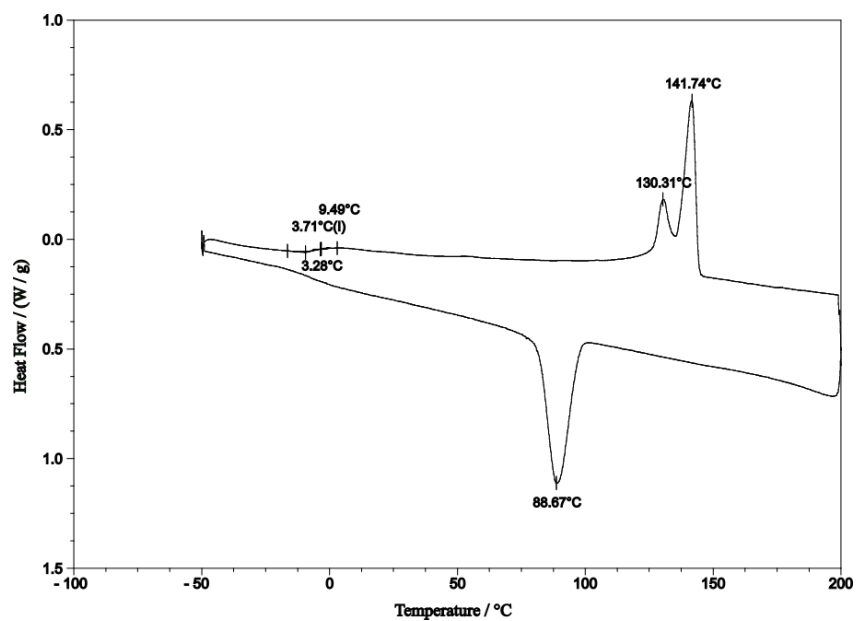
Figure S46: DSC analysis of entry 3.
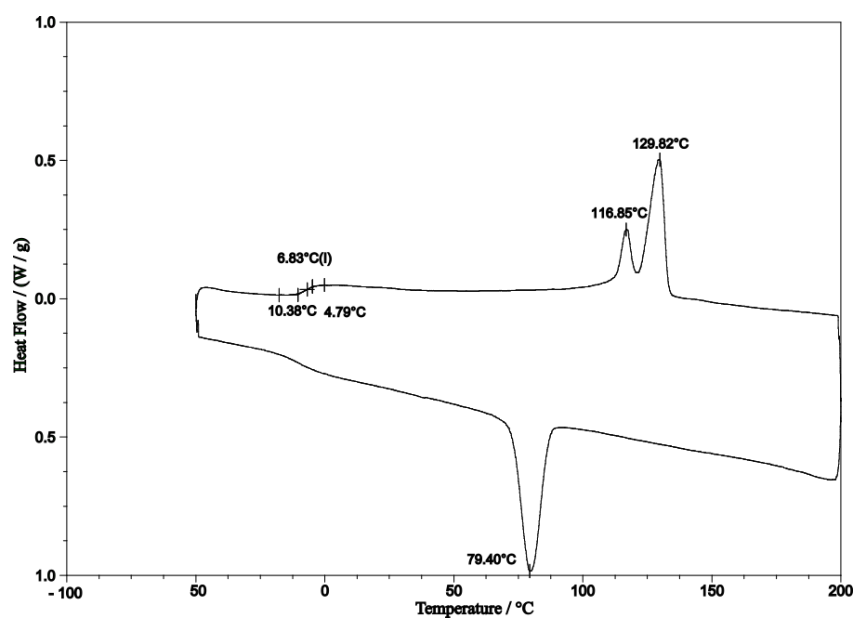
Figure S47: DSC analysis of entry 4.
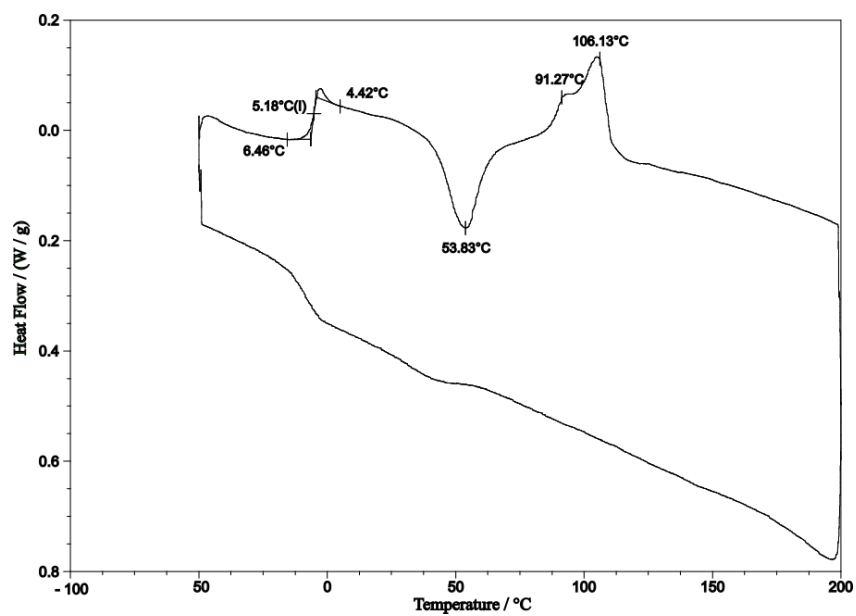
Figure S48: DSC analysis of entry 5.
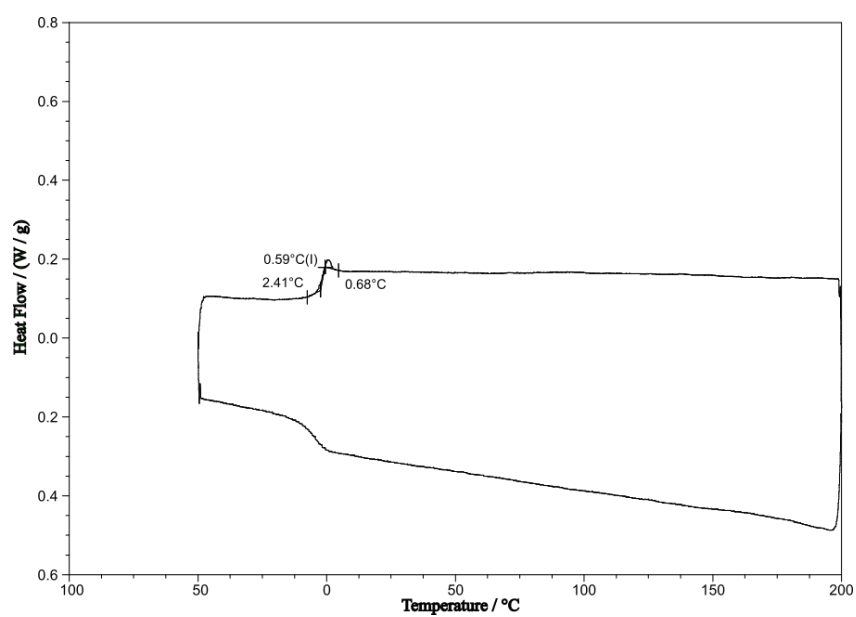
Figure S49: DSC analysis of entry 6. Exemplary for elastic, non-crystalline *s*PP.
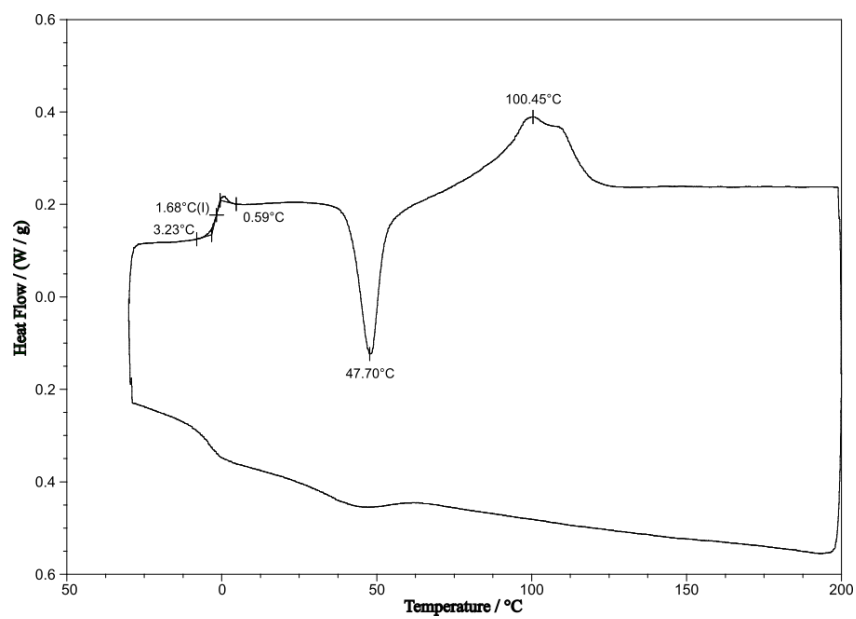
Figure S50: DSC analysis of entry 9.
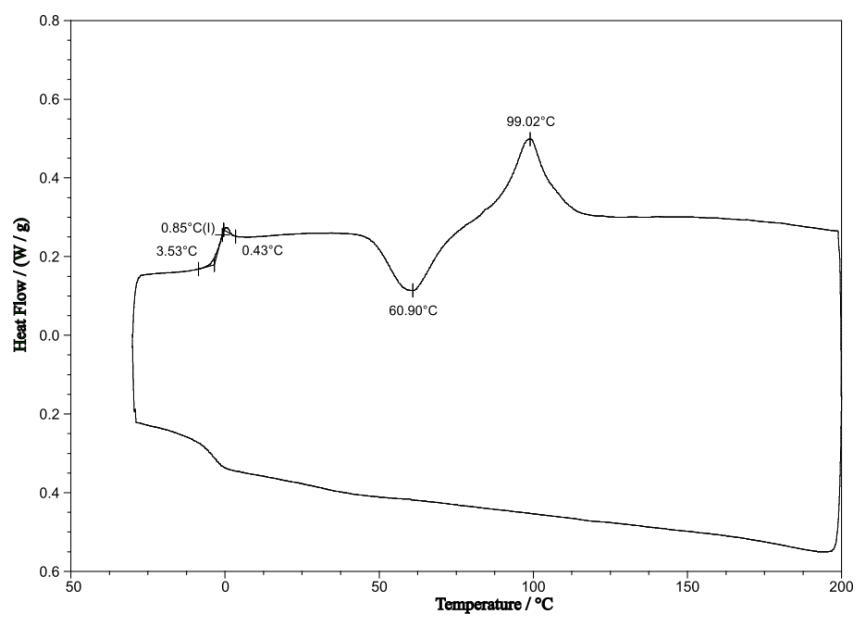
Figure S51: DSC analysis of entry 15.
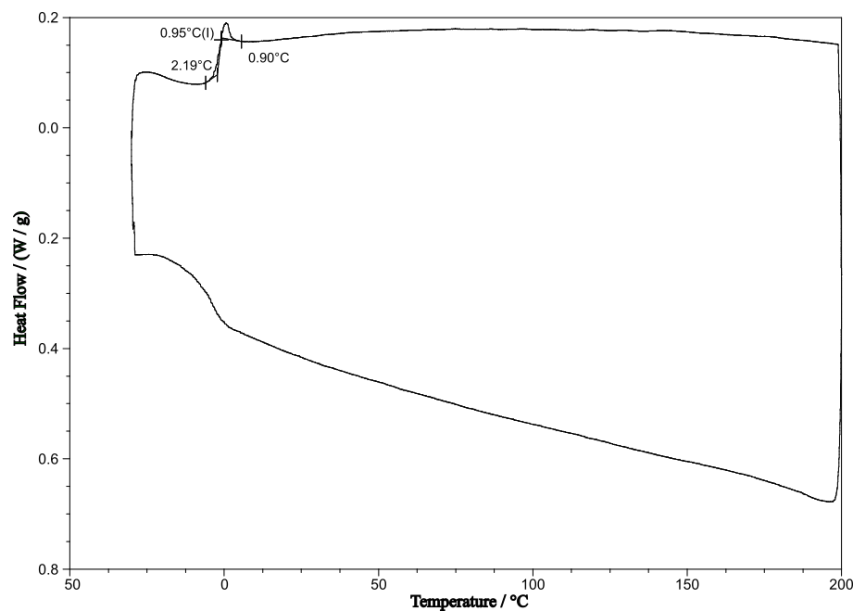
Figure S52: DSC analysis of entry 18.
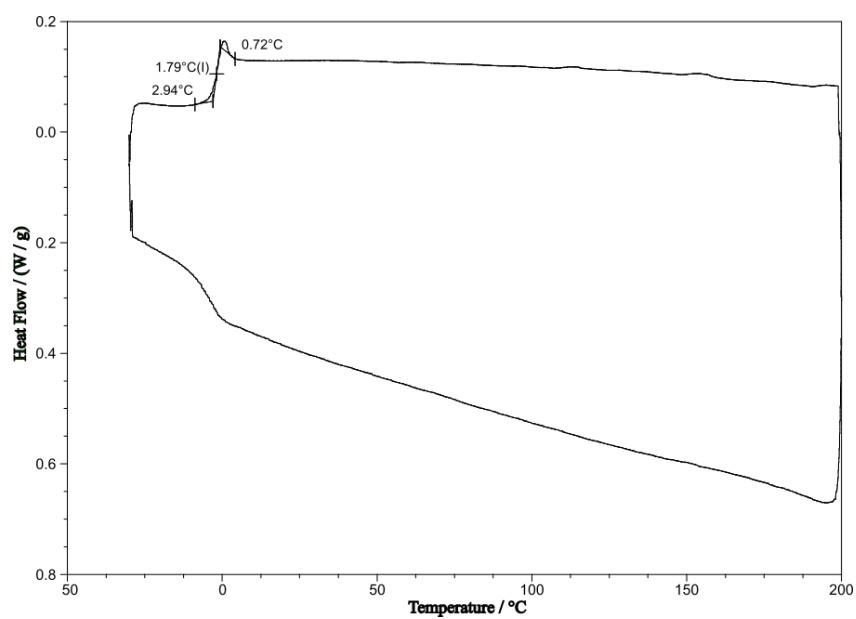
Figure S53: DSC analysis of entry 21.

GC-MS elugrams
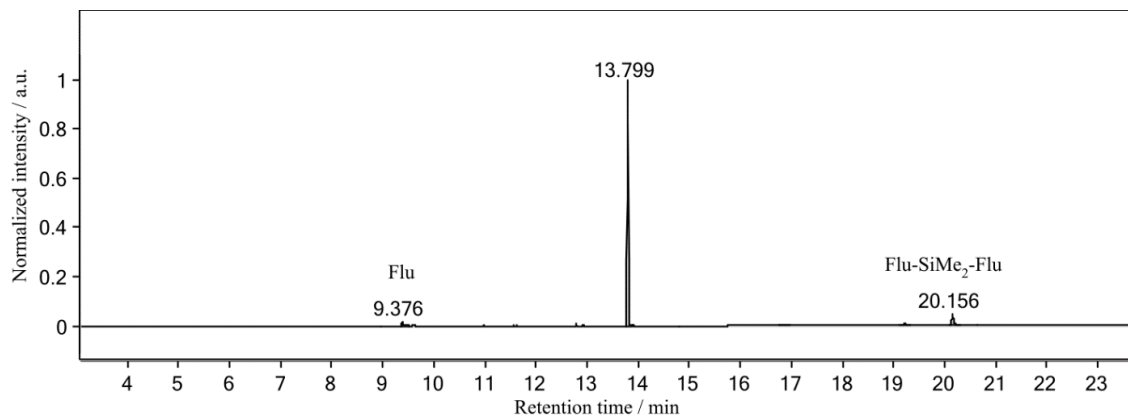
Figure S54: GC-MS elugram of *Flu-SiMe₂-Cp* **4a** with assignment of impurities.
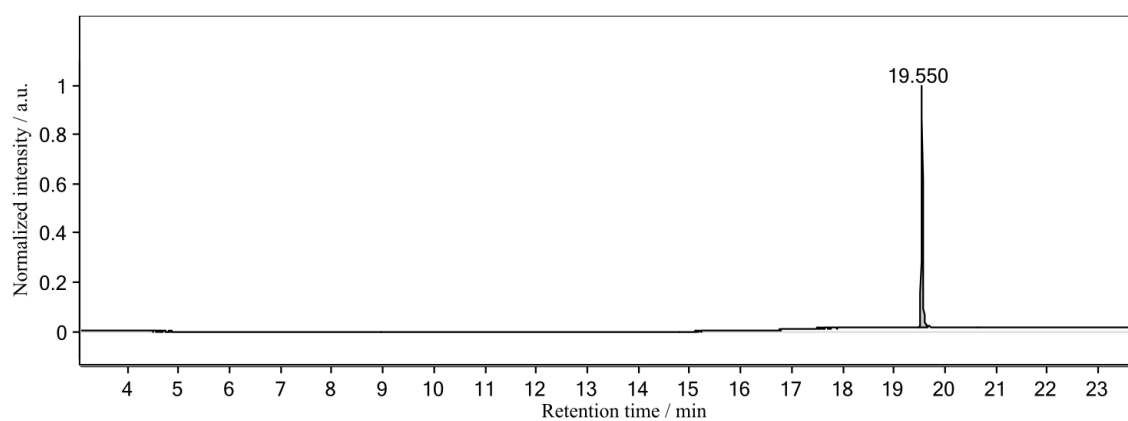
Figure S55: GC-MS elugram *of Flu-SiPh₂-Cp* **4b**.

Single crystal XRD (SC-XRD) data

The crystal structures of complexes **Ia** (CCDC: 1190113)[6], **Ib** (CCDC: 1168308)[6], **II** (CCDC: 1232978)[7] and **IV** (CCDC: 152546)[8] are literature known and were received by the Cambridge Crystallographic Data Centre (CCDC). Single crystals of complex **III** were obtained by slow diffusion of pentane into a toluene solution of **III** at 4 °C over the course of 10 days and were measured following the details given below. Characteristic distances and angles of all complexes were determined (see Figure S54) and are represented in Table 1 in the manuscript. The corresponding *D*-value was calculated by solving the nonlinear system of equations.
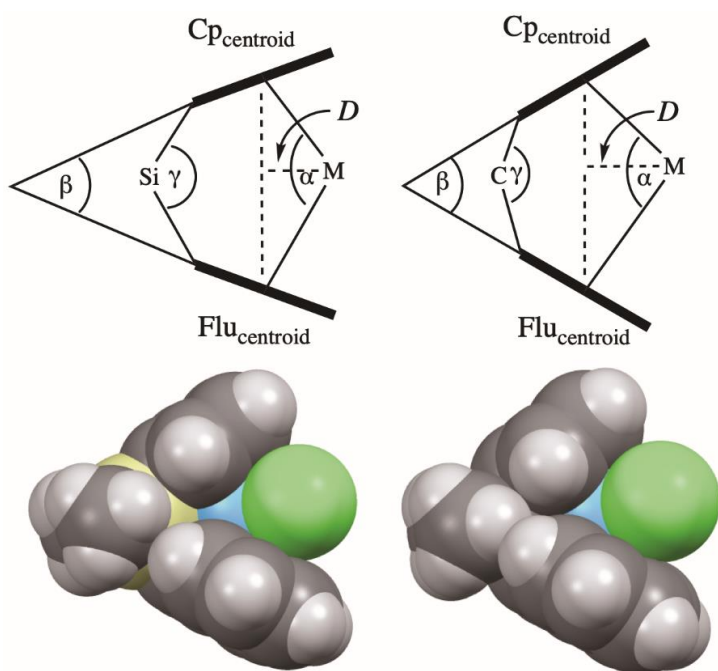
Figure S56: Schematic representation of the influence of the bridging atom on selected geometrical parameters of bridged fluorenyl-cyclopentadienyl metallocenes (top) with the bridging atom (Si, C), M = central metal (Zr, Hf), γ = bite angle (around the bridging atom), β = dihedral angle (between planes constructed through Cp, Flu), α = Flu-M-Cp (angle around the central metal), *D* = distance central metal to Cp-Flu centroid axis. Space filling representation (bottom) of Si and C bridged complexes **Ib** (right) and **III** (left).
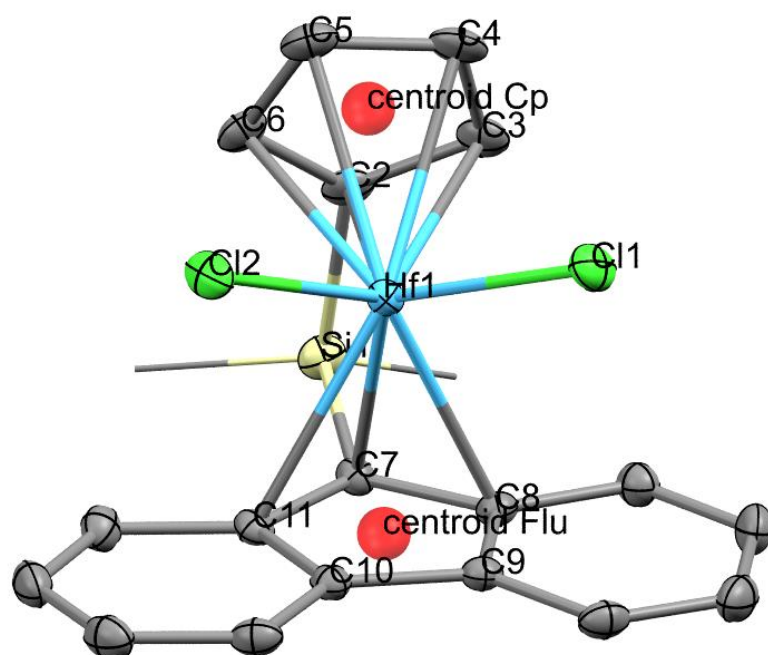
Figure S57: Molecular structure and numbering scheme of complex **III**: Displacement ellipsoids are drawn at the 50% probability level, backbone methyl groups are displayed in wireframe style for clarity. Hydrogen atoms are omitted for clarity.

General procedure

The X-ray data were collected on an X-ray single crystal diffractometer equipped with a CMOS detector (Bruker Photon-100), an IMS microsource with MoKα radiation (λ=0.71073Å) and a Helios mirror optic by using the APEX III software package.[7] The crystal was fixed on top of a microsampler using perfluorinated ether, transferred to the diffractometer and measured under a stream of cold nitrogen. A matrix scan was used to determine the initial lattice parameters. Reflections were corrected for Lorentz and polarization effects, scan speed, and background using SAINT.[8] Absorption corrections, including odd and even ordered spherical harmonics were performed using SADABS.[8] Space group assignments were based upon systematic absences, *E* statistics, and successful refinement of the structures. Structures were solved by SHELXT[9] (intrinsic phasing) with the aid of successive difference Fourier maps, and were refined against all data using with SHELXL2018[10] in conjunction with SHELXLE.[11] Methyl hydrogen atoms were refined as part of rigid rotating groups, with a C–H distance of 0.98 Å and Uiso(H)= 1.5·Ueq(C). Other H atoms were placed in calculated positions and refined using a riding model, with methylene and aromatic C–H distances of 0.99 and 0.95Å, respectively, and Uiso(H)= 1.2·Ueq(C). Non-hydrogen atoms were refined with anisotropic displacement parameters. Full-matrix least-squares refinements were carried out by minimizing $\Delta w(F_o^2-F_c^2)^2$ with the SHELXL[10] weighting scheme. Neutral atom scattering factors for all atoms and anomalous dispersion corrections for the non-hydrogen atoms were taken from *International Tables for Crystallography*.[12] Images of the crystal structures were generated with

MERCURY.[13] Crystallographic data are also deposited at the Cambridge Crystallographic Data Centre (CCDC 2059775) and are available free of charge *via* www.ccdc.cam.ac.uk/structures/.

Table S1: Crystallographic data for complex **III** (CCDC 2059775).

Diffractometer operator Christian Jandl
scanspeed 4.5s per frame
dx 40 mm
3214 frames measured in 18 data sets
phi-scans with delta_phi = 0.5
omega-scans with delta_omega = 0.5
shutterless mode

Crystal data

$C_{20}H_{18}Cl_2HfSi$	
$M_r = 535.84$	$D_x = 1.985$ Mg m^{-3}
Monoclinic, $P2_1/c$	Melting point: ? K
Hall symbol: -P 2ybc	Mo $K\alpha$ radiation, $\lambda = 0.71073$ Å
$a = 10.5378\ (5)$ Å	Cell parameters from 9607 reflections
$b = 9.2677\ (5)$ Å	$\theta = 2.5–26.7°$
$c = 18.6760\ (9)$ Å	$\mu = 6.18$ mm^{-1}
$\beta = 100.515\ (2)°$	$T = 123$ K
$V = 1793.29\ (16)$ Å^3	Fragment, orange
$Z = 4$	$0.20 \times 0.12 \times 0.06$ mm
$F(000) = 1032$	

Data collection

Bruker Photon CMOS diffractometer	3665 independent reflections
Radiation source: IMS microsource	3447 reflections with $I > 2\sigma(I)$
Helios optic monochromator	$R_{int} = 0.048$
Detector resolution: 16 pixels mm^{-1}	$\theta_{max} = 26.4°$, $\theta_{min} = 2.0°$
phi– and ω–rotation scans	$h = -13 \quad 13$
Absorption correction: multi-scan *SADABS* 2016/2, Bruker, 2016	$k = -11 \quad 11$

$T_{min} = \underline{0.612}$, $T_{max} = \underline{0.745}$	$l = \underline{-23}$ $\underline{23}$
$\underline{94151}$ measured reflections	

Refinement

Refinement on $\underline{F^2}$	Secondary atom site location: <u>difference Fourier map</u>
Least-squares matrix: <u>full</u>	Hydrogen site location: <u>inferred from neighbouring sites</u>
$R[F^2 > 2\sigma(F^2)] = \underline{0.012}$	<u>H-atom parameters constrained</u>
$wR(F^2) = \underline{0.027}$	$\underline{W = 1/[\Sigma^2(FO^2) + (0.0068P)^2 + 2.1875P]}$ $\underline{WHERE\ P = (FO^2 + 2FC^2)/3}$
$S = \underline{1.08}$	$(\Delta/\sigma)_{max} = \underline{0.001}$
$\underline{3665}$ reflections	$\Delta\rho_{max} = \underline{0.36}$ e Å^{-3}
$\underline{219}$ parameters	$\Delta\rho_{min} = \underline{-0.42}$ e Å^{-3}
$\underline{0}$ restraints	Extinction correction: <u>none</u>
$\underline{?}$ constraints	Extinction coefficient: $\underline{?}$
Primary atom site location: <u>iterative</u>	

S34

LIFDI-MS Spectra

Figure S58: Full range LIFDI mass spectrum of **III**.
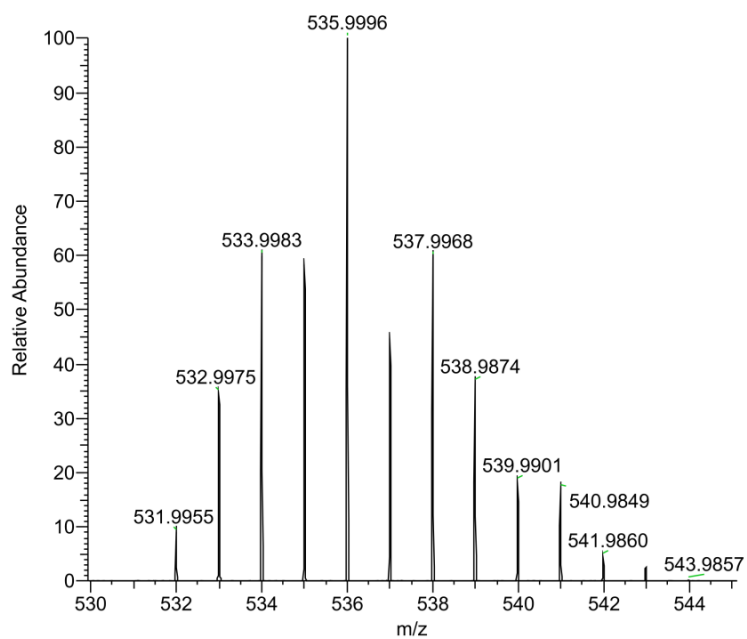
Figure S59: Zoomed in LIFDI mass spectrum of **III**.

References

1.   Gluyas, J. B.; Brown, N. J.; Farmer, J. D.; Low, P. J., Optimised syntheses of the half-sandwich complexes FeCl (dppe) Cp*, FeCl (dppe) Cp, RuCl (dppe) Cp*, and RuCl (dppe) Cp. *Aust. J. Chem.* **2017,** *70*, 113-119.

2.   Mazzotta, F.; Zitzer, G.; Speiser, B.; Kunz, D., Electron-Deficient Imidazolium Substituted Cp Ligands and their Ru Complexes. *Chemistry – A European Journal* **2020,** *26*, 16291-16305.

3.   Cortial, G.; Le Goff, X.-F.; Bousquié, M.; Boisson, C.; Le Floch, P.; Nief, F.; Thuilliez, J., Neutral ansa-bis(fluorenyl)silane neodymium borohydrides: synthesis, structural study and behaviour as catalysts in butadiene–ethylene copolymerisation. *New J. Chem.* **2010,** *34*, 2290-2297.

4.   Stone, K. J.; Little, R. D., An exceptionally simple and efficient method for the preparation of a wide variety of fulvenes. *J. Org. Chem.* **1984,** *49*, 1849-1853.

5.   Chajara, K.; Ottosson, H., An improved pathway to 6, 6-disubstituted fulvenes. *Tetrahedron Lett.* **2004,** *45*, 6741-6744.

6.   Razavi, A.; Ferrara, J., Preparation and crystal structures of the complexes (η5-C5H4CMe2η5-C13H8) MCl2 (M= Zr, Hf) and their role in the catalytic formation of syndiotactic polypropylene. *J. Organomet. Chem.* **1992,** *435*, 299-310.

7.   Razavi, A.; Atwood, J. L., Preparation and crystal structures of the complexes (η5-C5H4CPh2-η5-C13H8) MCl2 (M= Zr, Hf) and the catalytic formation of high molecular weight high tacticity syndiotactic polypropylene. *J. Organomet. Chem.* **1993,** *459*, 117-123.

8.   Izmer, V. V.; Agarkov, A. Y.; Nosova, V. M.; Kuz'mina, L. G.; Howard, J. A. K.; Beletskaya, I. P.; Voskoboynikov, A. Z., ansa-Metallocenes with a Ph2Si bridge: molecular structures of HfCl2[Ph2Si(η5-C13H8)(η5-C5H4)] and HfCl2[Ph2Si(C13H9)(η5-C5H4)]2. *J. Chem. Soc., Dalton Trans.* **2001**, 1131-1136.

10.1.2 Supporting Information for Chapter 5

Perfectly Isotactic Polypropylene upon In Situ Activation of Ultrarigid meso Hafnocenes

Lucas Stieglitz,[a]‡ Tim M. Lenz,[a]‡ Andreas Saurwein[a] and Bernhard Rieger[a]*

[a]Wacker-Lehrstuhl für Makromolekulare Chemie, Catalysis Research Center, Technische Universität München, Lichtenbergstrasse 4, 85748 Garching bei München, Germany.

Table of Contents

General

All manipulations with air and moisture sensitive compounds were carried out either under argon using standard Schlenk techniques or in an argon (4.6) filled glove box from *MBraun*. If not otherwise mentioned, all chemicals are commercially available, purchased from *Aldrich*, *Acros*, *ABCR* or *VWR*, and used without further purification. All deuterated solvents for NMR measurements were obtained from *Sigma-Aldrich*. Dry solvents were obtained from a *MBraun* MB-SPS-800 solvent purification system or dried over Al_2O_3 and stored over molecular sieve 3 Å.

NMR measurements have been performed on a *Bruker* AVHD500, *Bruker* AV500-C, *Bruker* AVHD400 or *Bruker* ARX-300. Chemical shifts were referenced to signals from C_6D_6 (7.16 ppm: ^1H and 128.1 ppm: ^{13}C), toluene-d_8 (2.09 ppm: ^1H and 20.4 ppm: ^{13}C) and internally added tetramethylsilane (0.00 ppm: ^{29}Si). Polymer ^{13}C NMR spectra were measured with an ARX-300 spectrometer at 140 °C in bromobenzene-d_5 with 40−60 mg mL^{-1} and 14k scans with 5 mm OD tubes. Acquisition conditions were: 30° flip angle; 1.82 sec acquisition time, 2 sec relaxation delay. Broad-band proton decoupling was achieved with a WALTZ16 sequence. The degree of isotacticity was determined *via* the integration of the corresponding [mmmm]-pentade (21.85 ppm)[1] against the region of 19.5−22.0 ppm.

Gel permeation chromatography (GPC) was performed with a PL- GPC 220 instrument equipped with 2x Olexis 300 mm × 7.5 mm columns and triple detection via a differential refractive index detector, a PL-BV 400 HT viscometer, and light scattering (Prescision Detectors Model 2040, 15 and 90°). Measurements were performed at 160 °C using HPLC-grade 1,2,4-trichlorobenzene (TCB; 100 mg L^{-1} BHT) from Sigma-Aldrich with a constant flow rate of 1 mL/min and a calibration set with narrow-MWD polyethylene (PE) and polystyrene (PS) standards. Samples were prepared by dissolving 0.5−0.7 mg of the polymer in 1.0 mL of stabilized TCB for 1 h at 140 °C immediately before each measurement. The molecular mass was determined absolutely against PS standards by using dn/dc = 0.097 mL g^{-1}.[2]

Differential scanning calorimetry (DSC) analysis was conducted on a DSC Q2000 instrument. The polymer (4−5 mg) was sealed into a DSC aluminum pan and heated from 50 to 200 °C at 10 °C/min. After the temperature was held for 2 min, the sample was cooled to 50 °C at 10 °C/min and heated again in the same manner. The reported values are those determined in the second heating cycle.

Liquid injection field desorption ionization mass spectrometry (LIFDI-MS) was carried out directly from an inert-atmosphere glovebox with a Thermo Fisher Scientific Exactive Plus Orbitrap instrument equipped with an ion source from Linden CMS.[3]

2

Syntheses

meso-dimethylsilanediylbis[(4-(3'-5'-di-tert-butylphenyl)-7-methoxy-2-methylindenyl)]hafnium dichloride meso-I

1

meso-**I**

$C_{52}H_{66}Cl_2HfO_2Si$

M: 1000,57 g/mol
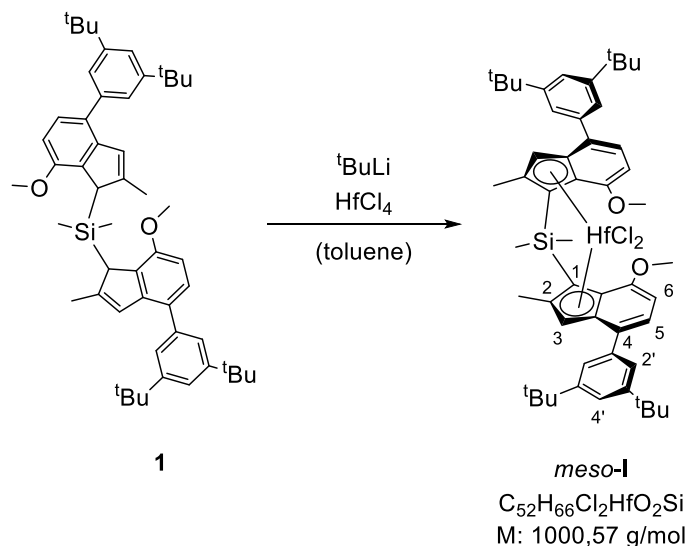
meso-**I** was synthesized according to a modified literature procedure.[4,5] Bis[4-(3,5-di-tert-butylphenyl)-7-methoxy-2-methylindenyl)dimethyl silane **1** (500 mg, 0.66 mmol, 1.00 eq.) was dissolved in dry toluene (40 mL). At 0 °C, ^{t}BuLi (1.70 M, 0.82 mL, 1.39 mmol, 2.10 eq.) in hexane was added dropwise and the mixture was stirred at 0 °C for 30 minutes. The mixture was warmed to room temperature and stirred for three hours. At −78 °C, the yellow suspension was transferred via cannula to a suspension of $HfCl_4$ (213 mg, 0.66 mmol, 1.00 eq.) in dry toluene (20 mL). The orange suspension was warmed to room temperature while stirring over a course of 20 hours. In a glovebox, the suspension was filtered through a syringe filter and the solvent was evaporated. The orange solid was dissolved in toluene (5 mL) and pentane (2.5 mL). Over the course of 16 hours at −32 °C, an orange precipitate formed. Removal of the overlaying solution and drying under vacuum yielded the pure meso isomer meso-dimethylsilanediylbis[(4-(3'-5'-di-tertbutylphenyl)-7-methoxy-2-methylindenyl)]hafnium dichloride **I** (86.3 mg, 86:2 µmol, 13%) as an orange crystalline solid. Single crystals suitable for X-ray diffraction analysis were obtained by diffusing pentane into a saturated solution of the complex in toluene at 4 °C.

^{1}H NMR (400 MHz, 298 K, C$_6$D$_6$) δ (ppm) = 7.93 (d, ^3J = 1.8 Hz, 4H, H-2'), 7.63 (t, ^3J = 1.8 Hz, 2H, H-4'), 7.23 (d, ^3J = 7.7 Hz, 2H, H-5), 7.02 (s, 2H, H-2), 5.91 (d, ^3J = 7.8 Hz, 2H, H-6), 3.33 (s, 6H, OCH$_3$), 2.32 (s, 6H, CH$_3$), 1.48 (s, 36H, CMe$_3$), 1.27 (s, 3H, SiCH$_3$), 0.92 (s, 3H, SiCH$_3$).

^{13}C {1H} NMR (101 MHz, 298 K, C$_6$D$_6$) δ (ppm) = 156.2, 150.9, 139.7, 135.3, 134.9, 130.9, 123.9, 123.6, 120.7, 120.0, 102.5, 85.5, 54.5, 35.0, 31.6, 18.9, 5.9, 5.3.

3

^{29}Si NMR (99 MHz, 298 K, toluene-d$_8$) δ (ppm) = −11.1.

LIFDI-MS: m/z calcd 1000.3675, measd 1000.3634.

meso-dimethylsilanediylbis[(4-(3'-5'-di-tert-butylphenyl)-7-methoxy-2-methylindenyl)] dimethylhafnium _meso_-I$_{Me}$

meso-**I**

meso-**IMe**

C$_{54}$H$_{72}$HfO$_2$Si

M: 959,74 g/mol
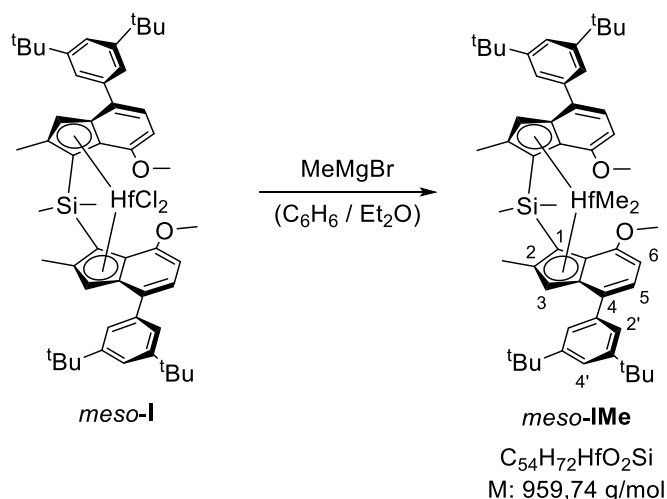
meso-dimethylsilanediylbis[(4-(3'-5'-di-tert-butylphenyl)-7-methoxy-2-methylindenyl)]hafnium dichloride **I** (20.0 mg, 20.0 µmol, 1.00 eq.) was dissolved in dry benzene (10 mL) and a solution of MeMgBr (3.00 M, 0.67 mL, 200 µmol, 10.0 eq.) in Et$_2$O was added. The reaction mixture was stirred at 50 °C for 18 hours. The solvent was evaporated and the orange solid was dissolved in C$_6$D$_6$ and syringe-filtered to yield meso-dimethylsilanediylbis[(4-(3'-5'-di-tertbutylphenyl)-7-methoxy-2-methylindenyl)]dimethyl hafnium _meso_-**I$_{Me}$** in a quantitative yield. Single crystals suitable for X-ray diffraction analysis were obtained by diffusing pentane into a saturated solution of the complex in benzene at 6 °C.

^{1}H NMR (400 MHz, 298 K, C$_6$D$_6$) δ(ppm) = 7.79 (d, ^{3}J = 1.9 Hz, 4H, H-2'), 7.61 (t, ^{3}J = 1.8 Hz, 2H, H-4'), 7.26 (d, ^{3}J = 7.7 Hz, 2H, H-5), 7.09 (s, 2H, H-2), 5.96 (d, ^{3}J = 7.8 Hz, 2H, H-6), 3.35 (s, 6H, OCH$_3$), 2.19 (s, 6H, CH$_3$), 1.43 (s, 36H, CMe$_3$), 1.26 (s, 3H, SiCH$_3$), 0.91 (s, 3H, SiCH$_3$), 0.54 (s, 3H, HfCH$_3$), −1.54 (s, 3H, HfCH$_3$).

^{13}C {1H} NMR (101 MHz, 298 K, C$_6$D$_6$) δ (ppm) = 157.2, 151.1, 141.0, 135.0, 131.7, 131.2, 126.0, 123.9, 121.3, 121.0, 117.6, 101.8, 81.4, 54.7, 46.3, 37.7, 35.3, 31.9, 18.8, 6.5, 6.0.

^{29}Si NMR (99 MHz, 298 K, toluene-d$_8$) δ (ppm) = −12.6.

LIFDI-MS: m/z calcd 960.4767, measd 960.4739.

4

NMR Experiments

Conversion of *meso*-I with TIBA at 100 °C
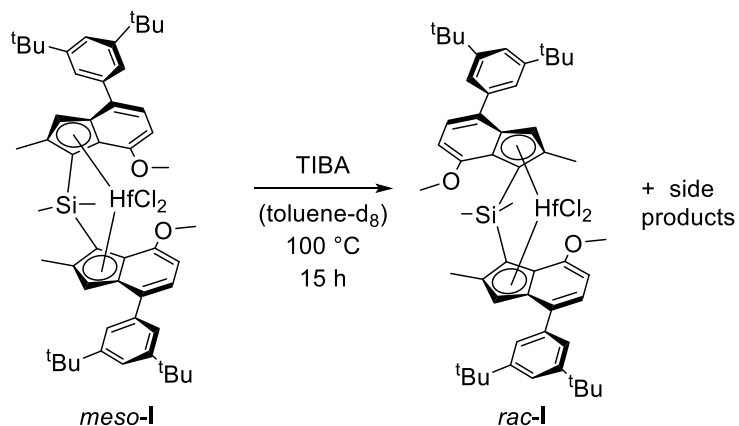
meso-I (3.00 mg, 3.00 µmol, 1.00 eq.) was dissolved in dry toluene-d$_8$ (0.4 mL, J. Young NMR tube). Subsequently, a solution of TIBA (11.0 mM, 0.27 mL, 3.00 µmol, 1.00 eq.) in toluene-d$_8$ was added and the reaction mixture was heated to 100 °C. After 15, 30, 60, 90, 120, 300 and 900 minutes at 100 °C, ^{1}H NMR spectra of the reaction mixture were recorded.

Conversion of *rac*-I with TIBA at 100 °C
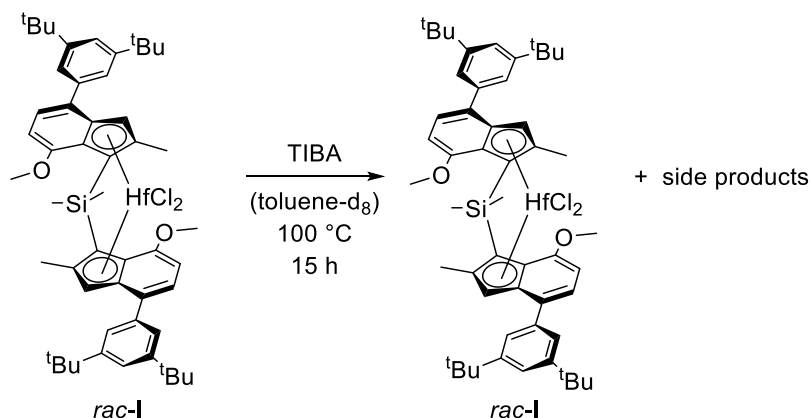
rac-I (3.00 mg, 3.00 µmol, 1.00 eq.) was dissolved in dry toluene-d$_8$ (0.4 mL, J. Young NMR tube). Subsequently, a solution of TIBA (11.0 mM, 0.27 mL, 3.00 µmol, 1.00 eq.) in toluene-d$_8$ was added and the reaction mixture was heated to 100 °C for 15 hours.

5

Conversion of *meso*-**I** with TIBA at 60 °C
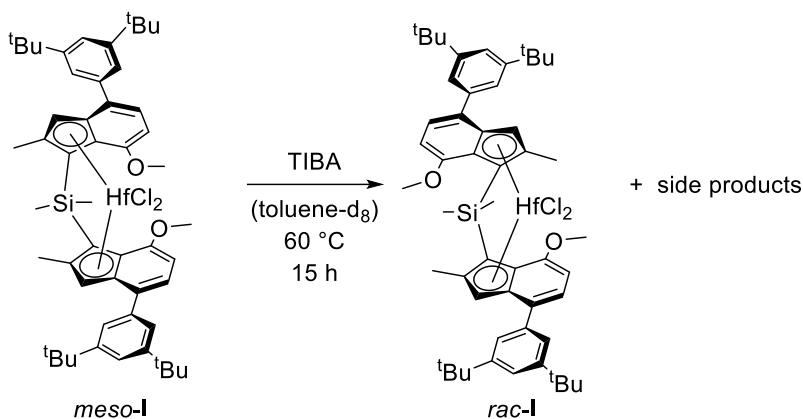
meso-**I** (3.00 mg, 3.00 µmol, 1.00 eq.) was dissolved in dry toluene-d$_8$ (0.4 mL, J. Young NMR tube). Subsequently, a solution of TIBA (0.11 M, 0.27 mL, 30.0 µmol, 10.0 eq.) in toluene-d$_8$ was added and the reaction mixture was heated to 60 °C for 15 hours.

Conversion of *rac*-**I** with TIBA at 60 °C

rac-**I** (3.00 mg, 3.00 µmol, 1.00 eq.) was dissolved in dry toluene-d$_8$ (0.4 mL, J. Young NMR tube). Subsequently, a solution of TIBA (0.11 M, 0.27 mL, 30.0 µmol, 10.0 eq.) in toluene-d$_8$ was added and the reaction mixture was heated to 60 °C for 15 hours.

6

Conversion of *meso*-I with TMA at 100 °C
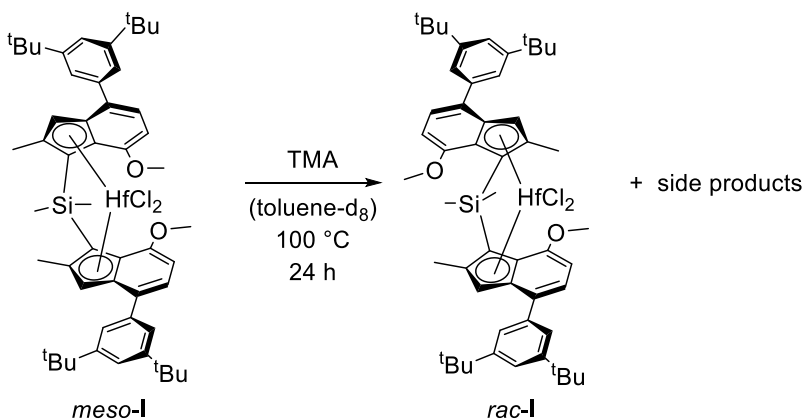
meso-I (3.00 mg, 3.00 µmol, 1.00 eq.) was dissolved in dry toluene-d$_8$ (0.4 mL, J. Young NMR tube). Subsequently, a solution of TMA (20.0 mM, 0.15 mL, 3.00 µmol, 1.00 eq.) in toluene-d$_8$ was added and the reaction mixture was heated to 100 °C. After 0.5, 1 and 24 hours at 100 °C, ^{1}H NMR spectra of the reaction mixture were recorded.

Conversion of *rac*-I with TMA at 100 °C
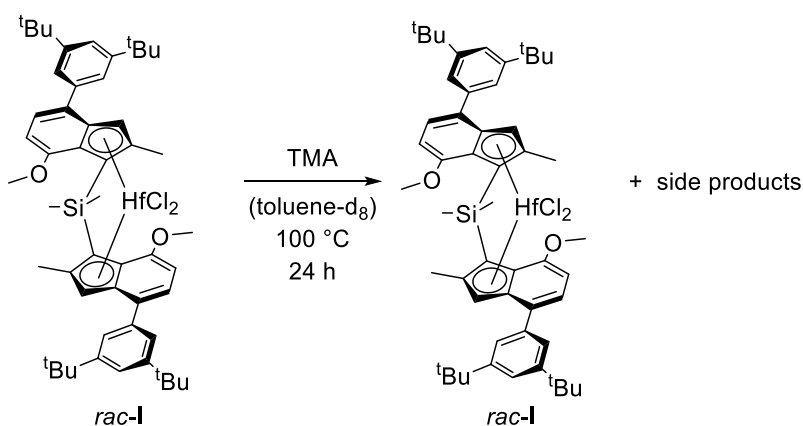
rac-I (3.00 mg, 3.00 µmol, 1.00 eq.) was dissolved in dry toluene-d$_8$ (0.4 mL, J. Young NMR tube). Subsequently, a solution of TMA (20.0 mM, 0.15 mL, 3.00 µmol, 1.00 eq.) in toluene-d$_8$ was added and the reaction mixture was heated to 100 °C. After 0.5, 1 and 24 hours at 100 °C, ^{1}H NMR spectra of the reaction mixture were recorded.

Conversion of *meso*-I with TMA and THF-d₈ at 100 °C
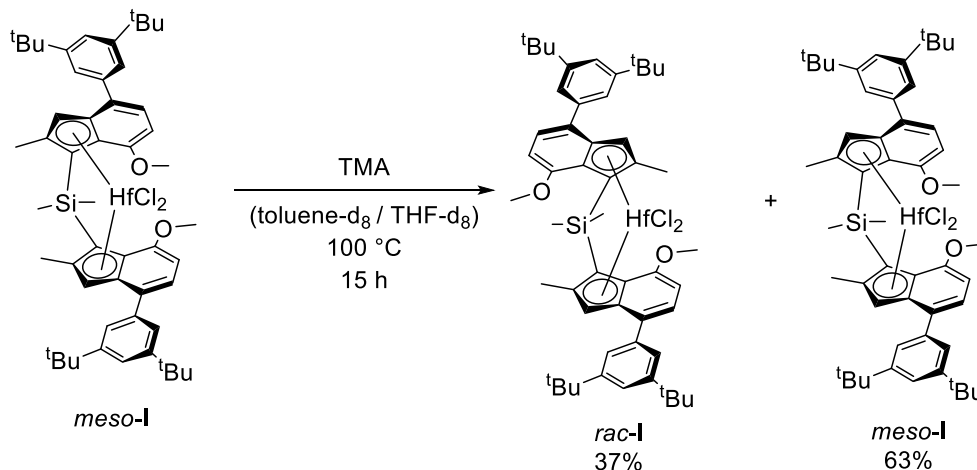
meso-I (3.00 mg, 3.00 µmol, 1.00 eq.) was dissolved in dry toluene-d8 (0.4 mL, J. Young NMR tube) and THF-d₈ (50 µL). Subsequently, a solution of TMA (20.0 mM, 0.15 mL, 3.00 µmol, 1.00 eq.) in toluene-d₈ was added and the reaction mixture was heated to 100 °C for 15 hours. The solvent was evaporated and the reaction mixture was dissolved in toluene-d₈, again. ¹H NMR revealed the presence of only *meso*-I (63%) and *rac*-I (37%) without any other species (**Fig. S7**).

Isomerization and subsequent activation of *meso*-I
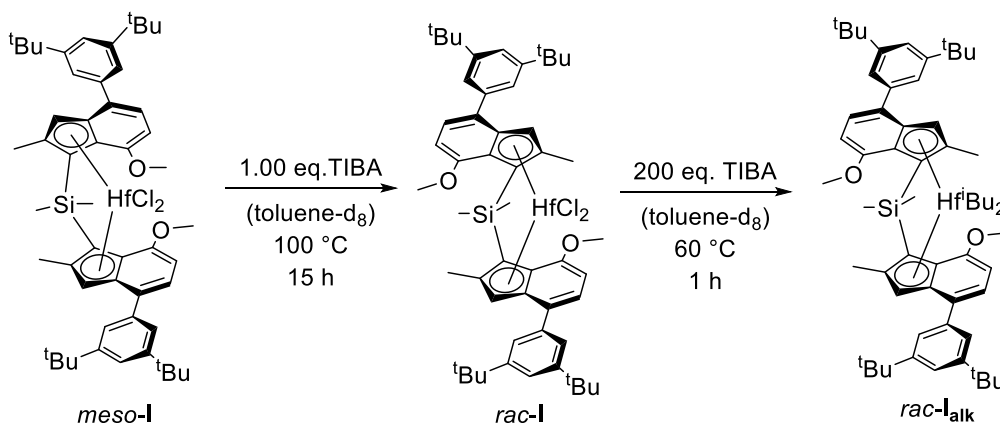
meso-I (1.65 mg, 1.65 µmol, 1.00 eq.) was dissolved in dry toluene-d8 (0.4 mL, J. Young NMR tube). Subsequently, a solution of TIBA (11.0 mM, 0.15 mL, 1.65 µmol, 1.00 eq.) in toluene-d₈ was added and the reaction mixture was heated to 100 °C for 16 hours. Further

8

TIBA (1.10 M, 0.30 mL, 0.33 mmol, 200 eq.) in toluene was added and the reaction mixture was heated to 60 °C for one hour.

Activation of *rac*-I
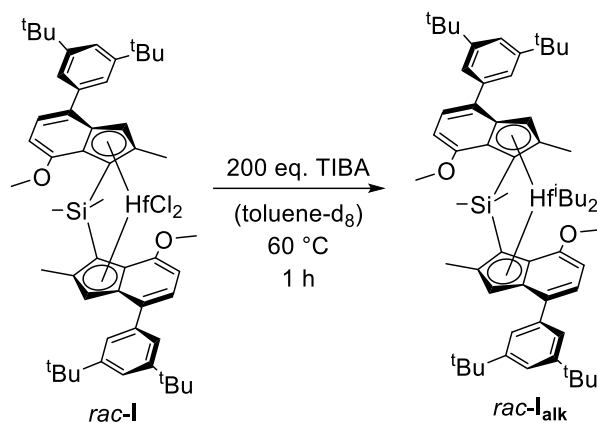
rac-I (1.65 mg, 1.65 μmol, 1.00 eq.) was dissolved in dry toluene-d_8 (0.4 mL, J. Young NMR tube). Subsequently, a solution of TIBA (1.10 M, 0.30 mL, 0.33 mmol, 200 eq.) in toluene was added and the reaction mixture was heated to 60 °C for one hour.

9

Polymerization

All polymerization reactions were performed in a 250 mL double-walled Büchi steel autoclave equipped with a KPG-stirrer (Heidolph, 1000 rpm), a temperature sensor, and a heating/cooling jacket attached to a cryo-/thermostat unit (Julabo F-25-ME). Ar pressure for all manipulations was set at 1.5 bar. Prior to polymerization, the autoclave was provided with 100 mL of dry toluene and 2 mL of 1.10 M TIBA in toluene and heated to 95 °C. After the temperature was maintained for 30 minutes, the scrubbing solution was released.

In situ Activation

For the polymerization, unless stated otherwise, the autoclave was charged with 100 mL of dry toluene and 0.5 mL of 1.10 M TIBA in toluene. The metallocene complex (1.00 eq.) was dissolved in 10 mL of dry toluene and preactivated with 200 eq. of TIBA at 60 °C for one hour. After the desired temperature was adjusted, the metallocene solution was transferred into the autoclave and pressurized with propylene. When the system was equilibrated and stable in terms of temperature and pressure, the polymerization was initiated by placing 5.00 eq. of $[Ph_3C][B(C_6F_5)_4]$ dissolved in 10 mL of dry toluene in the autoclave *via* a pressure burette (p_{Poly} + 0.5 bar).

MAO Activation

For the polymerization, the autoclave was charged with 110 mL of dry toluene and 2000 eq. of a MMAO-12 solution in toluene (7 wt% Al in toluene $[(CH_3)_{0.95}–(n\text{-}C_8H_{17})_{0.05}–AlO]_n$) was added. After the desired temperature was adjusted, the autoclave was pressurized with propylene. When the system was equilibrated and stable in terms of temperature and pressure, the polymerization was initiated by adding the metallocene complex (1.00 eq.) dissolved in 10 mL of dry toluene.

The polymerization was quenched with 2 mL of methanol, and the reaction mixture was poured into 600 mL of HCl-acidified methanol. The precipitated polymer was removed from the autoclave, and the combined polymer was washed thoroughly, first with methanol and then with acetone. The resulting polymer was suspended in acetone and treated with *Irganox* 1010 as a stabilizing agent in order to prevent rapid destruction of the polymer. After 20 minutes, the supernatant solution was decanted off and the resulting polymer was dried overnight at 70 °C.

UV-Vis spectrum

When activating *meso*-**I** *in situ* in toluene, a gradually loss of its distinct yellow color with increased activation time at 60 °C with 200 eq. TIBA was observed (see Figure S2). This degradation can be monitored *via* UV/Vis and is a hint, that *meso*-**I** is degraded when exposed to excess TIBA, as *rac*-**I** maintained its yellow color under the same conditions.
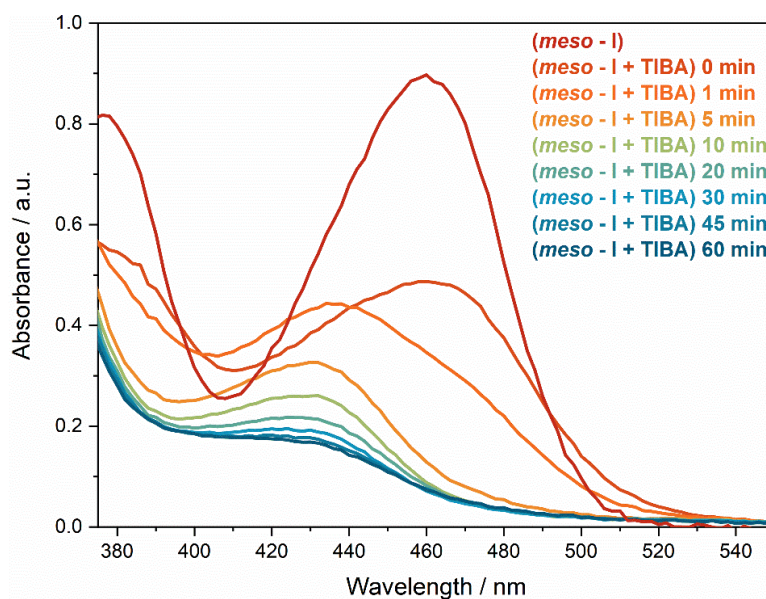
Figure S1. Stacked UV-Vis spectra of *meso*-**I** and its products upon conversion with 200 eq. TIBA at 60 °C (UV-Vis spectra were recorded at room temperature).
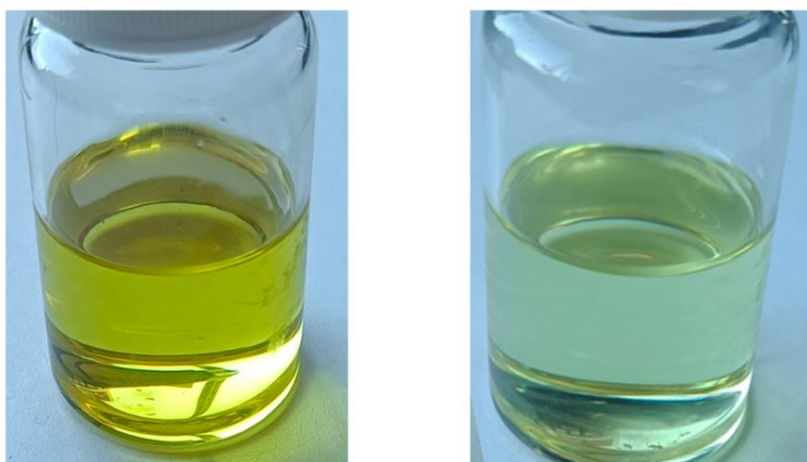
Figure S2. 1.65 mg of *meso*-**I** immediately after the addition of 200 eq. TIBA in 10 mL toluene (left) compared to after the *in situ* activation with 200 eq. TIBA in 10 mL toluene after 60 minutes at 60 °C (right).

11

12
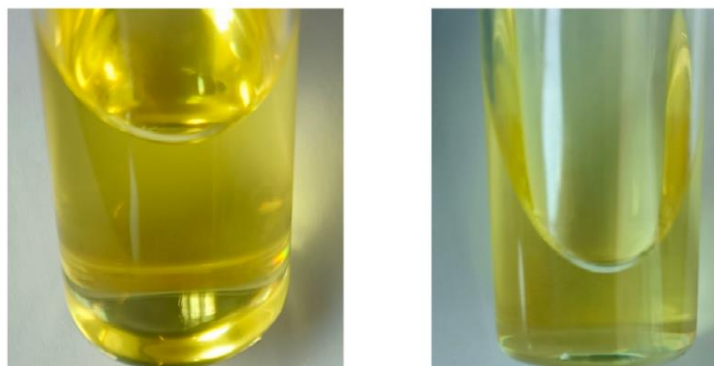
Figure S3. 1.65 mg of isomerized (1.00 eq. TIBA, 100 °C, 16h) *meso*-**I** immediately after the addition of 200 eq. TIBA in 10 mL toluene (left) compared to after the *in situ* activation with 200 eq. TIBA in 10 mL toluene after 60 minutes at 60 °C (right). Compared to Figure S2 no loss of color as an indication for a degradation was observed.

NMR-Spectra
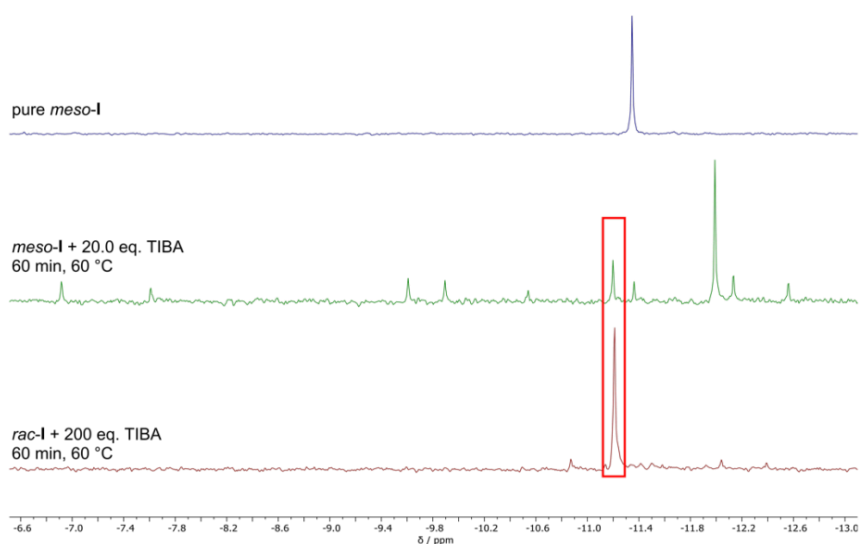
Figure S4. Excerpts of the ^{29}Si-inept NMR spectra in the range of δ = –6.6 ppm - –13.0 ppm of *meso*-**I** and its products upon conversion with 20.0 eq. TIBA at 60 °C after 60 minutes, as well as the activation product of *rac*-**I** with 200 eq. TIBA at 60 °C after 60 minutes (NMR-spectra were recorded at room temperature).
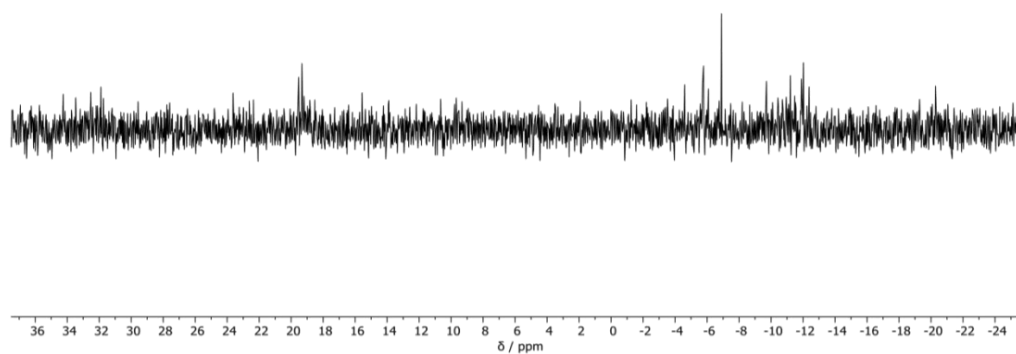
Figure S5. ^{29}Si-inept NMR of the decomposition products of *meso*-**I** with 200 eq. TIBA at 60 °C after 60 minutes (NMR-spectra were recorded at room temperature).

13
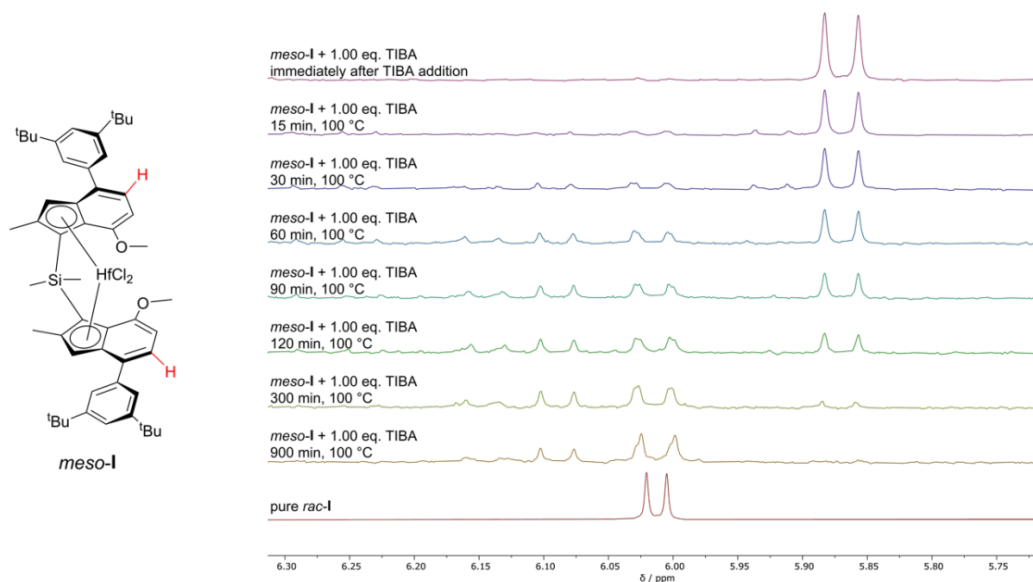
Figure S6. Excerpts of the ^{1}H NMR spectra in the range of δ = 6.30 ppm - 5.75 ppm of *meso*-**I** and its products upon conversion with 1.00 eq. TIBA at 100 °C (NMR-spectra were recorded at room temperature). The protons of *meso*-**I** corresponding to this signal are highlighted in red. For comparison, the ^{1}H NMR spectrum of *rac*-**I** in the respective range is also shown.
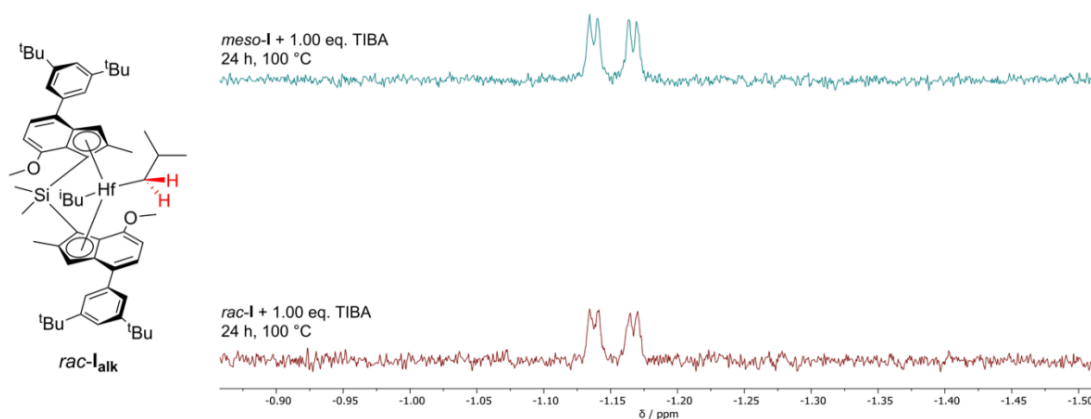
Figure S7. Excerpts of the ^{1}H NMR spectra in the range of δ = −0.90 ppm - −1.50 ppm of the products of the conversion of *meso*-**I** and *rac*-**I** with 1.00eq. TIBA at 100 °C (NMR- spectra were recorded at room temperature). The protons of the alkylated species *rac*-**I**$_{alk}$ corresponding to this signal are highlighted in red.

14

15
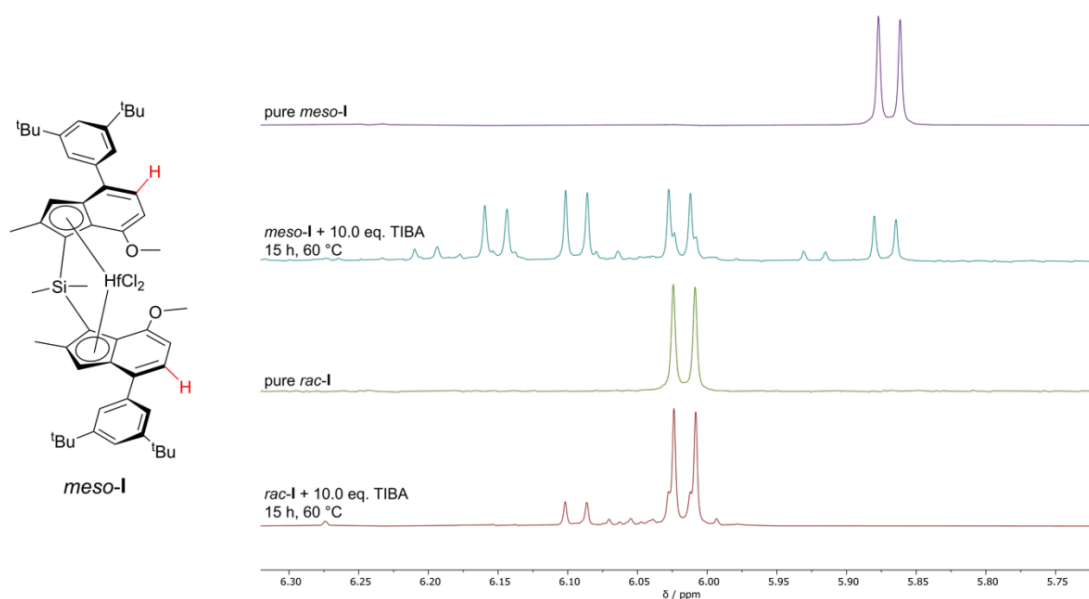
Figure S8. Excerpts of the ^{1}H NMR spectra in the range of δ = 6.30 ppm - 5.75 ppm of *meso-***I** and its products upon conversion with 10.0 eq. TIBA at 60 °C (NMR-spectra were recorded at room temperature). The protons of *meso-***I** corresponding to this signal are highlighted in red. For comparison, the ^{1}H NMR spectra of *rac-***I** and its products upon conversion with 10.0 eq. TIBA at 60 °C in the respective range are also shown.
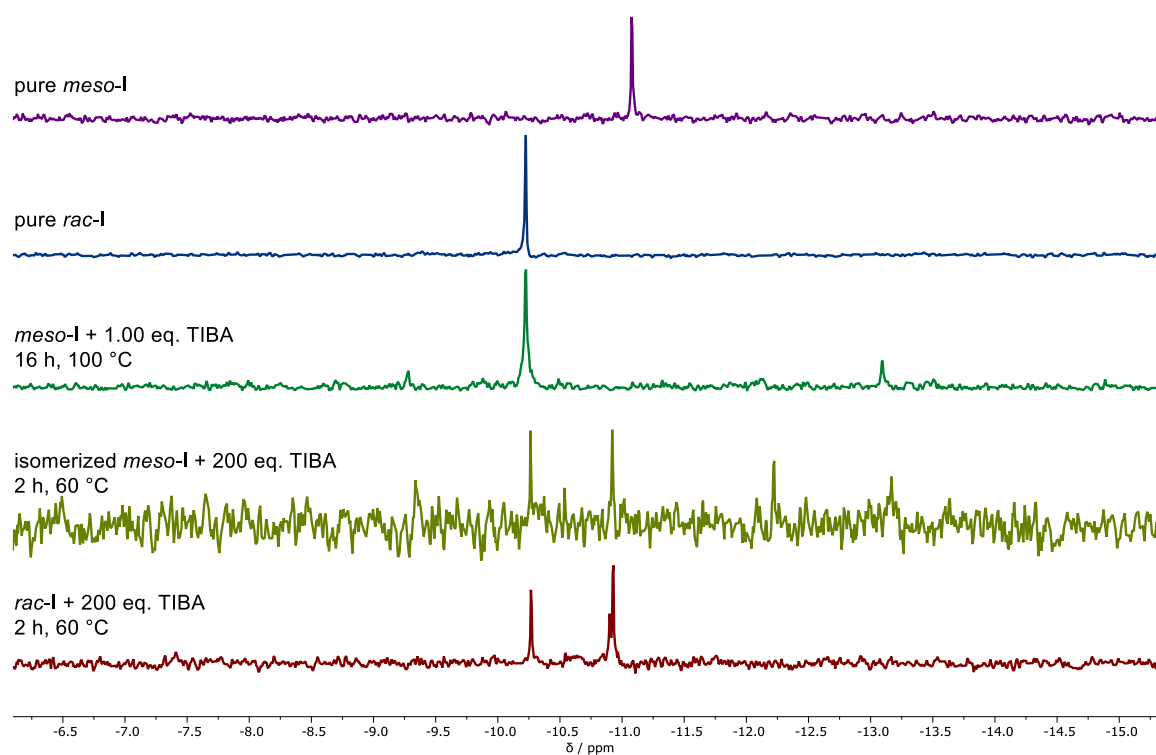
Figure S9. Excerpts of the ^{29}Si NMR spectra in the range of δ = −6.5 ppm - −15.0 ppm of the isomerization- and subsequent activation-products of *meso*-**I**. For comparison, the excerpts of spectra corresponding to pure *rac*-**I** and its activation products are also shown. The signals were internally referenced to tetramethylsilane (δ = 0.0 ppm).

16
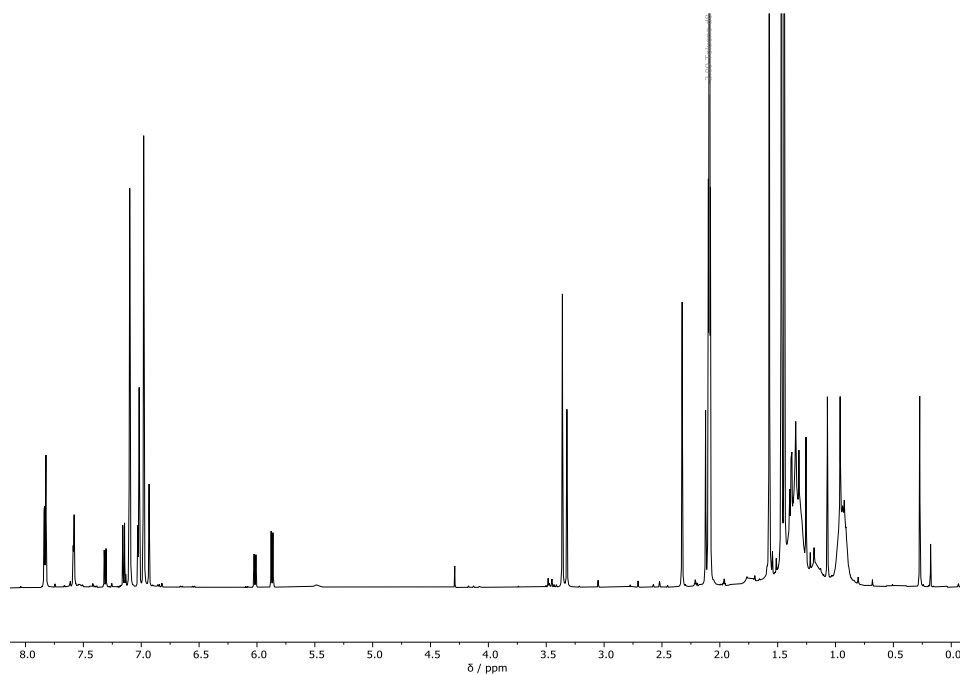
Figure S10. ^{1}H NMR spectrum of the conversion of *meso*-**I** with 1.00 eq. TMA and THF-d$_8$.

17
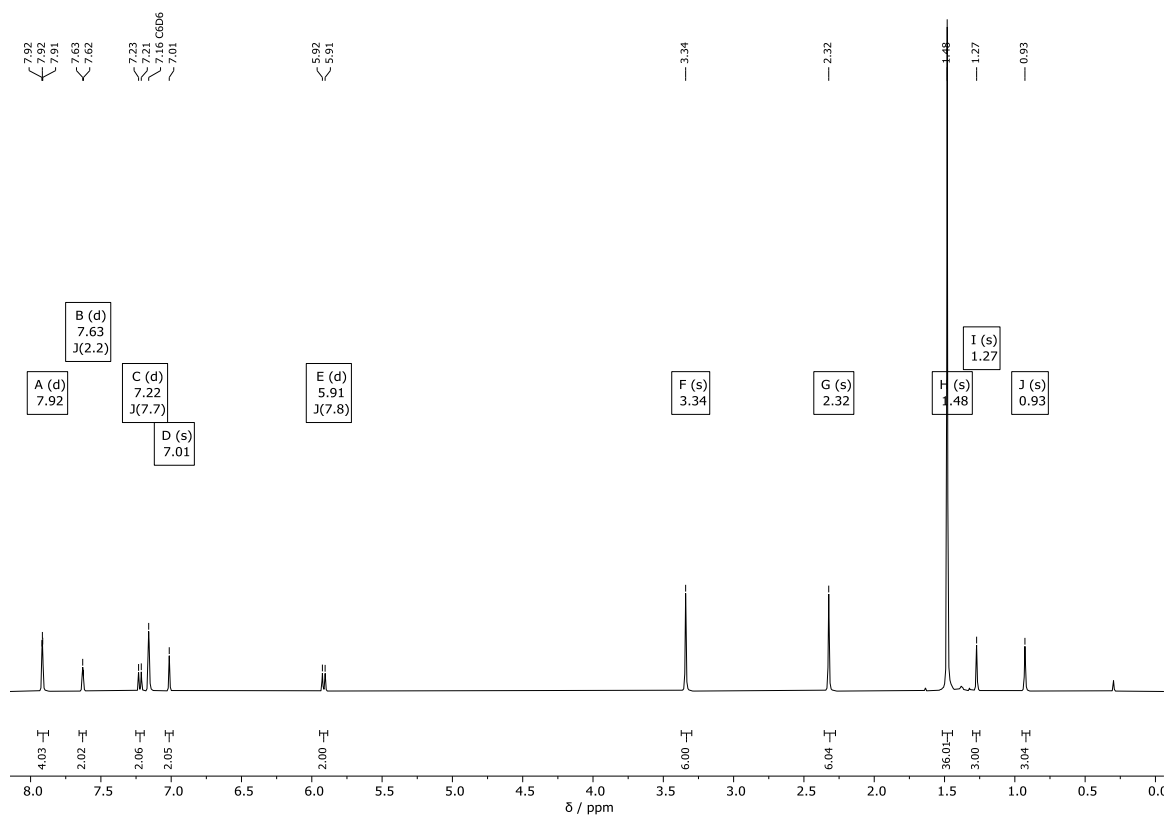
Figure S11. ^{1}H NMR spectrum of *meso*-**I**.
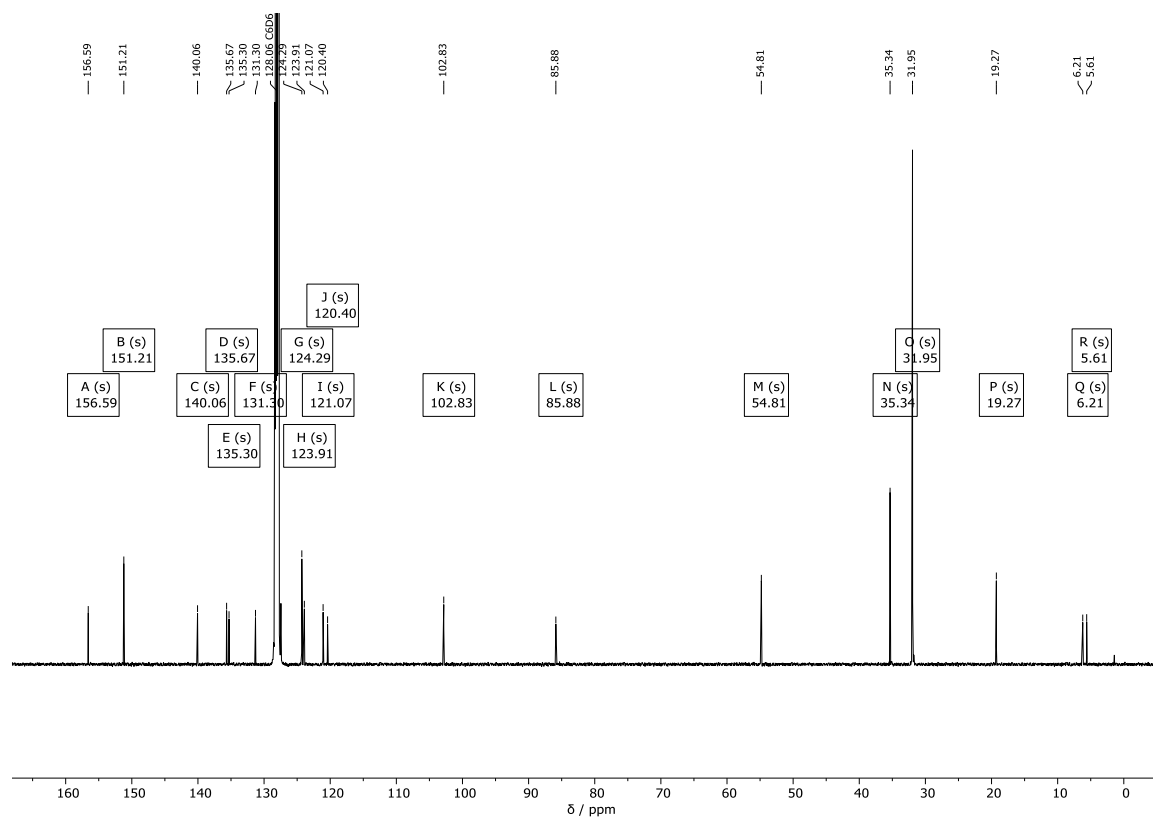
Figure S12. ^{13}C NMR spectrum of *meso*-**I**.
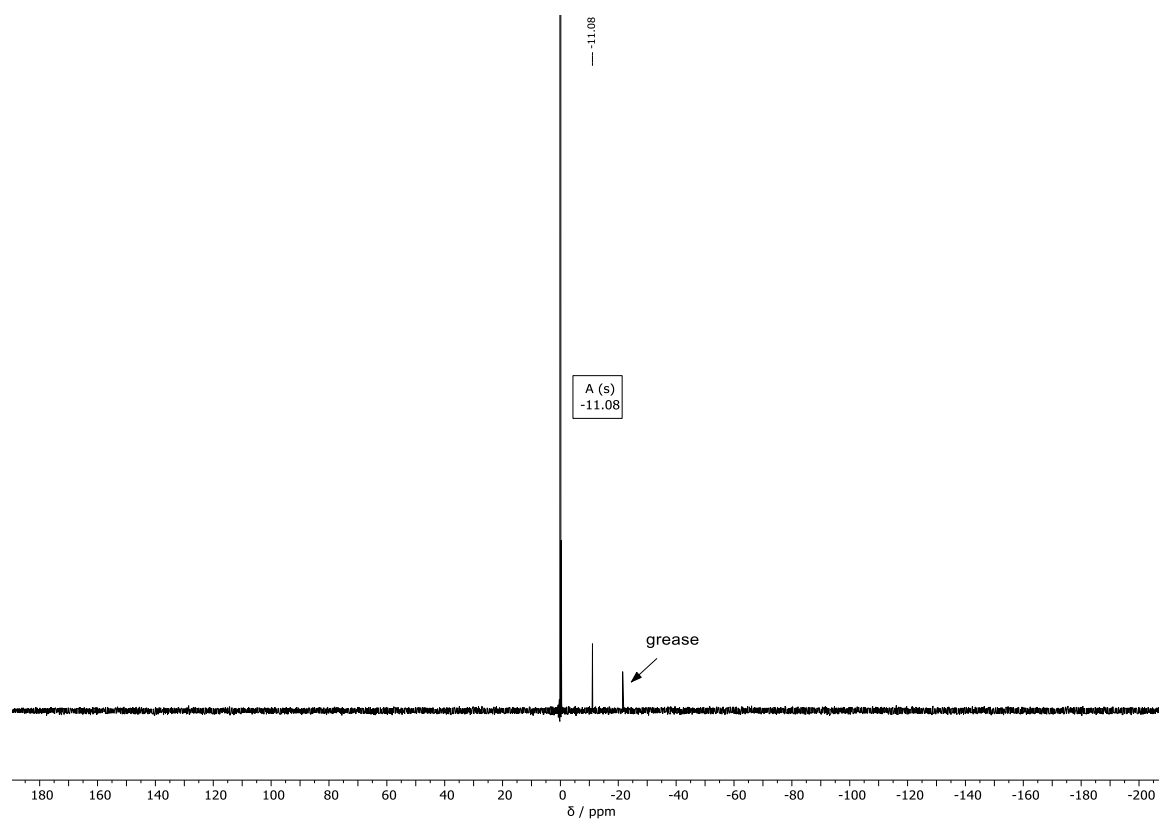
Figure S13. ^{29}Si- NMR spectrum of *meso*-**I**.

20
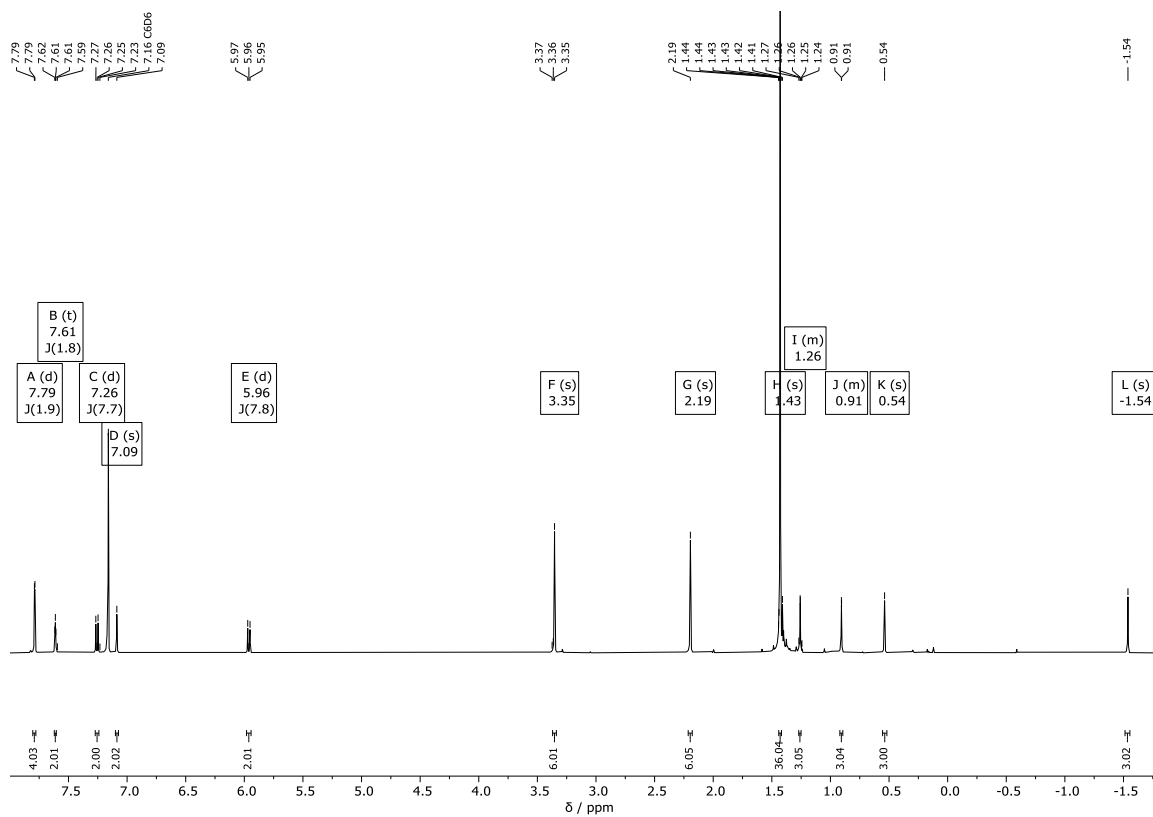
Figure S14. ^{1}H NMR spectrum of *meso*-**I$_{Me}$**.
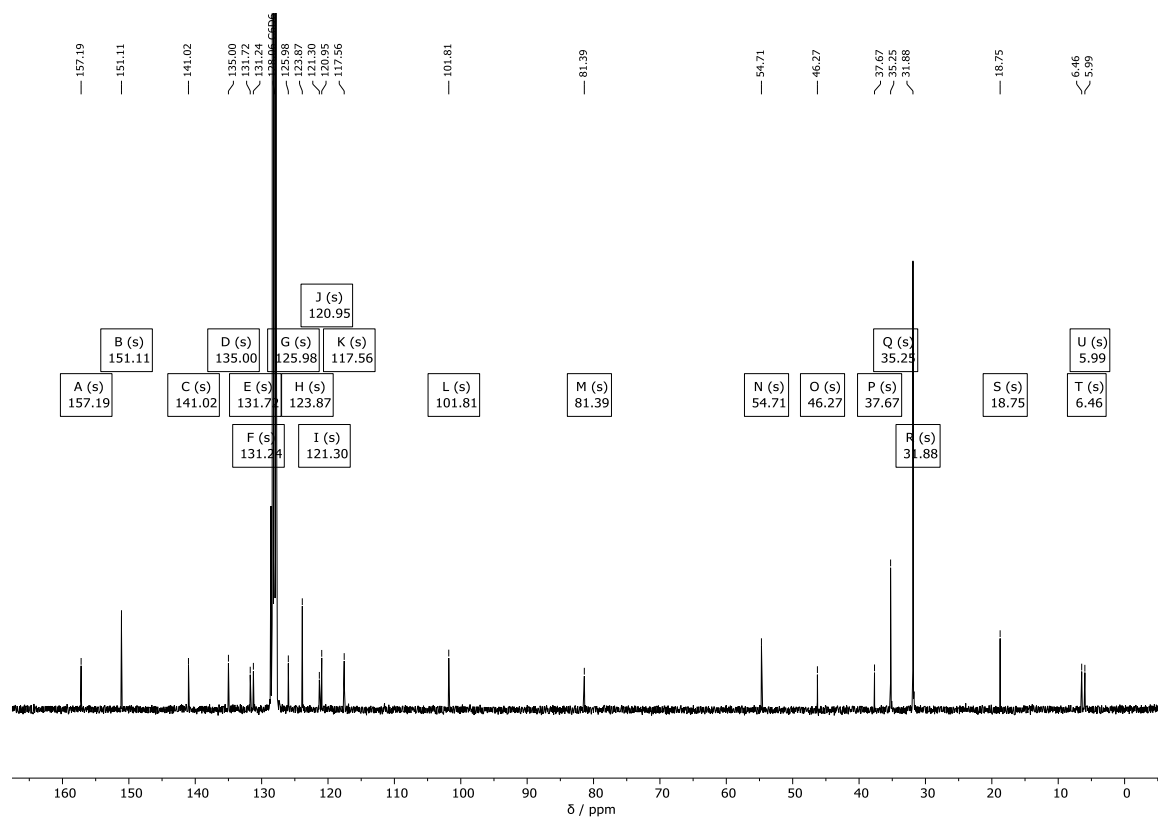
Figure S15. ¹³C NMR spectrum of *meso*-**I**_{Me}.

22
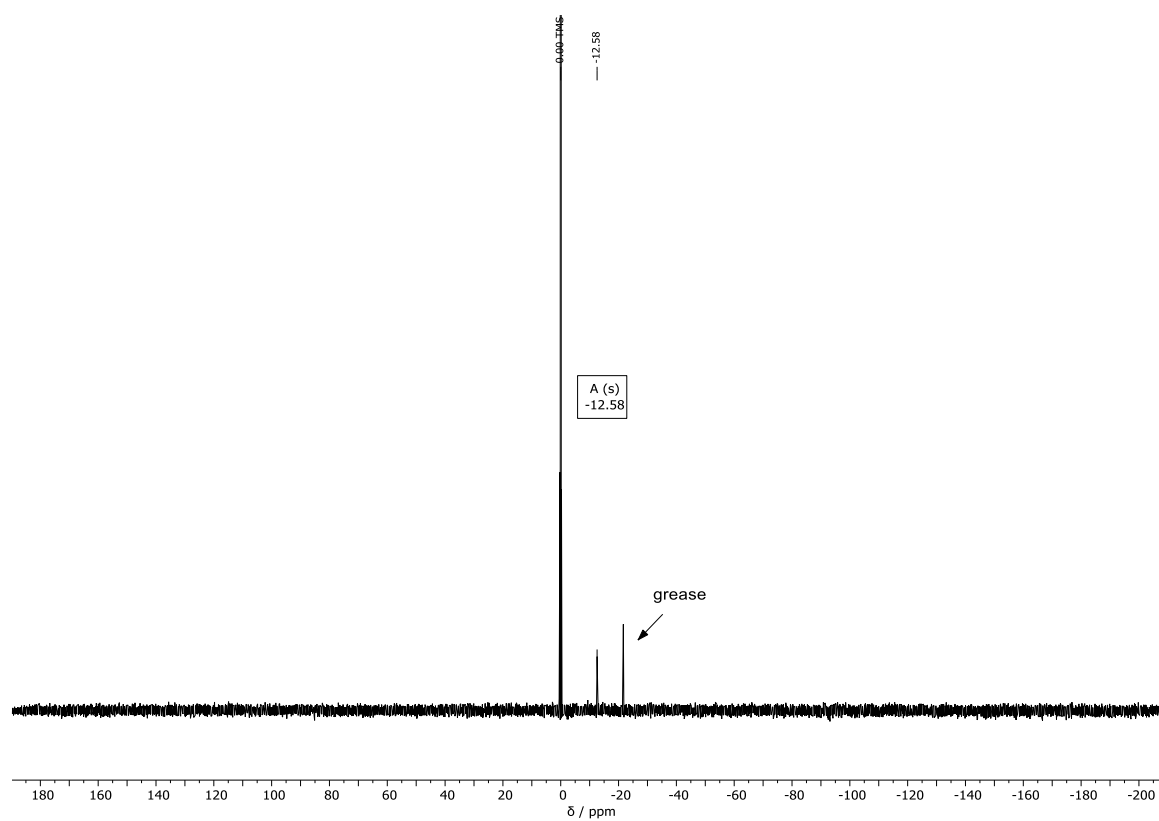
Figure S16. ^{29}Si NMR spectrum of *meso*-**I$_{Me}$**.

24

Polymer-Spectra
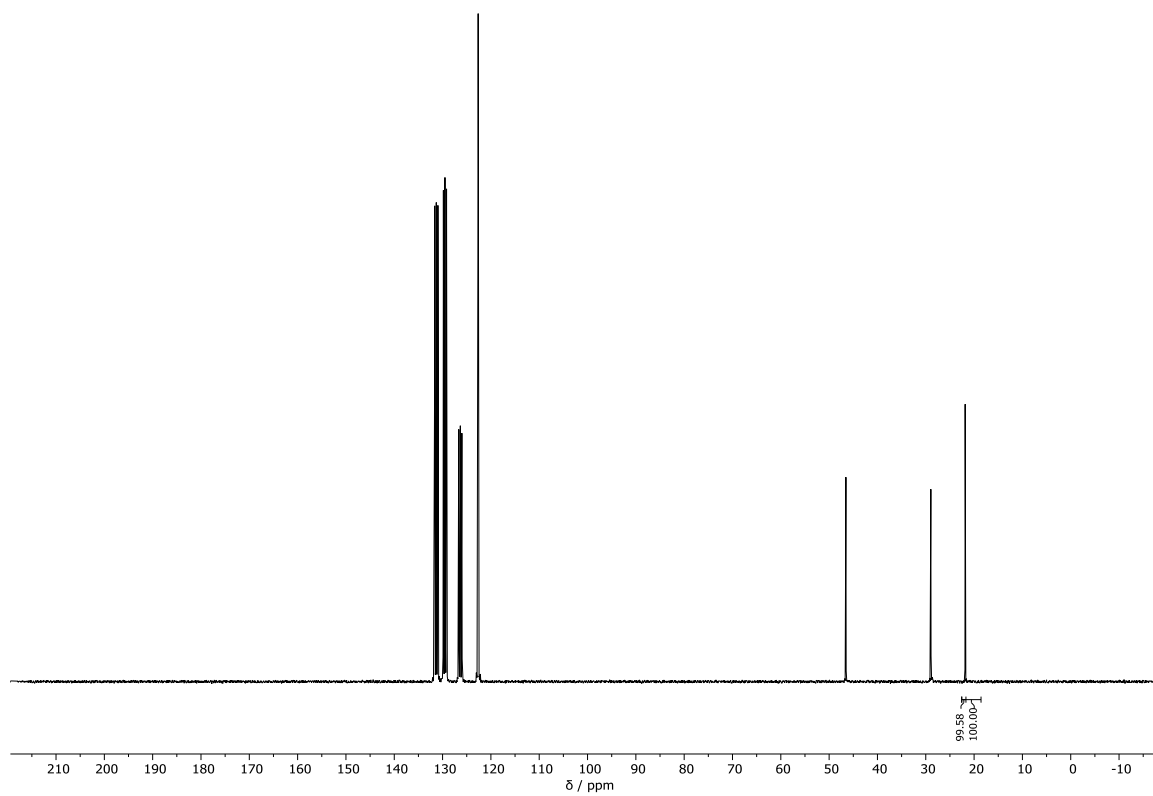
Figure S17. Full ^{13}C NMR spectrum of entry 1 (Table 1).
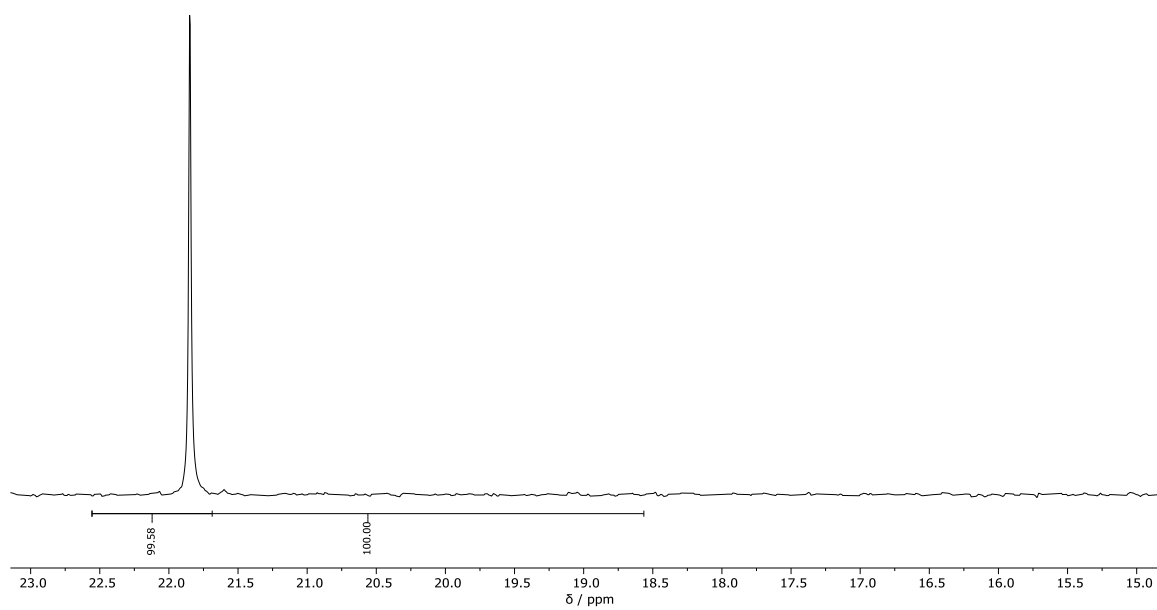
Figure S18. Excerpt of the ^{13}C NMR spectrum of entry 1 (Table 1).
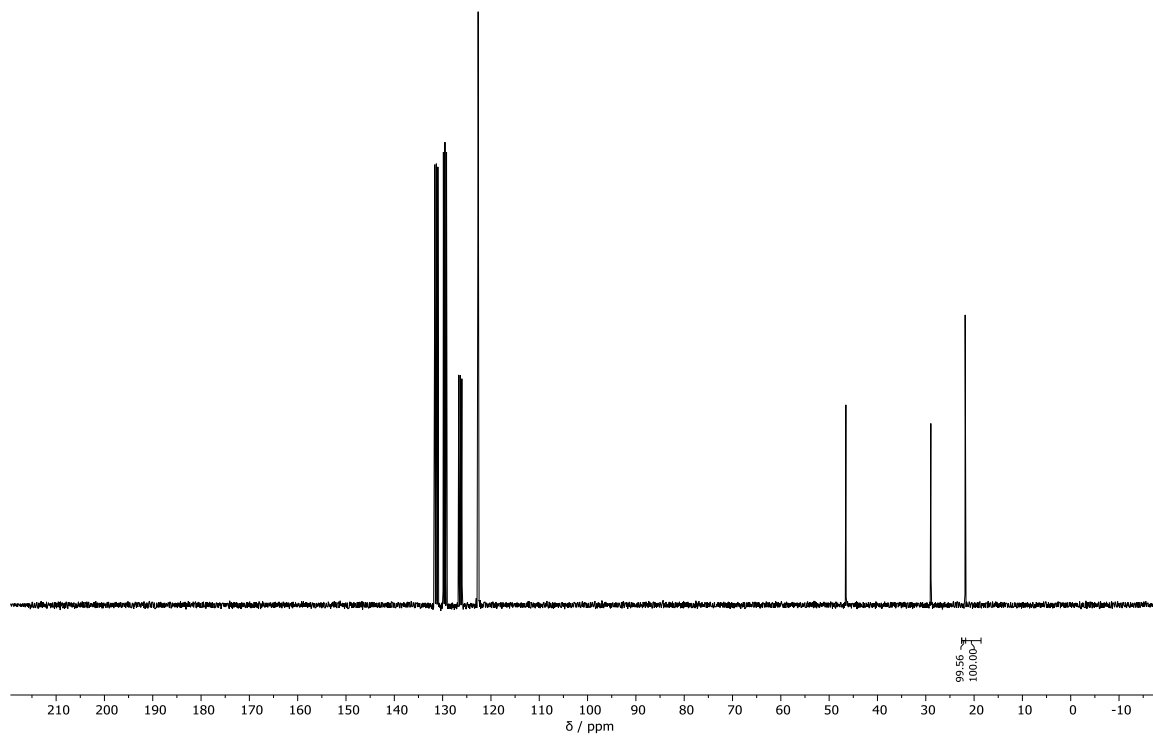
Figure S19. Full ^{13}C NMR spectrum of entry 2 (Table 1).

26
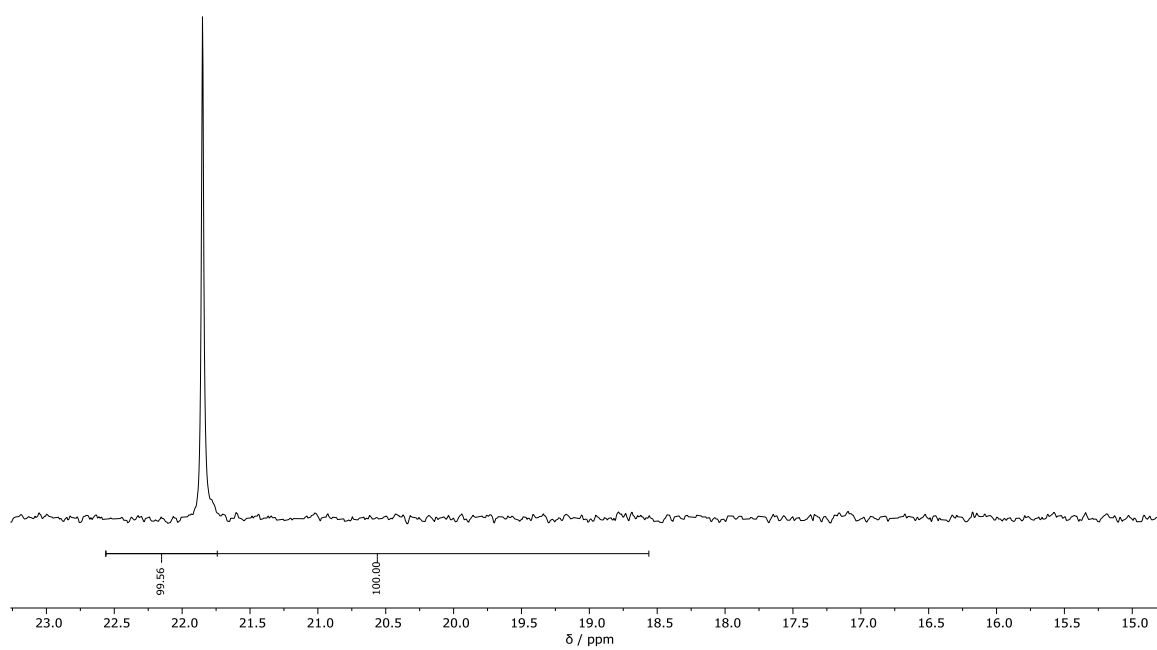
Figure S20. Excerpt of the ^{13}C NMR spectrum of entry 2 (Table 1).
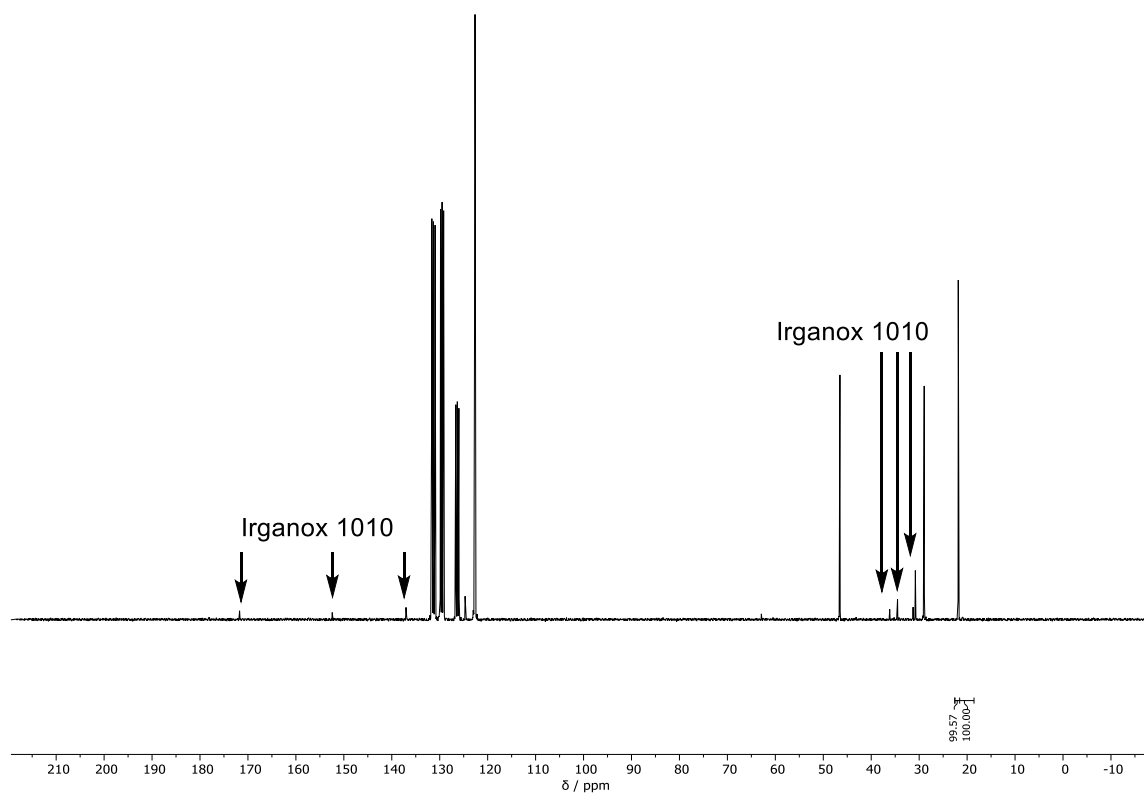
Figure S21. Full ^{13}C NMR spectrum of entry 3 (Table 1).

Irganox 1010
Stabilizing agent
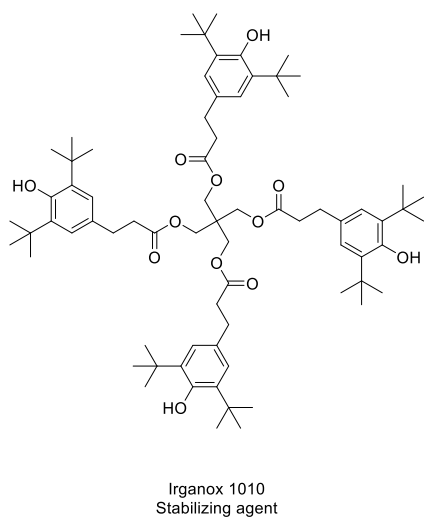
Figure S22. Chemical structure of the stabilizing agent Irganox 1010 visible in the ^{13}C NMR spectra of entry 3 and 4.

28
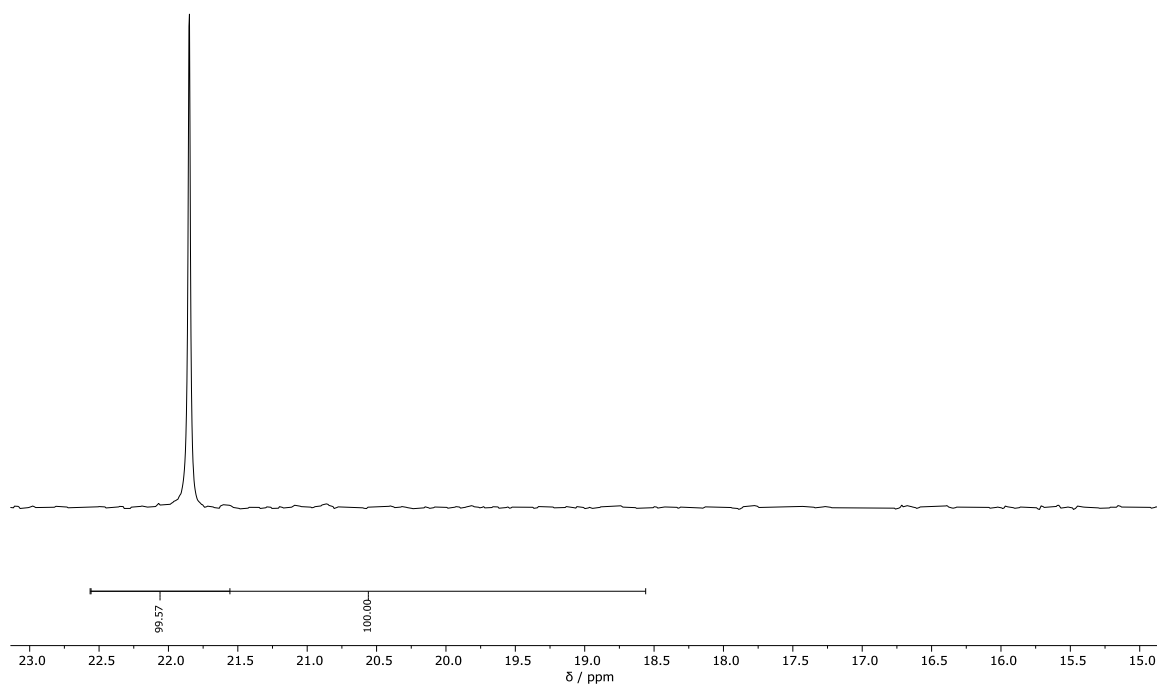
Figure S23. Excerpt of the ^{13}C NMR spectrum of entry 3 (Table 1).
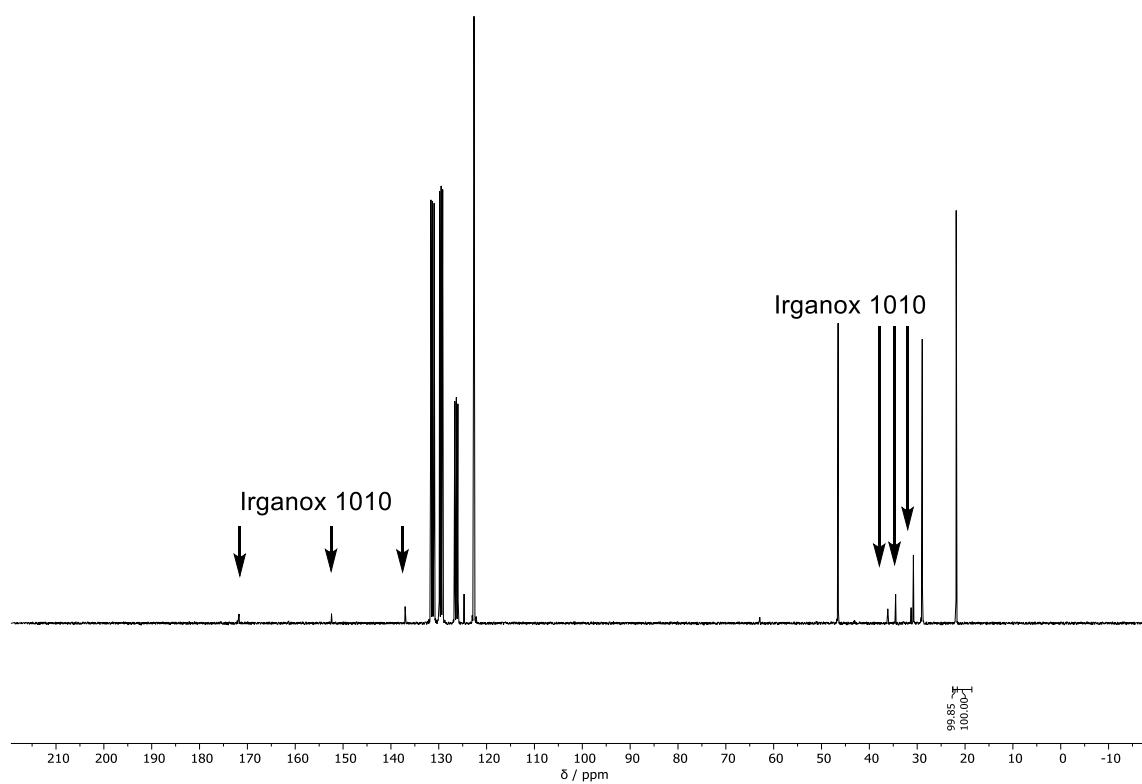
Figure S24. Full ^{13}C NMR spectrum of entry 4 (Table 1).

156
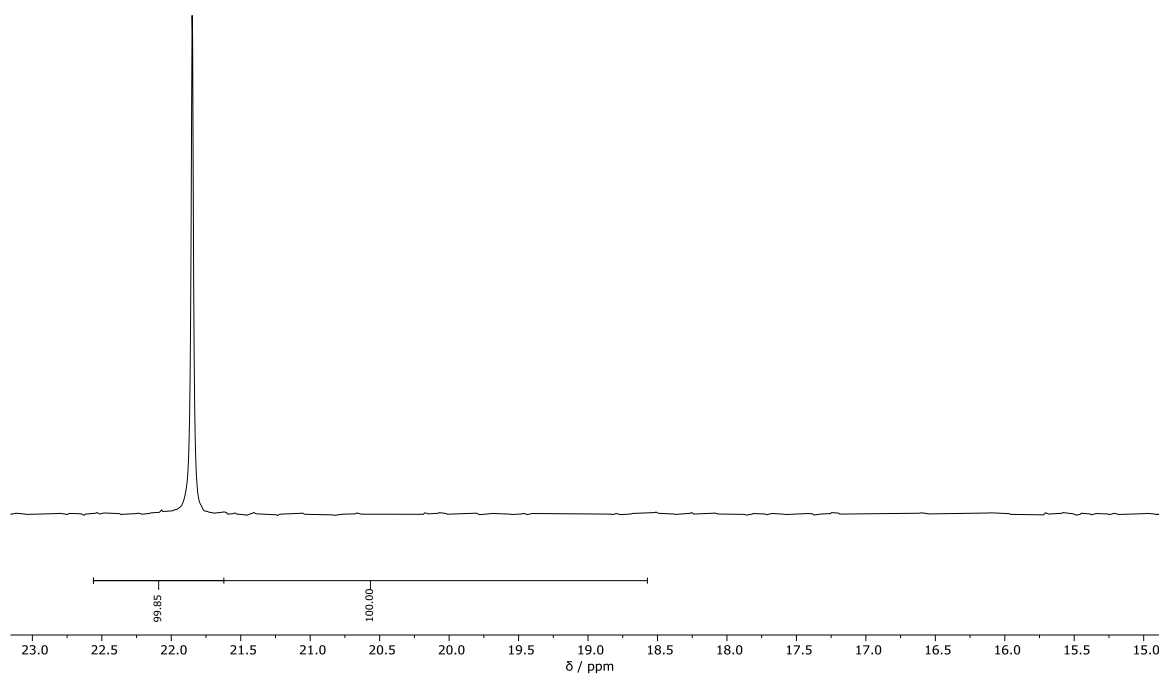
Figure S25. Excerpt of the ^{13}C NMR spectrum of entry 4 (Table 1).
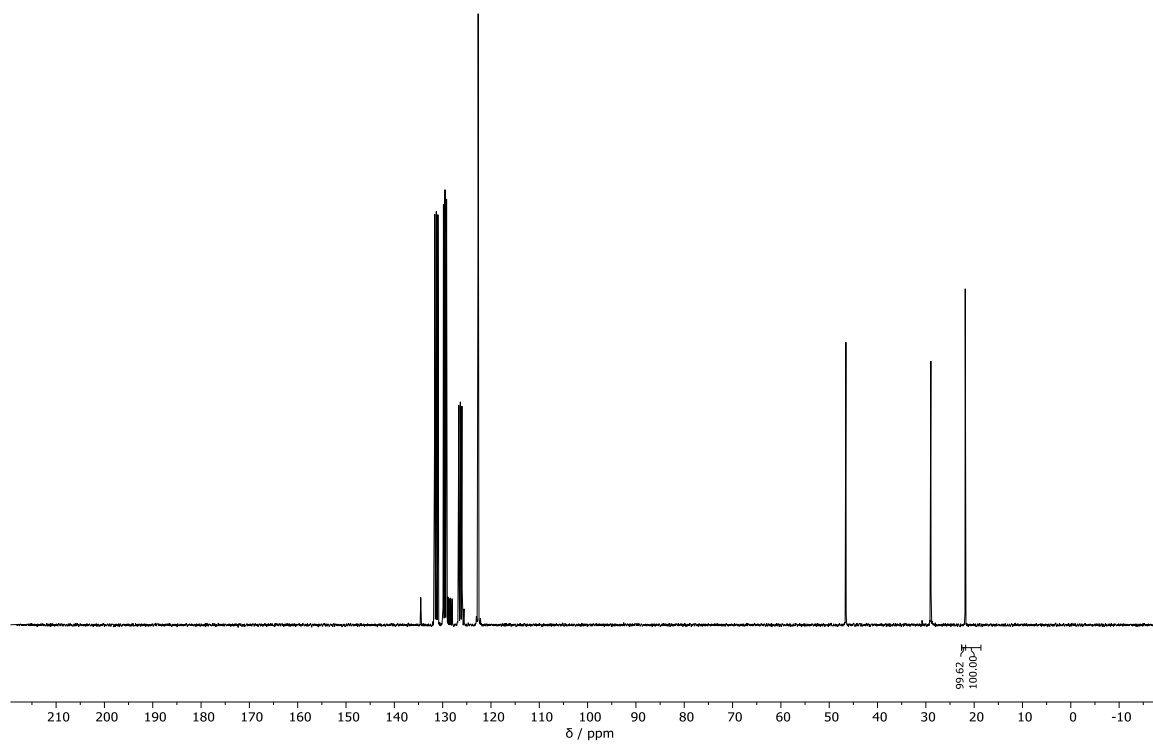
Figure S26. Full ^{13}C NMR spectrum of entry 5 (Table 1).
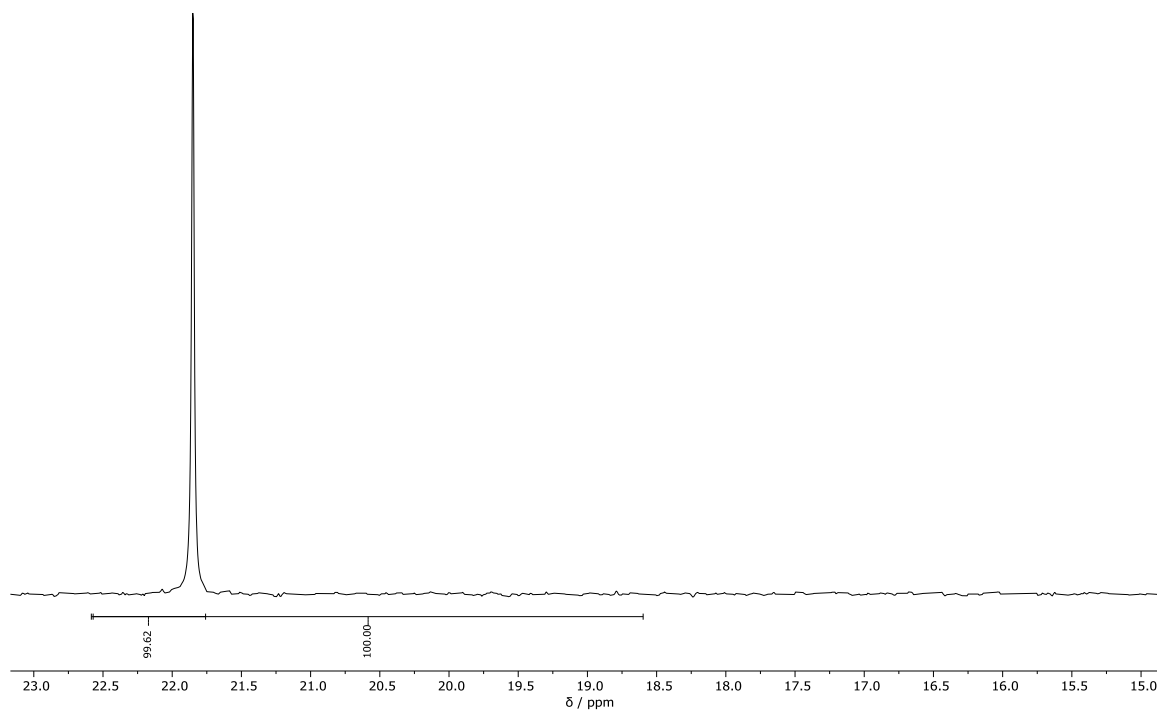
Figure S27. Excerpt of the ^{13}C NMR spectrum of entry 5 (Table 1).
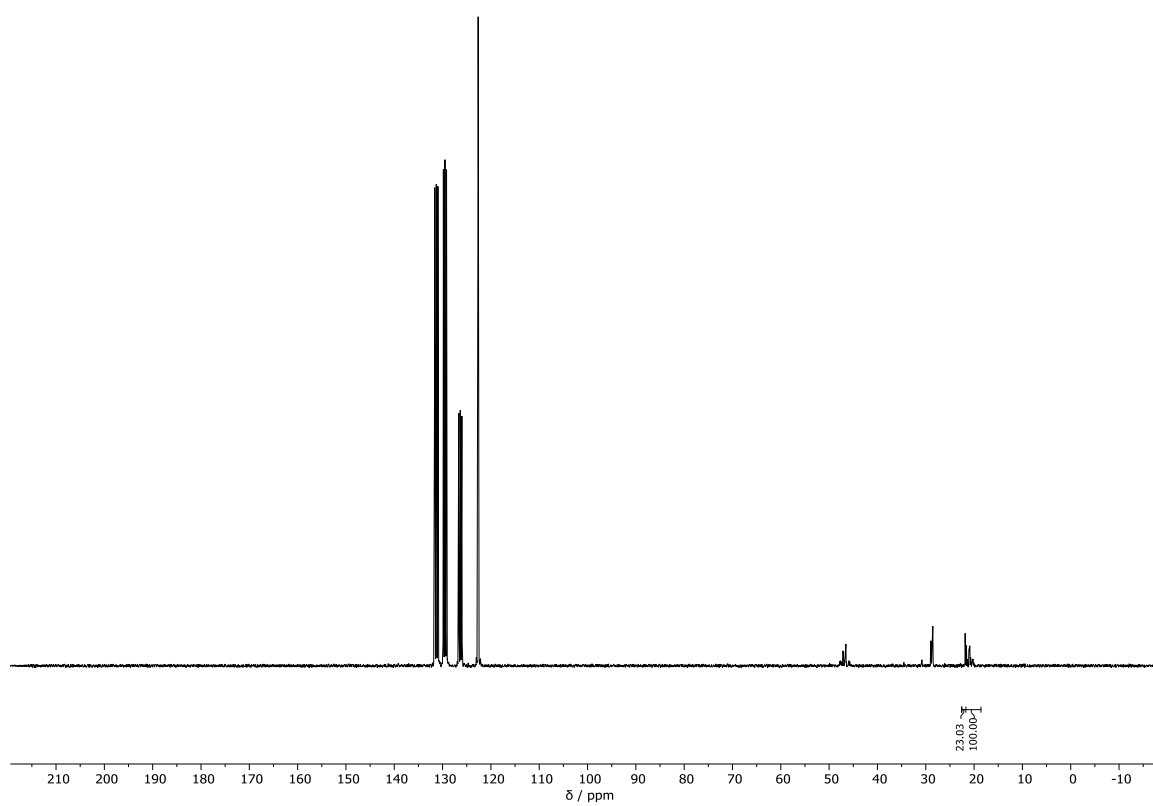
Figure S28. Full ^{13}C NMR spectrum of entry 6 (Table 1).
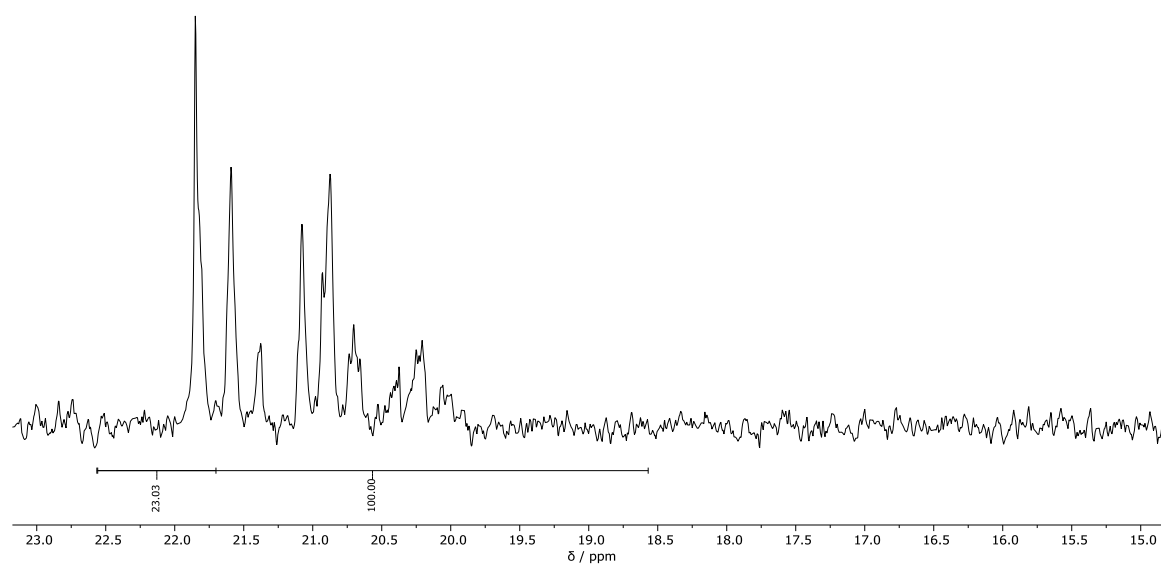
Figure S29. Excerpt of the ^{13}C NMR spectrum of entry 6 (Table 1).
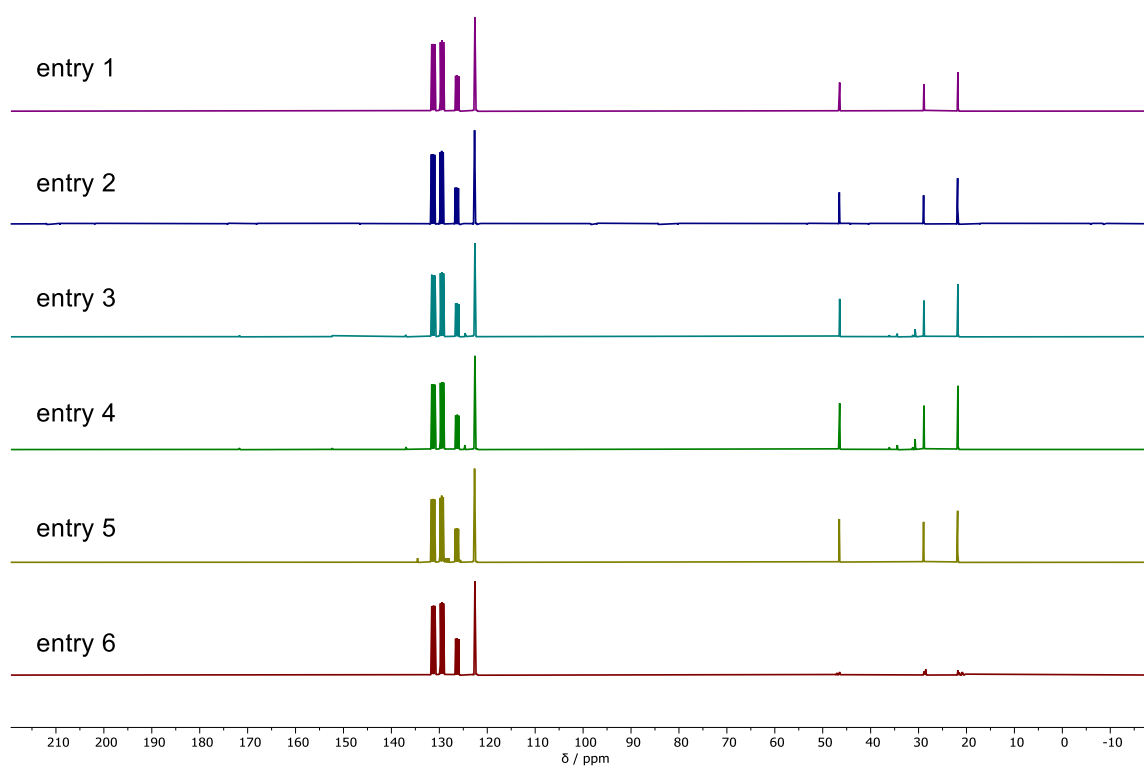
Figure S30. Stacked (full) ^{13}C NMR spectra of entries 1-6 (Table 1).
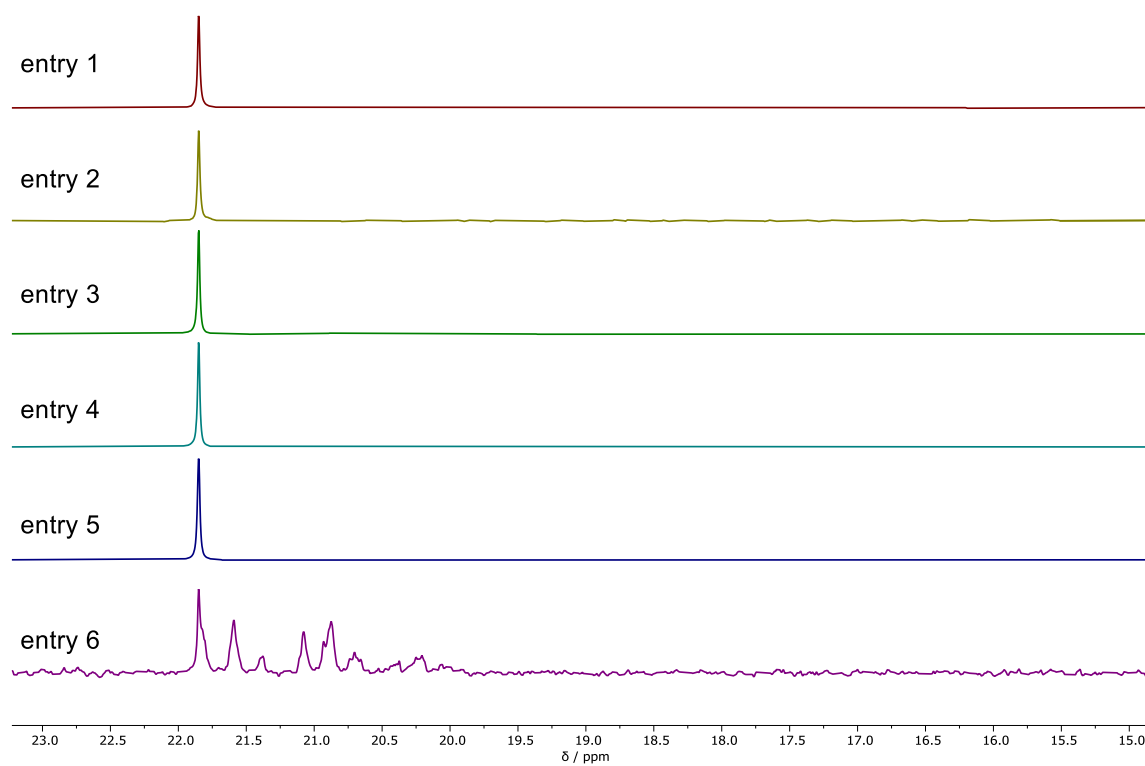
Figure S31. Stacked (excerpts) ^{13}C NMR spectra of entries 1-6 (Table 1).
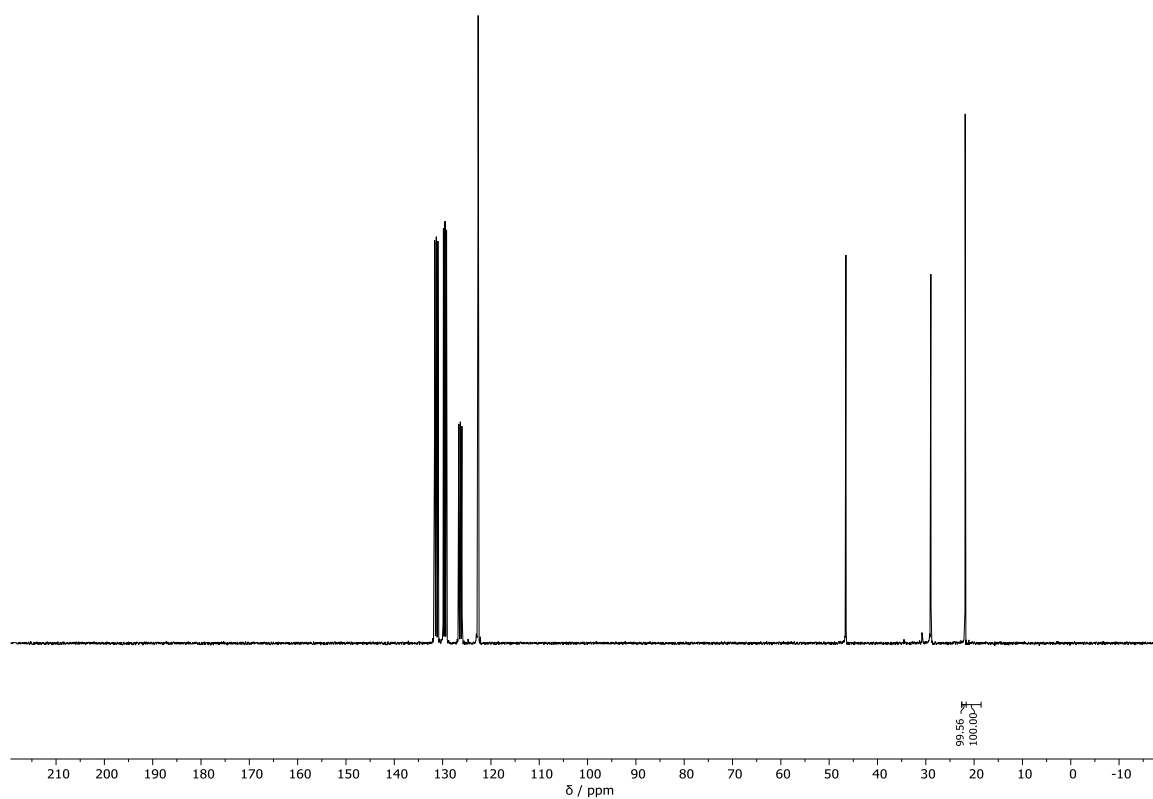
Figure S32. Full ^{13}C NMR spectrum of polypropylene produced by an isomeric mixture (*rac*/*meso* 1/3) of dimethylsilanediylbis(4-phenyl-7-methoxy-2-methylindenyl)- hafnium dichloride.

38
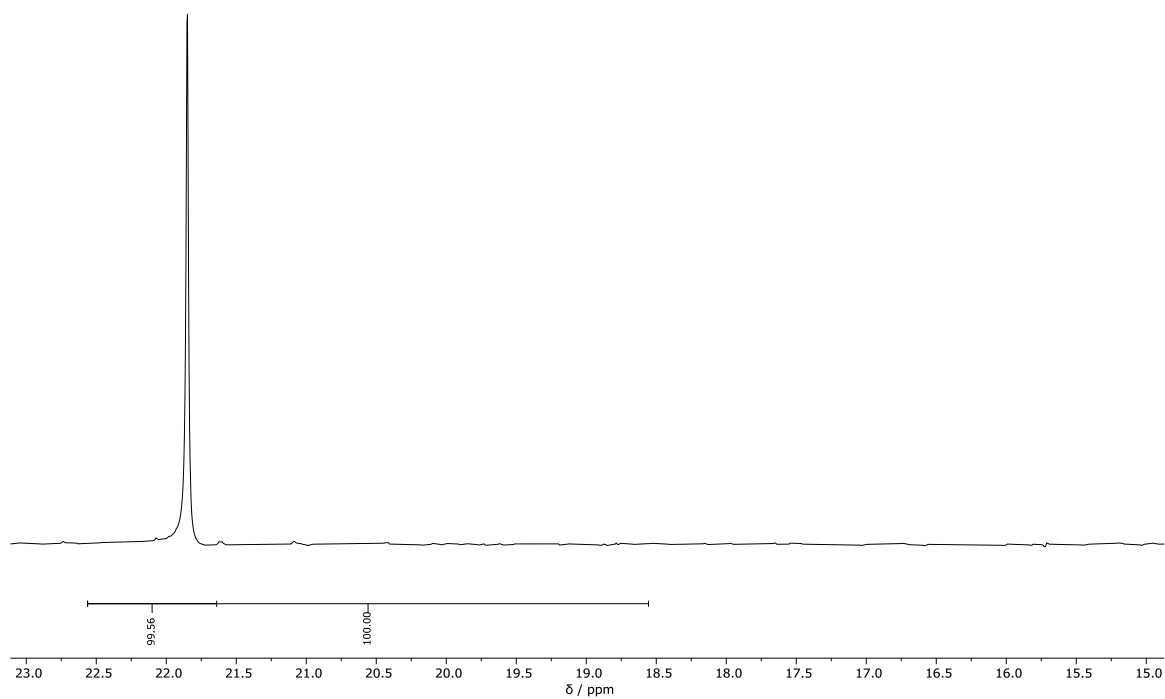
Figure S33. Excerpt of the ^{13}C NMR spectrum of polypropylene produced by an isomeric mixture (*rac*/*meso* 1/3) of dimethylsilanediylbis(4-phenyl-7-methoxy-2-methylindenyl)- hafnium dichloride.

39
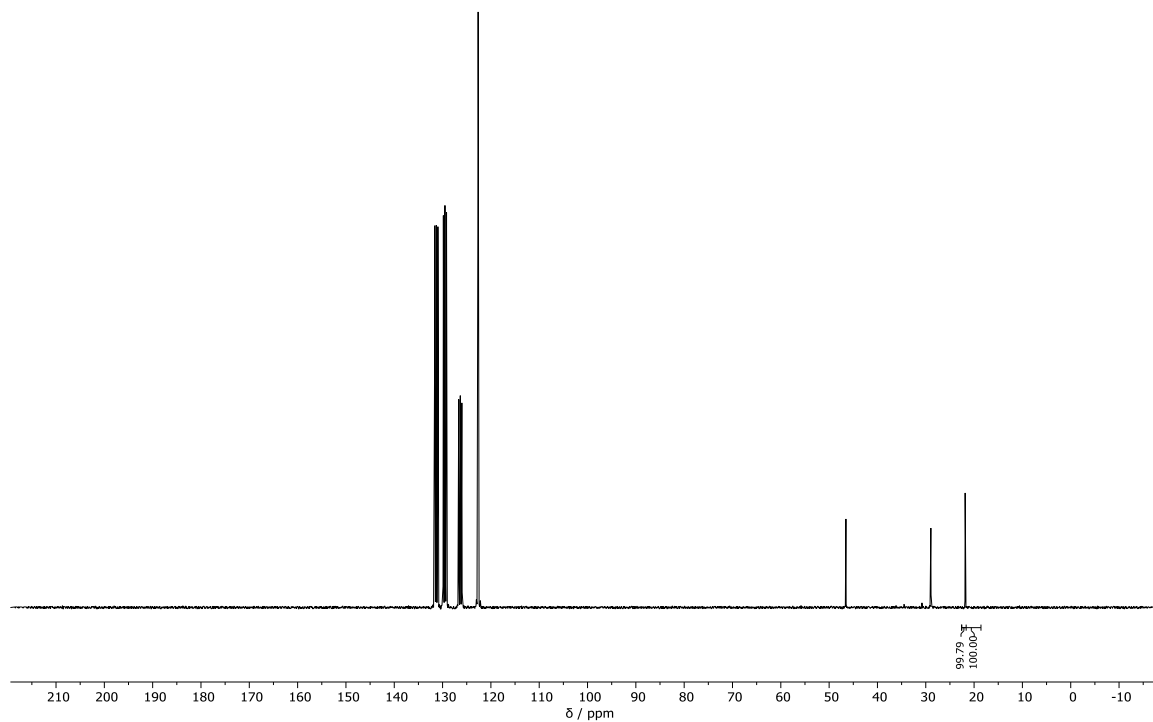
Figure S34. Full ^{13}C NMR spectrum of polypropylene produced by an isomeric mixture (*rac*/*meso* 1/3) of dimethylsilanediylbis(4-phenyl-7-methoxy-2-methylindenyl)- hafnium dichloride after the isomerization protocol was applied.

40
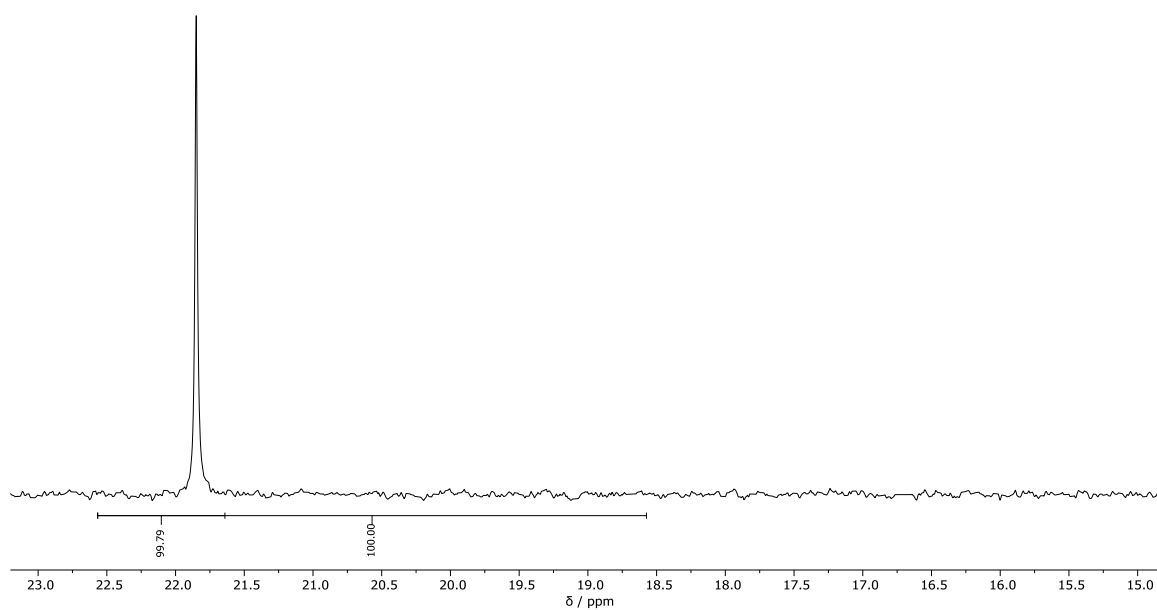
Figure S35. Excerpt of the ^{13}C NMR spectrum of polypropylene produced by an isomeric mixture (*rac*/*meso* 1/3) of dimethylsilanediylbis(4-phenyl-7-methoxy-2-methylindenyl)- hafnium dichloride after the isomerization protocol was applied.

41

Single-crystal X-ray diffraction

The X-ray data were collected on a single crystal X-ray diffractometer equipped with a CMOS detector (*Bruker* Photon-100), a TXS rotating anode with MoKα radiation (λ = 0.71073 Å) and a Helios mirror optic using the APEX4 software package.[6] The crystal was fixed on top of a kapton micro sampler coated with perfluorinated ether, transferred to the diffractometer and measured under a stream of cold nitrogen. A matrix scan was used to determine the initial lattice parameters. Reflections were corrected for Lorentz and polarization effects, scan speed, and background using SAINT.[7] Absorption corrections, including odd and even ordered spherical harmonics were performed using SADABS.[8] Space group assignments were based upon systematic absences, E statistics, and successful refinement of the structure. The structures were solved using SHELXT with the aid of successive difference Fourier maps and were refined against all data using SHELXL in conjunction with SHELXLE.[9-11] Hydrogen atoms (except on heteroatoms) were calculated in ideal positions as follows: Methyl hydrogen atoms were refined as part of rigid rotating groups, with a C–H distance of 0.98 Å and $U_{iso(H)} = 1.5 \cdot U_{eq(C)}$. Other H atoms were placed in calculated positions and refined using a riding model with methylene, aromatic and other C–H distances of 0.99 Å, 0.95 Å and 1.00 Å, respectively, and $U_{iso(H)} = 1.2 \cdot U_{eq(C)}$. Non-hydrogen atoms were refined with anisotropic displacement parameters. Full-matrix least-squares refinements were carried out by minimizing $\Sigma w(F_o^2 - F_c^2)^2$ with the SHELXL weighting scheme.[11] Neutral atom scattering factors for all atoms and anomalous dispersion corrections for the non-hydrogen atoms were taken from *International Tables for Crystallography*.[12] A split layer refinement was used to treat disordered groups and additional ISOR and DELU restraints were employed to stabilize the refinement of the layers. Images of the crystal structures were generated with MERCURY.[13]

42

SC-XRD structure of *meso*-I (CCDC 2179591)
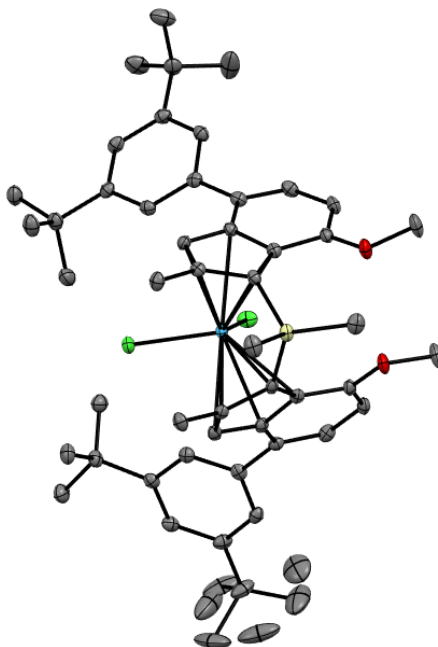
Diffractometer operator Andreas Saurwein
scanspeed 10 s per frame
dx 50 mm
3599 frames measured in 14 data sets
phi-scans with delta_phi = 0.5
omega-scans with delta_omega = 0.5
shutterless mode

Crystal data

$C_{52}H_{66}Cl_2HfO_2Si \cdot C_5H_{12}$

$M_r = 1072.67$	$D_x = 1.349$ Mg m^{-3}
Monoclinic, $P2_1/n$	Melting point: ? K
Hall symbol: -P 2yn	Mo $K\alpha$ radiation, $\lambda = 0.71073$ Å
$a = 14.361\ (7)$ Å	Cell parameters from 9652 reflections
$b = 13.421\ (6)$ Å	$\theta = 2.3–27.8°$
$c = 27.475\ (14)$ Å	$\mu = 2.14$ mm^{-1}
$\beta = 94.04\ (2)°$	$T = 100$ K
$V = 5282\ (4)$ Å^3	Fragment, yellow

43

$Z = 4$

$F(000) = 2224$

$0.35 \times 0.09 \times 0.07$ mm

Data collection

Bruker D8 Venture diffractometer	10620 independent reflections
Radiation source: IMS microsource	9171 reflections with $I > 2\sigma(I)$
Helios optic monochromator	$R_{int} = 0.081$
Detector resolution: 7.5 pixels mm^{-1}	$\theta_{max} = 26.2°$, $\theta_{min} = 2.1°$
phi– and ω–rotation scans	$h = -17 \quad 17$
Absorption correction: multi-scan *SADABS* 2016/2, Bruker, 2016	$k = -16 \quad 16$
$T_{min} = 0.663$, $T_{max} = 0.746$	$l = -34 \quad 34$
264400 measured reflections	

Refinement

Refinement on F^2	Secondary atom site location: difference Fourier map
Least-squares matrix: full	Hydrogen site location: inferred from neighbouring sites
$R[F^2 > 2\sigma(F^2)] = 0.022$	H-atom parameters constrained
$wR(F^2) = 0.050$	$W = 1/[\Sigma^2(FO^2) + (0.0215P)^2 + 4.5473P]$ WHERE $P = (FO^2 + 2FC^2)/3$
$S = 1.06$	$(\Delta/\sigma)_{max} = 0.004$
10620 reflections	$\Delta\rho_{max} = 0.48$ e Å^{-3}
619 parameters	$\Delta\rho_{min} = -0.70$ e Å^{-3}
36 restraints	Extinction correction: none
- constraints	Extinction coefficient: **-**
Primary atom site location: iterative	

44

SC-XRD structure of *meso*-I$_{Me}$ (CCDC 2179592)
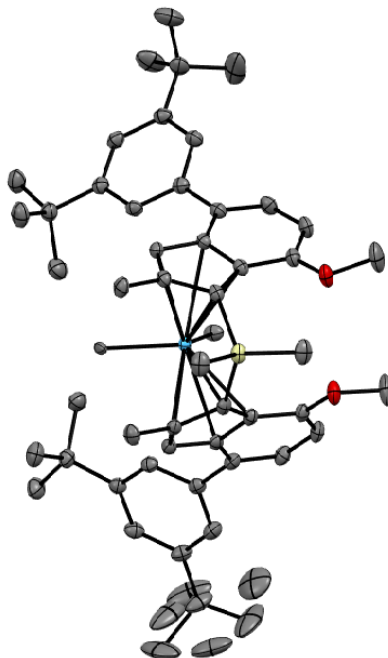
Diffractometer operator Andreas Saurwein
scanspeed 5 s per frame
dx 55 mm
2952 frames measured in 7 data sets
phi-scans with delta_phi = 0.5
omega-scans with delta_omega = 0.5
shutterless mode

Crystal data

$C_{54}H_{72}HfO_2Si \cdot C_5H_{12}$

$M_r = 1031.84$	$D_x = 1.294$ Mg m^{-3}
Monoclinic, $P2_1/n$	Melting point: ? K
Hall symbol: -P 2yn	Mo $K\alpha$ radiation, $\lambda = 0.71073$ Å
$a = 14.4047$ (10) Å	Cell parameters from 9640 reflections
$b = 13.3802$ (8) Å	$\theta = 2.8–28.3°$
$c = 27.5423$ (19) Å	$\mu = 2.03$ mm^{-1}

45

β = 94.079 (2)°

V = 5295.0 (6) Å^3

Z = 4

F(000) = 2160

T = 150 K

Fragment, yellow

0.32 × 0.17 × 0.11 mm

Data collection

Bruker D8 Venture diffractometer

Radiation source: TXS rotating anode

Helios optic monochromator

Detector resolution: 16 pixels mm^{-1}

phi– and ω–rotation scans

Absorption correction: multi-scan *SADABS* 2016/2, Bruker, 2016

T_{min} = 0.636, T_{max} = 0.746

155969 measured reflections

10804 independent reflections

10381 reflections with I > 2σ(I)

R_{int} = 0.032

θ$_{max}$ = 26.4°, θ$_{min}$ = 2.2°

h = −18 18

k = −16 16

l = −34 34

Refinement

Refinement on F^2

Least-squares matrix: full

$R[F^2 > 2σ(F^2)]$ = 0.016

$wR(F^2)$ = 0.040

S = 1.08

10804 reflections

621 parameters

1072 restraints

- constraints

Primary atom site location: iterative

Secondary atom site location: difference Fourier map

Hydrogen site location: inferred from neighbouring sites

H-atom parameters constrained

W = 1/[Σ^2(FO^2) + (0.0114P)^2 + 4.9103P] WHERE P = (FO^2 + 2FC^2)/3

(Δ/σ)$_{max}$ = 0.008

Δρ$_{max}$ = 0.60 e Å^{-3}

Δρ$_{min}$ = −0.56 e Å^{-3}

Extinction correction: none

Extinction coefficient: **-**

DSC Analysis

Figure S36. DSC analysis of entry 1, Table 1.
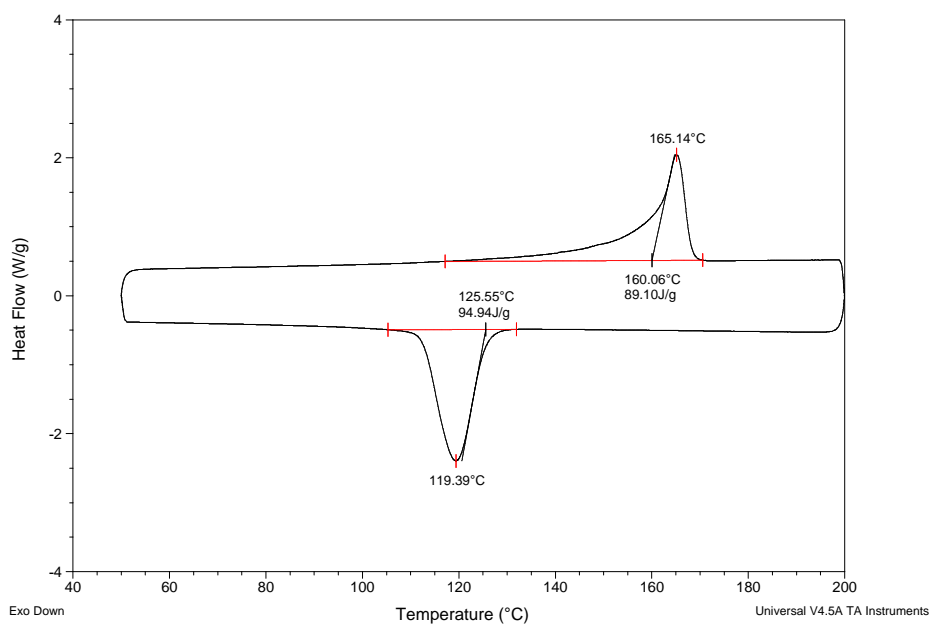
Figure S37. DSC analysis of entry 2, Table 1.
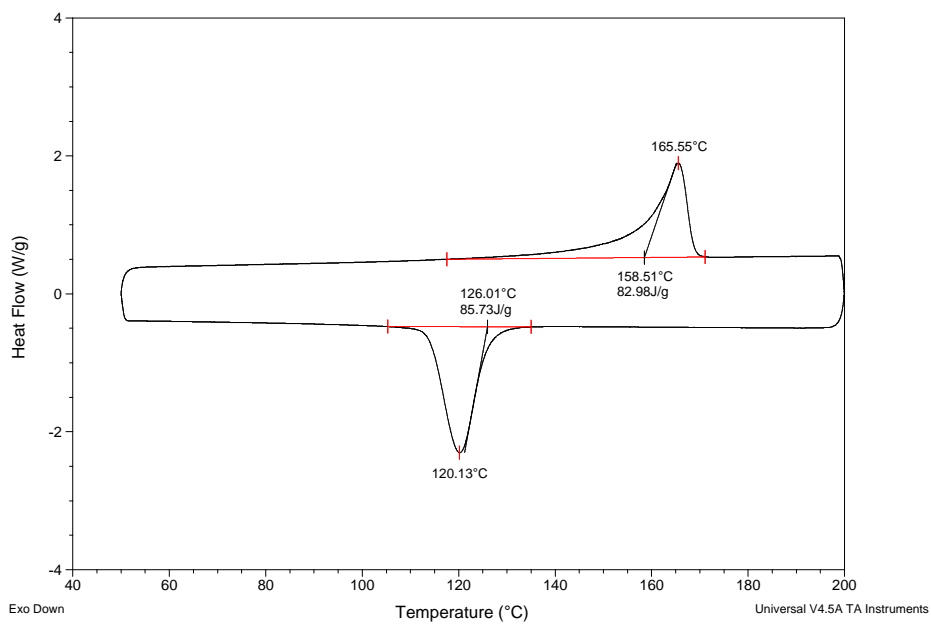
Figure S38. DSC analysis of entry 3, Table 1.
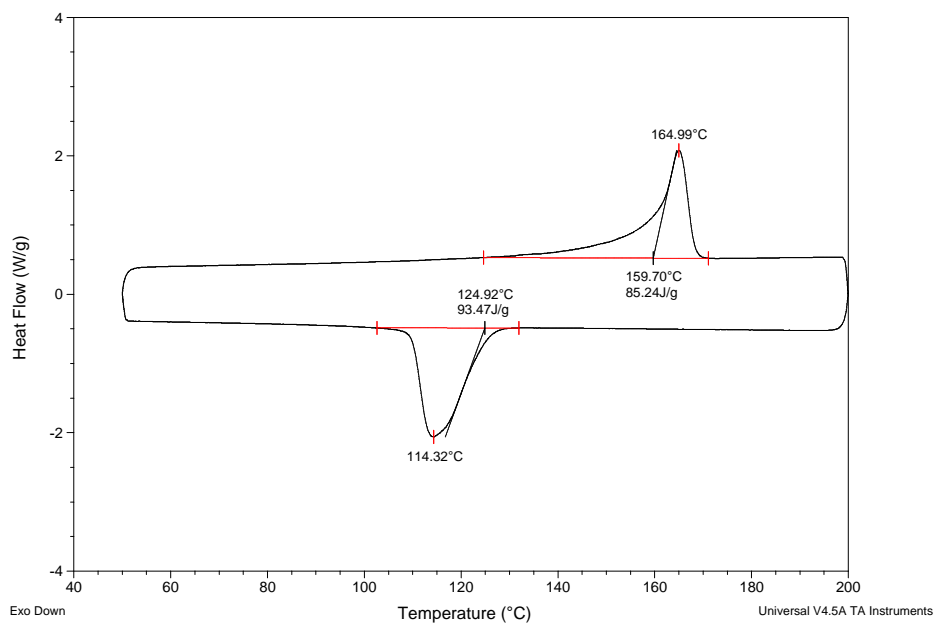
Figure S39. DSC analysis of entry 4, Table 1.
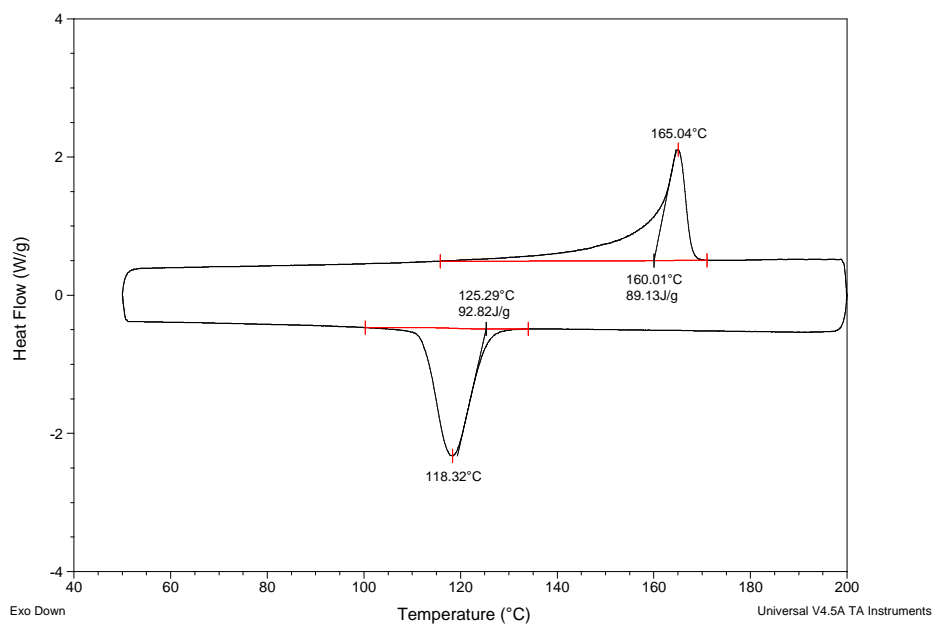
Figure S40. DSC analysis of entry 5, Table 1.
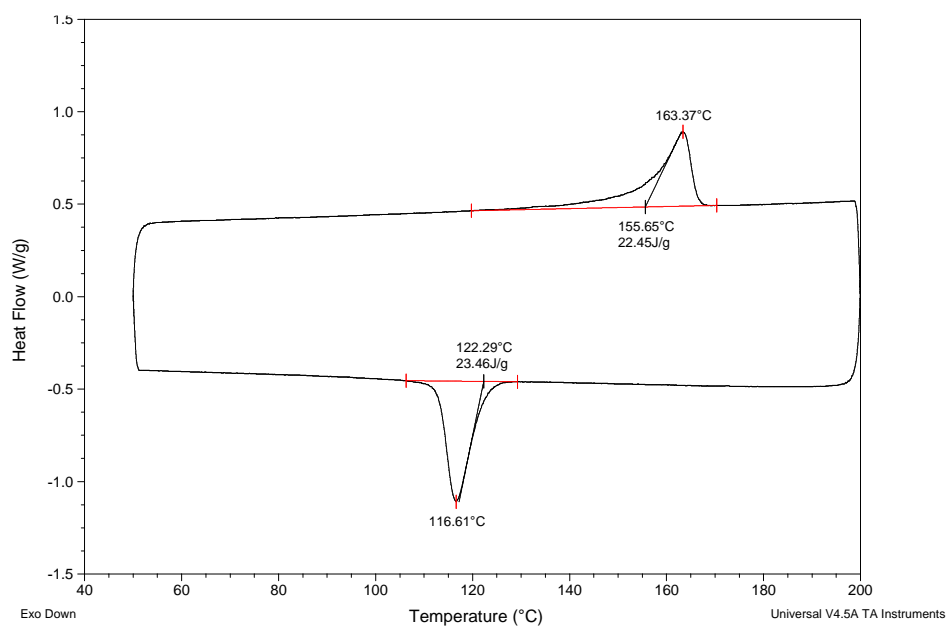
Figure S41. DSC analysis of entry 6, Table 1.

References

(1) H. H. Brintzinger, D. Fischer. R. Mühlhaupt, B. Rieger, R. M. Waymouth, *Angew. Chem. Int. Ed. Engl.* **1995**, 34, 1143-1170.

(2) B. Coto, J. M. Escola, I. Suárez, M. J. Caballero, *Polym. Test.* **2007**, 26, 568-575.

(3) M. Muhr, P. Heiß, P. M. Schütz, R. Bühler, C. Gemel, M. H. Linden, H. B.Linden, R. A. Fischer, *Dalton Trans.* **2021**, *50*, 9031-9036.

(4) A. Schöbel, E. Herdtweck, M. Parkinson, B. Rieger, *Chem. Eur. J.* **2012**, 18, 4174-4178.

(5) A. Vittoria, G. P. Goryunov, V. V. Izmer, D. S. Kononovich, O. V. Samsonov, F. Zaccaria,
G. Urciuoli, P. H. Budzelaar, V. Busico, A. Z. Voskoboynikov, *et al.*, *Polymers* **2021**, *13*, 2621.

(6) Bruker AXS Inc. *APEX suite of crystallographic software*; Madison, Wisconsin, USA, 2021.

(7) Bruker AXS Inc. *SAINT*; Madison, Wisconsin, USA, 2019.

(8) Bruker AXS Inc. *SADABS*; Madison, Wisconsin, USA, 2019.

(9) C. B. Hübschle, G. M. Sheldrick, B. Dittrich, *J. Appl. Cryst.* **2011**, *44*, 1281–1284.

(10) G. M. Sheldrick, *Acta Crystallogr. Sect. C* **2015**, *71*, 3–8.

(11) G. M. Sheldrick, *Acta Crystallogr. Sect. A* **2015**, *71*, 3–8.

(12) A. J. Wilson, *International Tables for Crystallography, Vol. C*; Kluwer Academic Publishers: Dordrecht, The Netherlands, **1992**.

(13) C. F. Macrae, I. J. Bruno, J. A. Chisholm, P. R. Edgington, P. McCabe, E. Pidcock, L. Rodriguez-Monge, R. Taylor, J. van de Streek, P. A. Wood, *J. Appl. Cryst.* **2008**, *41*, 466–470.

10.1.3 Supporting Information for Chapter 6

ChemPlusChem

Supporting Information

Fiber Spinning of Ultrahigh Molecular Weight Isotactic Polypropylene: Melt Spinning and Melt Drawing

Lucas Stieglitz, Christina Geiger, Paula F. Großmann, Moritz Kränzlein, Katia Rodewald, Peter Müller-Buschbaum, and Bernhard Rieger*

Table of Contents

Polymer NMR Spectra

Figure S1: ^{13}C NMR spectrum of **iPP-1**.
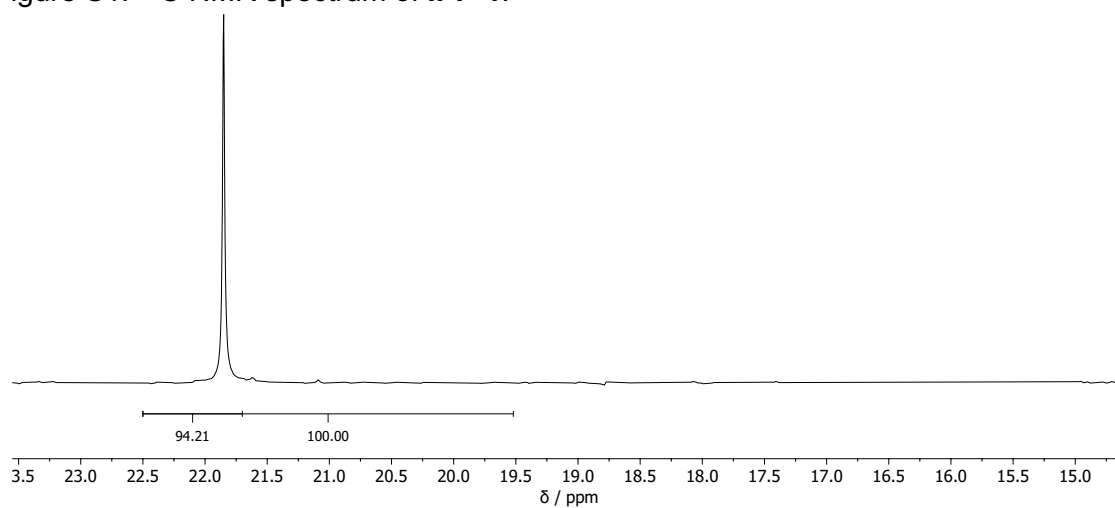
Figure S2: ^{13}C NMR spectrum of **iPP-2**.
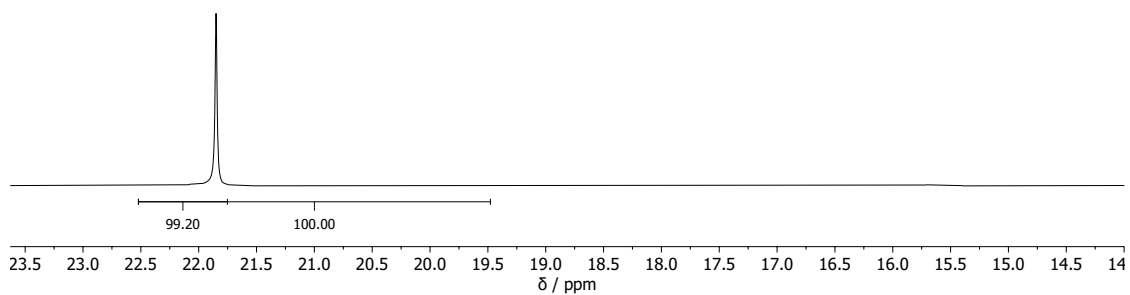
Figure S3: ^{13}C NMR spectrum of **iPP-3**.
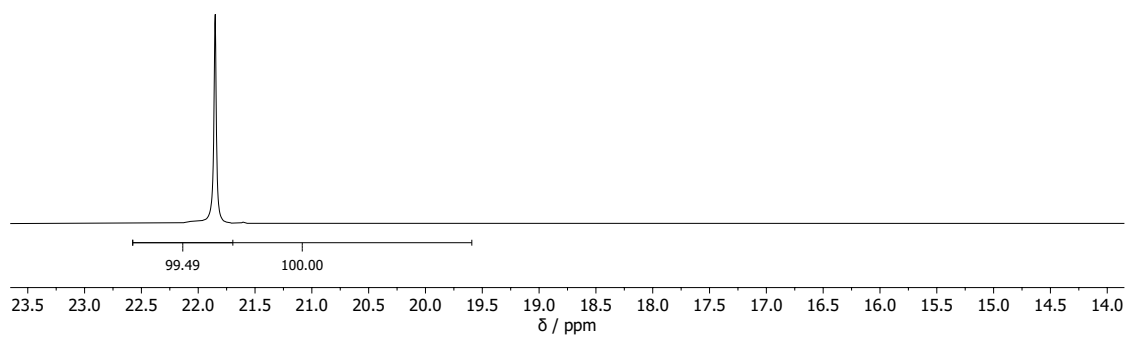
Figure S4: ^{13}C NMR spectrum of **iPP-4**.
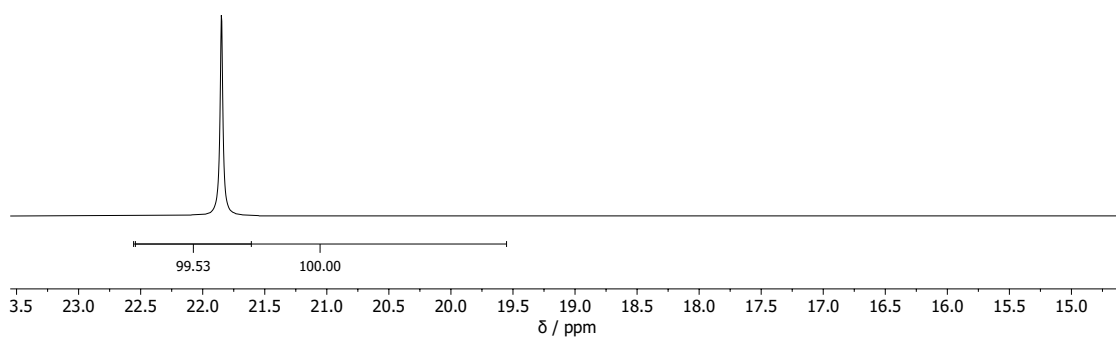
Figure S5: ^{13}C NMR spectrum of **iPP-5**.

S3

Polymer GPC Characterization
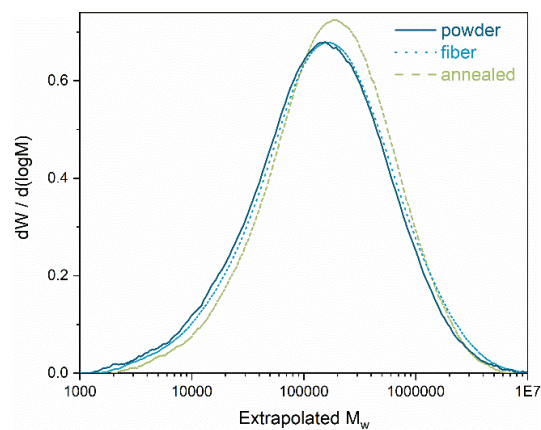
Figure S6: Molecular weight distribution of **iPP-1** (raw polymer, fiber and annealed fiber).
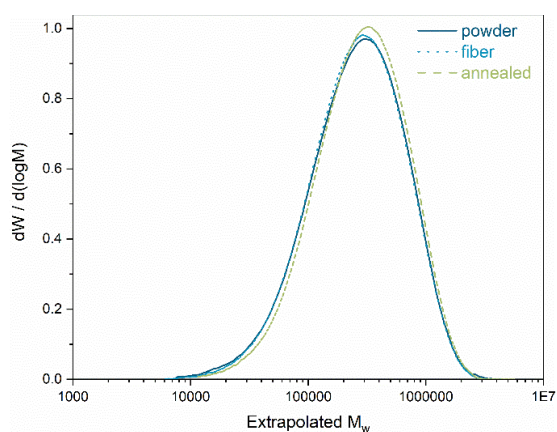
Figure S7: Molecular weight distribution of **iPP-2** (raw polymer, fiber and annealed fiber).
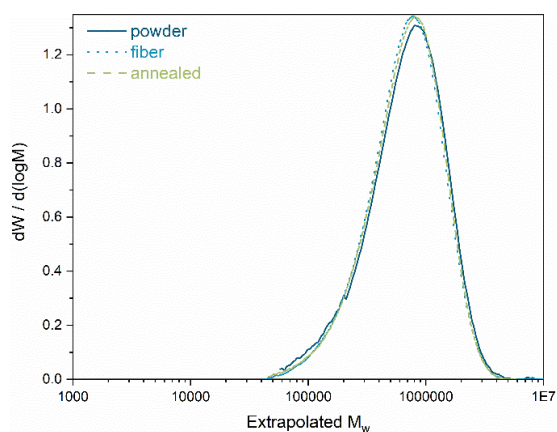
Figure S8: Molecular weight distribution of **iPP-3** (raw polymer, fiber and annealed fiber).

180
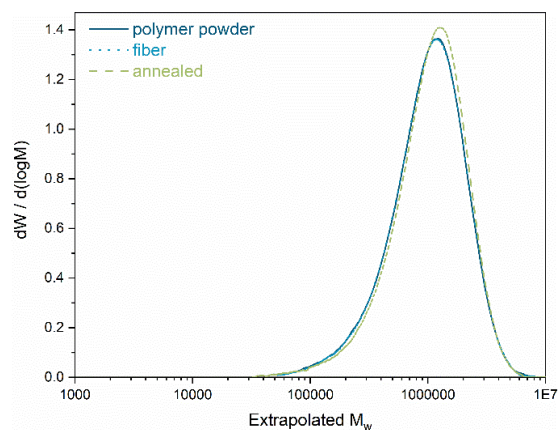
Figure S9: Molecular weight distribution of **iPP-4** (raw polymer, fiber and annealed fiber).
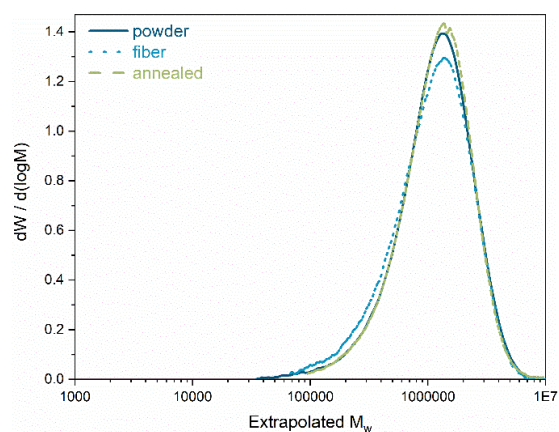
Figure S10: Molecular weight distribution of **iPP-5** (raw polymer, fiber and annealed fiber).
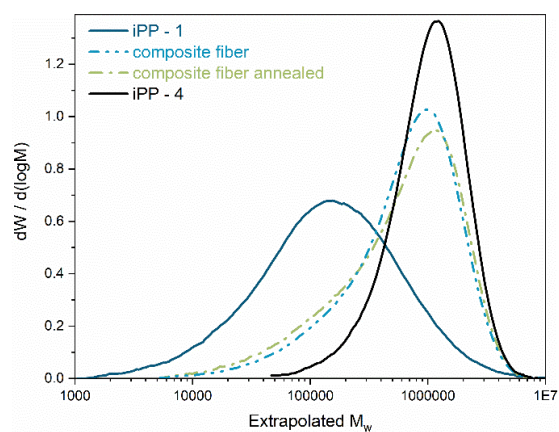
Figure S11: Molecular weight distribution of **composite fiber** (raw polymers **iPP-1** and **iPP-4**, composite fiber and annealed composite fiber).

181
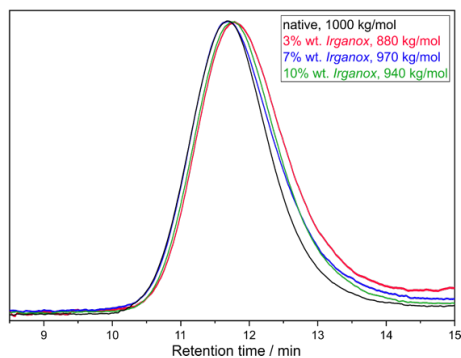
Figure S12: Elugram and molecular weight of a preliminary experiment using 1000 kg/mol iPP: screening for the required amount of stabilizing agent.
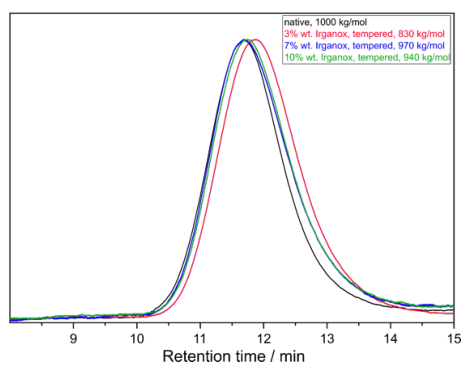
Figure S13: Elugram and molecular weight of a preliminary experiment using 1000 kg/mol iPP: Annealing/tempering at 140 °C for 20 h under Argon atmosphere.
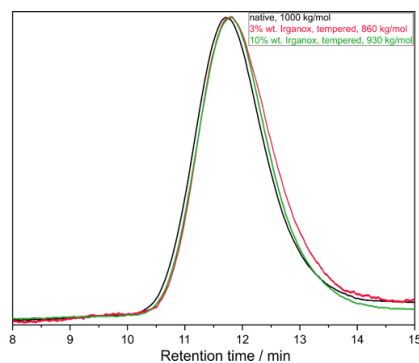
Figure S14: Elugram and molecular weight of a preliminary experiment using 1000 kg/mol iPP: Annealing/tempering at 150 °C for 67 h under Argon atmosphere.

S6
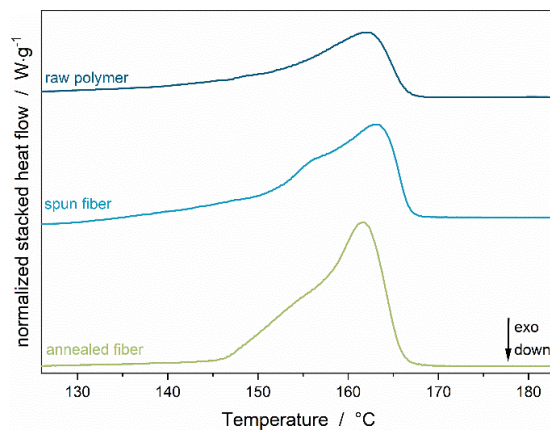
DSC Analysis

Figure S15: DSC analysis of **iPP-1** (raw polymer, fiber and annealed fiber).
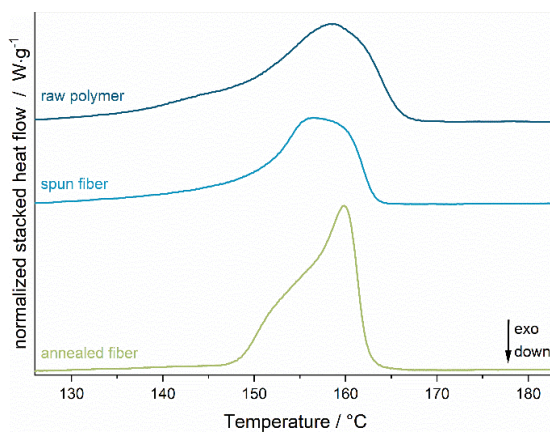
Figure S16: DSC analysis of **iPP-2** (raw polymer, fiber and annealed fiber).
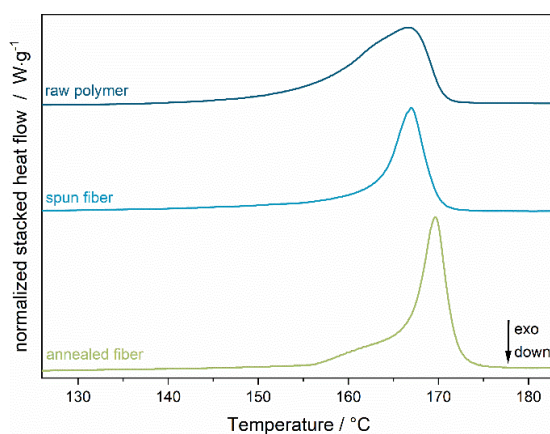
Figure S17: DSC analysis of **iPP-3** (raw polymer, fiber and annealed fiber).
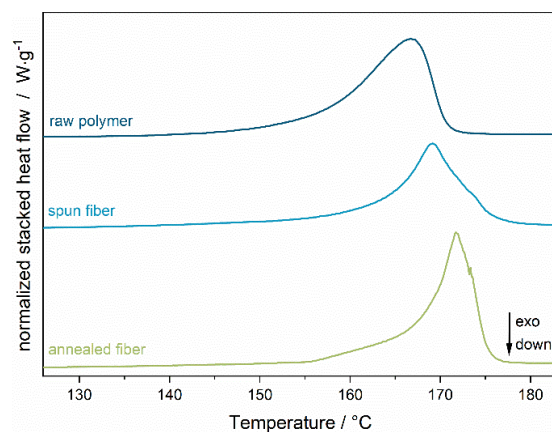
Figure S18: DSC analysis of **iPP-4** (raw polymer, fiber and annealed fiber).
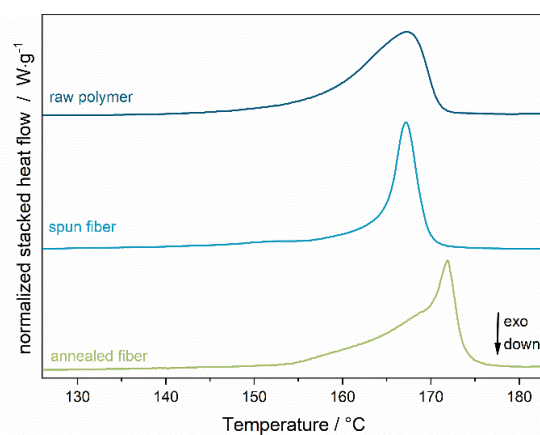
Figure S19: DSC analysis of **iPP-5** (raw polymer, fiber and annealed fiber).
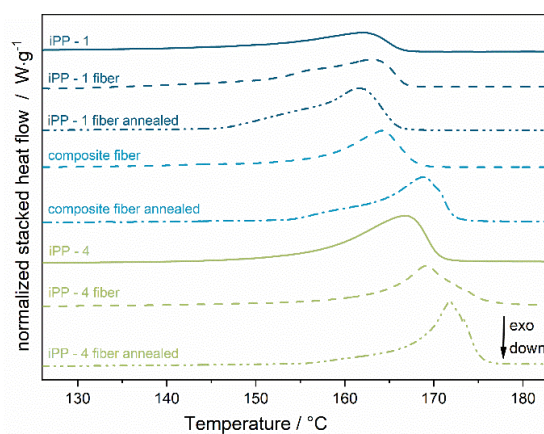
Figure S20: DSC analysis of **composite fiber** (raw polymers **iPP-1** and **iPP-4**, composite fiber and annealed composite fiber).
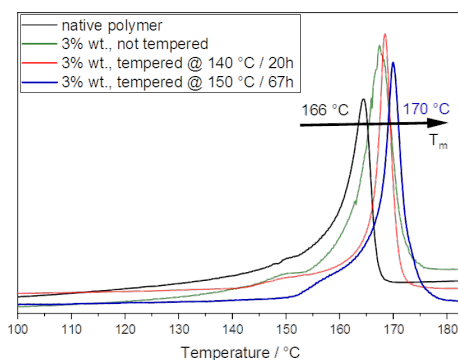
Figure S21: DSC analysis of a preliminary experiment using 1000 kg/mol iPP and 3 % wt. *Irganox 1010*: Annealing at 140 °C for 20 h and 150 °C for 67 h under Argon atmosphere.
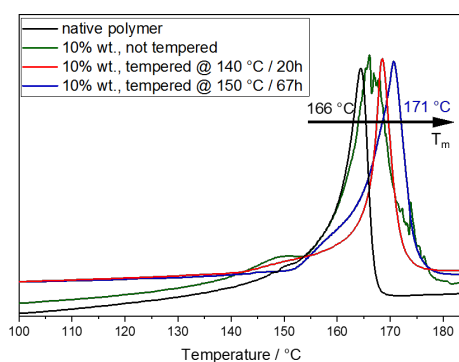
Figure S22: DSC analysis of a preliminary experiment using 1000 kg/mol iPP and 10 % wt. *Irganox 1010*: Annealing at 140 °C for 20 h and 150 °C for 67 h under Argon atmosphere.

Technical Drawings
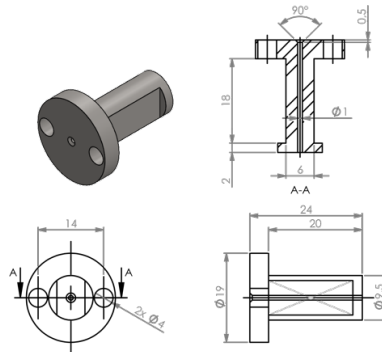
Figure S23: Technical drawing of **1 mm manufactured spinning nozzle**.
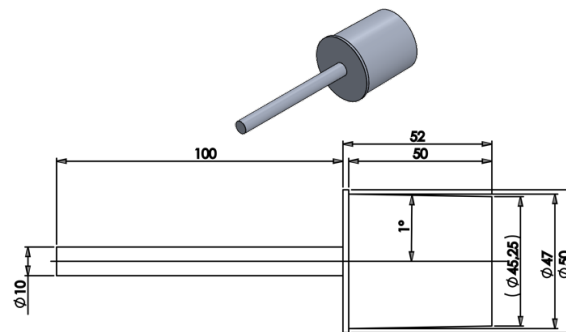
Figure S24: Technical drawing of **Fiber spinning cone 1**.
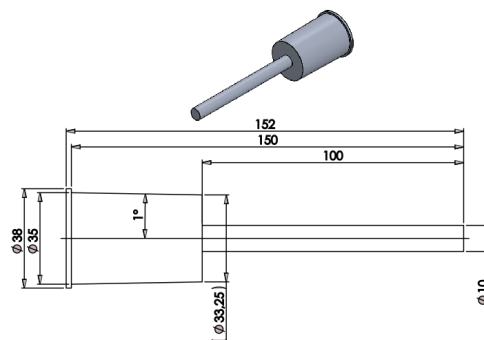
Figure S25: Technical drawing of **Fiber spinning cone 2**.

Optical light microscopy images

Figure S26: Thin fiber of **iPP-1**. Conditions: 1500 rpm extrusion speed, 350 rpm KPG stirrer spinning speed, 140 cm distance nozzle – cone, 1 mm manufactured spinning nozzle.
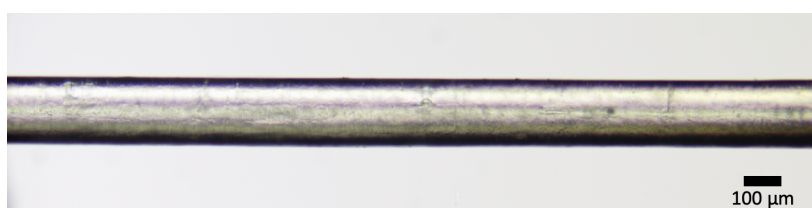
Figure S27: Thick fiber of **iPP-1**. Conditions: 800 rpm extrusion speed, 100 rpm KPG stirrer spinning speed, 55 cm distance nozzle – cone, 1 mm manufactured spinning nozzle.

Figure S28: Thin fiber of **iPP-2**. Conditions: 1400 rpm extrusion speed, 150 rpm KPG stirrer spinning speed, 30 cm distance nozzle – cone, 1 mm manufactured spinning nozzle.

Figure S29: Spun **iPP-2** fiber. Conditions: 1400 rpm extrusion speed, 100 rpm KPG stirrer spinning speed, 20 cm distance nozzle – cone, 1 mm manufactured spinning nozzle.

S11

Figure S30: Inhomogeneous spun **iPP-3** fiber. Conditions: 1400 rpm extrusion speed, 70 rpm KPG stirrer spinning speed, 20 cm distance nozzle – cone, 1 mm manufactured spinning nozzle.

Figure S31: Spun **iPP-3** fiber. Conditions: 1400 rpm extrusion speed, 78 rpm KPG stirrer spinning speed, 33 cm distance nozzle – cone, 2 mm extrusion nozzle.
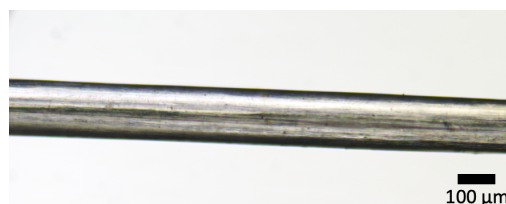
Figure S32: Spun **iPP-3** fiber. Conditions: 1400 rpm extrusion speed, 117 rpm KPG stirrer spinning speed, 37 cm distance nozzle – cone, 2 mm extrusion nozzle.

Figure S33: Drawn **iPP-4** fiber.

Figure S34: Spun **iPP-4** fiber. Conditions: 1500 rpm extrusion speed, 55 rpm KPG stirrer spinning speed, 18 cm distance nozzle – cone, 2 mm extrusion nozzle.

S12

Figure S35: Spun **iPP-4** fiber. Conditions: 1500 rpm extrusion speed, 55 rpm KPG stirrer spinning speed, 18 cm distance nozzle – cone, 2 mm extrusion nozzle.

Figure S36: Spun **iPP-4** fiber. Conditions: 1500 rpm extrusion speed, 120 rpm KPG stirrer spinning speed, 28 cm distance nozzle – cone, 2 mm extrusion nozzle.
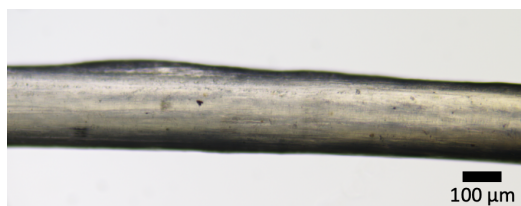
Figure S37: Spun **iPP-5** fiber. Conditions: 1500 rpm extrusion speed, 60 rpm KPG stirrer spinning speed, 25 cm distance nozzle – cone, 2 mm extrusion nozzle.

Figure S38: Spun **iPP-5** fiber. Conditions: 1500 rpm extrusion speed, 60 rpm KPG stirrer spinning speed, 25 cm distance nozzle – cone, 2 mm extrusion nozzle.

Figure S39: Spun **iPP-5** fiber. Conditions: 1500 rpm extrusion speed, 55 rpm KPG stirrer spinning speed, 23 cm distance nozzle – cone, 2 mm extrusion nozzle.

Figure S40: Spun **iPP-5** fiber. Conditions: 1500 rpm extrusion speed, 55 rpm KPG stirrer spinning speed, 20 cm distance nozzle – cone, 1 mm manufactured spinning nozzle.

Figure S41: Spun **iPP-5** fiber. Conditions: 1500 rpm extrusion speed, 55 rpm KPG stirrer spinning speed, 20 cm distance nozzle – cone, 1 mm manufactured spinning nozzle.

Figure S42: Spun **composite** fiber. Conditions: 1500 rpm extrusion speed, 78 rpm KPG stirrer spinning speed, 23 cm distance nozzle – cone, 1 mm manufactured spinning nozzle.

WAXS

Transmission mode wide-angle X-ray scattering (WAXS) data were collected using a Ganesha instrument (SAXSLAB) equipped with a Pilatus 300k (Dectris) area detector operating at an energy of 8.04 keV (1.54 Å), corresponding to the Cu-Kalpha radiation of the X-ray source (Xenocs GeniX3D). The samples were mounted at a sample-detector distance (SDD) of roughly 90.5 mm. The exact SDD was calculated for each sample individually, taking sample thicknesses into account. The samples were fixed in place by a sample holder from both ends, which in case of the fiber samples (extrudate, spun fiber, tempered fiber) ensured a perpendicular orientation of the macroscopic fiber direction to the incident beam (incident angle 0°). 'Fiber axis', as marked with arrows on the WAXS images, denotes the orientation of the fiber within this plane. Before recording the data, the flight tube was evacuated (5.02 × 10⁻³ mbar), to minimize contributions from air scattering. Fibers were aligned in the beam by scanning across the fiber by variation of the sample height and tracking the intensity of the WAXS signal.

WAXS data were recorded at two spots, spaced 1 mm apart along the samples, to ensure reliability of the results, as shown in Figure S43 (annotated images in the main text correspond to a), c), e) and g)). The differences between the measurements were found to be very small, indicating a high level of homogeneity within the samples. Image processing (summation, conversion to q-space, cuts along q) was done with the Matlab-based software GIXSGUI.[1] Phase identification and analysis of preferential orientation effects were done by analyzing cuts along q in the equatorial, meridional and direct beam (db) (111) directions (α-phase), as shown in Figure S44. For phase identification, reflections with the highest intensity were compared to the five most intense reflections of the α-, the two most intense reflections of the β-, and five most intense reflections of the γ-phase, as first referenced in (2). Each phase gives a scattering pattern including uniquely placed reflections (α: (130), β: (301), γ: (117)). All samples were found to be semicrystalline: an amorphous halo with sample-dependent intensity is seen in the q-range from 0.8 Å⁻¹ to 1.75 Å⁻¹.
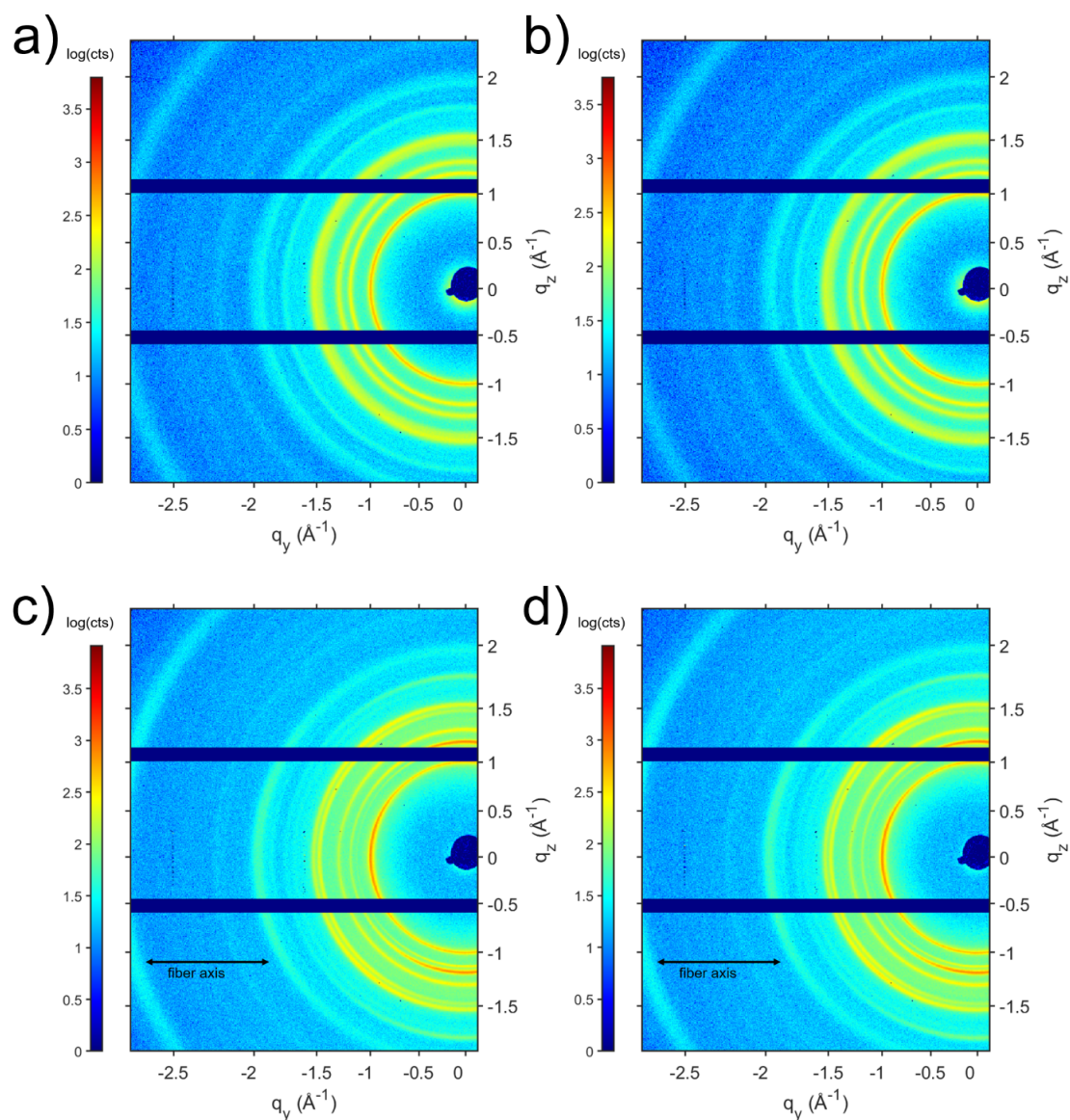
Figure S43: WAXS data corresponding to measurement spots spaced 1 mm from another to ensure the reliability of the results. The data sets correspond to UHMW **iPP-5** samples at different stages of the fiber manufacturing process. a), b) Raw polymer **iPP-5**. c), d) Extrudate.
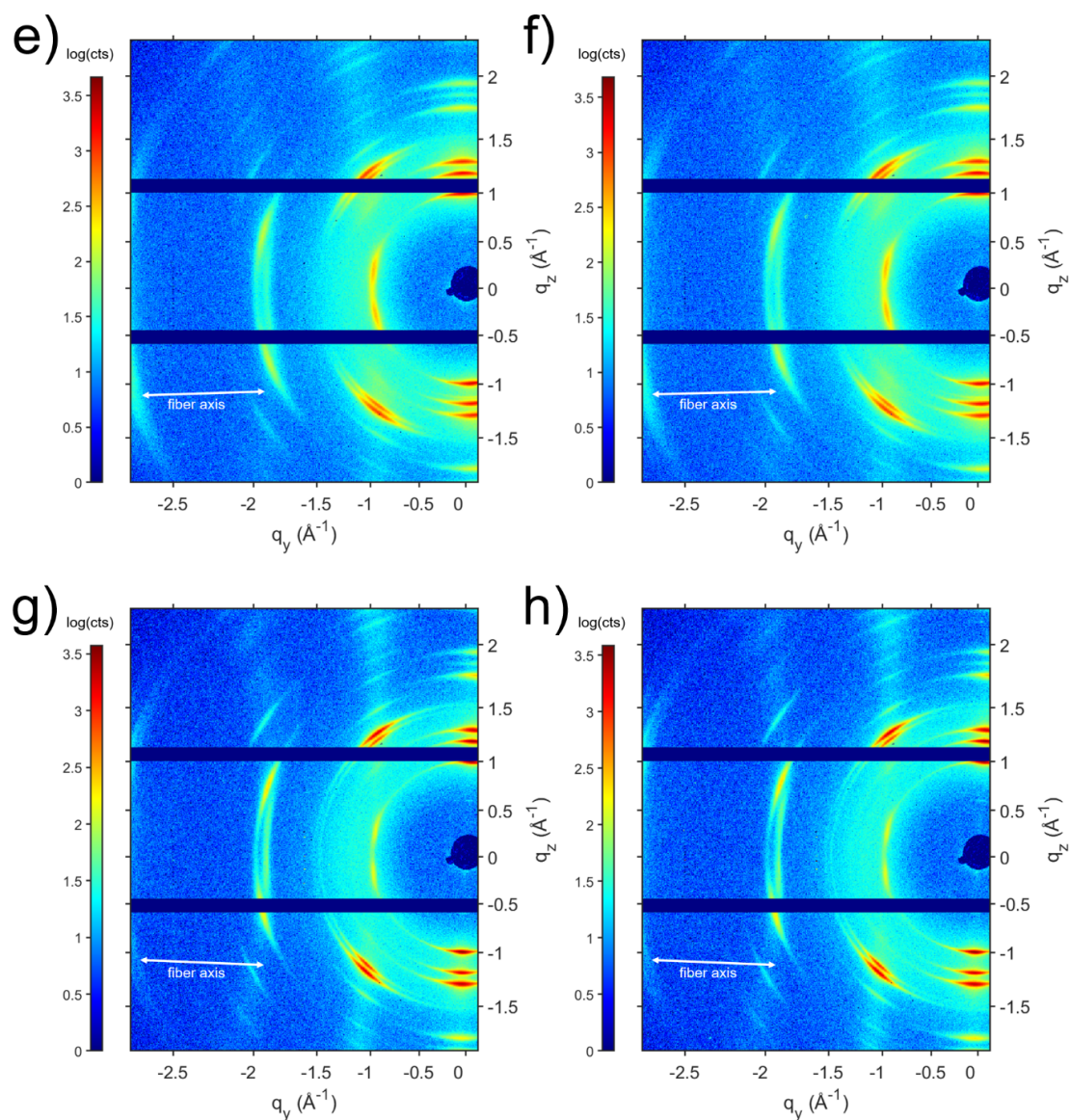
Figure S43: WAXS data corresponding to measurement spots spaced 1 mm from another to ensure the reliability of the results. The data sets correspond to UHMW **iPP-5** samples at different stages of the fiber manufacturing process. e), f) Spun fiber. g), h) Annealed fiber.
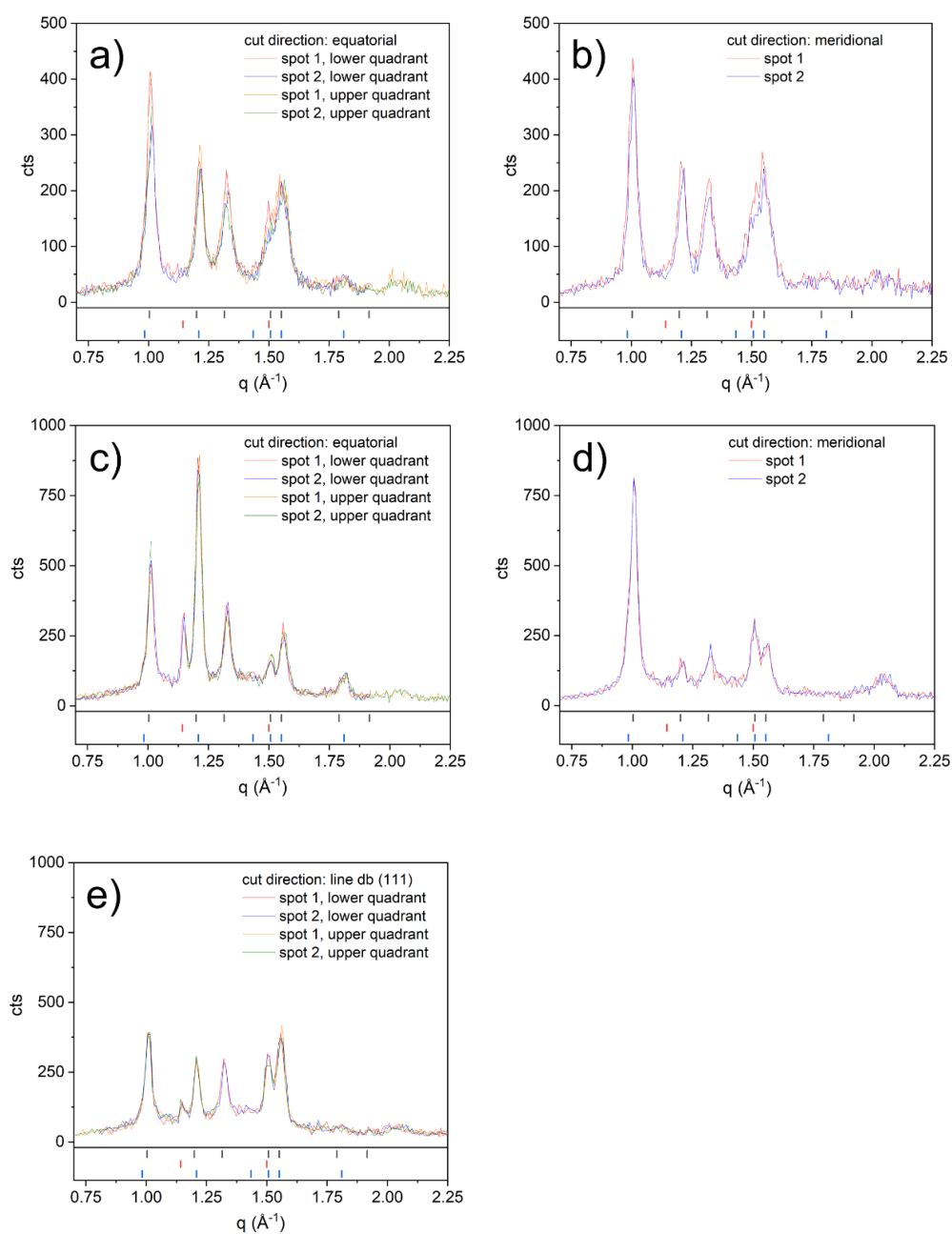
Figure S44: Equatorial (a) and meridional (b) cuts for the **iPP-5** raw polymer sample, as well as equatorial (c) and meridional (d) cuts, and cuts along the db (111) direction (α-phase) (e) for the **iPP-5** extrudate, for both measurement spots, and for lower and upper quadrant, if applicable. The positions of the most intense expected reflections of the α-, β- and γ-phase are marked in the rug plot in black, red, and blue, respectively.
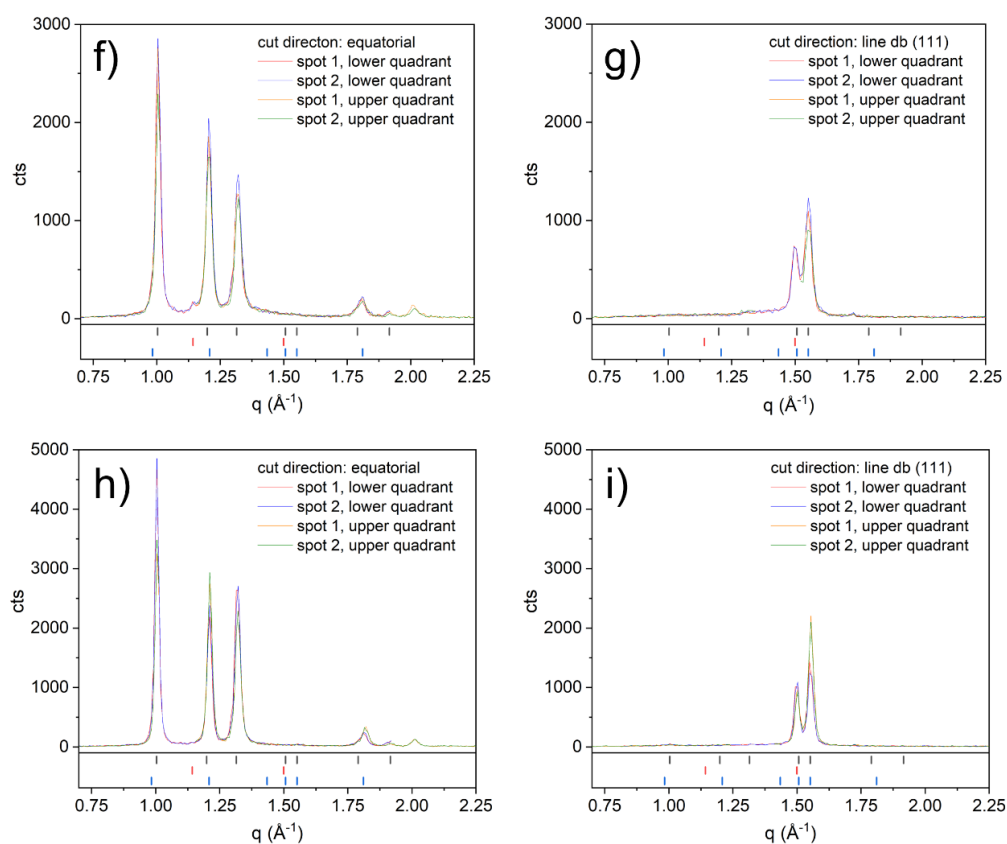
Figure S44: Equatorial (f) cuts and cuts along the db (111) direction (α-phase) (g) for the **iPP-5** spun fiber, as well as equatorial (h) cuts and cuts along the db (111) direction (α-phase) (i) for the **iPP-5** annealed fiber, for both measurement spots, and for lower and upper quadrant. The positions of the most intense expected reflections of the α-, β- and γ-phase are marked in the rug plot in black, red, and blue, respectively.

Applied Catalysts
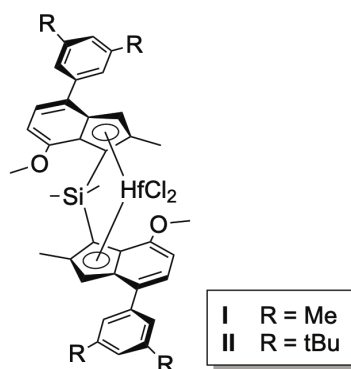
Figure S45. Benchmark catalyst system of *Rieger* et al. for tailoring isotactic polypropylene.[3,4]

References

(1) Jiang, Z. Gixsgui: a MATLAB toolbox for grazing-incidence X-ray scattering data visualization and reduction, and indexing of buried three-dimensional periodic nanostructured films. *J. Appl. Cryst.* **2015**, 48, 917-926.

(2) Turner-Jones, A.; Aizlewood, J. M.; Beckett, D. R. Crystalline forms of isotactic polypropylene. *Makromol. Chem*. **1964**, 75, 134-158.

(3) Schöbel, A.; Herdtweck, E.; Parkinson, M.; Rieger, B. Ultra-rigid metallocenes for highly iso- and regiospecific polymerization of propene: the search for the perfect polypropylene helix. *Chem. Eur. J.* **2012**, 18, 4174-8

(4) Machat, M. R.; Lanzinger, D.; Pöthig, A.; Rieger, B. Ultrarigid Indenyl-based Hafnocene Complexes for the Highly Isoselective Polymerization of Propene: Tunable Polymerization Performance Adopting Various Sterically Demanding 4-Aryl Substituents. *Organometallics* **2016**, 36, 399-408

10.1.4 Supporting Information for Chapter 7

Tailored syndiotactic polypropylene feedstock material for laser based powder bed fusion of polymers: material development and processability

Simon Cholewa,[a]‡ Lucas Stieglitz,[b]‡ Andreas Jaksch,[a] Bernhard Rieger*[b] and Dietmar Drummer*[a]

[a]Institute of Polymer Technology, Friedrich-Alexander-Universität Erlangen-Nürnberg, Am Weichselgarten 10, 91058 Erlangen-Tennenlohe, Germany. E-mail: dietmar.drummer@fau.de

[b]Wacker-Lehrstuhl für Makromolekulare Chemie, Catalysis Research Center, Technische Universität München, Lichtenbergstraße 4, 85748 Garching bei München, Germany. E-mail: rieger@tum.de

Table 1: Conditions and results for the polymerization of propylene with complex **I**[a]

entry	catalyst	n[b]	t_p[c]	P[d]	Y[e]
1	**I**	2.2	10	50000	42
2	**I**	1.6	15	38000	24
3	**I**	2.3	15	42000	33

[a]$V_{toluene}$ = 320 mL;   TIBA/TrBCF: initiator $[Ph_3C][B(C_6F_5)_4]$ = 5.0 eq.,   activator   (TIBA) = 200 eq.,   scavenger (TIBA) = 2.2 mmol; pressure p = p_{Ar} + $p_{propylene}$ = 6 bar, p_{Ar} = 1.3 bar; temperature T = 0 °C ± 2°C; [b]In micromoles. [c]Polymerization time in min. [d] Productivity in $kg_{PP} \cdot [mol_{cat} \cdot h]^{-1}$. [e]Polymer yield in g.

Figure S1. Precipitated **sPP** in the autoclave after polymerization with **I** (see entry 1-3, Table 1).
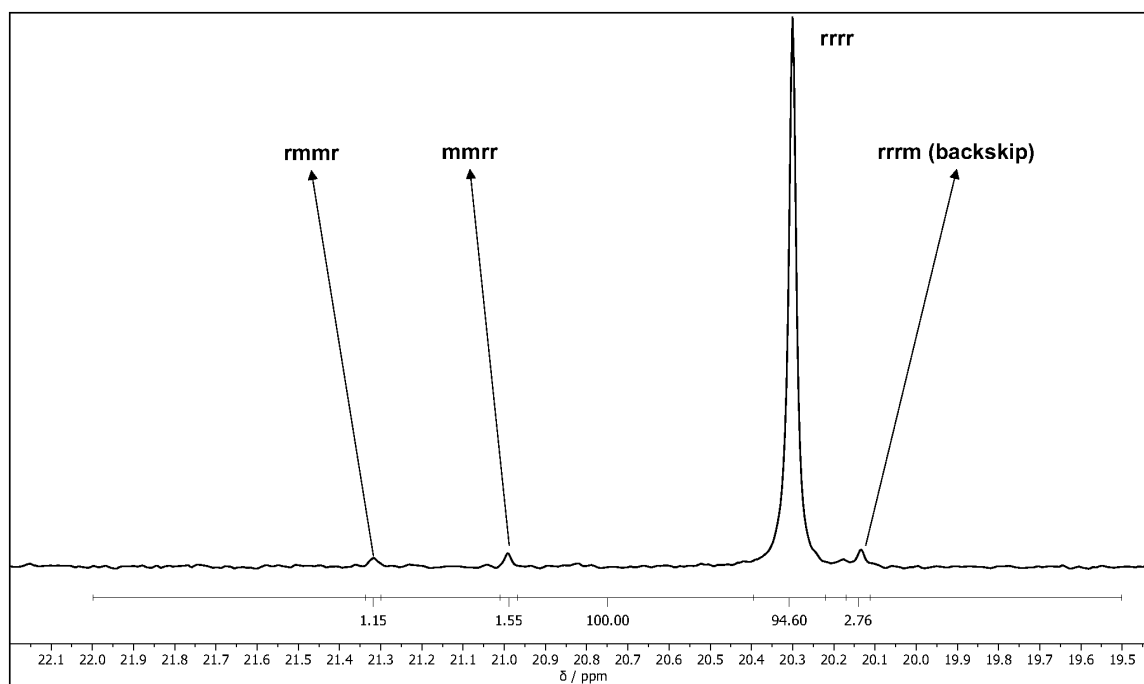
Figure S2: Pentad distribution of **I**-produced sPP in the ^{13}C NMR spectrum.

Typical crucial process for fulfilling the potential and determining the mechanical behavior are part bed temperature T_b, laser power P_L, hatch distance, layer thickness L_t scan speed v_s. To compare process parameters, the volume energy E_V is in Eq. 1

$$E_V = \frac{P_L}{v_s * h_s * L_t}$$
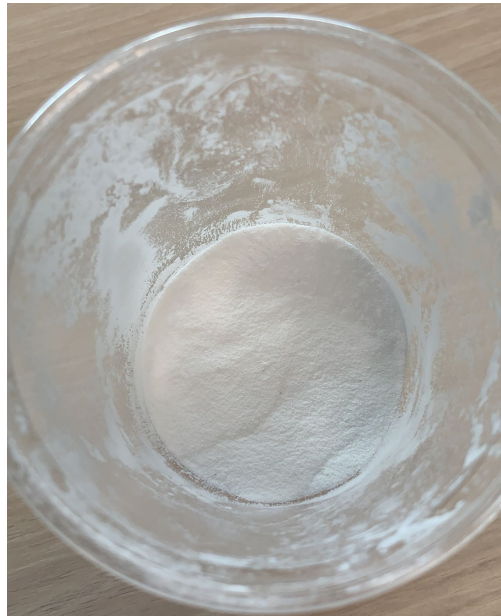
Figure S3. sPP particles before processing
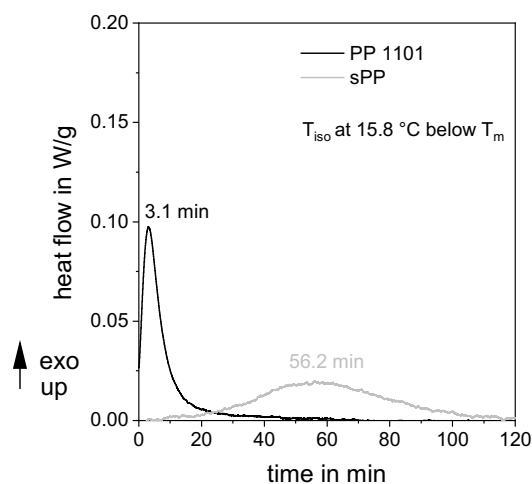
Figure S4. Comparison of isothermal crystallization between sPP and commercial powder PP1101 at comparable isothermal holding temperatures of 15.8 °C below the melting peak T_m (measured at a heating rate of 10 K/min)

Observations indicate that PP1101 undergoes crystallization prior to achieving the designated holding temperature. In comparison to PP101, sPP displays a significantly slower crystallization progress. Exhibiting crystallization progress (as measured by t peak) for sPP is 56.2 minutes versus 3.1 minutes for PP101.
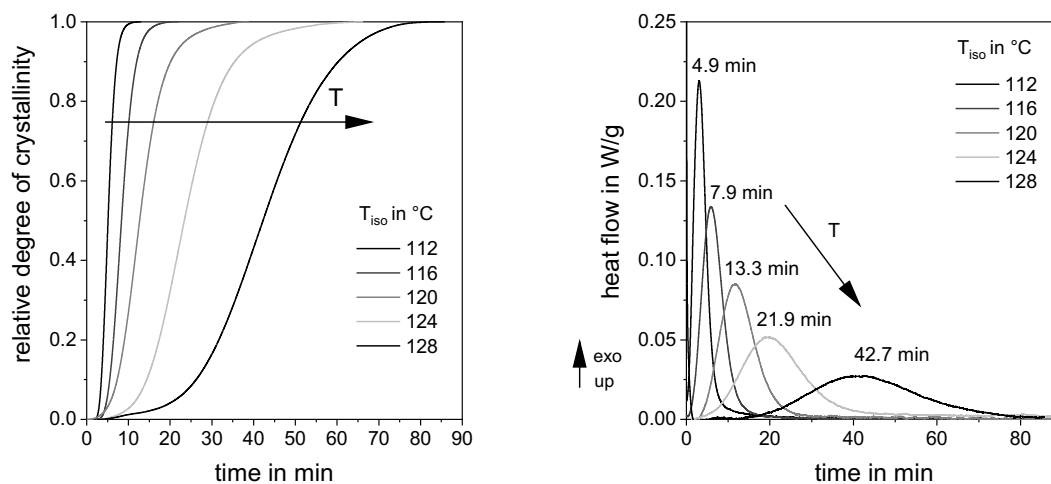
Figure S5. Isothermal DSC measurements for sPP. Relative degree of crystallinity over time (left) and corresponding exothermic heat flow (right)
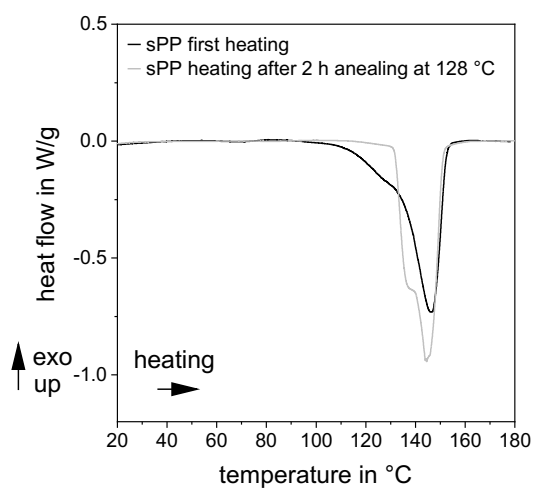
Figure S6. Dynamic DSC measurement with a heating rate of 10 K/min after annealing at 128 °C (building bed temperature) for 2 h (blue line) and first heating cycle for sPP (black line)

Rheological experiments:

Carreau-Yasuda Model

Function
$$y = A_2 + (A_1 - A_2)[1 + (tx)^a]^{\frac{n-1}{a}}$$

Meanings: *A1* = zero shear viscosity, *A2* = infinite shear viscosity, *t* = time constant, *a* = transition control factor, *n* = power index

For all Carreau fits the R-squared was higher than 0.99. Detailed information's depicted in table 2

Table 2: Carreau fit parameters

Temperature	A1	A2	t	a	n
T_m	19142 ± 865	33.27 ± 1216	0.032 ± 0.09	0.6 ± 0.02	0 ± 1.06
$T_{m+10 K}$	13096 ± 618	0 ± 1299	0.02 ± 0.07	0.57 ± 0.18	0 ± 1.45
$T_{m+20 K}$	9196 ± 329	0 ± 1025	0.0 ± 0.05	0.58 ± 0.16	0 ± 1.41
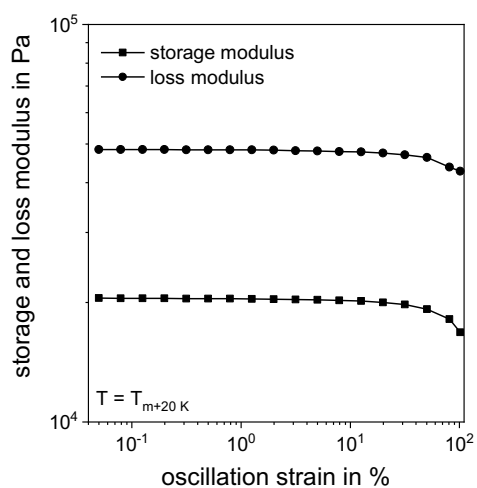
Figure S7. Amplitude sweep at 6.28 rad/s for the determination of the linear viscoelastic range

205
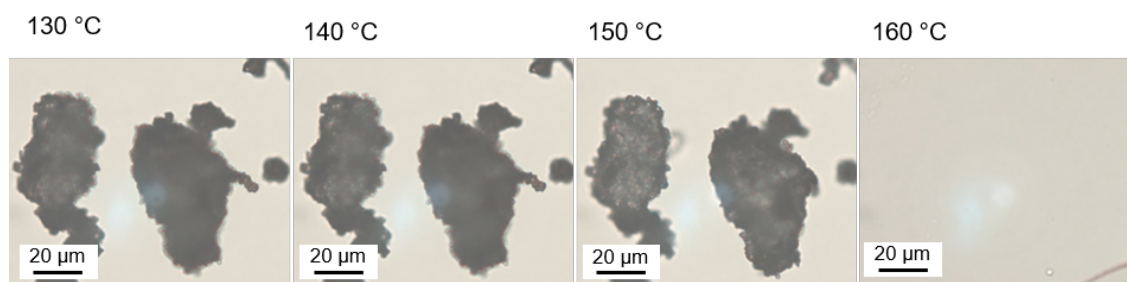
Figure S8

Powder particle coalescence detected by hot stage microscopy with a constant heating rate of 1 K/min
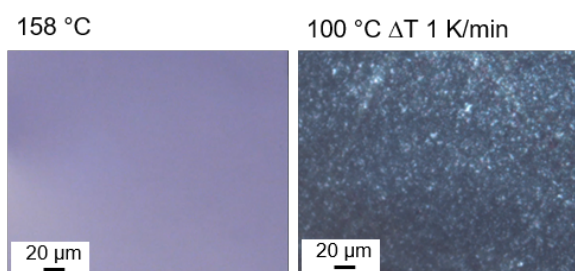
Figure S9. Hot stage image in polar field of a melt film at 158 °C (left) with subsequent cooling of 1 K/min at 100 °C (right). Photographs are intended to show that no crystallites are detected at 158 °C and thereby the particles have melted completely

Figure S10. Lateral view of the multilayer component

10.2 Reprint Permissions for Copyright Material

Figure 4 was reprinted with permission from Ref.[84] Copyright © 2005 by the American Chemical Society.

Figure 1 was reprinted with permission from Ref[5] R. Geyer, J. R. Jambeck, K. L. Law, *Sci. Adv.* **2017**, *3*, e1700782. Reprinted with permission from Ref[5]. Copyright © the authors, some rights reserved; exclusive licensee AAAS. Distributed under a CC BY-NC 4.0 License (http://creativecommons.org/licenses/by-nc/4.0/). "This is an open-access article distributed under the terms of the Creative Commons Attribution-NonCommercial license, which permits use, distribution, and reproduction in any medium, so long as the resultant use is not for commercial advantage and provided the original work is properly cited."

Figure 8 was reprinted with permission from Ref.[130] Copyright © 1991 by Elsevier.

209

Figure 9 was reprinted with permission from Ref.[137]. Copyright © 2019 by Springer.

Figure 10 was reprinted with permission from Ref.[160]. Copyright © 2014 by Wiley.

211

Figure 11 was reprinted with permission from Ref.[166]. Copyright © 2007 by Wiley.

The contents for Chapter 4 and the corresponding Supporting Information in Chapter 10.1.1 for the manuscript titled "*In Situ* Activation: Chances and Limitations to Form Ultrahigh Molecular Weight Syndiotactic Polypropylene with Metallocene Dichlorides" have been reprinted with permission from Ref.[218]. Copyright © 2021 by the American Chemical Society.

The contents for Chapter 5 and the corresponding Supporting Information in Chapter 10.1.2 for the manuscript titled "Perfectly Isotactic Polypropylene upon *In Situ* Activation of Ultrarigid *meso* Hafnocenes" have been reprinted with permission from Ref.[220]. Copyright © 2022 by John Wiley and Sons.

The contents for Chapter 6 and the corresponding Supporting Information in Chapter 10.1.3 for the manuscript titled "Fiber Spinning of Ultrahigh Molecular Weight Isotactic Polypropylene: Melt Spinning and Melt Drawing" do not require a copyright from Ref.[221], as the open access article is distributed under the terms of the Creative Commons CC BY license, which permits unrestricted use, distribution, and reproduction in any medium. provided the original work is properly cited.

The contents for Chapter 7 and the corresponding Supporting Information in Chapter 10.1.4 for the manuscript titled "Tailored Syndiotactic Polypropylene Feedstock Material for Laser-Based Powder Bed Fusion of Polymers: Material Development and Processability" have been reprinted with permission from Ref.[219]. Copyright © 2023 by the American Chemical Society.

CCC
RightsLink

🏠 Home   ❓ Help ⌄   📞 Live Chat   👤 Lucas Stieglitz ⌄

Tailored Syndiotactic Polypropylene Feedstock Material for Laser-Based Powder Bed Fusion of Polymers: Material Development and Processability

ACS Publications
Most Trusted. Most Cited. Most Read.

Author: Simon Cholewa, Lucas Stieglitz, Andreas Jaksch, et al
Publication: ACS Applied Polymer Materials
Publisher: American Chemical Society
Date: Mar 1, 2023

Copyright © 2023, American Chemical Society

PERMISSION/LICENSE IS GRANTED FOR YOUR ORDER AT NO CHARGE

This type of permission/license, instead of the standard Terms and Conditions, is sent to you because no fee is being charged for your order. Please note the following:

- Permission is granted for your request in both print and electronic formats, and translations.
- If figures and/or tables were requested, they may be adapted or used in part.
- Please print this page for your records and send a copy of it to your publisher/graduate school.
- Appropriate credit for the requested material should be given as follows: "Reprinted (adapted) with permission from {COMPLETE REFERENCE CITATION}. Copyright {YEAR} American Chemical Society." Insert appropriate information in place of the capitalized words.
- One-time permission is granted only for the use specified in your RightsLink request. No additional uses are granted (such as derivative works or other editions). For any uses, please submit a new request.

If credit is given to another source for the material you requested from RightsLink, permission must be obtained from that source.

BACK   CLOSE WINDOW

10.3 Statutory Declaration

Ich, Lucas Stieglitz, erkläre an Eides statt, dass ich die bei der promotionsführenden Einrichtung

TUM School of Natural Sciences

der TUM zur Promotionsprüfung vorgelegte Arbeit mit dem Titel:

Ultrahigh Molecular Weight Polypropylene – Synthesis and Processing of a High-Performance Polymer

unter der Anleitung und Betreuung durch: Prof. Dr. Dr. h. c. Bernhard Rieger ohne sonstige Hilfe erstellt

und bei der Abfassung nur die gemäß §7 Abs. 6 und 7 angegebenen Hilfsmittel benutzt habe.

☒ Ich habe keine Organisation eingeschaltet, die gegen Entgelt Betreuer*innen für die Anfertigung von

Dissertationen sucht, oder die mir obliegenden Pflichten hinsichtlich der Prüfungsleistungen für mich ganz

oder teilweise erledigt.

☒ Ich habe die Dissertation in dieser oder ähnlicher Form in keinem anderen Prüfungsverfahren als

Prüfungsleistung vorgelegt.

☐ Teile der Dissertation wurden in _____ veröffentlicht.

☒ Ich habe den angestrebten Doktorgrad noch nicht erworben und bin nicht in einem früheren Promo-

tionsverfahren für den angestrebten Doktorgrad endgültig gescheitert.

☐ Ich habe bereits am _____ bei der promotionsführenden Einrichtung

_____ der Hochschule

_____ unter Vorlage einer Dissertation mit dem Thema

_____ die Zulassung zur Promotion beantragt mit dem Ergebnis:

_____

☒ Ich habe keine Kenntnis über ein strafrechtliches Ermittlungsverfahren in Bezug auf wissenschaftsbezo-

gene Straftaten gegen mich oder eine rechtskräftige strafrechtliche Verurteilung mit Wissenschaftsbezug.

Die öffentlich zugängliche Promotionsordnung sowie die Richtlinien zur Sicherung guter wissenschaftlicher

Praxis und für den Umgang mit wissenschaftlichem Fehlverhalten der TUM sind mir bekannt, insbeson-

dere habe ich die Bedeutung von §27 PromO (Nichtigkeit der Promotion) und §28 PromO (Entzug des

Doktorgrades) zur Kenntnis genommen. Ich bin mir der Konsequenzen einer falschen Eidesstattlichen

Erklärung bewusst.

Mit der Aufnahme meiner personenbezogenen Daten in die Alumni-Datei bei der TUM bin ich

☒ einverstanden,　　　　　☐ nicht einverstanden.

_____

München, 29.03.2023